Superchaotropic Polyoxometalates – From Fundamental Investigations Towards Potential Applications

Dissertation

Zur Erlangung des Doktorgrades der Naturwissenschaften (Dr. rer. nat.)

der Fakultät für Chemie und Pharmazie der

Universität Regensburg

submitted by

Philipp Schmid

from Eglsee

August 2022

The practical work was performed from November 2019 until May 2022 at the Institute of Inorganic Chemistry at the University of Regensburg in the working group of Prof. Dr. Arno Pfitzner and at the Insitut de chimie séparative de Marcoule (ICSM, France) in the group of Dr. Pierre Bauduin during two research stays in December 2019 and January 2022.

This work was supervised by Prof. Dr. Arno Pfitzner.

Submission of the PhD thesis: August 03, 2022

Date of the oral exam: October 24, 2022

Examination Committee:

Chairman: Prof. Dr. Frank-Michael Matysik

1st Examiner: Prof. Dr. Arno Pfitzner

2nd Examiner: Dr. habil. Pierre Bauduin

Further examiner: Prof. Dr. Werner Kunz

»Wenn es überhaupt eine gute Idee gibt,
dann die Idee der Skepsis gegenüber allen guten Ideen.«

***Gerhard Polt**,*
bayerischer Kabarettist und Schauspieler

»Die Gaudi is' mir ernst!«

Josef Menzl,
bayerischer Volksmusikant und Kapellmeister

Acknowledgement

First and foremost, I would like to express my sincere gratitude to my PhD supervisor Prof. Dr. Arno Pfitzner who made this thesis possible. His style of supervision combining large freedom, to develop my own ideas, with great support and guidance in the decisive moments during the last three years enabled countless unsurpassed opportunities.

I would like to express my heartly thanks to my second PhD supervisor Dr. Pierre Bauduin, without whom this PhD would also have been impossible. His supervision, support and patience with scientific problems, and especially with me, created a perfect atmosphere for our Bavarian-French collaboration.

I am grateful to Prof. Dr. Werner Kunz for his contribution as third examiner of this thesis, that he introduced me to the world of colloids during my COSOM studies and for our collaboration on POM co-assembly with hydrotropes. Likewise, I am thankful to Prof. Dr. Frank-Michael Matysik for his participation in the committee of the PhD defense.

I heartly thank Dr. Olivier Diat and Dr. Didier Touraud for our numerous collaborations and for their continuous support, advice, help and fruitful discussions on every imaginable (scientific) question.

I am heartly thankful to Dr. Thomas Buchecker for paving the way for superchaotropic polyoxometalates from Marcoule to Regensburg, introducing me to the topic and his guidance, especially in my young years of being a chemist. Likewise, I heartly thank Dr. Max Hohenschutz for our collaboration on POM self-assembly phenomena.

I am deeply grateful to my master and bachelor students and research interns Gasper Jost, Martin Schmauser, Xaver Graß, Melissa Janesch, Michael Witzmann, Seyedehelahe Bagherimetkazini, Philipp Brand, Christoph Bruckschlegel, Katharina Poiger, Selina Reigl and Maximilian Widmann who contributed with crucial experiments to different topics.

I am heartfully thankful to Bianca Frömel and Katharina Trögl who cared about all administrative issues, which I could not have been able to handle myself.

I am very thankful to Dr. Marc Schlosser for our close collaboration in our practical lab courses and for letting me enjoy one of the driest and at the same time funniest humors.

I am grateful to the technical staff at the University of Regensburg: Ulrike Schießl, Ferdinand Gigl, Florian Truksa and Joachim Rewitzer for their outstanding technical and administrational support.

Of course, I want to thank all my colleagues at the Institute of Inorganic Chemistry, University of Regensburg: Salil Bal, Elisabeth Bauer, Serkan Damnali, Dr. Claudia De Giorgi, Dr. Sebastian Fäth, Daniela Garcia, Bastian Höfler, Jasmin Hüller, Elisabeth Huf, Franziska Kamm, Dr. Christian Klimas,

Michael Kulschar, Dr. Ria Mandal, Maximilian Obermeier, Heidi Paulus, Dr. Florian Pielnhofer, Dr. Igor Plokhikh, Susan Rank, Martin Rosenhammer, Rafal Samp, Sven Schedlowski, Julian Schiller, Martin Schmid, Michael Stammler, Felix Uhlig, Florian Wegner and Dr. Florian Wisser.

I also want to thank Dr. Pierre Bauduin, Dr. Olivier Diat, Dr. Luc Girard, Dr. Max Hohenschutz, Alban Jonchère, Dr. Isabelle Grillo and Dr. Sebastian Mühlbauer for their priceless help and expertise during the very exhausting SANS-runs at the Institut Laue-Langevin (ILL) in Grenoble and the Forschungs-Neutronenquelle Heinz Maier-Leibnitz (FRM II) in Munich.

Some very special thanks go to my lab mate Dr. Maximilian Sehr with whom I spent these three years in a common laboratory and who gave me advice in every life situation – professional and private. I also would like to express my gratitude to Dr. Christoph Meier-Rümmele for our Schafkopf nights and our friendship.

I am grateful to all my friends who support me whenever it is needed. In particular, I want to thank Jonas Blahnik, Evamaria Hofmann, Maximilian Röhrl and Simon Stemplinger for their friendship and constant support during our studies.

Last but not least, I deeply thank my parents Johann and Elisabeth Schmid, my brother Bastian Schmid and my girlfriend Lilly Graßl for their love, encouraging support, continuous confidence in me and patience with me during these three years and my whole life.

THANK YOU!

Preface

This thesis aims at the characterization and discussion of superchaotropic polyoxometalates, covering different studies on fundamental aspects towards concepts for applications. For this reason, the present thesis was written so that each chapter can be read independently. Therefore, each chapter is shaped according to usual conventions: Abstract, Introduction, Results and Discussion, Conclusion, Bibliography (and Supporting Information). The different studies led to works which are published or ready to submit. These contributions, including all Co-Authors, are summarized in the following Table. A complete list of scientific contributions is given in chapter 9.

Chapter	Publication
2	P. Schmid, X. Graß, P. Bahadur, I. Grillo, O. Diat, A. Pfitzner, P. Bauduin; Polymeric Surfactant P84/Polyoxometalate α-$PW_{12}O_{40}^{3-}$ – A Model System to Investigate the Interplay between Chaotropic and Hydrophobic Effects. *Colloids and Interfaces* **2022**, *6(1)*, 16.
3	P. Schmid, T. Buchecker, A. Koshsima, D. Touraud, O. Diat, W. Kunz, A. Pfitzner, P. Bauduin; Self-assembly of a short amphiphile in water controlled by superchaotropic polyoxometalates: $H_4SiW_{12}O_{40}$ *vs.* $H_3PW_{12}O_{40}$. *Journal of Colloid and Interface Science* **2021**, *587*, 347-357.
4	P. Schmid, M. Hohenschutz, X. Graß, M. Witzmann, D. Touraud, O. Diat, A. Pfitzner, P. Bauduin; Counterion effect on α-Keggin polyoxometalates in water: the peculiar role of H^+ on their salting-in effect and co-assembly with organics. *Journal of Molecular Liquids* **2022**, *359*, 119214.
5	P. Schmid, D. Touraud, M. Hohenschutz, O. Diat, A. Pfitzner, P. Bauduin; The potential role of chaotropic polyoxometalates in the origin of life. *Nature Chemistry* **2022**, ready to submit.
6	P. Schmid, X. Graß, D. Touraud, A. Pfitzner, P. Bauduin; A paradox: Hydrophilic molecular metal-oxides are selective solubilizers for moderately hydrophobic compounds. *Chemical Communications* **2022**, ready to submit.
7	P. Schmid, G. Jost, X. Graß, D. Touraud, O. Diat, A. Pfitzner, P. Bauduin; {2-Phases 2-reactions 1-catalyst} concept for the sustainable performance of coupled reactions. *Green Chemistry* **2022**, *24*, 2516-2526.

Abstract

In 2015, the remarkable propensity of low charge density nanometric ions, *e.g.* anionic boron clusters or polyoxometalates (POMs), to bind strongly non-covalently to neutral, solvated organic (molecular) surfaces in aqueous solution, was reported. Their binding was explained by a solvent-mediated driving force – called the superchaotropic (SC) effect: hydration water molecules of the weakly hydrated nanometric ion and the surface moieties of the organic substrate are partially released to the bulk water upon their association. Therefore, the SC effect is an entropy (release of H_2O molecules to bulk) and enthalpy (regain of H-bonds in bulk water) driven phenomenon which is discussed as an extension of the well-known Hofmeister series observed for classical chaotropic ions, such as SCN^- or I^-.

Even though the general concept of the SC effect is now well accepted in the scientific community, countless phenomena related to superchaotropicity and the combination of the SC effect of POMs with some of their outstanding properties, *e.g.* catalytic activity, molecular magnetism, application in medicine, biology or material science are barely investigated so far. Therefore, the intention of this thesis is to extend the fundamental knowledge of the SC effect of POMs and to exploit their superchaotropic property for potential applications.

For this purpose, diverse organic substances in aqueous solution served as model systems to investigate the effect of SC POMs within the framework of this thesis. The hydrophobic character of the organic substance was successively increased from rather hydrophilic polymeric surfactants, over partially water-miscible hydrotropes and short-chain alcohols to water-immiscible long-chain alcohols. The investigation of such complex multinary systems (ternary (water-substrate-POM) up to quinternary (water-substrate-POM-additive 1-additive 2)) requires a broad spectrum of (analytical) techniques and methods, which were applied in this thesis, namely: cloud point measurements, microscopy, manifold scattering and diffraction experiments, diverse types of spectroscopic, computational and further standard techniques.

The targeted combination and detailed evaluation of the aforementioned techniques allows us to portray fundamental aspects related to superchaotropicity, such as *(i)* the selective binding of SC POMs to block copolymers (chapter 2), *(ii)* the co-assembly of SC POMs with a partially water-miscible hydrotrope (chapter 3), *(iii)* counterion effects in the SC effect of POMs and its implications for classical Hofmeister effects (chapter 4), *(iv)* the potential role of chaotropicity in the origin of life (chapter 5), as well as potential applications: *(v)* SC POMs as selective, functional solubilizers for moderately hydrophobic molecules (chapter 6) and *(vi)* low charge density POMs as catalysts for a new sustainable approach in chemical synthesis (chapter 7).

Kurzfassung

2015 wurde die bemerkenswerte Eigenschaft von nanometrischen Ionen mit niedriger Ladungsdichte, *z.B.* anionische Borcluster und Polyoxometallate (POMs), berichtet, stark und nicht-kovalent an neutrale, solvatisierte organische (molekulare) Oberflächen in wässriger Lösung zu binden. Diese Assoziation wurde durch eine Solvens-vermittelte Triebkraft – den sogenannten superchaotropen (SC) Effekt – erklärt: Wassermoleküle aus der Hydrathülle des schwach hydratisierten nanometrischen Ions und bestimmter Oberflächeneinheiten des organischen Substrats werden durch ihre Bindung teilweise an das Volumenwasser abgegeben. Der SC-Effekt ist damit ein Entropie- (Abgabe von H_2O Molekülen an Volumenwasser) und Enthalpie-getriebenes (Wiedergewinnung von H-Brücken im Volumenwasser-Netzwerk) Phänomen, das als Erweiterung der hochbekannten Hofmeister-Reihe diskutiert wird.

Wenngleich das allgemeine Konzept des SC-Effekts inzwischen in der wissenschaftlichen Gemeinschaft wohl akzeptiert ist, sind unzählige Phänomene im Zusammenhang mit Superchaotropie und der Kombination des SC-Effekts von POMs mit deren herausragenden Eigenschaften, wie *z.B.* katalytische Aktivität, molekularer Magnetismus, Anwendungen in Medizin, Biologie oder Materialwissenschaften bisher kaum erforscht. Ziel dieser Arbeit ist es daher, das grundlegende Wissen über den SC-Effekt von POMs zu erweitern und ihre superchaotrope Eigenschaft für potenzielle Anwendungen zu nutzen.

Zu diesem Zweck dienen in dieser Arbeit unterschiedliche organische Substanzen in wässriger Lösung als Modellsysteme, um die Wirkung von SC-POMs zu untersuchen. Der hydrophobe Charakter der organischen Substanz wurde dabei von eher hydrophilen polymeren Tensiden, über teilweise mit Wasser mischbare Hydrotrope und kurzkettige Alkohole, bis hin zu mit Wasser nicht mischbaren langkettigen Alkoholen sukzessive erhöht. Die Untersuchung solch komplexer, multinärer Systeme (ternär (Wasser-Substrat-POM) bis hin zu quinternär (Wasser-Substrat-POM-Additiv 1-Additiv 2)) erfordert ein breites Spektrum an (analytischen) Methoden, nämlich: Trübungspunktmessungen, Mikroskopie, vielfältige Streuungs- und Beugungsexperimente, diverse Formen der Spektroskopie, Computer-gestützte Methoden und weitere Standardtechniken.

Die gezielte Kombination und detaillierte Auswertung der aufgeführten Techniken ermöglicht es, nachfolgend grundlegende Aspekte der Superchaotropie zu porträtieren: *(i)* die selektive Bindung von SC-POMs an Blockcopolymere (Kap. 2), *(ii)* die Co-Assemblierung von SC-POMs mit teils Wasser-mischbaren Hydrotropen (Kap.3), *(iii)* Gegenioneneffekte im SC-Effekt von POMs und deren Bedeutung für klassische Hofmeister-Effekte (Kap. 4), *(iv)* die potentielle Rolle der Chaotropie bei der Entstehung des Lebens (Kap. 5), sowie potenzielle Anwendungen: *(v)* SC-POMs als selektive, funktionelle Lösungsvermittler für mäßig hydrophobe Moleküle (Kap. 6) und *(vi)* niedrig geladene POMs als Katalysatoren für einen neuen, nachhaltigen Ansatz für organische Reaktionen (Kap. 7).

Table of Contents

1 Introduction 1

1.1 Polyoxometalates – an introduction 1

1.2 Specific ion effects 3

1.3 Superchaotropicity of nano-ions 7

1.4 Goals of this thesis and synopsis 10

1.4.1 Extension: The interaction of POMs with organic molecules 11

1.4.2 Superchaotropic POMs in unconventional ion effects and the origin of life 12

1.4.3 Applications of low charge density polyoxometalates 13

1.5 Bibliography 14

2 Polymeric surfactant P84/polyoxometalate α-$PW_{12}O_{40}^{3-}$ - A model system to investigate the interplay between chaotropic and hydrophobic effects 22

2.1 Preface and Abstract 22

2.2 Introduction 23

2.3 Experimental section 25

2.4 Results and Discussion 27

2.4.1 P84: Phase diagram and aggregation 27

2.4.2 P84: Cloud point evolution upon addition of HPW 28

2.4.3 Association of HPW with P84 unimers 29

2.4.4 Association of HPW with P84 micelles 31

2.5 Conclusion 33

2.6 Bibliography 34

3 Self-assembly of a short amphiphile in water controlled by superchaotropic polyoxometalates: $H_4SiW_{12}O_{40}$ *vs.* $H_3PW_{12}O_{40}$ 38

3.1 Preface and Abstract 38

3.2 Introduction 39

3.3 Experimental section 42

3.4 Results and Discussion 43

3.4.1 POMs in diluted C_3P_2 aqueous solution 43

3.4.2 Investigation of $[POM]_m[C_3P_2]_n$ colloids 49

3.4.3 Effect of POMs on concentrated C_3P_2 solution 53

3.5 Conclusion 58

3.6 Bibliography 59

4 Counterion effect on α-Keggin polyoxometalates in water: the peculiar role of H^+ on their salting-in effect and co-assembly with organics 63

4.1 Preface and Abstract 63
4.2 Introduction 64
4.3 Experimental section 67
4.4 Results and Discussion 68
4.4.1 CP evolution upon POM addition and inhibition of POM-hydrolysis 68
4.4.2 Counterion effects on POM/C_3P_2 assembly 73
4.4.3 How to turn salting-out anions into salting-in anions? 76
4.5 Conclusion 77
4.6 Bibliography 78

5 The potential role of chaotropic polyoxometalates in the origin of life 83

5.1 Preface and Abstract 83
5.2 Introduction 84
5.3 Experimental section 85
5.4 Results and Discussion 86
5.5 Conclusion 89
5.6 Supporting Information 90
5.6.1 Investigations on phosphotungstate speciation 90
5.6.2 Oxidation of C_3P_2 as counter reaction of phosphotungstate reduction 93
5.6.3 SAXS spectra and data processing 95
5.6.4 Adaption to day/night cycle 99
5.7 Bibliography 101

6 A paradox: Hydrophilic molecular metal-oxides are selective solubilizers for moderately hydrophobic compounds 105

6.1 Preface and Abstract 105
6.2 Introduction 106
6.3 Experimental section 107
6.4 Results and Discussion 108
6.5 Conclusion 115
6.6 Supporting Information 116
6.6.1 Additional solubilization measurements and data treatment 116
6.6.2 ^{1}H-NMR experiments 120
6.6.3 SAXS spectra and data fitting 123
6.6.4 Bathochromic shift of POM-aromatic molecules solutions 133

6.7 Bibliography 138

7 {2-phases 2-reactions 1-catalyst} concept for the sustainable performance of coupled reactions 143

7.1 Preface and Abstract 143
7.2 Introduction 144
7.3 Experimental section 146
7.4 Results and Discussion 149
7.4.1 Distribution of α-Keggin POMs in biphasic water:alcohol systems 149
7.4.2 Oxidation in the organic phase: Organic synthesis 152
7.4.3 Oxidation in the organic phase: Degradation of dyes 153
7.4.4 Reduction in the aqueous phase: Metal recovery 154
7.4.5 Reduction in the aqueous phase: UV-light controlled complexometry 155
7.4.6 Combined oxidation-reduction reactions 157
7.4.7 Applicability, economy and sustainability of {2-phases 2-reactions 1-catalyst} 157
7.5 Conclusion 158
7.6 Bibliography 160

8 Conclusion and Outlook 165

8.1 Discussion 165
8.2 Bibliography 169

9 List of scientific contributions 172

10 Declaration of Authorship 175

1 Introduction

1.1 Polyoxometalates – an introduction

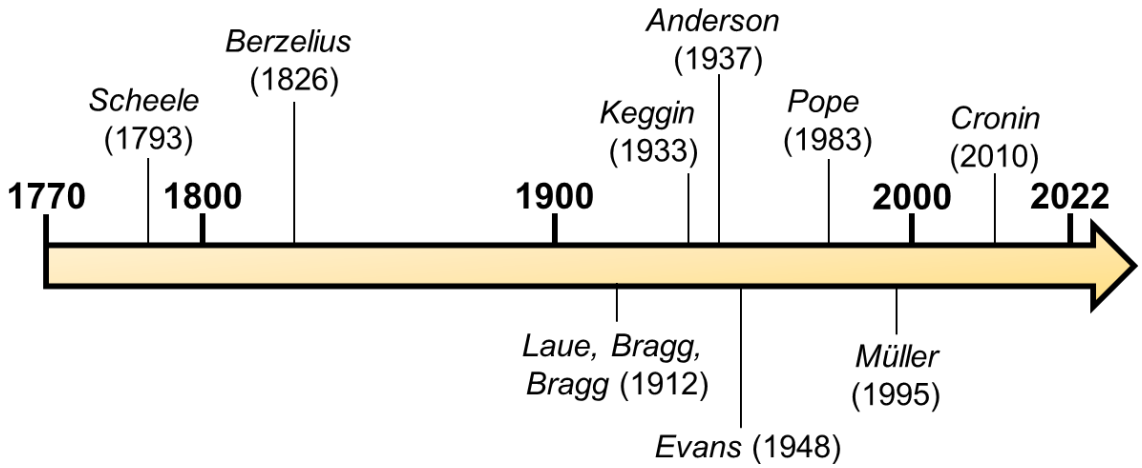

Figure 1.1. Timeline showing the most important scientists, who contributed with decisive findings to POM chemistry including the year of their key publication.

Polyoxometalate (POM) chemistry has emerged already in the late 18th century when Carl Wilhelm Scheele occasionally noticed the deep blue color of the famous "molybdenum blue" – nowadays a summary term for diverse species of reduced Mo-POMs – during his research on the element Molybdenum.[1,2] In 1826, Jöns Jakob Berzelius demonstrated the first synthesis of a POM compound via precipitation from aqueous solution.[3] Based on this finding, leading chemists around the world attempted to understand and characterize the precise structure and composition of POMs and pave the way for targeted POM synthesis.[4–6] Only the discovery of the principles of X-ray diffraction methods, such as single crystal X-ray diffraction and X-ray powder diffraction, by Max von Laue[7] and William Henry Bragg[8]/William Lawrence Bragg[9] in 1912 and the rapid development of these techniques enabled to solve those tasks. Finally, in 1933 James Fargher Keggin successfully solved the chemical structure of the probably most famous POM, the phosphotungstic acid hydrate, $H_3PW_{12}O_{40} \cdot xH_2O$.[10] In honor of his finding, this POM structure was named after its explorer, *i.e.* Keggin-structure. The identification of further well-known POM structures followed immediately by John Stuart Anderson (1937)[11] and Howard Tasker Evans (1948).[12] Later, in the early 1980s, Michael Thor Pope presented POM science to a broad audience with the publication of his book entitled "Heteropoly and Isopoly Oxometalates".[13] In the 1990s, Achim Müller exploited this deep knowledge on POMs to access synthetic routes towards "gigantic" (> 1 nm) POMs.[14] The understanding of POM synthesis was further deepened in the 2000s/2010s by Leroy Cronin who enabled the production of asymmetric (hybrid) POM clusters.[15] This compendium on the emergence and evolution of POM chemistry is graphically shown in the

timeline in Fig. 1.1. A similar, but more detailed timeline on the POM research development is given by Rosnes *et al*.[6]

Nowadays, POMs are in general described as ionic (poly-)condensates of (octahedral) metal-oxo (M-O) units of early transition metals in high oxidation states (d^0 and d^1). In particular group V and VI metals, *i.e.* V, Nb, Ta, Mo and W are found, while V, Mo and W represent the most common transition metals, which are incorporated in POMs.[16,17] If polyoxometalates are exclusively built by one metal-oxo type they are called homopolyanions. In contrast, POMs containing *p*-block elements in their center(s), *e.g.* B, Al, Si, Ge, P, As, Sb, Te or I, are called heteropolyanions.[13] It is worth to note that literature also reports on cationic metal-oxo polyions in very few cases.[18–20]

The enormous versatility of POMs already manifests in the existence of diverse sizes and architectures. A typical representative of sub-nm POMs is the so-called Lindquist-type[21,22] (*e.g.* $Mo_6O_{19}^{2-}$, $\{Mo_6\}$)[23] which consists of six edge-sharing M-O octahedra, see Fig. 1.2a. A similar sized POM type is described by the Anderson-Evans-structure.[24] With an approximate diameter of 1 nm, the Keggin-structure, the most famous POM structure, is shown in Fig. 1.2b. Here, the metal-oxo octahedra share corners, as well as edges. By removing a triade of edge-sharing M-O octahedra and condensing two equivalents of the remaining metal-oxo cluster, the nanometric Wells-Dawson-structure[25] is reached, see Fig. 1.2c. More recently, much emphasis was laid upon the synthesis of gigantic polyoxometalates and a prestigious race for the largest POMs was aroused. Especially Achim Müller and some of his former students (*e.g*. Leroy Cronin, Tianbo Liu, *etc.*) took a leading role. Müller himself discovered the famous $\{Mo_{154}\}$ cluster which is composed of 154 Mo-O

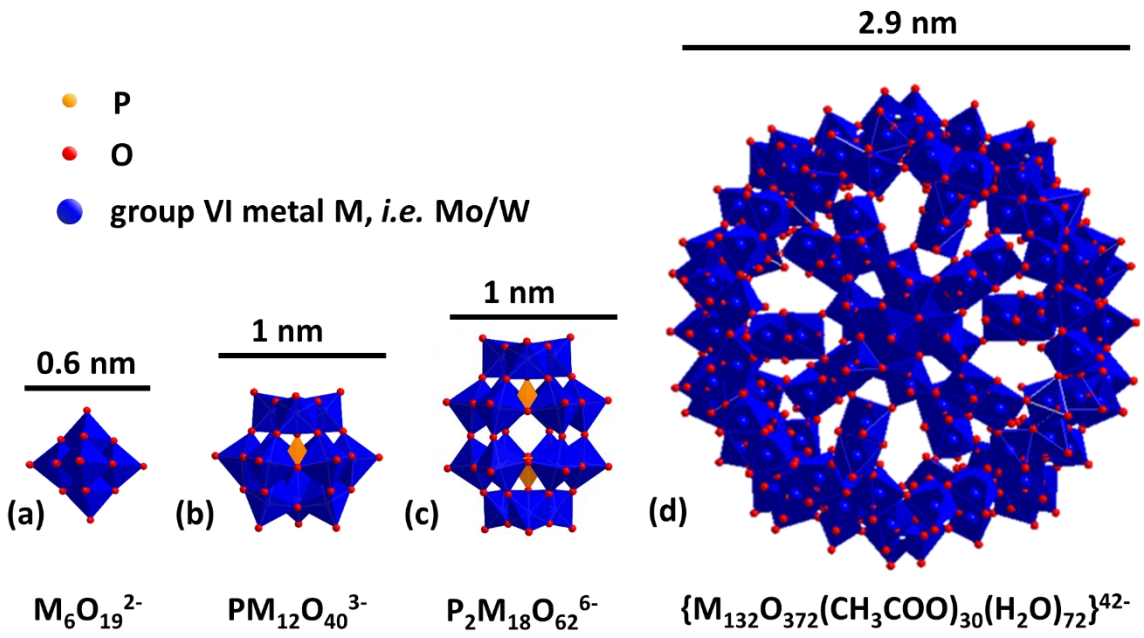

Figure 1.2. Four representative molecular structures of important polyoxometalates, namely (a) Lindquist-, (b) Keggin-, (c) Wells-Dawson- and (d) Keplerate-type and their relative sizes. The focus in this thesis is put on Keggin-type POMs, see (b). Molecular structures are drawn to scale.

polyhedra, forming a solid torus ("donut structure") with an inner diameter of roughly 2 nm and an outer diameter of 3.6 nm, respectively.[14] It is worth to mention that these gigantic {Mo_{154}} POMs, among other molybdenum blues, are built by 126 Mo^{VI}-O polyhedra as well as 28 Mo^{V}-O octahedra, leading to their strong blue colour.[26] Cronin succeeded to incorporate a {Mo_{36}} homopolyanion (> 1 nm, unofficially known as Krebs-structure[27,28]) into the core of such a solid torus POM.[26] Furthermore, the existence of the ball-shaped Keplerate POMs (*e.g.* $\{Mo_{132}O_{372}(CH_3COO)_{30}(H_2O)_{72}\}^{42-}$, {$Mo_{132}$}, approximate diameter of 2.9 nm) in aqueous solution could be demonstrated experimentally, see Fig. 1.2d.[29] Nevertheless, it was left to Müller again, to synthesize the largest POM, and subsequently also the largest known inorganic molecular compound: the lemon-shaped {Mo_{368}} cluster, with a maximum diameter of 6 nm and a molar mass of roughly 62,000 g mol^{-1}.[30] The finding of {Mo_{368}} was entitled "Inorganic Chemistry goes Protein Size" which can be impressively visualized by comparing its molar mass to the molar mass of the well-known oxygen-transporter protein hemoglobin (*ca.* 64,000 g mol^{-1}).[31]

Owing to the structural variety (sizes, architectures), in line with their electronic versatility (heteroatoms, $metal^{VI}$/$metal^{V}$ species, *etc.*), POMs are found in many applications. For example, they are commonly used as (photo-)catalysts in diverse reaction processes,[32–35] in biology[36,37] and medicine,[38–40] in molecular and composite materials[41–43] and in the treatment of radioactive waste.[44] Their remarkable magnetic properties[45,46] are used for quantum computing applications[47] and their peculiar solution behavior[48] can be exploited to perform site-specific protein crystallography/precipitation.[49,50]

1.2 Specific ion effects

Already during the 19th century, the influence of salts on macromolecules and living tissue in aqueous solution has been intensively investigated. Indeed, the pioneer of specific ion or salt effects, Franz Hofmeister, explored the remarkable property of salts to precipitate/solubilize proteins from/in aqueous solution in the year 1888. Depending on the type of salt, *i.e.* rather the term "salt effect" than "ion effect" is correct within their literal meaning, and its concentration, Hofmeister found an increase or decrease of the protein solubility, called salting-in and salting-out, respectively.[51] To obtain an independent ranking of ions according to their salting-in/out property, he fixed the salt`s cation-type and varied the anion-type and *vice versa*.[52] The qualitative ordering of ions in this "Hofmeister series" is shown in Fig. 1.3, which separates salting-in and salting-out ions. For further discussion, the focus is made on the Hofmeister series of anions, while details on the Hofmeister series of cations are given *e.g.* in ref. [52]. Kosmotropic anions, such as phosphate, PO_4^{3-}, were found to decrease the protein solubility strongly, *i.e.* to lead to precipitation (salting-out). Chaotropic anions, such as thiocyanate, SCN^-, were shown to increase the protein solubility

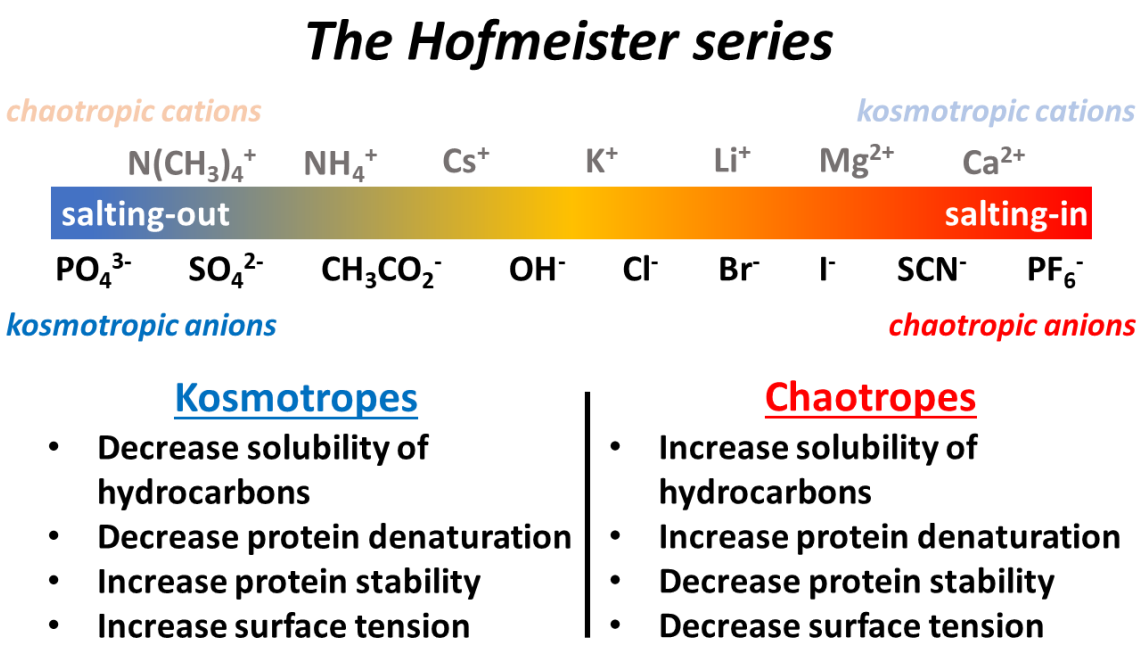

Figure 1.3. Classical Hofmeister series of cations and anions and their influence on solution properties, such as surface tension, solubility of hydrocarbons and their effect on the denaturation of proteins. Image adapted and redesigned from Werner Kunz.[52]

(salting-in). As a first approximation, kosmotropic (sometimes also referred to as anti-chaotropic) anions are highly charged, strongly hydrated and commonly discussed as hard ions (according to Pearson`s hard and soft acids and bases (HSAB) concept[53]). Chaotropes, on the contrary, are lowly charged, weakly hydrated and known as soft ions according to the HSAB concept.

The general concept of Hofmeister series was extended and shown to be valid not only for aqueous protein solutions but also for many different solutes, such as polymers,[54–58] micellar systems,[59,60] polymeric surfactants,[61] hydrotropes,[62,63] vesicular assemblies[64] and many more.[52,65] Even though the Hofmeister series concept is applicable for such a broad spectrum of solutes, its understanding on an atomistic scale was constantly developed.

A first attempt for an explanation was the relation of chaotropic anions as “water-structure breaker” and kosmotropic anions as “water-structure maker”.[52,64,66] These ideas were dismissed again, as it was shown theoretically that neither chaotropes nor kosmotropes affect the water network structure beyond their first two layers of hydration water (maximum distance 0.5 nm from ion center).[67–69] Specific ion effects were therefore proposed to arise from interfacial effects.[70–72] Indeed, ions were found to interact with interfaces, as they affect the surface tension of water-air[73–75] and water-oil:[76] chaotropes decrease the surface tension and kosmotropes increase the surface tension. In general, kosmotropes are repelled from hydrophobic surfaces while chaotropes are attracted.[77,78] As a conclusion, specific ion effects or Hofmeister effects result from the subtle balance of different parameters:[52]

(i) Charge density of an ion[79]

(ii) Ion polarizability and the related dispersion forces[80]

(iii) Counter-cations may affect specific ion effects of anions[81]

(iv) Nature of the substrate (*e.g.* global and local charges on macromolecules, hydrophobic character, surface patches, *etc.*) and the accompanied solvation structure

(v) Common physicochemical parameters, such as concentration, pH, ionic strength, intermolecular attraction or repulsion (*e.g.* Coulomb interactions or π-stacking), temperature

This large list of parameters implies that the prediction of specific ion effects is a challenging task. Consequently, simple but efficient tools to forecast ion behavior were searched for a long time and finally Kim Collins established the "law of matching water affinities" (also known as Collins` concept), see Fig. 1.4.[82]

Collins approximates ions as spherical objects with a point charge in their center. Kosmotropic ions are represented by small, highly hydrated spheres, exhibiting a high charge density. On the contrary, large, weakly hydrated spheres with a low charge density are referred to as chaotropic ions. As a first assumption, it is reasonably considered that oppositely charged ions are attracted and evenly charged ions are repelled from each other, driven by Coulombic forces. The hydration of ions acts as a repulsive force between oppositely charged ions keeping them separated and is quantified by their free energy of hydration. Small ions with high charge densities, *i.e.* kosmotropes, exhibit strongly bound water molecules in their hydration shell and therefore the motional freedom of hydration water is decreased, leading to an entropic penalty. Large ions with low charge density,

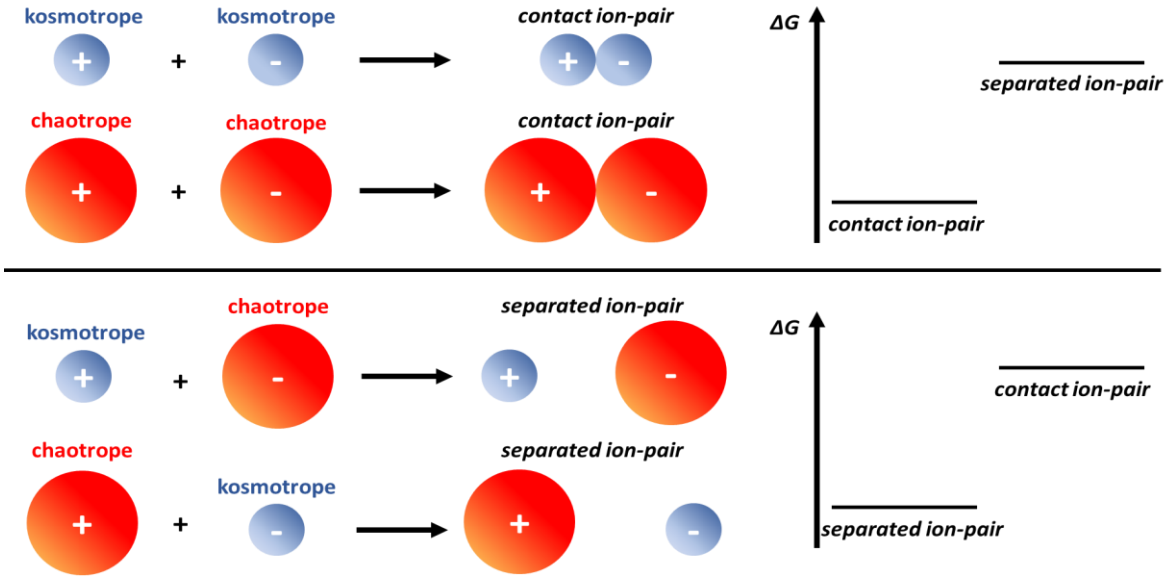

Figure 1.4. Scheme of the law of matching water affinities as proposed by Collins. Oppositely charged ions (represented by spherical objects with a point charge) attract each other due to Coulomb`s law. Nevertheless, contact ion-pairs are only formed by ions of similar hydration, *i.e.* kosmotrope-kosmotrope or chaotrope-chaotrope. The combination of kosmotrope-chaotrope and *vice versa* leads to separated ion-pairs. This scheme is inspired by Iwahara *et al.*[83]

i.e. chaotropes, show a loosely bound hydration shell leading to an entropically favorable (high motional freedom of water) solvation.[84–86] Anions are in general more strongly hydrated than cations, as the H-bond (H_{water}-anion) is stronger than the interaction O_{water}-cation.[87,88] Nevertheless, the free energy of hydration is similar for two small or big oppositely charged ions, whereas the free energy of hydration for oppositely charged ions of different size differs strongly.

In his theoretical concept, Collins assumes that free energy of hydration is an opposing force to Coulombic attraction. For example, two oppositely charged kosmotropic ions are attracted (Coulomb), but the free energy of hydration still needs to be overcome. Indeed, for two kosmotropes this energy is expended, and the formation of a contact ion-pair occurs (except for 1:1 salts). For two chaotropes, the Coulomb attraction is weaker compared to kosmotropes, but also their free energy of hydration is lower and therefore contact ion-pair formation appears. For the combination of a kosmotropic cation and a chaotropic anion, and *vice versa*, the free energy of hydration cannot be overcome, and separated ion-pairs are present.

As a conclusion, the law of matching water affinities allows to predict the formation of contact ion-pairs by considering electrostatic forces, free energy of hydration and entropy. According to this concept, contact ion-pairs are formed for oppositely charged ions of similar hydration energy and separated ion-pairs for ions of different hydration energy.

In 2004, Leontidis and co-workers extended the law of matching water affinities to the interaction of ionic species with organic, hydrophobic solutes, *i.e.* lipids.[71] They described the potential association of ions with lipids as a battle for interfacial sites and hydration water. In fact, large chaotropic anions were proposed to adsorb on lipid surfaces as both provide a similar free energy of hydration. Kosmotropes, on the contrary, are not expected to interact with such organic solutes as they show strong differences in the hydration shell binding. This concept was further supported by theoretical studies which examined the adsorption propensity of ions on macroscopic surfaces providing different charge and polarizability.[70,89]

According to the law of matching water affinities and its extension made by Leontidis, the adsorption of chaotropic ions to neutral (more or less) hydrophobic molecular surfaces can be explained. It is worth to note here that hydrophobicity/hydrophilicity *per se* is a qualitative, arbitrary concept which enables only to compare different solutes/surfaces. Hydrophobicity/hydrophilicity is difficult to express quantitatively and subsequently a general distinction between hydrophilic and hydrophobic molecules is problematic to access. Fully in line with this limitation, it was found that chaotropic anions do not interact with small hydrophilic monomers, *e.g.* ethylene glycol (PEG-1), but they strongly bind to larger surfaces as provided by polymers and oligomers, *e.g.* oligoethylene glycol (PEG-*n*), which comprise several repetition units of PEG-1. For example, SCN^- does not associate with PEG-1, but it strongly associates with the

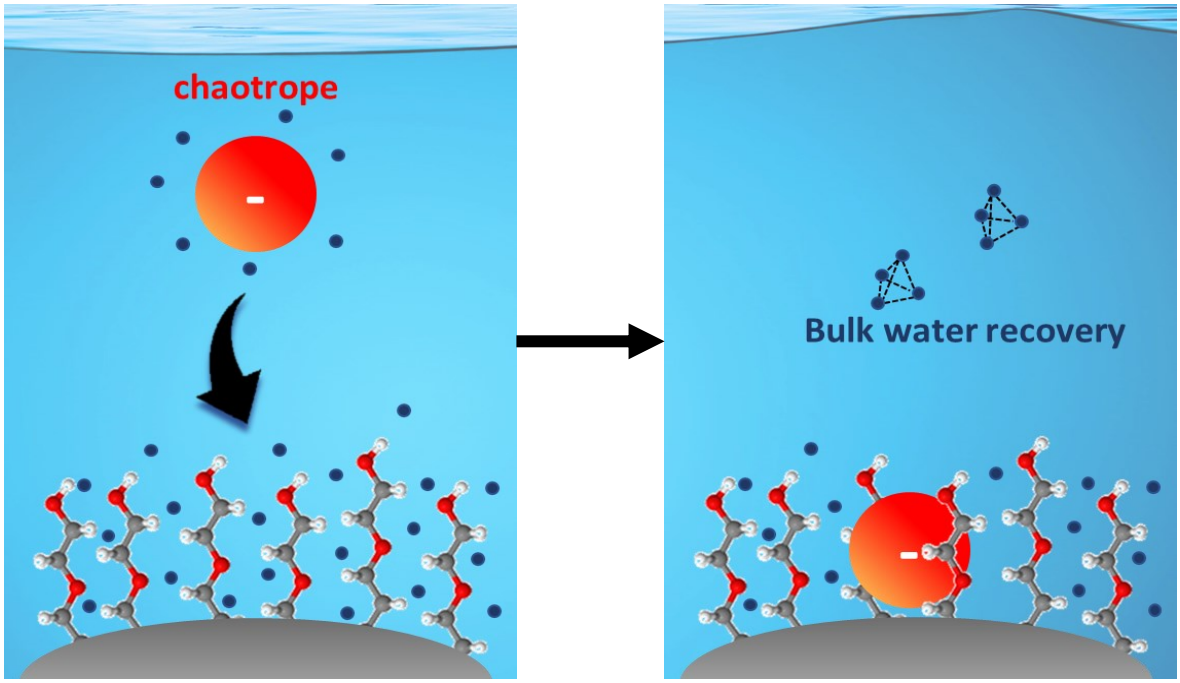

Figure 1.5. Schematic representation of the (super-)chaotropic effect. Initially (left), well hydrated surfaces (*e.g.* from an ethoxylated solute) are present. A chaotropic anion (weakly hydrated) tends to bind to the solute`s surface driven by the extended law of matching water affinities, *i.e.* partial dehydration. Finally, bulk water is recovered (enthalpy and entropy gain) and a [chaotrope-solute] complex is formed.

centered ethylene glycol unit(s) in pentaethylene glycol (PEG-5).[90] This phenomenon was explained by the more disrupted and therefore more hydrophobic water network around the centered ethylene glycol unit(s) than around a terminal ethylene glycol unit or even around PEG-1. The strong interaction of a chaotropic ion with such surfaces is explained by the partial dehydration of the ion and the organic solute, leading to the recovery of bulk water, *i.e.* a strong gain in entropy (release of water molecules to bulk water) and enthalpy (regain of H-bonds in bulk water). This water-mediated phenomenon is generally discussed as the chaotropic effect,[91] which is schematically shown in Fig. 1.5.

1.3 Superchaotropicity of nano-ions

Some years ago, classical anions, such as I^- or SCN^- were believed to be the most chaotropic ions.[92] Accordingly, much effort was put on the search for ions which exceed the chaotropic character of I^-/SCN^-. In 2015, three groups (Werner Nau, Fraser Stoddart, Pierre Bauduin/Olivier Diat) independently showed the strong chaotropic character of nanometric anions with low charge densities, such as anionic boron clusters and POMs.[93–95] These low charge density, nanometric anions are commonly discussed under the umbrella term nano-ions (NIs). Interestingly, NIs were shown to bind much more strongly to organic solutes compared to classical chaotropes: the association constant of chaotropic POMs towards a non-ionic surfactant was shown to exceed the

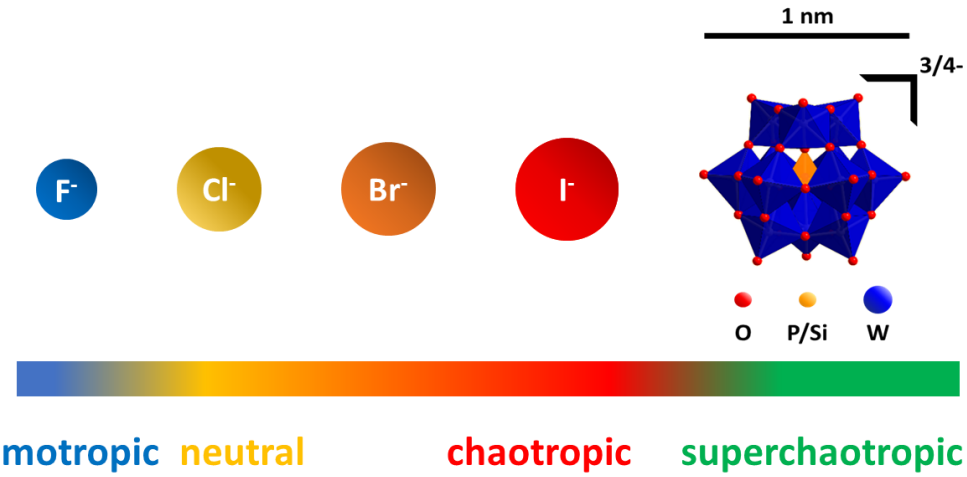

Figure 1.6. Extension of the Hofmeister series of anions. All anions are drawn to scale. Atomic radii were obtained from Shannon *et al.* (for halides)[96] and Naskar *et al.* (for POMs).[95] This image was inspired by ref. [95].

one of SCN^- up to a factor of 10^3.[79] As a consequence, such highly chaotropic species were called "superchaotropes". Therefore, superchaotropic α-Keggin POMs, *i.e.* $SiW_{12}O_{40}^{4-}$ or $PW_{12}O_{40}^{3-}$, extend the Hofmeister series further on the chaotropic side (see Fig. 1.6), which is – essentially – quantified by their much lower charge density compared to common chaotropes such as I^- or even kosmotropes such as F^-, see Table 1.1.

Table 1.1. Charge densities of halides and the α-Keggin POMs $SiW_{12}O_{40}^{4-}$ and $PW_{12}O_{40}^{3-}$, calculated from the ionic radii, taken from Shannon *et al.* for halides[96] and Naskar *et al.* for POMs.[95] q represents the charge of ions. The charge density allows to classify/rank the presented ions.

Species	Ionic radius / nm	Ionic volume / nm^3	Charge density / $\lvert q\ nm^{-3}\rvert$	Classification
F^-	0.13	0.009	108	Kosmotropic
Cl^-	0.18	0.024	40.9	Neutral
Br^-	0.2	0.034	29.8	Chaotropic
I^-	0.22	0.045	22.4	Chaotropic
$SiW_{12}O_{40}^{4-}$	0.44	0.357	11.2	Superchaotropic
$PW_{12}O_{40}^{3-}$	0.44	0.357	8.41	Superchaotropic

After the discovery of superchaotropic NIs in 2015, several working groups focused on the investigation of the chaotropic effect of NIs and its implications. Accordingly, the interaction of different NIs with a broad spectrum of solutes has been investigated. As an attempt to give an overview on the variety of different scientific contributions, Table 1.2 summarizes key publications dealing with superchaotropic NIs and the chaotropic effect. The large number of published works

on the chaotropic effect since its introduction, highlights its growing interest in diverse fields of chemistry: inorganic, organic, physical, supramolecular and material chemistry.

Table 1.2. Key publications in the research field of superchaotropicity since the discovery year 2015. The table summarizes the publication year, working group, the substrate that interacts with a NI and the precise investigated interaction. Following abbreviations were used: *β*, *γ*-cyclodextrin (*β*, *γ*-CD), tetraethylene glycol *n*-octyl ether (C_8E_4), $[Mo_{154}O_{462}H_{14}(H_2O)_{70}]^{14-}$ ({Mo_{154}}), polyethylene glycol 200 (PEG200), cobaltabisdicarbollide (COSAN), poly-*N*-isopropylacrylamide (PNiPAM), octyl glucopyranoside (C_8G_1), 4,4'-dipyridyl-*N,N'*-dioxide (dpdo), pentaethylene glycol *n*-dodecylether ($C_{12}E_5$), hen egg white lysozyme (HEWL), dipropylene glycol *n*-propylether (C_3P_2), polyoxyethylene (10) oleyl ether (BrijO10) and pluronic® P84 (P84).

Year	Working group	Substrate	Investigated interaction
2015	Nau[93]	macrocyclic guest	Dodecaborate : *γ*-CD
2015	Stoddart[94]	macrocyclic guest	α-Keggin POM : *β*-CD, *γ*-CD
2015	Bauduin/Diat[95]	surfactant	α-Keggin POM : C_8E_4
2016	Nau/Gabel[97]	macrocyclic guest	Dodecaborate : *γ*-CD
2016	Nau/Gabel[98]	macrocyclic guest	Dodecaborate : *γ*-CD
2017	Cadot[99]	macrocyclic guest	$P_2W_{18}O_{62}^{6-}$: *γ*-CD
2017	Cadot[100]	macrocyclic guest	{Mo_{154}} : *γ*-CD : $P_2W_{18}O_{62}^{6-}$
2017	Nabika[101]	lipid	α-Keggin POMs : lipids
2017	Bauduin/Pfitzner[102]	oligomer	$PW_{12}O_{40}^{3-}$: PEG200
2018	Nau[91]	diverse (div.)	NI : div. substrates
2018	Gabel/Nau[103]	macrocyclic guest	Carboranes : CDs
2018	Cadot[23]	macrocyclic guest	$W_6O_{19}^{2-}$, $Mo_6O_{19}^{2-}$: *γ*-CD
2018	Cadot/Sokolov[104]	macrocyclic guest	{Re}-cluster : *γ*-CD
2018	Assaf/Gabel[105]	macrocyclic guest	Boron clusters : CDs, cucurbiturils
2018	Zhang[106]	macrocyclic guest	$B_{12}H_{12}^{2-}$: cucurbit[n=5-8]uril
2018	Zhang[107]	macrocyclic guest	$B_{12}H_{12}^{2-}$: cucurbit[7]uril
2018	Bauduin/Pfitzner[79]	surfactant	α-Keggin POMs : C_8E_4
2019	Nau[108]	macrocyclic guest	COSAN : *β*-CD, *γ*-CD
2019	Zhang[109]	macrocyclic guest	Dodecaborate : cucurbit[7]uril
2019	Bauduin/Pfitzner[110]	polymer	α-Keggin POMs : PNiPAM
2019	Bauduin/Diat[111]	surfactant	α-Keggin POMs : C_8E_4/C_8G_1
2019	Cadot[112]	macrocyclic guest	{Re}-cluster : *γ*-CD
2019	Cadot[113]	macrocyclic guest	{Re}-cluster : CDs
2019	Zhang[114]	macrocyclic guest	$B_{12}H_{12}^{2-}$: cucurbit[5]uril
2019	Rompel[115]	enzyme	α-Keggin POMs : proteinase K

2019	Bastos-González[116]	div.	$PW_{12}O_{40}^{3-}$: proteins/nanoparticles
2019	Nau/Gabel[117]	macrocyclic guest	div. boron clusters : γ-CD
2019	Cadot[118]	macrocyclic guest	Decaborate : CDs
2020	Liu[119]	arenes	α-Keggin POMs : dpdo
2020	Liu[120]	macrocyclic guest	Dodecaborate : γ-CD
2020	Bauduin/Diat[121]	surfactant	NI : $C_{12}E_5$
2020	Cadot[122]	macrocyclic guest	$P_2W_{18}O_{62}^{6-}$: γ-CD
2020	Carbó[123]	proteins	α-Keggin POMs : HEWL
2020	Cadot/Sokolov[124]	macrocyclic guest	{Nb}-cluster : γ-CD
2020	Bauduin/Diat[125]	div.	COSAN : div. substrates
2021	Cadot/Bauduin[126]	macrocyclic guest	$\{Mo_{154}\}$: γ-CD : $Mo_6O_{19}^{2-}$
2021	Cadot/Bauduin[127]	macrocyclic guest	α-Keggin POMs : γ-CD, C_8E_4
2021	Cadot[128]	macrocyclic guest	α-Keggin POMs : γ-CD
2021	Bauduin/Pfitzner[129]	hydrotrope	α-Keggin POMs : C_3P_2
2021	Bauduin/Diat[130]	surfactant foam	$SiW_{12}O_{40}^{4-}$: BrijO10
2021	Cadot[131]	macrocyclic guest	Preyssler POM : γ-CD
2021	Cadot[132]	macrocyclic guest	Hexavanadates : γ-CD
2022	Nau/Gabel[133]	macrocyclic guest	Dodecaborates : γ-CD
2022	Johnstone[134]	macrocyclic guest	Dodecaborate : γ-CD
2022	Cadot[135]	macrocyclic guest	α-Keggin POMs : CDs
2022	Bauduin/Pfitzner[136]	polymeric surfactant	$PW_{12}O_{40}^{3-}$: P84
2022	Cadot[137]	macrocyclic guest	Anderson POM : CDs
2022	Zhang[138]	*N*-heterocycles	$B_{12}H_{12}^{2-}$: 2,4,6-tri(4-pyridyl)-1,3,5-triazine
2022	Bauduin/Pfitzner[139]	long chain alcohols	$PW_{12}O_{40}^{3-}$: div. alcohols
2022	Nau[140]	membrane proteins	Dodecaborates : liposomes
2022	Kortz[20]	macrocyclic guest	Pd-oxo clusters : calixarenes

1.4 Goals of this thesis and synopsis

As shown in Table 1.2, the superchaotropicity of POMs (or in general NIs) was investigated on diverse solutes in aqueous solution. Therefore, a precise definition of the goals in the present work is important. In general, this thesis can be divided into three major objectives, which are presented in the following subchapters.

1.4.1 Extension: The interaction of POMs with organic molecules

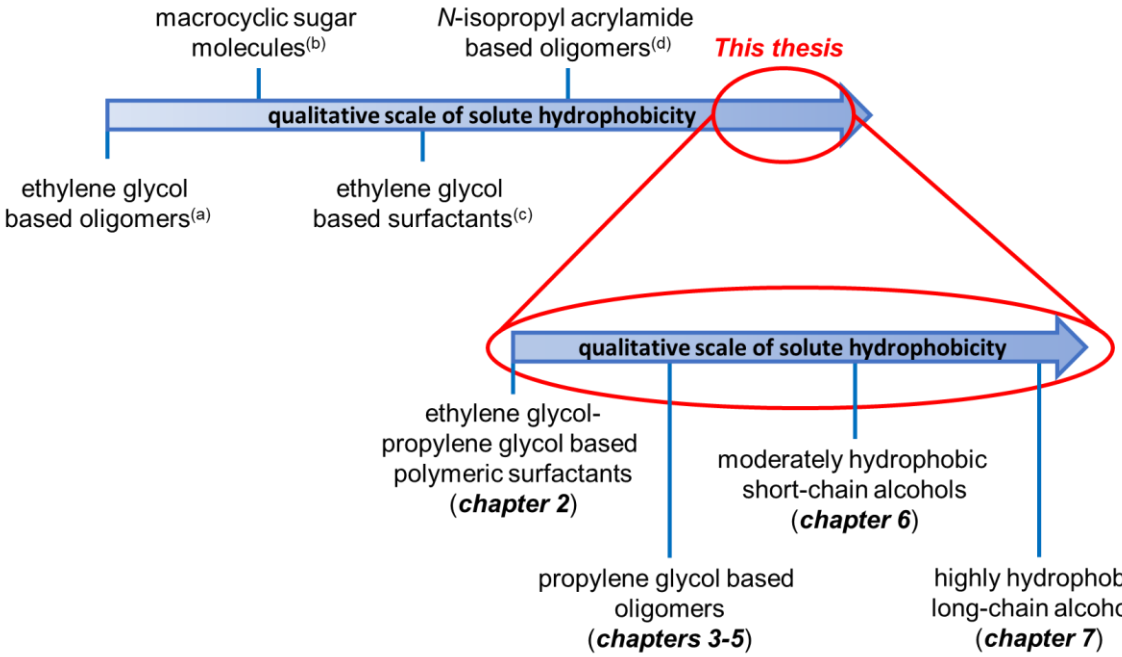

Figure 1.7. Ranking of different solutes, whose interaction with superchaotropic POMs was investigated so far, according to their hydrophobicity (top). This spectrum is extended towards more hydrophobic matter (marked in red ellipse) within this thesis. Letters in brackets summarize references: (a) refs. [102,141], (b) refs. [23,94,100,126–128], (c) refs. [79,95,121,142], (d) refs. [110,141].

In the recent years, the interaction of POMs with rather hydrophilic solutes was intensively investigated, see Fig. 1.7. For instance, the binding of $PW_{12}O_{40}^{3-}$ to ethylene glycol based oligomers or macrocyclic sugar molecules were found as new synthetic routes for single crystals.[23,94,100,102,126-128,141] These investigations were extended to ethylene glycol based surfactants,[79,95,121,142] which reasonably show a higher hydrophobicity than pure ethylene glycol based oligomers, based on an arbitrary scale of hydrophobicity. Lately, $PW_{12}O_{40}^{3-}$ was shown to drive the formation of nanometric to micrometric two-dimensional sheets composed of $PW_{12}O_{40}^{3-}$ and PNiPAM oligomers.[110] PNiPAM is known to exhibit a lower critical solution temperature and was therefore one of the most hydrophobic solutes whose interaction with superchaotropic POMs was investigated so far. One target of this thesis is to extend this spectrum of solutes/organic matter towards more hydrophobic molecules. Consequently, the hydrophobicity of the organic interacting molecules is successively increased throughout this thesis, ranging from ethylene glycol-propylene glycol based block copolymers ***(chapter 2)*** over propylene glycol based oligomers ***(chapters 3-5)*** and moderately hydrophobic short-chain alcohols ***(chapter 6)*** to highly hydrophobic long-chain alcohols ***(chapter 7)***.

In ***chapter 2 "Polymeric surfactant P84/polyoxometalate α-$PW_{12}O_{40}^{3-}$ – A model system to investigate the interplay between chaotropic and hydrophobic effects"***, the binding of $PW_{12}O_{40}^{3-}$ to a triblock copolymer, namely P84, is investigated. P84 is an ABA (A: ethylene glycol, B: propylene

glycol) polymeric surfactant. Therefore, P84 exhibits two building blocks of different hydration, *i.e.* ethylene glycol is well hydrated and propylene glycol is less hydrated. The architecture of P84 allows one to investigate, if $PW_{12}O_{40}^{3-}$ binds selectively to one of these blocks. Subsequently the understanding of the superchaotropic effect of POMs is deepened regarding changes/variations in the chemical structure of organic solutes. P84 undergoes the transition from unimers to spherical micelles by increasing temperature which is driven by dehydration of the PEO/PPO units and subsequently by a decrease in the solubility in water, *i.e.* an increase in the hydrophobicity. Therefore, two different assembly motives prevail in aqueous solutions containing $PW_{12}O_{40}^{3-}$ and P84 and allows us to answer

"How do the chaotropic effect and the hydrophobic effect compete/contribute as orthogonal assembly motives?"

Chapter 3 "Self-assembly of a short amphiphile in water controlled by superchaotropic Polyoxometalates: $H_4SiW_{12}O_{40}$ vs. $H_3PW_{12}O_{40}$" discusses the association of two α-Keggin POMs, $H_4SiW_{12}O_{40}$ and $H_3PW_{12}O_{40}$, with a short amphiphilic molecule based on oligoproylene glycol, *i.e.* dipropylene glycol *n*-propylether (C_3P_2). Compared to ***chapter 2***, the hydrophobicity of the solute, here C_3P_2, is further increased based on the comparison of the aqueous solubility of P84 and C_3P_2. In fact, C_3P_2 undergoes a liquid-liquid phase demixion, similar to a cloud point (CP), by increasing temperature. The CP is monitored as a function of increasing POM concentration: At high POM concentrations, $H_4SiW_{12}O_{40}$ produces a stronger CP increase compared to $H_3PW_{12}O_{40}$, which even leads to a CP decrease. This finding contradicts the classical direct Hofmeister series and therefore represents a partial Hofmeister series inversion. A combination of spectroscopic and sophisticated scattering techniques is applied to explain this phenomenon and the findings were put into the context of self-assembling POMs by comparison to studies in literature.

In ***chapter 4 and 5***, the system POM-C_3P_2 in aqueous solution is further investigated and their specific goals are discussed in chapter 1.4.2. ***Chapter 6*** deals with the POM-mediated selective solubilization of short-chain alcohols (being more hydrophobic than C_3P_2) in water, which is further discussed in chapter 1.4.3. Water-immiscible long-chain alcohols were chosen as organic substances, which appear to be good solvents for low charge density POMs, in ***chapter 7***, see chapter 1.4.3.

1.4.2 Superchaotropic POMs in unconventional ion effects and the origin of life

In ***chapter 4 "Counterion effect on α-Keggin polyoxometalates in water: the peculiar role of H^+ on their salting-in effect and co-assembly with organics"***, the effect of several additives on the model

system POM-C_3P_2 (and POM-C_8E_4) is investigated. CP measurements from ***chapter 3*** are extended to $SiW_{12}O_{40}^{4-}$ and $PW_{12}O_{40}^{3-}$ in combination with different monovalent cations, *i.e.* H^+, Li^+, Na^+ and K^+. Interestingly, only the combination of H^+ with $PW_{12}O_{40}^{3-}$ produces a CP decrease of aqueous C_3P_2 mixtures at high POM concentrations. In the framework of this chapter an explanation for the peculiar behavior of this cation-anion combination is searched. It is found that by titrating H^+, the peculiarity of large assemblies ($H_3PW_{12}O_{40}$ with C_3P_2), leading to a CP decrease, can be overcome. As a first approach, titrations are performed by using classical inorganic and organic bases. Similarly, titrations are performed with basic salts, such as SO_4^{2-} or PO_4^{3-}. As a consequence, the addition of SO_4^{2-} or PO_4^{3-} leads to a salting-in effect in the system $H_3PW_{12}O_{40}$-C_3P_2. Sulfate, and even more phosphate, are usually considered as strongly salting-out anions and therefore the observed salting-in behavior is highly remarkable. These results highlight the duality of salting-out anions, *i.e.* kosmotropicity *vs.* basicity, which is commonly neglected.

Chapter 5 "The potential role of chaotropic polyoxometalates in the origin of life" investigates and discusses, if superchaotropic POMs could have played a role during the evolution of life. Again, an aqueous solution containing $H_3PW_{12}O_{40}$ and C_3P_2 is used as a model system. Based on findings in ***chapter 3***, large aggregates of $H_3PW_{12}O_{40}$-C_3P_2 form, driven by the chaotropic effect. Upon *in-situ* photoreduction, $PW_{12}O_{40}^{3-}$ can be transferred into $PW_{12}O_{40}^{4-}$. Due to this additional charge, the large aggregates disassemble. By reoxidizing $PW_{12}O_{40}^{3-}$ to $PW_{12}O_{40}^{4-}$ with environmental oxygen, large co-assemblies reassemble. This disassembly-assembly cycle is synchronized with the day/night rhythm, *i.e.* disassembly during day (sunlight) and assembly during night (oxygen). In this chapter, it is discussed:

"May a phenomenon, related to the chaotropic effect, have occurred in the prebiotic world and have promoted the emergence of life?"

To this purpose, the experimental findings are put in context to biology, mineralogy and evolution science.

1.4.3 Applications of low charge density polyoxometalates

In ***chapter 6 "A paradox: Hydrophilic molecular metal-oxides are selective solubilizers for moderately hydrophobic compounds"***, superchaotropic α-Keggin POMs are proposed as a novel class of solubilizers for moderately hydrophobic alcohols. Indeed, solubilization experiments show that especially $Na_3PW_{12}O_{40}$ solubilizes aliphatic short-chain alcohols, such as 1-butanol or 1-pentanol, to a similar extent as the model surfactant sodium dodecyl sulfate (SDS). Moreover, $Na_3PW_{12}O_{40}$ is also shown to solubilize hydrophobic aromatic molecules, *e.g.* toluene or benzyl alcohol. Here, the solubilization efficiency even exceeds the one of SDS and it is concluded that strong interaction occurs between $PW_{12}O_{40}^{3-}$ and π-electron containing molecules. Owing to this

strong POM-π-electron interaction, $PW_{12}O_{40}^{3-}$ exclusively binds to aromatic alcohols in competitive media (solutions containing mixtures of aromatic alcohols and aliphatic alcohols). This enzyme-like selective binding is exploited to use superchaotropic POMs as selective solubilizers.

Chapter 7 "{2-phases 2-reactions 1-catalyst} concept for the sustainable performance of coupled reactions" deals with liquid-liquid biphasic systems with water being one phase and a water-immiscible alcohol the second phase. Owing to its low charge density, $H_3PW_{12}O_{40}$ distributes mainly in the organic phase. Upon photoreduction, the more hydrophilic $PW_{12}O_{40}^{4-}$ is formed which subsequently migrates to the aqueous phase. Therefore, the biphasic reaction system is separated in oxidative conditions (organic phase, $PW_{12}O_{40}^{3-}$) and reductive conditions (aqueous phase, $PW_{12}O_{40}^{4-}$). The big advantage of this system is that two reactions (oxidation and reduction) can be performed in two phases using only one catalyst, which represents the basic idea of the {2-phases 2-reactions 1-catalyst} concept. Several examples of coupled reactions are presented in this chapter according to the {2-phases 2-reactions 1-catalyst} concept. Its advantages and disadvantages are summarized and discussed within the framework of sustainability and green chemistry.

1.5 Bibliography

[1] C. W. Scheele, *Sämtliche Physische Und Chemische Werke*, Reprint: Original 1793, Niederwalluf/Wiesbaden, **1971**.

[2] P. Gouzerh, M. Che, *Actual. Chim.* **2006**, *298*, 9–22.

[3] J. J. Berzelius, *Ann. Phys.* **1826**, *82*, 369–392.

[4] L. Pauling, *J. Am. Chem. Soc.* **1929**, *51*, 2868–2880.

[5] A. Werner, *Zeitschrift für Anorg. Chemie* **1893**, *3*, 267–330.

[6] M. Rosnes, C. Yvon, D. Long, L. Cronin, *Dalt. Trans.* **2012**, *41*, 10071–10079.

[7] W. Friedrich, P. Knipping, M. von Laue, *Interferenz-Erscheinungen Bei Röntgenstrahlen*, Verl. der Kgl. Bayer. Akad. der Wiss., München, **1912**.

[8] W. H. Bragg, *Nature* **1912**, *90*, 219.

[9] W. L. Bragg, *Nature* **1912**, *90*, 410.

[10] J. F. Keggin, *Nature* **1933**, *132*, 351.

[11] J. S. Anderson, *Nature* **1937**, *140*, 850.

[12] H. T. Evans, *J. Am. Chem. Soc.* **1948**, *70*, 1291–1292.

[13] M. T. Pope, *Heteropoly and Isopoly Oxometalates*, Springer, Berlin, **1983**.

[14] A. Müller, E. Krickemeyer, J. Meyer, H. Bögge, F. Peters, W. Plass, E. Diemann, S. Dillinger, F. Nonnenbruch, M. Randerath, *Angew. Chem.* **1995**, *107*, 2293–2295.

[15] M. H. Rosnes, C. Musumeci, C. P. Pradeep, J. S. Mathieson, D. Long, Y. Song, B. Pignataro, R. Cogdell, L. Cronin, *J. Am. Chem. Soc.* **2010**, *132*, 15490–15492.

[16] J. J. Borrás-Almenar, E. Coronado, A. Müller, M. Pope, *Polyoxometalate Molecular Science*, Springer, Netherlands, Dondrecht, **2003**.

[17] M. T. Pope, A. Müller, *Angew. Chem. - Int. Ed.* **1991**, *30*, 34–48.

[18] P. Mialane, A. Dolbecq, L. Lisnard, A. Mallard, J. Marrot, F. Secheresse, *Angew. Chem. - Int. Ed.* **2002**, *41*, 2398–2401.

[19] M. Simunekova, D. Prodius, V. Mereacre, P. Schwendt, C. Turta, M. Bettinelli, A. Speghini, Y. Lan, C. E. Anson, A. K. Powell, *RSC Adv.* **2013**, *3*, 6299–6304.

[20] S. Bhattacharya, A. Barba-Bon, T. Zewdie, A. Müller, T. Nisar, A. Chmielnicka, I. Rutkowska, C. Schürmann, V. Wagner, N. Kuhnert, P. Kulesza, W. Nau, U. Kortz, *Angew. Chem. - Int. Ed.* **2022**, e202203114.

[21] I. Lindquist, *Ark Kemi* **1952**, *5*, 247–250.

[22] M. Nyman, *Dalt. Trans.* **2011**, *40*, 8049–8058.

[23] C. Falaise, M. A. Moussawi, S. Floquet, P. A. Abramov, M. N. Sokolov, M. Haouas, E. Cadot, *J. Am. Chem. Soc.* **2018**, *140*, 11198–11201.

[24] A. Blazevic, A. Rompel, *Coord. Chem. Rev.* **2016**, *307*, 42–64.

[25] C. R. Graham, R. G. Finke, *Inorg. Chem.* **2008**, *47*, 3679–3686.

[26] H. N. Miras, G. J. T. Cooper, D. L. Long, H. Bögge, A. Müller, C. Streb, L. Cronin, *Science* **2010**, *327*, 72–74.

[27] B. Krebs, I. Paulat-Böschen, *Acta Crystallogr. B* **1982**, *38*, 1710–1718.

[28] B. Krebs, S. Stiller, K. H. Tytko, J. Mehmke, *Eur. J. Solid State Inorg. Chem.* **1991**, *28*, 883–903.

[29] S. Roy, K. L. Planken, R. Kim, D. v. d. Mandele, W. K. Kegel, *Inorg. Chem.* **2007**, *46*, 8469–8471.

[30] A. Müller, E. Beckmann, H. Boegge, M. Schmidtmann, A. Dress, *Angew. Chem. - Int. Ed.* **2002**, *41*, 1162–1167.

[31] G. Braunitzer, *Bibl Haemotol.* **1964**, *18*, 59–60.

[32] C. Streb, K. Kastner, J. Tucher, *Phys. Sci. Rev.* **2019**, *4*, 1–10.

[33] C. L. Hill, *J. Mol. Catal. A Chem.* **2007**, *262*, 2–6.

[34] E. Papaconstantinou, *Chem. Soc. Rev.* **1989**, *18*, 1–31.

[35] S.-S. Wang, G.-Y. Yang, *Chem. Rev.* **2015**, *115*, 4893–4962.

[36] H. Stephan, M. Kubeil, F. Emmerling, C. E. Müller, *Eur. J. Inorg. Chem.* **2013**, *2013*, 1585–1594.

[37] M. Aureliano, G. Fraqueza, C. A. Ohlin, *Dalt. Trans.* **2013**, *42*, 11770-11777.

[38] J. T. Rhule, C. L. Hill, D. A. Judd, R. F. Schinazi, *Chem. Rev.* **1998**, *98*, 327–357.

[39] R. Prudent, V. Moucadel, B. Laudet, C. Barette, L. Lafanechère, B. Hasenknopf, J. Li, S. Bareyt, E. Lacôte, S. Thorimbert, M. Malacria, P. Gouzerh, C. Cochet, *Chem. Biol.* **2008**, *15*, 683–692.

[40] M. Fukuma, Y. Seto, T. Yamase, *Antiviral Res.* **1991**, *16*, 327–339.

[41] G. Izzet, F. Volatron, A. Proust, *Chem. Rec.* **2017**, *17*, 250–266.

[42] H. N. Miras, J. Yan, D.-L. Long, L. Cronin, *Chem. Soc. Rev.* **2012**, *41*, 7403-7430.

[43] Y.-F. Song, R. Tsunashima, *Chem. Soc. Rev.* **2012**, *41*, 7384-7402.

[44] M. T. Pope, J. Bryan, *Polyoxometalates for Radioactive Waste Treatment - Final Report - 06/15/1996 - 09/14/2000*, **2000**.

[45] A. Müller, F. Peters, M. T. Pope, D. Gatteschi, *Chem. Rev.* **1998**, *98*, 239–272.

[46] U. Kortz, A. Müller, J. Van Slageren, J. Schnack, N. S. Dalal, M. Dressel, *Coord. Chem. Rev.* **2009**, *253*, 2315–2327.

[47] J. M. Clemente-Juan, E. Coronado, A. Gaita-Ariño, *Chem. Soc. Rev.* **2012**, *41*, 7464-7478.

[48] A. Misra, K. Kozma, C. Streb, M. Nyman, *Angew. Chem. - Int. Ed.* **2019**, *59*, 596–612.

[49] A. Bijelic, A. Rompel, *Coord. Chem. Rev.* **2015**, *299*, 22–38.

[50] A. Bijelic, C. Molitor, S. G. Mauracher, R. Al-Oweini, U. Kortz, A. Rompel, *ChemBioChem* **2014**, *16*, 233–241.

[51] F. Hofmeister, *Arch. Exp. Pathol. Pharmakol.* **1888**, *25*, 1–30.

[52] W. Kunz, *Curr. Opin. Colloid Interface Sci.* **2010**, *15*, 34–39.

[53] R. G. Pearson, *J. Chem. Educ.* **1968**, *45*, 581–587.

[54] Y. Zhang, S. Furyk, D. E. Bergbreiter, P. S. Cremer, *J. Am. Chem. Soc.* **2005**, *127*, 14505–14510.

[55] Y. Zhang, S. Furyk, L. B. Sagle, Y. Cho, D. E. Bergbreiter, P. S. Cremer, *J. Phys. Chem. C* **2007**, *111*, 8916–8924.

[56] Y. Zhang, P. S. Cremer, *Annu. Rev. Phys. Chem.* **2010**, *61*, 63–83.

[57] E. A. Algaer, N. F. A. van der Vegt, *J. Phys. Chem. B* **2011**, *115*, 13781–13787.

[58] L. Pérez-Fuentes, D. Bastos-González, J. Faraudo, C. Drummond, *Soft Matter* **2018**, *14*, 7818–7828.

[59] P. Parekh, U. R. Yerramilli, P. Bahadur, *Indian J. Chem.* **2013**, *52A*, 1284–1290.

[60] E. Leontidis, *Curr. Opin. Colloid Interface Sci.* **2002**, *7*, 81–91.

[61] M. Khimani, U. Rao, P. Bahadur, P. Bahadur, *J. Dispers. Sci. Technol.* **2014**, *35*, 1599–1610.

[62] G. Grundl, M. Müller, D. Touraud, W. Kunz, *J. Mol. Liq.* **2017**, *236*, 368–375.

[63] J. Mehringer, E. Hofmann, D. Touraud, S. Koltzenburg, M. Kellermeier, W. Kunz, *Phys. Chem. Chem. Phys.* **2021**, *23*, 1381–1391.

[64] R. J. Clarke, C. Lüpfert, *Biophys. J.* **1999**, *76*, 2614–2624.

[65] W. Kunz, J. Henle, B. W. Ninham, *Curr. Opin. Colloid Interface Sci.* **2004**, *9*, 19–37.

[66] P. H. Von Hippel, T. Schleich, *Acc. Chem. Res.* **1969**, *2*, 257–265.

[67] J. D. Batchelor, A. Olteanu, A. Tripathy, G. J. Pielak, *J. Am. Chem. Soc.* **2004**, *126*, 1958–1961.

[68] A. W. Omta, M. F. Kropman, S. Woutersen, H. J. Bakker, *Science* **2003**, *301*, 347–349.

[69] K. D. Collins, G. W. Neilson, J. E. Enderby, *Biophys. Chem.* **2007**, *128*, 95–104.

[70] N. Schwierz, D. Horinek, R. R. Netz, *Langmuir* **2010**, *26*, 7370–7379.

[71] E. Leontidis, M. Christoforou, C. Georgiou, T. Delclos, *Curr. Opin. Colloid Interface Sci.* **2014**, *19*, 2–8.

[72] C. Calero, J. Faraudo, D. Bastos-González, *J. Am. Chem. Soc.* **2011**, *133*, 15025–15035.

[73] W. Melander, *Arch. Biochem. Biophys.* **1977**, *183*, 200–215.

[74] P. Weissenborn, P. Robert, *J. Colloid Interface Sci.* **1996**, *184*, 550–563.

[75] A. P. dos Santos, Y. Levin, *Faraday Discuss.* **2013**, *160*, 75–87.

[76] A. P. dos Santos, Y. Levin, *Langmuir* **2012**, *28*, 1304–1308.

[77] M. Lund, L. Vrbka, P. Jungwirth, *J. Am. Chem. Soc.* **2008**, *130*, 11582–11583.

[78] L. Vrbka, M. Mucha, B. Minofar, P. Jungwirth, E. C. Brown, D. J. Tobias, *Curr. Opin. Colloid Interface Sci.* **2004**, *9*, 67–73.

[79] T. Buchecker, P. Schmid, S. Renaudineau, O. Diat, A. Proust, A. Pfitzner, P. Bauduin, *Chem. Commun.* **2018**, *54*, 1833–1836.

[80] B. W. Ninham, V. Yaminsky, *Langmuir* **1997**, *13*, 2097–2108.

[81] R. J. Clarke, C. Lüpfert, *Biophys. J.* **1999**, *76*, 2614–2624.

[82] K. D. Collins, *Methods* **2004**, *34*, 300–311.

[83] J. Iwahara, A. Esadze, L. Zandarashvili, *Biomolecules* **2015**, *5*, 2435–2463.

[84] Y. Marcus, *Chem. Rev.* **2009**, *109*, 1346–1370.

[85] G. Stirnemann, E. Wernersson, P. Jungwirth, D. Laage, *J. Am. Chem. Soc.* **2013**, *135*, 11824–11831.

[86] G. A. Krestov, *Thermodynamics of Solvation*, Ellis Horwood, New York **1991**.

[87] L. Yang, Y. Fan, Y. Q. Gao, *J. Phys. Chem. B* **2011**, *115*, 12456–12465.

[88] K. D. Collins, *Q. Rev. Biophys.* **2019**, *52*, 1–19.

[89] D. Horinek, A. Serr, D. J. Bonthuis, M. Boström, W. Kunz, R. R. Netz, *Langmuir* **2008**, *24*, 1271–1283.

[90] B. A. Rogers, H. I. Okur, C. Yan, T. Yang, J. Heyda, P. S. Cremer, *Nat. Chem.* **2022**, *14*, 40–45.

[91] K. I. Assaf, W. M. Nau, *Angew. Chem. - Int. Ed.* **2018**, *57*, 13968–13981.

[92] B. C. Gibb, *Nat. Chem.* **2018**, *10*, 997–998.

[93] K. I. Assaf, M. S. Ural, F. Pan, T. Georgiev, S. Simova, K. Rissanen, D. Gabel, W. M. Nau, *Angew. Chem. - Int. Ed.* **2015**, *54*, 6852–6856.

[94] Y. Wu, R. Shi, Y. Wu, J. M. Holcroft, Z. Liu, M. Frasconi, M. R. Wasielewski, H. Li, J. F. Stoddart, *J. Am. Chem. Soc.* **2015**, *137*, 4111–4118.

[95] B. Naskar, O. Diat, V. Nardello-Rataj, P. Bauduin, *J. Phys. Chem. C* **2015**, *119*, 20985–20992.

[96] R. D. Shannon, *Acta Crystallogr. A* **1976**, *32*, 751-767.

[97] K. I. Assaf, O. Suckova, N. Al Danaf, V. Von Glasenapp, D. Gabel, W. M. Nau, *Org. Lett.* **2016**, *18*, 932–935.

[98] K. I. Assaf, D. Gabel, W. Zimmermann, W. M. Nau, *Org. Biomol. Chem.* **2016**, *14*, 7702–7706.

[99] M. A. Moussawi, N. Leclerc-Laronze, S. Floquet, P. A. Abramov, M. N. Sokolov, A. Ponchel, E. Monflier, H. Bricout, D. Landy, M. Haouas, J. Marrot, E. Cadot, *J. Am. Chem. Soc.* **2017**, *139*, 12793–12803.

[100] M. A. Moussawi, M. Haouas, S. Floquet, W. E. Shepard, P. A. Abramov, M. N. Sokolov, V. P. Fedin, S. Cordier, A. Ponchel, E. Monflier, J. Marrot, E. Cadot, *J. Am. Chem. Soc.* **2017**, *139*, 14376–14379.

[101] D. Kobayashi, H. Nakahara, O. Shibata, K. Unoura, H. Nabika, *J. Phys. Chem. C* **2017**, *121*, 12895–12902.

[102] T. Buchecker, X. LeGoff, B. Naskar, A. Pfitzner, O. Diat, P. Bauduin, *Chem. - A Eur. J.* **2017**, *23*, 8434–8442.

[103] J. Nekvinda, B. Grüner, D. Gabel, W. M. Nau, K. I. Assaf, *Chem. - A Eur. J.* **2018**, *24*, 12970–12975.

[104] A. A. Ivanov, C. Falaise, P. A. Abramov, M. A. Shestopalov, K. Kirakci, K. Lang, M. A. Moussawi, M. N. Sokolov, N. G. Naumov, S. Floquet, D. Landy, M. Haouas, K. A. Brylev, Y. V. Mironov, Y. Molard, S. Cordier, E. Cadot, *Chem. - A Eur. J.* **2018**, *24*, 13467–13478.

[105] K. I. Assaf, J. Wilinska, D. Gabel, in *Boron-Based Compd. Potential Emerg. Appl. Med.* (Eds.: E. Hey-Hawkins, C. Vinas Teixidor), Wiley Online Library, Oxford, **2018**, 109–125.

[106] B. Qi, X. Li, L. Sun, B. Chen, H. Chen, C. Wu, H. Zhang, X. Zhou, *Nanoscale* **2018**, *10*, 19846–19853.

[107] W. Wang, X. Wang, J. Cao, J. Liu, B. Qi, X. Zhou, S. Zhang, D. Gabel, W. M. Nau, K. I. Assaf, H. Zhang, *Chem. Commun.* **2018**, *54*, 2098–2101.

[108] K. I. Assaf, B. Begaj, A. Frank, M. Nilam, A. S. Mougharbel, U. Kortz, J. Nekvinda, B. Grüner, D. Gabel, W. M. Nau, *J. Org. Chem.* **2019**, *84*, 11790–11798.

[109] W. Wang, X. Wang, C. Xiang, X. Zhou, D. Gabel, W. M. Nau, K. I. Assaf, H. Zhang, *ChemNanoMat* **2019**, *5*, 124–129.

[110] T. Buchecker, P. Schmid, I. Grillo, S. Prévost, M. Drechsler, O. Diat, A. Pfitzner, P. Bauduin, *J. Am. Chem. Soc.* **2019**, *141*, 6890–6899.

[111] L. Girard, B. Naskar, J. F. Dufrêche, J. Lai, O. Diat, P. Bauduin, *J. Mol. Liq.* **2019**, *293*, 111280.

[112] A. A. Ivanov, C. Falaise, D. Landy, M. Haouas, Y. V Mironov, M. A. Shestopalov, E. Cadot, *Chem. Commun.* **2019**, *55*, 9951–9954.

[113] A. A. Ivanov, C. Falaise, K. Laouer, F. Hache, P. Changenet, Y. V. Mironov, D. Landy, Y. Molard, S. Cordier, M. A. Shestopalov, M. Haouas, E. Cadot, *Inorg. Chem.* **2019**, *58*, 13184–13194.

[114] B. Qi, L. Du, F. Yao, S. Xu, X. Deng, M. Zheng, S. He, H. Zhang, X. Zhou, *ACS Appl. Mater. Interfaces* **2019**, *11*, 23445–23453.

[115] J. Breibeck, A. Bijelic, A. Rompel, *Chem. Commun.* **2019**, *55*, 11519–11521.

[116] C. Drummond, L. Pérez-Fuentes, D. Bastos-González, *J. Phys. Chem. C* **2019**, *123*, 28744–28752.

[117] S. El Anwar, K. I. Assaf, B. Begaj, M. A. Samsonov, Z. Růžičková, J. Holub, D. Bavol, W. M. Nau, D. Gabel, B. Grüner, *Chem. Commun.* **2019**, *55*, 13669–13672.

[118] M. Diab, S. Floquet, M. Haouas, P. A. Abramov, X. Lopez, D. Landy, A. Damond, C. Falaise, V. Guerineau, D. Touboul, D. Naoufal, E. Cadot, *Eur. J. Inorg. Chem.* **2019**, *2019*, 3373–3382.

[119] B. Qi, S. An, J. Luo, T. Liu, Y.-F. Song, *Chem. - A Eur. J.* **2020**, *26*, 16802–16810.

[120] J. Chen, J. Luo, S. Bekele, M. Tsige, T. Liu, *ChemPlusChem* **2020**, *85*, 2316–2319.

[121] M. Hohenschutz, I. Grillo, O. Diat, P. Bauduin, *Angew. Chem.- Int. Ed.* **2020**, *59*, 8084–8088.

[122] A. A. Ivanov, C. Falaise, A. A. Shmakova, N. Leclerc, S. Cordier, Y. Molard, Y. V Mironov, M. A. Shestopalov, P. A. Abramov, M. N. Sokolov, M. Haouas, E. Cadot, *Inorg. Chem.* **2020**, *59*, 11396–11406.

[123] A. Solé-Daura, J. M. Poblet, J. J. Carbó, *Chem. - A Eur. J.* **2020**, *26*, 5799–5809.

[124] A. A. Ivanov, T. N. Pozmogova, A. O. Solovieva, T. S. Frolova, O. I. Sinitsyna, O. V. Lundovskaya, A. R. Tsygankova, M. Haouas, D. Landy, E. Benassi, L. V. Shestopalova, C. Falaise, E. Cadot, M. A. Shestopalov, P. A. Abramov, M. N. Sokolov, *Chem. - A Eur. J.* **2020**, *26*, 7479–7485.

[125] A. T. Merhi, A. Jonchère, L. Girard, O. Diat, M. Nuez, C. Viñas, P. Bauduin, *Chem. - A Eur. J.* **2020**, *26*, 13935–13947.

[126] C. Falaise, S. Khilfi, P. Bauduin, P. Schmid, W. E. Shepard, A. A. Ivanov, M. N. Sokolov, M. A. Shestopalov, P. A. Abramov, S. Cordier, J. Marrot, M. Haouas, E. Cadot, *Angew. Chem. - Int. Ed.* **2021**, *60*, 14146–14153.

[127] S. Yao, C. Falaise, A. A. Ivanov, N. Leclerc, M. Hohenschutz, M. Haouas, D. Landy, M. A. Shestopalov, P. Bauduin, E. Cadot, *Inorg. Chem. Front.* **2021**, *8*, 12–25.

[128] S. Yao, C. Falaise, S. Khilfi, N. Leclerc, M. Haouas, D. Landy, E. Cadot, *Inorg. Chem.* **2021**, *60*, 7433–7441.

[129] P. Schmid, T. Buchecker, A. Khoshsima, D. Touraud, O. Diat, W. Kunz, A. Pfitzner, P. Bauduin, *J. Colloid Interface Sci.* **2021**, *587*, 347–357.

[130] M. Hohenschutz, I. Grillo, C. D. Dewhurst, P. Schmid, L. Girard, A. Jonchère, O. Diat, P. Bauduin, *J. Colloid Interface Sci.* **2021**, *603*, 141–147.

[131] N. Leclerc, M. Haouas, C. Falaise, S. Al Bacha, L. Assaud, E. Cadot, *Molecules* **2021**, *26*.

[132] I. Fa Bamba, C. Falaise, J. Marrot, P. Atheba, G. Gbassi, D. Landy, W. E. Shepard, M. Haouas,

E. Cadot, *Chem. - A Eur. J.* **2021**, *27*, 15516–15527.

[133] T. Marei, M. Al-Joumhawy, M. Alnajjar, W. M. Nau, K. I. Assaf, D. Gabel, *Chem. Commun.* **2022**, *58*, 2363–2366.

[134] S. E. Hollow, T. C. Johnstone, *Chem. Commun.* **2022**, *58*, 2375–2378.

[135] S. Yao, C. Falaise, N. Leclerc, C. Roch-Marchal, M. Haouas, E. Cadot, *Inorg. Chem.* **2022**, *61*, 4193-4203.

[136] P. Schmid, X. Graß, P. Bahadur, I. Grillo, O. Diat, A. Pfitzner, P. Bauduin, *Colloids and Interfaces* **2022**, *6*, 16.

[137] S. Khlifi, J. Marrot, M. Haouas, W. E. Shepard, C. Falaise, E. Cadot, *J. Am. Chem. Soc.* **2022**, *144*, 4469-4477.

[138] W.-Z. Li, H. Chen, M.-N. Shen, Z. Yang, Z. Fan, J. Xiao, J. Chen, H. Zhang, Z. Wang, X.-Q. Wang, *Small* **2022**, *18*, 2108055.

[139] P. Schmid, G. Jost, X. Grass, D. Touraud, O. Diat, A. Pfitzner, P. Bauduin, *Green Chem.* **2022**, *24*, 2516–2526.

[140] A. Barba-Bon, G. Salluce, I. Lostalé-Seijo, K. I. Assaf, A. Henning, J. Montenegro, W. M. Nau, *Nature* **2022**, *603*, 637–642.

[141] T. Buchecker, Dissertation, Universität Regensburg, **2018**.

[142] M. Hohenschutz, Dissertation, Université Montpellier, **2020**.

2 Polymeric surfactant P84/polyoxometalate α-$PW_{12}O_{40}^{3-}$ - A model system to investigate the interplay between chaotropic and hydrophobic effects

2.1 Preface and Abstract

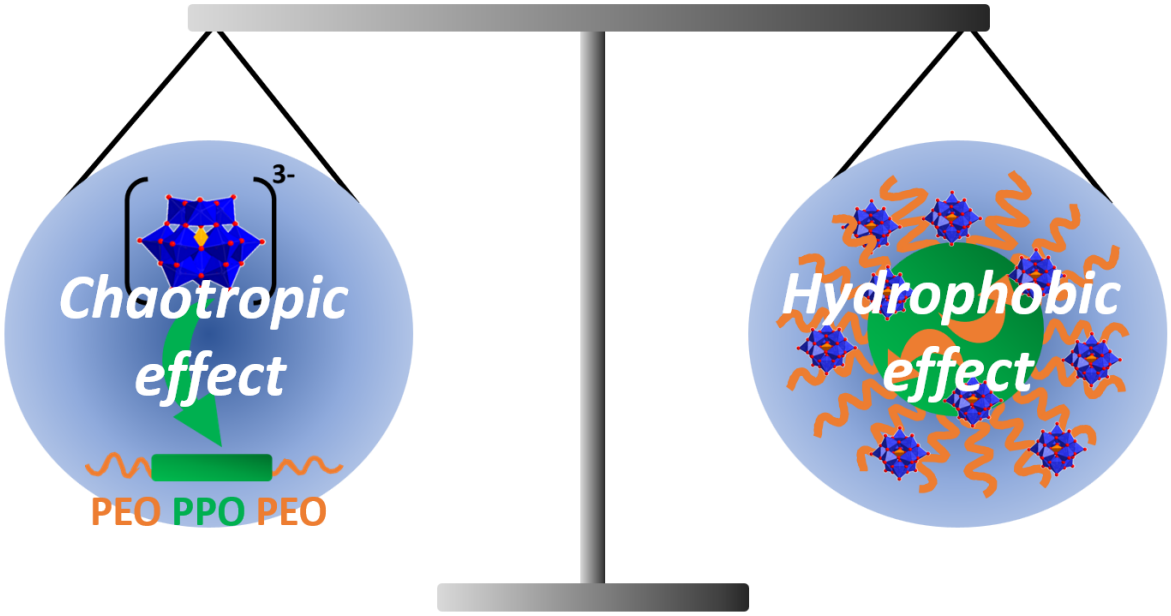

Figure 2.1. Graphical Abstract of the published article in *Colloids and Interfaces*.

This chapter was published in the peer-reviewed Journal *Colloids and Interfaces* of the publisher MDPI (DOI: doi.org/10.3390/colloids6010016). At this place also the electronic supplementary information (ESI) can be found. Reproduced with permission from MDPI. Figures and text may differ from the published version. Several other people contributed to this work:

- Xaver Graß contributed with experiments regarding ternary phase diagrams.
- Prof. Dr. Pratap Bahadur provided polymeric surfactants and proof-read the manuscript.
- Dr. Isabelle Grillo was the local contact at the ILL in Grenoble for SANS measurements. Shortly after our SANS-run, Dr. Isabelle Grillo unexpectedly deceased. Therefore, the corresponding article and this chapter here is dedicated to her memory.
- Dr. Olivier Diat was responsible of the SANS-run in Grenoble, contributed with fruitful discussion and improved the manuscript.
- Prof. Dr. Arno Pfitzner supervised the project, contributed with fruitful discussion, provided resources and improved the manuscript.
- Dr. Pierre Bauduin supervised the project, conceptualized experiments, contributed with fruitful discussion, wrote and improved the manuscript and is corresponding author.

- Philipp Schmid conceptualized and performed all experiments, designed the figures, wrote and improved the manuscript. Preliminary experiments were performed during the author`s master thesis in the group of Dr. Olivier Diat and Dr. Pierre Bauduin (February 2019-October 2019).

Abstract: Low charge density nanometric ions were recently shown to bind strongly to neutral hydrated matter in aqueous solution. This phenomenon, called (super-)chaotropic effect, arises from the partial dehydration of both, the nano-ion and the solute, leading to a high gain in enthalpy. Here, we investigate the chaotropic effect of the polyoxometalate α-$PW_{12}O_{40}^{3-}$ on the triblock copolymer P84: $(EO)_{19}(PO)_{43}(EO)_{19}$ with $(EO)_{19}$ the polyethoxylated and $(PO)_{43}$ the polypropoxylated chains. The combination of phase diagrams, spectroscopic (nuclear magnetic resonance) and scattering (small angle neutron/X-ray scattering) techniques reveals that *(i)* below the micellization temperature of P84, $PW_{12}O_{40}^{3-}$ exclusively binds to the propylene oxide moiety of P84 unimers and *(ii)* above the micellization temperature, $PW_{12}O_{40}^{3-}$ mostly adsorbs on the ethylene oxide micellar corona. The preferential binding of the $PW_{12}O_{40}^{3-}$ to the PPO chain over the PEO chains suggests that the binding is driven by the chaotropic effect and reinforced by the hydrophobic effect. At higher temperatures, the copolymer micellization leads to the displacement of $PW_{12}O_{40}^{3-}$ from the PPO chain to the PEO chains. This study deepens the understanding of the subtle interplay between the chaotropic and hydrophobic effects in complex salt-organic matter solutions.

2.2 Introduction

Polyoxometalates (POMs) show a continuously growing interest in chemistry due to their outstanding properties, *e.g.* their (photo-)catalytic activity,[1–3] applications in medicine[4–6] and many more.[7,8] Currently, the solution behavior of POMs in aqueous medium has attracted much attention in the literature.[9,10] It was demonstrated that POMs with a low charge density, such as phosphotungstate (α-$PW_{12}O_{40}^{3-}$, PW), see Fig. 2.2a, bind strongly and non-covalently to neutral hydrated surfaces of non-ionic micelles in aqueous solution.[11] This phenomenon – known as the (super-)chaotropic effect – has been described as a water-mediated effect: the hydration shells of both, the POM and (surface) moieties are partially stripped off during binding. The superchaotropic effect is an enthalpy driven process which has been discussed as an extension of the well-known Hofmeister series observed for smaller classical chaotropic ions, such as I^- or SCN^-, on many physico-chemical and biological phenomena.[12,13] The association constants of superchaotropic POMs and other nano-ions (NIs), *e.g.* ionic boron clusters, with neutral organic solutes/surfaces is typically around three orders of magnitude stronger than for common chaotropic ions. For this reason, low charge density NIs were called “superchaotropes”.[11,14–16]

A broad spectrum of non-ionic systems was probed regarding their binding with superchaotropic NIs, such as small aromatic molecules,[17] surfactant self-assemblies,[11,15,18,19] oligo- and polymers,[18,20,21] macrocyclic molecules[14,16,22–24] and short-chain amphiphiles.[25]

In a previous contribution, our group has explicitly drawn a focus on the interaction of PW with polyethylene oxide (PEO) oligomers. We showed that PW in its acidic form, *i.e.* $H_3PW_{12}O_{40}$ (HPW), and PEO form nano-assemblies comprising one PW and approximately two PEO oligomers.[20] Such strong binding of POMs on PEO chains was also observed on non-ionic PEO surfactant micelles.[11] The binding of NIs to the PEO corona of these PEO surfactant micelles was monitored by the surfactant`s cloud point (CP) evolution which was used as a powerful tool to rank the NIs according to their superchaotropicity.[15,19,23] Later, the interaction of HPW with polypropylene oxide (PPO) based chains was investigated. In the presence of dipropylene oxide *n*-propylether (C_3P_2), HPW forms nano- to mesoscopic self-assemblies in aqueous solution.[25]

As a conclusion, the interaction of HPW was intensively investigated with *(i)* polymers, *(ii)* non-ionic surfactant micelles, *(iii)* PEO-based and *(iv)* PPO-based compounds. A class of compounds, gathering all four features *(i-iv)*, are triblock copolymers with an ABA architecture (A: PEO and B: PPO). ABA triblock copolymers are present as unimers (unaggregated form) at low temperature and as micellar aggregates at elevated temperatures (above their critical micellization temperature (CMT))

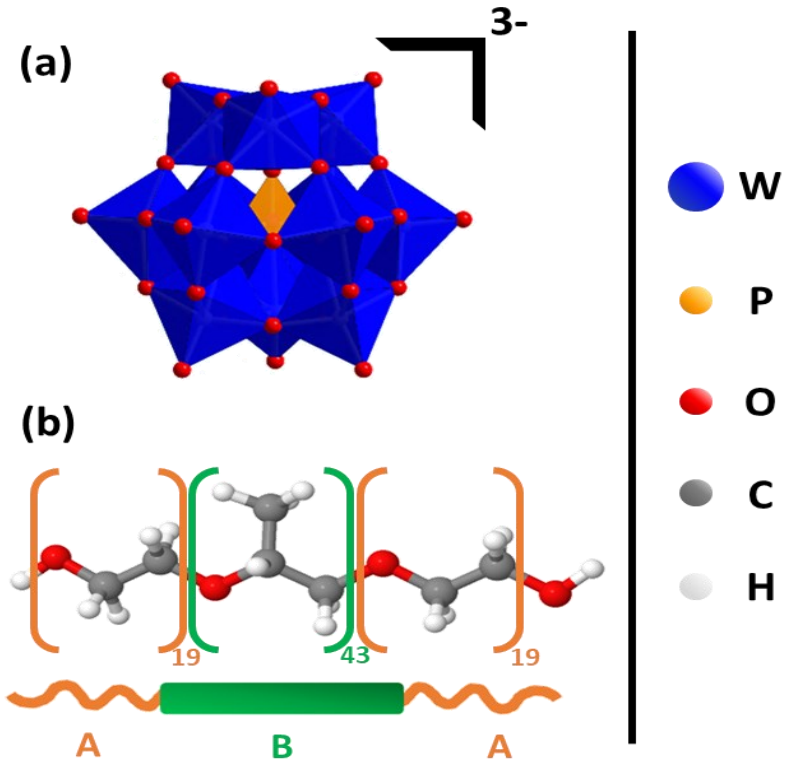

Figure 2.2. Molecular representation of (a) the α-Keggin-type anion phosphotungstate ($PW_{12}O_{40}^{3-}$, PW) and (b) the triblock copolymer P84, providing an ABA architecture (Pluronic®-type) with A: ethylene oxide and B: propylene oxide. A sketch of P84 is shown below the molecular structure.

in aqueous solution.[26–29] Such well-known polymeric surfactants (Pluronic® or Poloxamer®) are used in a broad field of applications, as they solubilize oily compounds,[26,30] are used as drug delivery systems[31,32] or templates in the synthesis of mesoporous materials.[33,34] Therefore, a controlled manipulation (*e.g.* controlling physicochemical solution properties such as the aggregation state or as rheology/viscosity) of polymeric surfactants via the chaotropic effect can be of high interest for a broad field of applications.

The goal of the present work is to gain a deeper knowledge on the interactions between a POM (HPW) and organic molecules of different polarity (hydrophilicity/hydrophobicity) in water. It is well-known that superchaotropic POMs interact with both PEO and PPO chains, but we do not know to what extent. Therefore, the underlying question of this work is: Is the interaction of HPW specific to PEO or to PPO chains? In other words: What is the effect of increasing hydrophobicity from PEO to PPO on the binding strength of HPW? To answer this question, we investigated the chaotropic effect of the α-Keggin POM, HPW, on the Pluronic® surfactant P84, $(EO)_{19}(PO)_{43}(EO)_{19}$, see Fig. 2.2b. We monitored the CP of P84 as a function of HPW concentration to investigate the HPW-P84 association in water. At low temperatures (P84 unimers), ^{1}H-nuclear magnetic resonance (^{1}H-NMR) was used to probe the local environment of the PPO and PEO blocks. Above the CMT (P84 micelles), scattering techniques, *i.e.* small angle X-ray and neutron scattering (SAXS and SANS, respectively), were used to investigate shape/charge of the micellar assemblies. HPW was chosen as a model POM as it was shown previously to be the most superchaotropic POM among the well-studied Keggin-type POMs. P84 was used because it allows *(i)* working on unimers and micelles in a temperature range, between room temperature and 60 °C, and it allows *(ii)* to measure a CP and its evolution upon POM addition which enables to evaluate simply the superchaotropic effect. The obtained experimental results are discussed in the context of two water mediated driving forces:[16] the chaotropic effect (interaction of POM and P84) and the hydrophobic effect (micellization of P84).

2.3 Experimental section

Materials. Phosphotungstic acid hydrate ($H_3PW_{12}O_{40} \cdot xH_2O$, HPW, M = 2898 g/mol, 99.995% purity) was purchased from Sigma Aldrich. Concentration calculations were done with $x_{HPW} = 17$ (calculated from TGA measurement). P84 (M = 4200 g/mol) was received as a gift from BASF (Ludwigshafen, Germany) and used as obtained. Milli-Q water was used with a conductivity lower than 10.5 µS/cm and a total organic carbon content of 400 ppb.

Cloud point (CP) measurements/phase diagrams. For phase diagrams, 3 g of binary/ternary mixtures were prepared into screwable tubes from borosilicate glass and the samples were heated

in a thermostat (Thermomix_1460, B. Braun Melsungen AG) in special tube holders. The thermostat was heated with a rate of 1 °C min^{-1}. The expected precision of the measurements is ± 1 °C.

^{1}H-nuclear magnetic resonance (^{1}H-NMR). Solution ^{1}H-NMR spectra were recorded with an Avance300 (Bruker) spectrometer using tetramethyl silane as an internal standard. Chemical shifts (δ) are provided in parts per million (ppm) and coupling constants (J) are reported in Hertz (Hz). D_2O was used instead of H_2O.

Small angle X-ray scattering (SAXS). SAXS measurements, using Mo-$K_{\alpha1}$ radiation (λ_{Mo} = 0.071 nm), were performed on a bench built by XENOCS. The scattered beam was recorded using a large online scanner detector (diameter: 345 mm, from MAR Research). A large q-range (0.2 to 40 nm^{-1}) was covered with an off-center detection. The collimation was applied using a 12:∝ multilayer Xenocs mirror (for Mo radiation) coupled to two sets of scatter less FORVIS slits providing a 0.8 mm × 0.8 mm X-ray beam at the sample position. Pre-analysis of data was performed using FIT2D software. 1 mm and 2 mm quartz glass capillaries were used as sample containers for the solutions. The samples were thermostated at given temperatures. Usual corrections for background (empty cell and detector noise) subtractions and intensity normalization using a high-density polyethylene film as a standard were applied. Experimental resolution was $\Delta q/q$ = 0.05. Silver behenate in a sealed capillary was used as the scattering vector calibration standard.

Small angle neutron scattering (SANS). All measurements were performed on beamline D33 at the Institut Laue-Langevin (ILL) in Grenoble, France. The applied measurement mode was a monochromatic mode ($\lambda_{neutron}$ = 0.6 nm). Detection was done at 2 and 5 m. Quartz cuvettes from Hellma with thicknesses of 1 mm or 2 mm were used as sample containers. The samples were thermostated at given temperatures. The acquisition times were set to 15 minutes taking into consideration sample thickness and composition, *i.e.* the scattering. Water was used as a calibrant in order to obtain absolute intensities. The spectra were treated and normalized using the available software on site. Note that the presented SANS spectra are subtracted by the signal of D_2O but do contain incoherent scattering. The apparatus was controlled by the NOMAD software and the data treatment was done with the GRASP software on site.[35]

Light scattering. Samples were measured using a Zetasizer Nano ZS from Malvern Instruments. The samples were illuminated with a 632.8 nm laser and detection was done in backscattering position at an angle of 173 °. 1 cm quartz glass cuvettes with a plastic cap served as sample containers. Once set into the measurement chamber the samples were equilibrated for 300 s at the set temperature before the acquisition started. Count rates were collected in triplicates for each sample where one measurement consisted of 10 runs of 10 seconds each, which would then be automatically averaged.

2.4 Results and Discussion

2.4.1 P84: Phase diagram and aggregation

We investigated first the binary phase diagram of P84 and water at c(P84) ≤ 10 wt%, see Fig. 2.3a. This phase diagram shows three different regions, *i.e.* a transparent (black star), a blueish (red star) and a turbid phase (green star), see images in Fig. 2.3a. For c(P84) > 1 wt%, the phase transitions appear at rather constant temperatures: 60 ± 4°C (transparent to blueish) and 74 ± 3 °C (blueish to turbid), respectively. Here, the blueish to turbid phase transition temperature is attributed to the CP.[29,36] For c(P84) < 1 wt%, the two phase transitions are shifted to much higher temperatures by decreasing P84 concentration. In the following, a concentration of P84 of 2.5 wt% (6 mmol L^{-1}) was chosen to ensure *(i)* low concentration dependence on the phase transitions of P84 and *(ii)* weak inter-micellar interaction that is required for a more convenient fitting and interpretation of the scattering experiments.

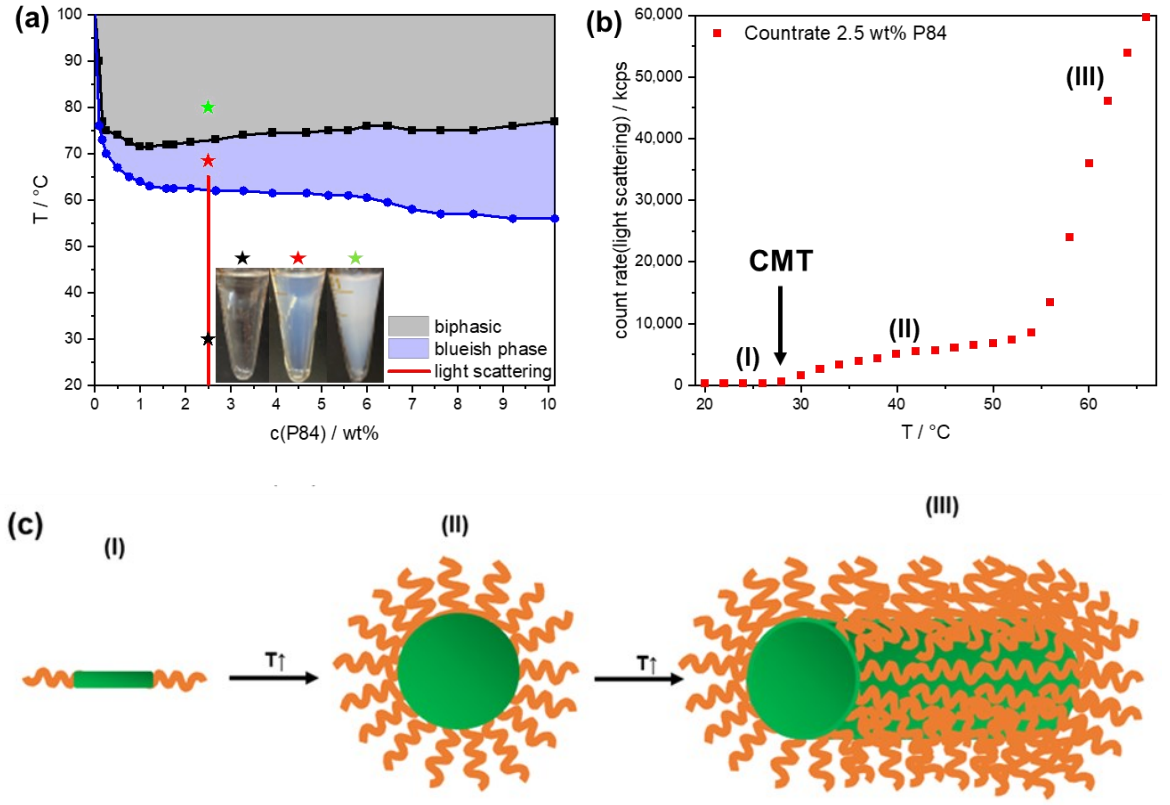

Figure 2.3. (a) The binary phase diagram of water and P84 up to c(P84) = 10 wt% shows the presence of a transparent, a blueish and a turbid phase, which is related to the CP of P84. (b) Count rate in light scattering of 2.5 wt% P84 as a function of temperature, see red line in (a), indicating the presence of three types of aggregation of P84 ((I) - (III)). (c) Schematic representation of the P84 transition with increasing temperature. At room temperature (I) unimers are present which self-assemble to spherical micelles in (II) and to rod-like micelles in (III). In the following, emphasis is put on unimers and spherical micelles.

The count rate of a 2.5 wt% P84 solution was measured as a function of temperature (along red line in Fig. 2.3a), see Fig. 2.3b. The count rate evolution can be divided in three different temperature regimes, called (I), (II) and (III) hereafter. In regime (I) (20-28 °C) the count rate is low (around 300 kcps) as expected for the scattering of unaggregated P84 unimers. In regime (II) (28-54 °C) the count rate increases strongly upon heating. This increase in the scattered light intensity can be attributed to the formation of spherical micelles above 28 °C, which corresponds to the CMT as expected from previous works.[37] Above the CMT, the micellar core is formed by the partially dehydrated PPO chains and the micellar corona contains the well-hydrated PEO chains.[37,38] At higher temperatures in regime (III), above 55 °C, a drastic increase in the count rate is observed. This high increase in the scattered intensity is attributed to the formation of rod-like micelles, see Fig. 2.3c. Indeed, this is in agreement with previous works where a transition from spherical to rod-like micelles was reported at 55 °C.[38] Reasonably, the blueish phase obtained in Fig. 2.3a, is likely to arise from elongating rod-like micelles (Tyndall scattering typically in the (sub-)µm regime). In the present study, the focus is on unimers and spherical micelles. Therefore, we investigated P84 (2.5 wt%) at 20 °C (unimers) and 50°C (spherical micelles).

2.4.2 P84: Cloud point evolution upon addition of HPW

The CP evolution of a non-ionic surfactant upon the addition of POMs was established as a simple, but efficient tool to classify the adsorption of NIs on micelles.[15] Hence, the CP and occurrence of

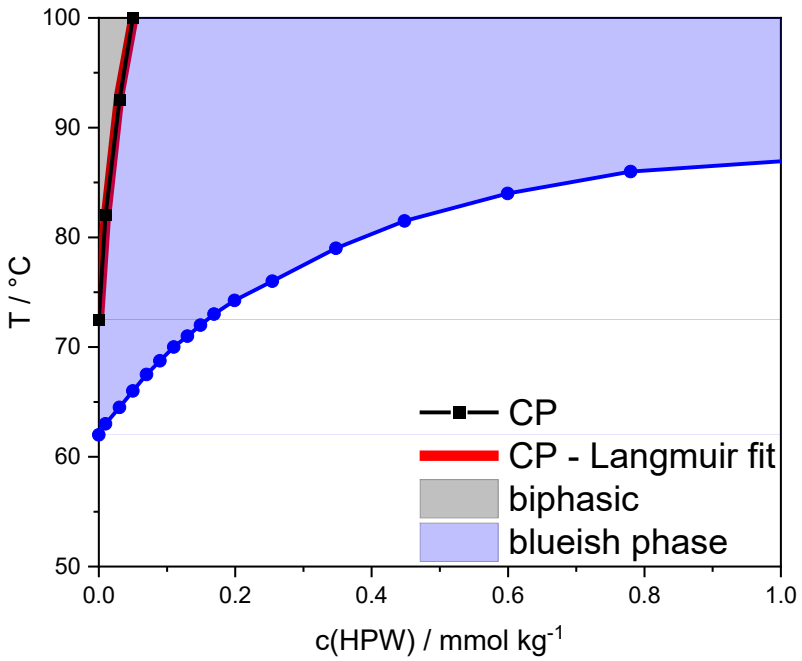

Figure 2.4. Phase diagram of 2.5 wt% P84 as a function of c(HPW) showing a tremendous CP increase (dark squares) and a strong increase in the temperature of appearance of the blueish phase (blue circles).

the blueish phase at 2.5 wt% P84 is recorded as a function of c(HPW), see Fig. 2.4. In absence of HPW, the blueish phase occurs at 62 °C and the CP at 72.5 °C. The blueish phase shifts to higher temperatures upon increasing HPW concentration (87 °C for 1 mmol kg^{-1} HPW), while the temperature of the transparent-to-blueish transition increases and then levels off upon HPW addition. The CP increase is tremendous, as it increases from 72.5 °C up to 100 °C in a very narrow range of concentration (from 0 to 0.05 mmol kg^{-1} HPW). Such a strong CP increase at low HPW concentration indicates a strong association constant, K_A, that can be roughly estimated ($K_A \approx 20.0\ mM^{-1}$, see the fitting results, red curve in Fig. 2.4) from a Langmuir fit according to a previous procedure.[15] The association of HPW with P84 is then around one order of magnitude stronger than with previously investigated systems (using CP measurement to estimate the association constant): poly-*N*-isopropylacrylamide (PNiPAM10000, $K_A \approx 2.1\ mM^{-1}$),[21] polyethoxylated micelles (C_8E_4, $K_A \approx 1.4\ mM^{-1}$)[15]. This stronger association constant obtained with P84 is likely to be due to stronger binding to the more hydrophobic (but still hydrated) PPO chains. Note that above 6 mmol kg^{-1} HPW the system phase separates (precipitation) which is likely to arise from the strong HPW-P84 binding. The ternary phase diagram water-P84-HPW at room temperature is given in Fig. S1 (ESI).

2.4.3 Association of HPW with P84 unimers

To access detailed information on the interaction of HPW with P84, unimeric P84 (20 °C, 2.5 wt%) is investigated by ^{1}H-NMR in the presence of HPW. First, we checked that P84 remains in the unimeric form in the presence of HPW by SANS (Fig. S2, ESI) and SAXS (Fig. S3-4, ESI), see the corresponding discussion in section S2 (ESI). ^{1}H-NMR spectrum for P84 2.5 wt% in D_2O is given in Fig. 2.5b. P84 exhibits several NMR-active protons: *(i)* CH_2 protons of the PEO moieties (red ellipse), *(ii)* the quaternary proton (yellow circle) in PPO, *(iii)* CH_2 protons (green ellipse) in PPO and *(iv)* protons in the methyl group (blue ellipse) in PPO, see Fig. 2.5a. These protons were assigned using Shoolery`s rules, see Fig. 2.5b bottom spectrum.[39]

(i) The CH_2 protons of PEO produce a sharp singlet at 3.55 ppm.

(ii) The quaternary proton of PPO produces a multiplet at around 3.49 ppm as it couples with all the neighboring CH_2/CH_3 protons in PPO via a ^{3}J coupling.

(iii) The CH_2 protons of PPO are detected at around 3.41 ppm as a doublet that is overlayed by the multiplet of the PPO quaternary proton (ii).

(iv) The CH_3 protons of PPO produce a doublet at 1.01 ppm.

^{1}H-NMR was measured for 2.5 wt% P84 in the presence of HPW, for c(HPW) ≤ 5.5 mmol kg^{-1}, see Fig. 2.5b and Fig. S5 (ESI). A broadening of all peaks is observed by increasing HPW concentration. This peak broadening results from a decreased diffusion of the P84 molecules in solution, *i.e.* due

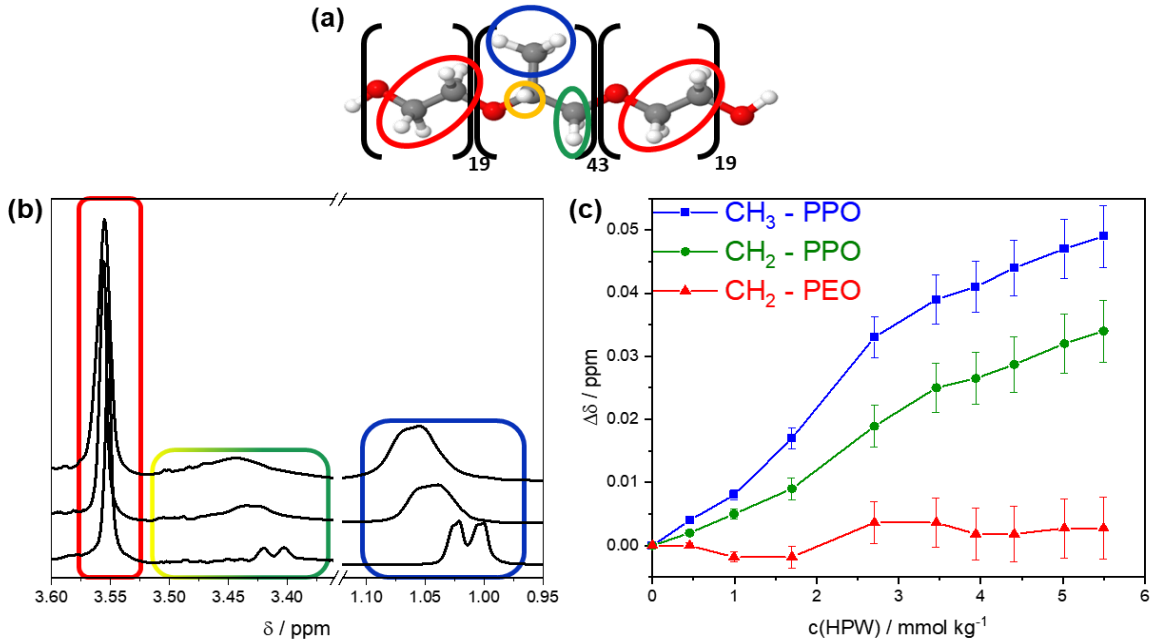

Figure 2.5. (a) Molecular representation of P84 with ^{1}H-NMR active protons marked in colored ellipses with following scheme: CH_2 protons of the PEO moieties in red and the CH_3 protons of the methyl group (blue), CH_2 protons (green) and the quaternary proton (yellow) in the PPO moiety. (b) Evolution of the ^{1}H-NMR spectrum of 2.5 wt% P84 upon an increasing concentration of HPW (0, 2.75 and 5 mmol kg^{-1} from bottom to top). Spectra measured at 20 °C. The color code corresponds to the colors in (a) and therefore indicates the signals stemming from these specific protons. (c) Shift of the chemical shift, *i.e.* Δδ, of protons in P84 as a function of c(HPW) indicating a strong interaction of HPW exclusively with the PPO part of P84.

to the formation of [HPW-P84] assemblies, as previously observed by investigating the superchaotropic effect of HPW on PEO oligomers[20] and γ-cyclodextrin.[23]

Fig. 2.5c shows the shift of chemical shifts, Δδ, of signals stemming from P84 as a function of c(HPW). The CH_2 protons of PEO moieties (singlet) is unaffected upon the addition of HPW. On the contrary, the peak positions of CH_2 and CH_3 protons of the PPO moieties are strongly down-field shifted, *i.e.* shifted to higher chemical shifts (ppm): Δδ of +0.035 ppm and +0.05 ppm respectively for CH_2 and CH_3 protons upon addition of 5.5 mmol kg^{-1} HPW. Note that Δδ cannot be determined for the quaternary proton in PPO due to a strong peak broadening, see Fig. S5 (ESI).

As a conclusion, HPW binds to P84 unimers due to its polymeric nature (81 repetition units) via the chaotropic effect. On the contrary, monomeric species (*e.g.* only one “repetition” unit) are not expected to associate with a chaotropic anion[40] such as PW. Here, the HPW binds selectively to the PPO moiety over to the PEO moieties of P84 unimers. PPO is more hydrophobic than PEO, and therefore, less or weaker hydrated. Subsequently, the stronger and selective adsorption of HPW to PPO results from a combination of the chaotropic and hydrophobic effects. The adsorption of HPW to PPO here cannot be clearly assigned to one of both effects and therefore represents a boarder case of chaotropic and hydrophobic effect.

2.4.4 Association of HPW with P84 micelles

Figure 2.6a&b show the SANS and SAXS spectra respectively of 2.5 wt% P84 in water (green rectangles) at 50 °C, *i.e.* above the CMT. The SANS spectrum of 2.5 wt% P84 in D_2O (green symbols in Fig. 2.6a) shows the typical shape obtained for isotropic scattering objects which can be attributed to P84 micelles. To obtain more information on the micelles, a core (PPO-part)-shell (PEO-part) sphere model was used to fit the experimental data (red line in Fig. 2.6a). The influence of micelle-micelle interactions was considered by using a hard-sphere structure factor *S(q)*, see details in section S4.2 and Table S3 (ESI). The fit could well reproduce the experimental data and revealed a micellar radius of 6.5 nm, with a core radius is 4.1 nm (PPO part) and a shell thickness (PEO corona) of 2.4 nm, an aggregation number of around 60. These values are in good agreement with literature,[29,41] see also Table S2 (ESI).

In Fig. 2.6b the SAXS spectrum of 2.5 wt% P84 in H_2O (green rectangles) is shown. The SAXS spectrum differs strongly from the SANS spectrum because of the different scattering length density (ρ) profiles of the micelles in SAXS and SANS, see the orange (SAXS) and red (SANS) curves in Fig. 2.6c. SAXS is mostly sensitive to the (higher electron density) PEO-corona whereas SANS is mostly sensitive to the dehydrated micellar PPO-core.[26] A fit was applied to the SAXS spectrum, which perfectly reproduces the experimental spectrum (details see section S4.2 and Table S4, ESI). The fitting results are in good agreement with the literature.[29]

SANS and SAXS spectra were collected in the presence of HPW (2 mmol kg^{-1}) for 2.5 wt% P84 (blue circles). HPW is "invisible" in SANS, as its scattering length density is close to the one of D_2O, whereas it shows a large contrast with H_2O and P84 in SAXS, see Table S1 (ESI). The SANS spectrum of 2.5 wt% P84 - 2 mmol kg^{-1} HPW shows a similar shape as the spectrum of 2.5 wt% P84 for $q > 0.4$ nm^{-1}. At $q = 0.26$ nm^{-1} a pronounced correlation peak occurs in the presence of HPW. The correlation peak and the low scattered intensity in the low q (< 0.26 nm^{-1}) reflect strong repulsive micelle-micelle interactions (*S(q)*). These repulsive interactions upon addition of HPW are attributed to electrostatic repulsions resulting from the adsorption of the negatively charged PWs on the micelles. To obtain more information, the experimental SANS spectrum was fitted by using a core-shell sphere model with a Hayter-MSA *S(q)* that takes into account for electrostatic repulsions.[42,43] The fit reproduces the experimental data perfectly. The result of the fit revealed a micellar radius of 5.5 nm with a micellar core (PPO) radius of 3.6 nm and a shell thickness (PEO) of 1.9 nm (details see section S4.2 and Table S5, ESI). Therefore, SANS suggests that upon the addition of HPW, the radius of P84 micelles shrinks from 6.5 nm to 5.5 nm. This effect is reasonable, as especially PEO is known to "wrap around" PW upon their binding.[11,20] The charge of the micelles obtained from the fitting is 47. From the micelle charge, the number of PW anions per micelle was estimated at around 16, *i.e.* 47/3, if full dissociation of HPW is considered.

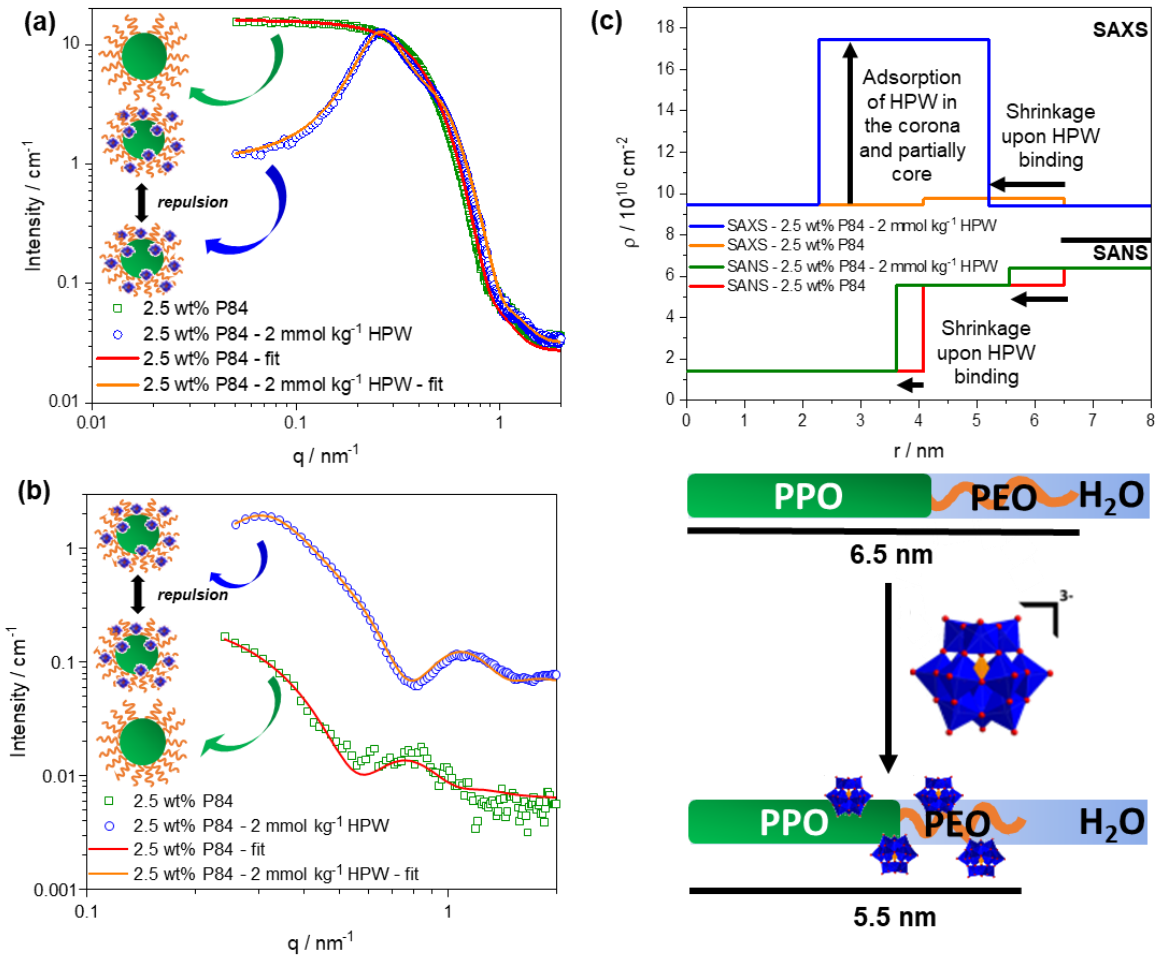

Figure 2.6. (a) SANS and (b) SAXS spectra of 2.5 wt% P84 in water (D_2O or H_2O respectively) and in the presence of 2 mmol kg^{-1} HPW at 50 °C, including fits. (c) Scattering length density profiles of a P84 micelle in aqueous solution showing that the major contrast giving moiety is PPO in SANS and PEO in SAXS in absence of POM. In presence of HPW, the scattering length density in SAXS is dominated by PW anions, which are located mostly in the PEO corona. The sketch represents the size shrinkage of P84 micelles and the penetration of PW anions in the micellar PEO corona and partially the micellar PPO core. In the sketch, one P84 represents the whole micelle.

The SAXS spectrum of 2.5 wt% P84 - 2 mmol kg^{-1} HPW (blue circles in Fig. 2.6b) differs greatly from the SAXS spectrum of 2.5 wt% P84 (green squares in Fig. 2.6b): *(i)* the overall scattered intensity is strongly increased (by a factor of ten), *(ii)* a correlation peak occurs at 0.31 nm^{-1}, *(iii)* an oscillation appears at 1.12 nm^{-1} and *(iv)* the scattered intensity decreases at $q < 0.31$ nm^{-1}. The overall intensity increase is attributed to the adsorption of the high electron density (ρ^{SAXS}) HPW. The location of the correlation peak and the pronounced oscillation can only be explained by a tremendous change of the scattering length density profile of P84 micelles. The decreased scattered intensity in the low q-regime results from the adsorption of PW anions on the charged micelles, that induces strong electrostatic repulsions between the micelles, as observed in the SANS spectrum (Fig. 2.6a blue circles). Therefore, a core-shell model with a Hayter-MSA $S(q)$ was used to fit the experimental data. The fit gives a micellar core radius is 2.3 nm, composed of PPO, and a shell thickness 2.9 nm,

composed partly of the PPO chains and of the PEO chains with adsorbed HPW (see section S4.2 and Table S6, ESI). HPW is mostly located in the well-hydrated PEO chains and only partly in the dehydrated PPO micellar core, close the PEO-PPO region (as in the sketch in the lower part of Fig. 2.6c.). These results were precisely confirmed by evaluating the effect of each parameter in the fit, see section S4.2, Fig. S6 and Table S7 (ESI).

The SAXS/SANS fitting results are well summarized in Fig. 2.6c that shows the ρ profiles in 1D along the micelle (*i.e.* from its center to the surrounding water) in SANS (green and red curves) and SAXS (blue and orange curves) of P84 micelles in presence (green and blue curves) and absence (red and orange curves) of HPW. *r* is the distance from the center of the micelle to the surrounding (heavy) water. In SANS for P84 micelles in D_2O (red line in Fig. 2.6c), ρ of the PPO micellar core and of the PEO corona were fitted (ρ_{PPO}^{SANS} = 1.40 · 10^{10} cm^{-2} and ρ_{PEO}^{SANS} = 5.55 · 10^{10} cm^{-2}) and the values were found to be in agreement with those in the literature.[26] $\rho_{D_2O}^{SANS}$ for the solvent was fixed to 6.40 · 10^{10} cm^{-2}. Upon addition of HPW, the ρ profiles inform clearly on the micelle shrinkage (from red to green curve in Fig. 2.6c). In SAXS for P84 micelles in H_2O (orange line in Fig. 2.6c) the major contrast is produced between the PEO (ρ_{PEO}^{SAXS} = 9.75 · 10^{10} cm^{-2}) and PPO/H_2O (ρ_{PPO}^{SAXS} = 9.47 · 10^{10} cm^{-2} ≈ $\rho_{H_2O}^{SAXS}$ = 9.40 · 10^{10} cm^{-2}). Upon the addition of HPW, the ρ^{SAXS} profile drastically changes (from orange to blue curve in Fig. 2.6c). A strong increase in ρ up to 18.70 · 10^{10} cm^{-2} is obtained for 2.3 ≤ *r* ≤ 5.1 nm, which can only be attributed to the presence of PW.

We conclude by combining SAXS and SANS results that the *(i)* addition of HPW to P84 micelles leads to a size decrease of P84 micelles and *(ii)* HPW mostly adsorbs on the PEO micelle corona, see sketch in Fig. 2.6c.

2.5 Conclusion

In the first part, we investigated the different aggregation states of the polymeric P84 (ABA block copolymer) surfactant in aqueous solution. At 2.5 wt%, unimers of P84 are present at 20 °C. By increasing temperature above the CMT (28 °C) spherical micelles are observed at 50 °C. The micelles undergo a sphere-to-rod transition at > 55 °C. The tremendous CP increase of 2.5 wt% P84 in presence of micromolar concentrations of HPW confirmed strong association between HPW and P84 with an adsorption constant of K_A ≈ 20.0 mM^{-1}. Interestingly, such a high K_A was never observed for the binding of HPW with other polymers (PNiPAM) or surfactants (C_8E_4).

It was shown by ^{1}H-NMR experiments that HPW selectively binds to the PPO moiety of P84 unimers (below the CMT at 20 °C). This effect was attributed to a combination of the chaotropic and hydrophobic effects due to the higher hydrophobicity of PPO over PEO.

Via the combination of SANS/SAXS and modelisation, spherical micelles of P84 with a radius of 6.5 nm (4.1 nm PPO core and 2.4 nm PEO corona) were observed in absence of HPW above the CMT at 50 °C. Upon the addition of HPW the micelle shrinks in size down to a radius of 5.5 nm. HPW were found to be mostly located in the micellar PEO corona and only partially located in the PPO micellar core (close the PEO-PPO region). Therefore, upon heating above the CMT, the micellization of P84 – driven by the hydrophobic effect – leads to a displacement of HPW from PPO to PEO, as PPO is "hidden" in the micellar core.

This study shines light on the subtle balance of two effects: the chaotropic effect (binding of HPW to P84) and the hydrophobic effect (driving the micellization of P84 and the binding of HPW to P84). We have shown here that HPW selectively adsorbs on the PPO moieties over the PEO chains, and therefore we could conclude that HPW interacts more strongly with PPO as a result of an increased hydrophobic character compared to PEO. A deeper knowledge on the interactions between POMs and organic molecules in water is a first step towards designing formulations containing POM building blocks showing specific interactions, *i.e.* towards molecular recognition. This deeper knowledge is required for future development of POM applications, for instance in the medical field,[4] for which pharmaceutical formulations containing POM and organic molecules (such as polymeric additives)[44] could be developed and specific interactions with biological molecules may be required. We also can foresee applications of our findings for the control of polymeric surfactants as oil solubilizers or delivery systems, as the binding of POMs is likely to strongly impact the solubilizing efficiency of polymeric surfactant micelles. In conclusion, the balance of the chaotropic effect and the hydrophobic effect may play a decisive role in assembly of hierarchical functional systems.

2.6 Bibliography

[1] G. Bernardini, A. G. Wedd, C. Zhao, A. M. Bond, *Proc. Natl. Acad. Sci.* **2012**, *109*, 11552–11557.

[2] S. S. Wang, G. Y. Yang, *Chem. Rev.* **2015**, *115*, 4893–4962.

[3] S. Krickl, T. Buchecker, A. U. Meyer, I. Grillo, D. Touraud, P. Bauduin, B. König, A. Pfitzner, W. Kunz, *Phys. Chem. Chem. Phys.* **2017**, *19*, 23773–23780.

[4] J. T. Rhule, C. L. Hill, D. A. Judd, R. F. Schinazi, *Chem. Rev.* **1998**, *98*, 327–357.

[5] M. Fukuma, Y. Seto, T. Yamase, *Antiviral Res.* **1991**, *16*, 327–339.

[6] H. Stephan, M. Kubeil, F. Emmerling, C. E. Müller, *Eur. J. Inorg. Chem.* **2013**, *2013*, 1585–1594.

[7] T. Yamase, *Chem. Rev.* **1998**, *98*, 307–326.

[8] A. Bijelic, A. Rompel, *Coord. Chem. Rev.* **2015**, *299*, 22–38.

[9] A. Misra, K. Kozma, C. Streb, M. Nyman, *Angew. Chem. - Int. Ed.* **2019**, *59*, 596–612.

[10] M. K. Bera, B. Qiao, S. Seifert, B. P. Burton-Pye, M. Olvera De La Cruz, M. R. Antonio, *J. Phys. Chem. C* **2016**, *120*, 1317–1327.

[11] B. Naskar, O. Diat, V. Nardello-Rataj, P. Bauduin, *J. Phys. Chem. C* **2015**, *119*, 20985–20992.

[12] F. Hofmeister, *Arch. Exp. Pathol. Pharmakol.* **1888**, *25*, 1–30.

[13] W. Kunz, J. Henle, B. W. Ninham, *Curr. Opin. Colloid Interface Sci.* **2004**, *9*, 19–37.

[14] K. I. Assaf, M. S. Ural, F. Pan, T. Georgiev, S. Simova, K. Rissanen, D. Gabel, W. M. Nau, *Angew. Chem. - Int. Ed.* **2015**, *54*, 6852–6856.

[15] T. Buchecker, P. Schmid, S. Renaudineau, O. Diat, A. Proust, A. Pfitzner, P. Bauduin, *Chem. Commun.* **2018**, *54*, 1833–1836.

[16] K. I. Assaf, W. M. Nau, *Angew. Chem. - Int. Ed.* **2018**, *57*, 13968–13981.

[17] B. Qi, S. An, J. Luo, T. Liu, Y.-F. Song, *Chem. - A Eur. J.* **2020**, *26*, 16802–16810.

[18] A. T. Merhi, A. Jonchère, L. Girard, O. Diat, M. Nuez, C. Viñas, P. Bauduin, *Chem. - A Eur. J.* **2020**, *26*, 13935–13947.

[19] M. Hohenschutz, I. Grillo, O. Diat, P. Bauduin, *Angew. Chem. - Int. Ed.* **2020**, *59*, 8084–8088.

[20] T. Buchecker, X. LeGoff, B. Naskar, A. Pfitzner, O. Diat, P. Bauduin, *Chem. - A Eur. J.* **2017**, *23*, 8434–8442.

[21] T. Buchecker, P. Schmid, I. Grillo, S. Prévost, M. Drechsler, O. Diat, A. Pfitzner, P. Bauduin, *J. Am. Chem. Soc.* **2019**, *141*, 6890–6899.

[22] C. Falaise, M. A. Moussawi, S. Floquet, P. A. Abramov, M. N. Sokolov, M. Haouas, E. Cadot, *J. Am. Chem. Soc.* **2018**, *140*, 11198–11201.

[23] S. Yao, C. Falaise, A. A. Ivanov, N. Leclerc, M. Hohenschutz, M. Haouas, D. Landy, M. A. Shestopalov, P. Bauduin, E. Cadot, *Inorg. Chem. Front.* **2021**, *8*, 12–25.

[24] K. I. Assaf, B. Begaj, A. Frank, M. Nilam, A. S. Mougharbel, U. Kortz, J. Nekvinda, B. Grüner, D. Gabel, W. M. Nau, *J. Org. Chem.* **2019**, *84*, 11790–11798.

[25] P. Schmid, T. Buchecker, A. Khoshsima, D. Touraud, O. Diat, W. Kunz, A. Pfitzner, P. Bauduin, *J. Colloid Interface Sci.* **2021**, *587*, 347–357.

[26] I. Grillo, I. Morfin, S. Prévost, *Langmuir* **2018**, *34*, 13395–13408.

[27] A. Šturcová, P. Schmidt, J. Dybal, *J. Colloid Interface Sci.* **2010**, *352*, 415–423.

[28] J. G. Álvarez-Ramírez, V. V. A. Fernández, E. R. Macías, Y. Rharbi, P. Taboada, R. Gámez-Corrales, J. E. Puig, J. F. A. Soltero, *J. Colloid Interface Sci.* **2009**, *333*, 655–662.

[29] N. J. Jain, V. K. Aswal, P. S. Goyal, P. Bahadur, *Colloids Surfaces A* **2000**, *173*, 85–94.

[30] H.-Y. Liu, S. Prevost, M. Gradzielski, *Zeitschrift fur Phys. Chemie* **2012**, *226*, 675–694.

[31] A. M. Bodratti, P. Alexandridis, *J. Funct. Biomater.* **2018**, *9*, 11.

[32] E. V Batrakova, A. V Kabanov, *J. Control. Release* **2008**, *130*, 98–106.

[33] M. B. Yue, Y. Chun, Y. Cao, X. Dong, J. H. Zhu, *Adv. Funct. Mater.* **2006**, *16*, 1717–1722.

[34] T. K. Bronich, S. Bontha, L. S. Shlyakhtenko, L. E. V Bromberg, T. A. Hatton, A. V Kabanov, *J. Drug Target.* **2006**, *14*, 357–366.

[35] C. D. Dewhurst, I. Grillo, D. Honecker, M. Bonnaud, M. Jacques, C. Amrouni, A. Perillo-Marcone, G. Manzin, R. Cubitt, *J. Appl. Crystallogr.* **2016**, *49*, 1–14.

[36] T. Patel, P. Bahadur, J. Mata, *J. Colloid Interface Sci.* **2010**, *345*, 346–350.

[37] P. Alexandridis, J. F. Holzwarth, T. A. Hatton, *Macromolecules* **1994**, *27*, 2414–2425.

[38] M. Khimani, U. Rao, P. Bahadur, P. Bahadur, *J. Dispers. Sci. Technol.* **2014**, *35*, 1599–1610.

[39] J. Mohan, *Organic Spectroscopy: Principles and Applications*, Alpha Science, France, Paris **2004**.

[40] B. A. Rogers, H. I. Okur, C. Yan, T. Yang, J. Heyda, P. S. Cremer, *Nat. Chem.* **2022**, *14*, 40–45.

[41] Y. Liu, S. Chen, J. S. Huang, **1998**, *9297*, 2236–2244.

[42] J. B. Hayter, J. Penfold, *Mol. Phys.* **1981**, *42*, 109–118.

[43] J. Hansen, J. B. Hayter, *Mol. Phys.* **1982**, *46*, 651–656.

[44] A. Pitto-Barry, N. P. E. Barry, *Polym. Chem.* **2014**, *5*, 3291–3297.

3 Self-assembly of a short amphiphile in water controlled by superchaotropic polyoxometalates: $H_4SiW_{12}O_{40}$ *vs.* $H_3PW_{12}O_{40}$

3.1 Preface and Abstract

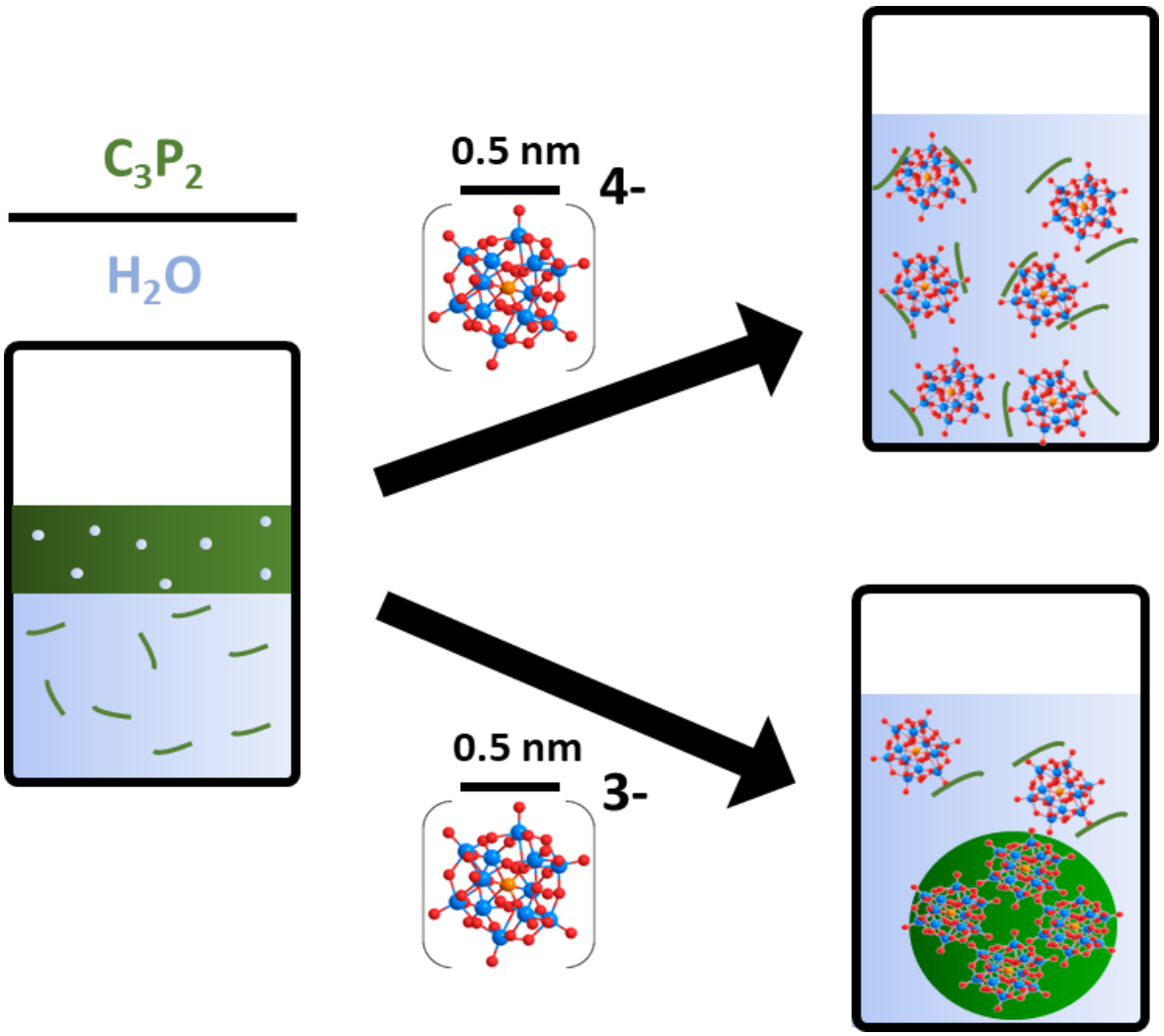

Figure 3.1. Graphical Abstract of the published article in *Journal of Colloid and Interface Science*.

This chapter was published in the peer-reviewed *Journal of Colloids and Interface Science* of the publisher Elsevier (DOI: doi.org/10.1016/j.jcis.2020.12.003). At this place also the electronic supplementary information (ESI) can be found. Reproduced with permission from Elsevier. Figures and text may differ from the published version. Several other people contributed to this work:

- Dr. Thomas Buchecker and Dr. Ali Khoshsima performed a part of SAXS and cloud point measurements, respectively, at high C_3P_2 concentrations.
- Dr. Didier Touraud, Dr. Olivier Diat and Prof. Dr. Werner Kunz contributed with fruitful discussions and improved the manuscript.
- Prof. Dr. Arno Pfitzner supervised the project, contributed with fruitful discussion, provided resources and improved the manuscript.

- Dr. Pierre Bauduin supervised the project, conceptualized experiments, contributed with fruitful discussion, wrote and improved the manuscript and is corresponding author.
- Philipp Schmid conceptualized and performed experiments, designed the figures, wrote and improved the manuscript. Preliminary experiments were performed during the author`s master thesis in the group of Dr. Olivier Diat and Dr. Pierre Bauduin (February 2019-October 2019).

Abstract: Nanometric ions, such as polyoxometalates (POMs) or ionic boron clusters, with low charge density have previously shown a strong propensity to bind to macrocycles and to adsorb to neutral surfaces: micellar, surfactant covered water-air and polymer surfaces. These association phenomena were shown to arise from a solvent-mediated effect, called the (super-)chaotropic effect. We show here by combining cloud point (CP) measurements, scattering (SAXS/SANS) and spectroscopic techniques (NMR) that α-Keggin POMs, $H_4SiW_{12}O_{40}$ (SiW) and $H_3PW_{12}O_{40}$ (PW), induce the self-assembly of an organic solvent, dipropylene glycol *n*-propylether (C_3P_2), in water. The strong interaction between SiW/PW with C_3P_2 leads to a drastic increase in the CP, and aqueous solubility, of C_3P_2, *e.g.* SiW enables reaching full water-C_3P_2 co-miscibility at room temperature. At high POM concentrations, SiW leads to a continuous increase of the CP, forming $[SiW][C_3P_2]_{1-2}$ complexes, whereas PW produces a decrease in the CP attributed to the formation of nearly “dry”, spherical $[PW]_m[C_3P_2]_n$ colloids, with m ≈ 4 and n ≈ 30. At high PW/C_3P_2 contents, the $[PW]_m[C_3P_2]_n$ colloids turn into large interconnected structures, delimiting two pseudo-phases: a PW-C_3P_2-rich phase and a water-rich phase. It is proposed that the stronger electrostatic repulsions between SiW (4-), compared to PW (3-), prevents the formation of mesoscopic colloids.

3.2 Introduction

Only recently, nanometric ions, called nano-ions (NIs), have been shown to strongly *(i)* adsorb to surfaces covered with hydrated moieties, *e.g.* sugars, polyethylene glycols at micellar or water-air surfaces,[1–3] and *(ii)* to bind to the cavity of macrocycles, *e.g.* cyclodextrins.[4,5] The unexpectedly strong binding of NIs with these electrically neutral systems was described as a “superchaotropic” behavior[1,4,6] by comparison with the effect of classical (smaller) chaotropic ions such as iodide (I^-) or thiocyanate (SCN^-), usually classified in the Hofmeister series.[7,8] It was proposed that the superchaotropic effect, or superchaotropicity (SC), is a solvent- (water-)mediated phenomenon, emerging from the favorable release of (high energy) water molecules from the hydrated surface moieties (or the interior of macrocycles) and from the weakly hydrated NIs towards bulk water upon adsorption/binding.[1] The strength of the SC effect of different polyoxometalates (POMs) was

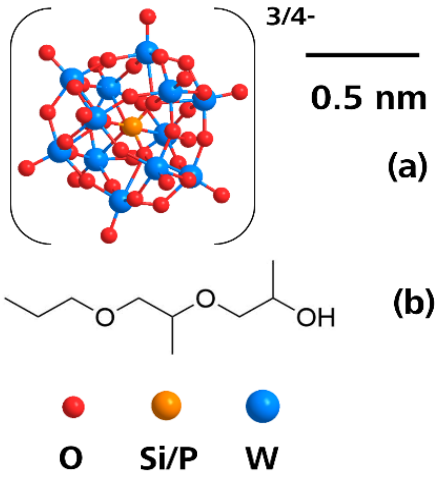

Figure 3.2. (a) Representative structure of an α-Keggin-type polyoxometalate anion (*i.e.* $PW_{12}O_{40}^{3-}$ (PW), $SiW_{12}O_{40}^{4-}$ (SiW)) and (b) an isomer of dipropylene glycol *n*-propylether (C_3P_2). Note that in the present study only the acidic forms of the POMs, *i.e.* $H_3PW_{12}O_{40}$ and $H_4SiW_{12}O_{40}$, are considered.

evaluated by their influence on the clouding temperature of a non-ionic surfactant, tetraethylene glycol *n*-octylether (C_8E_4), and by the strength of their adsorption on C_8E_4 micelles which were characterized by an adsorption constant in the millimolar range.[2] From the classification of different POMs obtained with this approach, it was concluded that the overall charge density of the NIs is a decisive parameter for their SC behavior, *i.e.* the lower the charge density, the stronger the SC behavior, the stronger the binding. Remarkably, the SC effect appeared to be independent of the chemical nature of the NIs. Indeed, a wide variety of nano-ions, such as boron clusters[4,6] and hydrophobic ions, *e.g.* tetraphenyl-borate or -phosphonium[9,10] were classified as superchaotropes. In a recent work, all these nano-ions were investigated and unified regarding their effect on the phase behavior of non-ionic polyethoxylated surfactants (C_iE_j).[11] It was concluded that NIs, independently of their chemical nature, act similarly to ionic surfactants when mixed with polyethoxylated surfactants, *i.e.* both, NIs and ionic surfactants bring charges to the non-ionic surfactant aggregates (micelles or lyotropic phase). The mechanism of NIs differs from the one of (anionic) surfactants, as NIs stick at the surface of non-ionic aggregates by a dehydration process, *i.e.* upon the SC effect, whereas for anionic surfactants their alkyl chains are anchored in the non-ionic aggregates by the hydrophobic effect. However NIs, with some exceptions such as the boron clusters from the metallabis(dicarbollide) class,[12] are not surfactants by themselves as they are not surface-active, neither form micelles nor lyotropic phases in water. It is worth mentioning here that an official definition of SC, and clear distinction between SC and hydrophobicity, is still missing and actively under debate in the community.[13] In the recent years, the binding of POMs was observed on hydrophilic neutral solutes, namely (oligomeric) polyethylene glycol (PEG)[3] and poly-*N*-isopropylacrylamide (PNiPAM)[14]. Both systems are linear chains, non-amphiphilic and they do not self-assemble at low concentrations when they are in water. Nevertheless, POMs of the α-Keggin-

type, namely the phosphotungstate, $PW_{12}O_{40}^{3-}$ (PW), and silicotungstate, $SiW_{12}O_{40}^{4-}$ (SiW), see Fig. 3.2a, were found to interact strongly, through the SC effect, with PEG and PNiPAM to form nano-assemblies: PEG-decorated POMs and large sheet-/globular structures respectively.[3,14] There, exclusively the acidic POM forms were used which is noteworthy, as POMs already provide different behaviors in water by exchanging the POM`s cation.[15] As a conclusion, the binding (or SC behavior) of NIs with these latter hydrophilic polymeric solutes induces their self-assembly in a wide variety (size and shape) of supramolecular structures. It was also shown that the binding of POMs with neutral macrocycles enabled to elaborate complex hybrid materials with nanometric structuration.[16] In the present contribution, we investigate further the interaction between NIs and organic neutral solutes, by focusing on PW and SiW in water with an organic solvent, which is a short chain amphiphilic molecule, the dipropylene glycol *n*-propylether (C_3P_2), see Fig. 3.2b. C_3P_2 is an industrial organic solvent used in diverse application fields, such as in cleaners, cosmetics and coatings/paints.[17] It belongs to a class of molecules known as “hydrotrope”, which refers to short amphiphilic molecules.[18–20] The alkyl chain of a hydrotrope (its hydrophobic part) is too short (or too small) to induce micellization at relatively low concentrations (< 0.1 mol L^{-1}), as it is observed with true surfactants having a linear alkyl chain with at least seven carbon atoms.[21] Compared to surfactants, forming well-defined micelles at low concentrations (< 0.1 mol L^{-1}), most of the hydrotropes form ill-defined “aggregates” at high concentrations in water typically > 0.5 mol L^{-1}.[18,22] Hence, C_3P_2 is, compared to the previously investigated solutes, *i.e.* non-ionic polymers (PEG, PNiPAM), macrocycles and surfactants (C_iE_j)[2–4,14] an interesting candidate to investigate the SC effect of POMs as:

(i) it has a low molecular weight and shows a more pronounced hydrophobic character, leading to a partial co-miscibility with water at room temperature

(ii) it enables to work on both, the monomeric state (non-aggregated) at low C_3P_2 concentrations and on ill-defined aggregates (typical for hydrotropes) at high concentrations.

Moreover, C_3P_2 is well-known to be thermosensitive as it shows a cloud point (CP) in water with a lower critical solubilization temperature (LCST) at around 14 °C.[23,24] The evolution of the CP of C_3P_2 by adding different salts was previously proposed as a convenient and representative method to investigate the kosmotrope/chaotrope behavior of salts and therefore specific salt effects.[25] Consequently, the evolution of the CP of C_3P_2 by the addition of POMs is investigated here to monitor the SC effect. The results are compared to similar CP experiments, previously performed on other thermosensitive systems: C_8E_4 surfactant[1,2] and PNiPAM.[14] The formation of supramolecular structures, *i.e.* POM-C_3P_2 assemblies in water, in the PW(/SiW)/C_3P_2 aqueous systems is investigated by combining small angle X-ray and neutron scattering (SAXS and SANS) and

^{1}H-nuclear magnetic resonance (^{1}H-NMR).

3.3 Experimental section

Materials. Phosphotungstic acid hydrate ($H_3PW_{12}O_{40} \cdot xH_2O$, PW, MW = 2898 g/mol, 99.995% purity), silicotungstic acid hydrate ($H_4SiW_{12}O_{40} \cdot xH_2O$, SiW, MW = 2878 g/mol), phosphomolybdic acid hydrate ($H_3PMo_{12}O_{40} \cdot xH_2O$, PMo, MW = 1825 g/mol) and NaSCN were purchased from Sigma Aldrich and used without further purification. Concentration calculations were done with x_{PW} = 7 and x_{SiW} = 25. C_3P_2 was purchased from Sigma Aldrich and used as obtained. Milli-Q water was used with a conductivity lower than 10.5 µS/cm and a total organic carbon content of 400 ppb.

Cloud point (CP) measurements / pseudo-binary phase diagram. For CP measurements, 3 g of ternary (water, C_3P_2 and POM/salt) mixtures were prepared into screwable tubes of borosilicate glass. The tubes were put into a thermostat (Thermomix_1460, B. Braun Melsungen AG) in special tube holders. The thermostat was heated with a heating rate of approximately 1 °C min^{-1} and the phase separation was detected visually by the appearance of a white clouding in the sample. The expected precision of the measurements is approximately ± 1 °C.

Small angle X-ray scattering (SAXS). SAXS measurements, using Mo-$K_{\alpha1}$ radiation (λ_{Mo} = 0.071 nm), were performed on a bench built by XENOCS. The scattered beam was recorded using a large online scanner detector (diameter: 345 mm, from MAR Research). A large q-range (0.2 to 35 nm^{-1}) was covered with an off-center detection. The collimation was applied using a 12:∝ multilayer Xenocs mirror (for Mo radiation) coupled to two sets of scatter less FORVIS slits providing a 0.8 mm × 0.8 mm X-ray beam at the sample position. Pre-analysis of data was performed using the FIT2D software. The scattered intensities, Intensity or $I(q)$, are expressed versus the magnitude of scattering vector $q = [(4\pi)/\lambda]\sin(\vartheta/2)$, where λ is the wavelength of incident radiation and ϑ the scattering angle. 2 mm quartz capillaries were used as sample containers for the solutions. Usual corrections for background (empty cell and detector noise) subtractions and intensity normalization using a high-density polyethylene film as a standard were applied. Experimental resolution was $\Delta q/q$ = 0.05. Silver behenate in a sealed capillary was used as the scattering vector calibration standard. All experiments were performed at 22 ± 2 °C.

Small angle neutron scattering (SANS). All measurements were performed on beamline D33 at the Institut Laue-Langevin (ILL) in Grenoble, France. The measurements were made in time-of-flight (TOF) mode. All measurement parameters on D33 were controlled by the NOMAD software on site and were calibrated according to Dewhurst *et al*.[26] Sample-to-detector distances were at 3 and 7 m with collimation at 7.8 m. This enables to cover an even larger q-range than using solely one detector at a fixed position. Afterwards both parts of the SANS spectra, detected by a set of 4+1 detectors, were merged and treated with the GRASP software on site. Note that the merging of the

spectra of the different panels may produce some inhomogeneities in the spectra at *q* around 0.8 nm^{-1}. Water was used as a calibrant in order to obtain absolute intensities. Quartz cuvettes from Hellma with thicknesses of 1 mm or 2 mm were used as sample containers. The samples were thermostated at 20 ± 1 °C. The acquisition times were set to 15 minutes taking into consideration sample thickness and composition, *i.e.* the level of scattering. Note that the presented SANS spectra are subtracted by the signal of D_2O but contain incoherent scattering due to the presence of H-atoms in the samples.

^{1}H-nuclear magnetic resonance (^{1}H-NMR). Solution ^{1}H-NMR spectra were recorded (at room temperature) with an Avance300 (Bruker) spectrometer using tetramethyl silane as an internal standard. Chemical shifts (δ) are provided in parts per million (ppm) and coupling constants (J) are reported in Hertz (Hz). D_2O was used as solvent.

3.4 Results and Discussion

3.4.1 POMs in diluted C_3P_2 aqueous solution

Figure 3.3 shows the evolution of the CP of 10 wt% (0.57 mol kg^{-1}) C_3P_2 upon the addition of POMs: PW, SiW and phosphomolybdate (PMo). The CP of 10 wt% C_3P_2 is 45 °C which is in agreement with literature.[23,24] By adding POM, the CP evolution can be divided into two regimes: (I) with c(POM) ≤ 15 mmol kg^{-1} and (II) with c(POM) > 15 mmol kg^{-1}. In regime (I) the CP is strongly increased, up to 55 °C, upon adding POMs. A high increase in the CP was previously observed for C_8E_4 and PNiPAM systems upon the addition of different POMs.[1,14] There it was shown by SAXS and SANS that this strong salting-in effect is due to the binding of POMs to C_8E_4 micelles and to PNiPAM polymer chains. These native non-ionic systems become more hydrophilic upon binding with POMs because they acquire electrostatic repulsions from the bound, charged POMs. Therefore, the strong CP increase of C_3P_2 suggests that POMs interact with C_3P_2 in a comparable manner. In regime (I) the CP increase is more pronounced for PW and PMo compared to SiW. This trend, PW ≈ PMo > SiW, was previously observed with the C_8E_4 micellar system and it was attributed to the lower charge density of PW/PMo (3-) compared to SiW (4-), which subsequently leads to a stronger binding.[2] This difference was explained by a more favorable release of hydration water for PW/PMo compared to SiW, considering that the lower the charge density of the POM (or NI), the weaker their hydration. A stronger binding, *i.e.* a stronger SC behavior, for PW compared to SiW was also observed with cyclodextrin.[6] In regime (II) the CP is increased linearly upon further addition of SiW whereas the addition of PW and PMo causes a significant decrease of the CP. PW causes a more pronounced CP decrease, compared to PMo, even below the initial CP value of 45 °C. Hence, the

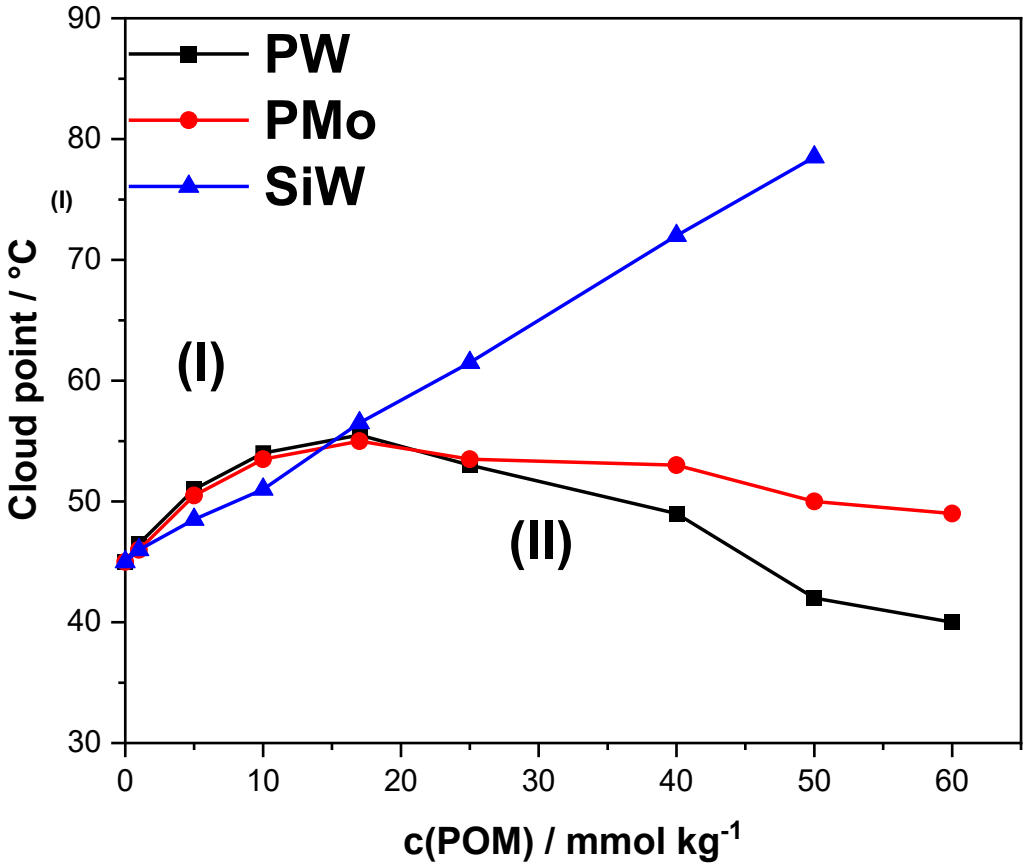

Figure 3.3. Cloud point evolution of 10 wt% C_3P_2 in water as a function of POM concentration.

increase in the POM concentration, in regime (II), produces a reversal of the series of the CP increase in regime (I): PW < PMo << SiW. Such a reversal in the SC behavior of POMs was, to the best of our knowledge, never reported in the literature so far.

In order to find an explanation for this unprecedented behavior, small angle X-ray and neutron scattering (SAXS and SANS) were performed on 10 wt% C_3P_2 solution with PW and SiW in regime (I) at 5 mmol kg^{-1} and in regime (II) at 50 mmol kg^{-1}, see Fig. 3.4. For SAXS measurements, comparison was made with the SAXS spectra of POMs in pure water, as the scattering of POMs mainly contributes to the SAXS spectra. Indeed, the C_3P_2-water contrast is much weaker than the POM-water (or POM-C_3P_2) contrast. The spectra show the scattered intensity, *I(q)* (provided in cm^{-1}), as a function of the wave vector, *q* (given in nm^{-1}). For isotropic dispersions of finite size scattering objects, the scattered intensity may be expressed as: $I(q) = I(0) \cdot P(q) \cdot S(q)$, where *I(0)* is the forward scattering, *cf.* Eq. S1 (ESI). *P(q)* and *S(q)* are the form and structure factors, which take into account respectively for the shape/size of the scattering objects and their interactions, which can be either repulsive or attractive depending on their size/shape/electrical charge and on the concentration of the scattering objects.

The SAXS spectra of SiW and PW in water in Fig. 3.4a&b show the typical scattering pattern of repulsive spherical (globular) scattering objects. The decrease in the scattered intensity visible for *q* values above around 2 nm^{-1} arises from the form factor, *P(q),* of the Keggin POMs, which can be

approximated as a sphere. The lower scattered intensity for q < 2 nm^{-1} arises from repulsive POM-POM interactions, *S(q)*, which is expected between electrically charged particles or scatterers in general. In case of 50 mmol kg^{-1} of POMs, the overall scattered intensity is around ten times stronger than at 5 mmol kg^{-1}, which is expected according to Eq. S2 (ESI). Moreover, broad peaks at intermediate q values (see green arrows in Fig. 3.4a&b) are clearly visible in the spectra at 50 mmol kg^{-1} for PW and SiW, indicating stronger POM-POM repulsive interactions. These broad peaks are further described by Eq. S3 (ESI). More detailed descriptions and fits of the *P(q)* and *S(q)* of POMs in water, which is out of scope here, have been the topic of previous contributions.[27–29]

By changing the solvent from water to an aqueous solution containing 10 wt% C_3P_2, the spectrum of 5 mmol kg^{-1} SiW shows nearly no evolution, whereas a slight modulation in the scattered intensity at intermediate q-range is observed for 50 mmol kg^{-1}, compared to the spectrum of 50 mmol kg^{-1} SiW in pure water. This modulation induced by the presence of C_3P_2 may be attributed to the formation of nano-assemblies, such as SiW decorated with C_3P_2. The formation of SiW-C_3P_2 nano-

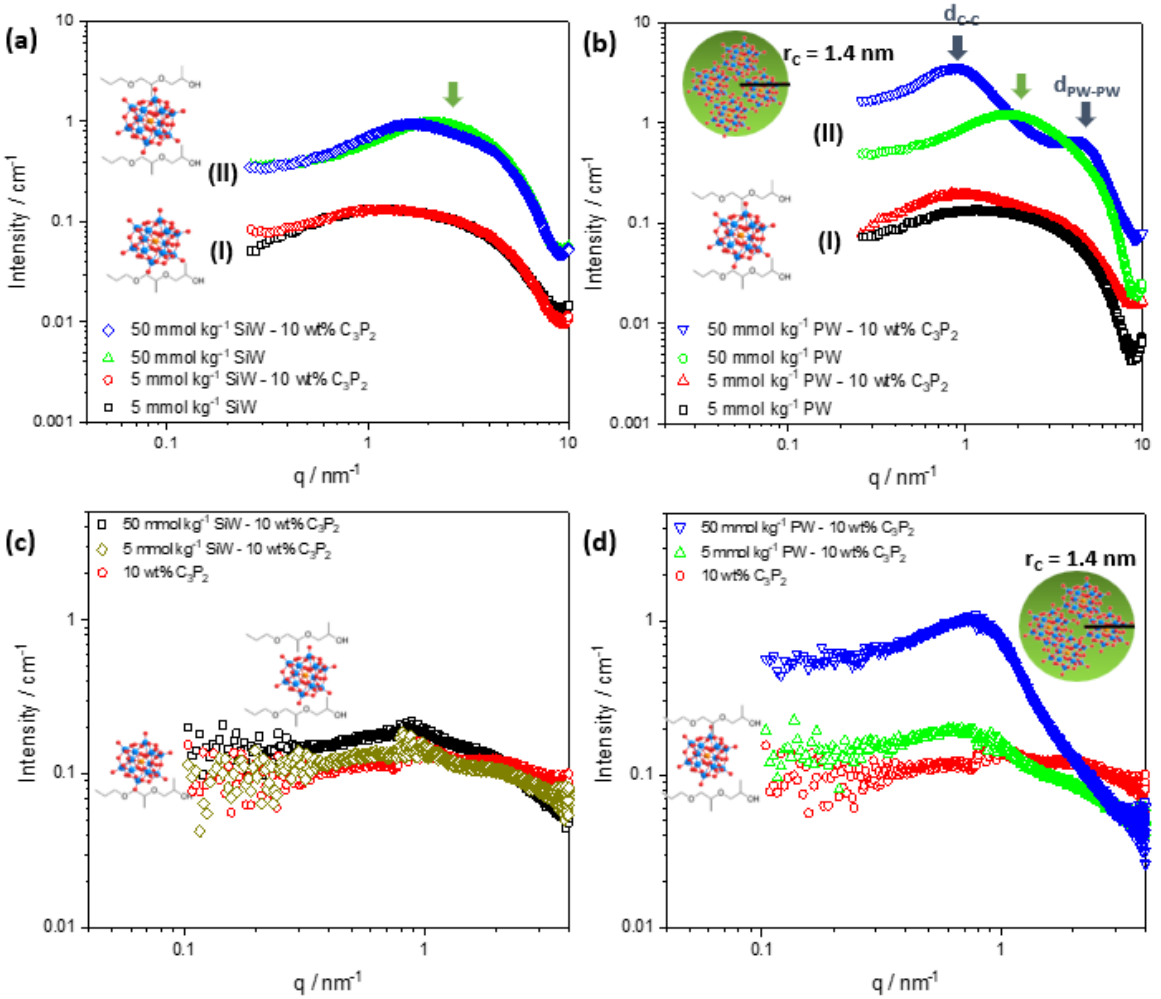

Figure 3.4. SAXS spectra of (a) SiW and (b) PW in aqueous solution and in presence of 10 wt% C_3P_2. (c) SANS spectra of SiW in 10 wt% C_3P_2 and (d) SANS spectra of PW in 10 wt% C_3P_2. D_2O was used as solvent for the SANS measurements and the spectrum of 10 wt% C_3P_2 in D_2O is given as a reference. All spectra are measured at room temperature, *i.e.* between 20 and 23 °C.

assemblies, and therefore the binding of SiW and C_3P_2, implies a change in the local electron density around SiW due to a change in the solvation shell of the POM, *i.e.* the POM solvation water being partially substituted by C_3P_2. It has been shown in a previous investigation that POMs form such nano-assemblies with short chain PEGs and that the formation of such nano-assemblies produces a comparable modulation in the SAXS spectrum.[3] However, here the change in the SAXS spectrum induced by C_3P_2 is very weak which may be related either to *(i)* the weak contrast of C_3P_2 with the water compared to the POM-water (or POM-C_3P_2) contrast or to *(ii)* a too small number of C_3P_2 molecules in the close vicinity of the POMs (forming the nano-assemblies). To prove the (strong) interaction between SiW and C_3P_2, as deduced by the strong CP increase, ^{1}H-NMR spectra of C_3P_2 (2 wt%) were recorded with an increasing concentration of SiW, see Figs. S1 and S2 (ESI). Interestingly, upon the addition of SiW all signals of C_3P_2 are shifted, and some are partially split showing different multiplicities, which supports the hypothesis of strong SiW-C_3P_2 interactions, even though no change in the SAXS and SANS (see below) spectra were observed. A more detailed description of the ^{1}H-NMR evolution is given in the supporting information (ESI).

For PW, the SAXS spectra are shown in Fig. 3.4b, for 5 and 50 mmol kg^{-1} in water and in an aqueous solution containing 10 wt% C_3P_2. These two POM concentrations are compositions in regime (I) and in regime (II) respectively, *cf.* Fig. 3.3. The SAXS spectrum of 5 mmol kg^{-1} PW in presence of 10 wt% C_3P_2 shows a significant excess scattering, at $q < 2$ nm^{-1}, as previously observed for PW-PEG assemblies, *i.e.* PW decorated by in average two PEG oligomers.[3] Therefore, this excess scattering suggests PW-C_3P_2 nano-assemblies are formed. Indeed, the PW-C_3P_2 nano-assemblies are expected to produce excess scattering in the low *q*-range compared to bare PW because nano-assemblies are larger than PW. Note that for SiW at 5 mmol kg^{-1} no excess scattering was observed suggesting that no (or too few) SiW-C_3P_2 nano-assemblies are formed at low SiW concentration. In case of 50 mmol kg^{-1} PW with 10 wt% C_3P_2 a much different scattering pattern is observed. Compared to the SAXS spectrum of 50 mmol kg^{-1} PW in water (Fig. 3.4b green symbols), a several fold increase in the scattered intensity in the low *q*-range is observed in 10 wt% C_3P_2 medium (Fig. 3.4b blue symbols). Such a large scattering excess in the low *q*-range can only be explained by a clustering of several PWs. Indeed, the electron density of PW is very high compared to water or C_3P_2. Consequently, the scattering in SAXS is here nearly exclusively produced by PW (or POM generally) and we can conclude that aggregates (or clusters) contain several PWs. Moreover, the excess scattering, due to these aggregates is observed in a *q*-range below 1.3 nm^{-1}, which informs on the size of the aggregates (3-5 nm). The SAXS spectrum also shows two strong correlation peaks at *(i)* $q_{max1} = 0.8$ nm^{-1} and *(ii)* $q_{max2} = 4$ nm^{-1}. The peak at $q_{max1} = 0.8$ nm^{-1} can be attributed to cluster-cluster correlations. The decrease in the scattered intensity at $q < 0.8$ nm^{-1} is a signature of strong repulsive interactions, which are expected here as the clusters are constituted by several

negatively charged POMs. According to Eq. S3 (ESI), the average cluster-cluster distance, $d_{C\text{-}C}$, is 7.9 nm. The correlation peak at q_{max2} = 4 nm^{-1} corresponds to correlations at much shorter distances and can be attributed to correlations between PWs in the clusters with a PW-PW distance of $d_{PW\text{-}PW}$ = 1.6 nm. Both, the correlation peaks and the presence of electrostatic repulsions indicate the formation of colloidal particles (aggregates) formed by PW and presumably C_3P_2. It is remarkable that the spectrum (blue symbols in Fig. 3.4b) shows an overall shape similar to the spectrum previously observed for a shell-decorated micelle consisting of a non-ionic surfactant and POMs in the micellar corona.[1,2] A fitting of this scattering curve is proposed in the following section.

In order to prove that the aggregates are constituted by C_3P_2 molecules, SANS was performed, see Fig. 3.4c&d, on samples with similar compositions as in Fig. 3.4a&b. However, D_2O was used instead of H_2O to produce a good contrast between the hydrogenated C_3P_2 and all other constituents (D_2O and POM). The advantage of using SANS is that POMs (PW, SiW) have a very weak contrast with D_2O, whereas (hydrogenated) matter or molecules (here C_3P_2) produce good scattering due to the high H/D contrast. The scattering length density of the different components used here are listed later in Table 3.1. Consequently, SANS is a complementary method to SAXS and enables to investigate the clustering of C_3P_2 molecules upon PW addition. The SANS spectrum of the aqueous 10 wt% C_3P_2 solution (red symbols in Fig. 3.4c&d) is almost flat, mainly due to incoherent scattering. It can be assumed that no significant aggregation occurs at 10 wt% C_3P_2, *i.e.* C_3P_2 molecules are well molecularly dispersed in D_2O (H_2O). This result agrees with the negligible scattering measured in dynamic light scattering (DLS), suggesting that C_3P_2 molecules do not self-assemble, see Fig. S3 (ESI). Upon the addition of 5 mmol kg^{-1} SiW the scattering curve remains unchanged. Hence, SANS does not show any larger nano-assemblies and supports the SAXS results (Fig. 3.4a red symbols). By increasing the concentration of SiW to 50 mmol kg^{-1} (Fig. 3.4c dark symbols), the whole scattering curve is shifted by a factor of approximately two (from the red to the dark curve). This result suggests that around two C_3P_2 molecules self-assemble, presumably at the surface of a SiW anion. Moreover, a weak correlation peak is present at *q* around 1 nm^{-1}, as observed in the SAXS spectrum (Fig. 3.4a blue symbols). As the correlation peaks are independent of the type of radiation used, it can be concluded that SAXS and SANS investigate the same scattering objects. Hence, the combination of SAXS and SANS indicates the formation of nano-assemblies, consisting of one SiW and approximately two C_3P_2 molecules, presumably replacing partially the SiW hydration water. Therefore, the combination of SANS, SAXS and ^{1}H-NMR leads us to the conclusion that 1:1 complexes between SiW and C_3P_2 complexes are formed at low concentrations (5 mmol kg^{-1}) of SiW and 1:2 complexes at high SiW concentrations (50 mmol kg^{-1}). This suggests successive formation of the complex with the following equilibria, C_3P_2 (*ca.* 0.57 mol kg^{-1}) being in these experiments always in large excess compared to SiW:

$$C_3P_2\,(\text{excess}) + \text{SiW} \leftrightarrow \text{SiW-}C_3P_2 \quad (3.1)$$

$$\text{SiW-}C_3P_2 + C_3P_2\,(\text{excess}) + \text{SiW} \leftrightarrow \text{SiW-}[C_3P_2]_2 \quad (3.2)$$

For PW, the SANS spectrum of 5 mmol kg^{-1} PW in 10 wt% C_3P_2 (Fig. 3.4d green symbols) shows *(i)* an increase in the overall scattering by a factor of two (compared to the spectrum without PW, red symbols in Fig. 3.4d) and *(ii)* a correlation peak at $q = 0.8\ nm^{-1}$. This correlation peak again corresponds to the correlation peak observed by SAXS, see Fig. 3.4b red symbols. Consequently, for 5 mmol kg^{-1} PW, SAXS and SANS suggest the presence of PW-C_3P_2 (1:2) nano-assemblies, *i.e.* PW-$[C_3P_2]_2$. In case of 50 mmol kg^{-1} PW in 10 wt% C_3P_2, the SANS spectrum shows, at $q < 1\ nm^{-1}$, a much stronger scattering, around eight to ten times stronger than the scattering obtained with 10 wt% C_3P_2. This is a clear signature of cluster formation containing several C_3P_2 molecules, with a size of around 3-5 nm. Moreover, a correlation peak is obtained at $q_{C\text{-}C} = 0.8\ nm^{-1}$, which is at the same position as the correlation peak observed in SAXS, q_{max1} in Fig. 3.4b blue symbols. Therefore, here SAXS and SANS probes the same aggregates, which are constituted by several PW anions and C_3P_2 molecules. Moreover, in the low q-range, below $0.8\ nm^{-1}$, the scattered intensity decreases which indicates repulsive interactions between $[PW]_m[C_3P_2]_n$ aggregates, presumably of electrostatic origin as PW anions are likely to remain electrically charged in the aggregates.

As a conclusion here, PW at low concentrations and SiW at high concentrations form nano-assemblies with one POM and two C_3P_2 molecules, whereas at high concentrations, PW shows a clear tendency to form colloidal sized aggregates, constituted by several PW and C_3P_2 molecules such as $[POM]_m[C_3P_2]_n$. Therefore, SiW and PW show a clear difference in their self-assembly behavior with C_3P_2, which can help to explain the different evolutions observed in the CP upon the addition of POM. Indeed, two regimes, (I) and (II), in the CP evolutions (Fig. 3.3) were distinguished and defined according to the different behavior of SiW and PW. In regime (I) the stronger increase in the CP obtained with PW (or PMo), compared to SiW, can be explained by a stronger binding constant with C_3P_2, as a result of a stronger superchaotropic character of PW compared to SiW. This assumption is further supported by SAXS and SANS, as PW forms PW-$[C_3P_2]_2$ nano-assemblies at lower concentrations compared to SiW. In regime (II) at 50 mmol kg^{-1}, SiW still forms POM-$[C_3P_2]_2$ nano-assemblies, which is associated to a further increase of the CP, whereas PW leads to the formation of larger $[POM]_m[C_3P_2]_n$ aggregates which are less stable towards a temperature increase, *i.e.* leading to a decrease in the CP. It can be concluded here that the stronger superchaotropic behavior of PW, compared to SiW, promotes self-assembly, as a result of a stronger SC effect and/or weaker POM-POM electrostatic repulsions.

The stability of charged colloid dispersions is, in most cases, well understood in terms of the famous Derjaguin-Landau-Verwey-Overbeek (DLVO) theory[30] and is dominated by electrostatic repulsions

and van der Waals attraction. More recent deviations from DLVO forces have been implemented by taking into account additional short-range repulsive "hydration" forces.[31,32] Here, the $[POM]_m[C_3P_2]_n$ colloids are charged and therefore stabilized by electrostatic repulsions, and most likely also by hydration forces. It is likely that the formation of $[POM]_m[C_3P_2]_n$ aggregates upon addition of PW reaches saturation, *i.e.* where a maximum amount of aggregate is formed. Indeed, CP evolution upon addition of (super)chaotropic salts have been previously fitted by a Langmuir adsorption isotherm model, which implies full coverage of surfaces by adsorbed species at high concentrations.[2,14,33] Further addition of PW, above the saturation limit, would therefore lead to unbound PW anions which can play the role of background salt and screen electrostatic repulsions between the $[POM]_m[C_3P_2]_n$ colloids. In previous contributions, the dual behavior of POMs, as background salts (3:1 or 4:1 salts) and as small charged colloids, has been discussed.[27] Therefore, we propose here that the decrease in the CP in the regime (II) arises from the destabilization of the $[POM]_m[C_3P_2]_n$ colloids by screening of the electrostatic repulsions due to excess (unbound) PW. It can be assumed that hydration forces are not sufficient to keep the colloids stable, which is expected as the SC effect results from the favorable dehydration process of nano-ions and solutes (or surface or macrocycle).

3.4.2 Investigation of $[POM]_m[C_3P_2]_n$ colloids

This subsection contains further characterizations of the $[POM]_m[C_3P_2]_n$ colloids, noted here *c*, observed for 10 wt% C_3P_2 and 50 mmol kg^{-1} of PW.

Table 3.1. Scattering length densities (ρ) of the different chemicals used in this study: PW, C_3P_2, H_2O and D_2O respectively for the SANS measurement.

Compound	ρ^{SANS} / 10^{10} cm^{-2}	ρ^{SAXS} / 10^{10} cm^{-2}
PW	5.92	86.9
H_2O	-	9.47
D_2O	6.33	-
C_3P_2	0.08	8.65

It is noteworthy that the compound giving the major contrast in SAXS is the electron rich PW, whereas it is C_3P_2 in SANS, see the scattering length densities (ρ) in Table 3.1. Therefore, it can be assumed that $\rho_{C_3P_2}^{SAXS} \approx \rho_{H_2O}^{SAXS}$ and $\rho_{PW}^{SANS} \approx \rho_{D_2O}^{SANS}$. Hence, the scattering length densities of the colloids, *c*, can be expressed as:

$$\rho_C^{SAXS} = \Phi_C^{PW}\rho_{PW}^{SAXS} + \Phi_C^{H_2O}\rho_{H_2O}^{SAXS} + \Phi_C^{C_3P_2}\rho_{C_3P_2}^{SAXS} = \Phi_C^{PW}\rho_{PW}^{SAXS} + (1 - \Phi_C^{PW})\,\rho_{H_2O}^{SAXS} \quad (3.3)$$

and

$$\rho_C^{SANS} = \Phi_C^{PW}\rho_{PW}^{SANS} + \Phi_C^{D_2O}\rho_{D_2O}^{SANS} + \Phi_C^{C_3P_2}\rho_{C_3P_2}^{SANS} = \Phi_C^{C_3P_2}\rho_{C_3P_2}^{SANS} + (1 - \Phi_C^{C_3P_2})\,\rho_{D_2O}^{SANS} \quad (3.4)$$

where Φ_C^i and $\rho_i^{SAXS/SANS}$ are the volume fraction and the scattering length density of the component *i* (*i* = PW, H_2O or C_3P_2) in the colloid *c*. The volume fraction of PW and C_3P_2 in the colloids can be expressed from Eq. 3.3 and 3.4 as

$$\Phi_C^{PW} = \frac{\rho_C^{SAXS} - \rho_{H_2O}^{SAXS}}{\rho_{PW}^{SAXS} - \rho_{H_2O}^{SAXS}} \quad (3.5)$$

$$\Phi_C^{C_3P_2} = \frac{\rho_C^{SANS} - \rho_{D_2O}^{SANS}}{\rho_{C_3P_2}^{SANS} - \rho_{D_2O}^{SANS}}. \quad (3.6)$$

The volume fraction of H_2O (or D_2O) of the colloids is expressed as

$$\Phi_C^{H_2O} = 1 - \Phi_C^{PW} - \Phi_C^{C_3P_2}. \quad (3.7)$$

The composition of the colloids, *i.e.* $\Phi_C^{H_2O}$, Φ_C^{PW} and $\Phi_C^{C_3P_2}$, can be determined from the scattering length density of the colloids: ρ_C^{SANS} and ρ_C^{SAXS}. Numerical values of these scattering length densities can be obtained by fitting simultaneously the experimental SAXS/SANS in absolute scattering scale. For the fitting procedure, we considered a model of spheres, $P^{sphere}(q, r_C)$, with a homogenous scattering length density in the colloids, ρ_C^{SANS} or ρ_C^{SAXS} respectively for SANS and SAXS. A Hayter-MSA structure factor,[34,35] $S^{HMSA}(q, R_{HS}, IS, \Phi_C, n_{charge})$, was used in order to take into account for the electrostatic repulsive interactions between the colloids. IS, Φ_C, n_{charge} are the ionic strength, the volume fraction of *c* and the number of electrical charges per colloids. Note that Φ_C is also contained and fitted in the prefactor, as $I(0) = n_c \cdot V_C^2 \cdot (\Delta\rho)^2 = \Phi_C \cdot V_C \cdot (\Delta\rho)^2$. This model was applied to the experimental SAXS and SANS spectrum, shown in Fig. 3.5. The experimental SAXS spectrum was subtracted by a constant of 0.55 cm^{-1} to remove the POM contribution, in the range $q > 3$ nm^{-1}. Consequently, the focus here is made on the colloids, which mainly contribute to the scattering in the small angle part, $q < 3$ nm^{-1}. The simultaneous SAXS/SANS fit enables to reproduce the experimental spectra perfectly in absolute values, see Fig. 3.5. The numerical values of the fitting parameters, obtained for the best fit, are collected in Table 3.2. More details on the fitting procedure are given in the supporting information, Fig. S4 - S8 (ESI) and Table S1 - S5 (ESI).

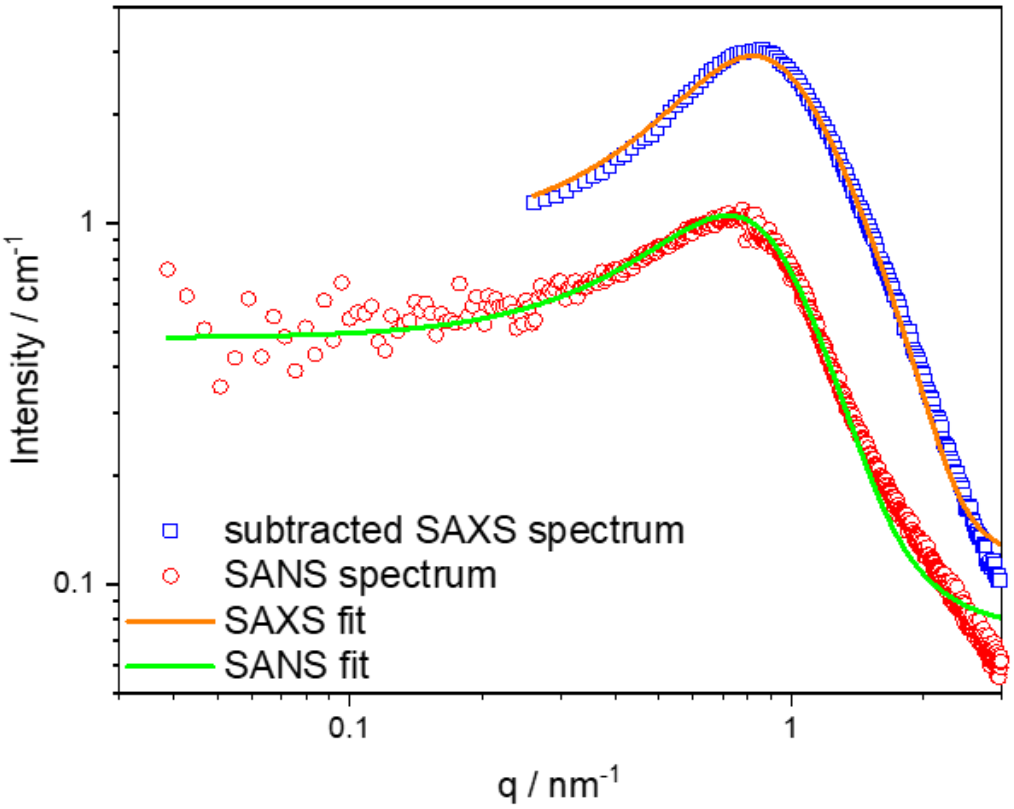

Figure 3.5. Subtracted SAXS spectrum and SANS spectrum of 10 wt% C_3P_2 and 50 mmol kg^{-1} of PW including a simultaneous fit (Hayter-MSA).

Table 3.2. Numerical output values obtained for the simultaneous fitting of the SAXS and SANS spectra presented in Fig. 3.5. r_C, Φ_C and n_{charge} are the colloids radius (from the form factor), the volume fraction and the number of charges of the colloid (from the structure factor). Φ_C was obtained from the prefactor *I(0)*.

Fitting Parameters	Value
ρ_C^{SAXS} / 10^{10} cm^{-2}	19.89
ρ_C^{SANS} / 10^{10} cm^{-2}	1.11
r_C / nm	1.40
Φ_C	0.02
$n_{charge}(c)$ / e^-	10.9

The volume fractions of the three components in the colloids were calculated by using equations 3.5 and 3.6, see Table 3.3. Therefore, the values of the scattering length densities, ρ_C^{SANS} and ρ_C^{SAXS}, obtained from the fit, *cf.* Table 3.2, were used. The number of PW, C_3P_2 and water molecules in a colloid (N_C^i) were consecutively calculated from the volume of the spherical colloids, $V_C = 4\pi r_C^3/3$, and Φ_C^i by

$$N_C^i = \frac{\Phi_C^i V_C}{V_i}. \tag{3.8}$$

Here V_i represents the molecular volume of the component *i*.

These results here enable to derive many representative conclusions on the formation of the colloids. They are mostly composed of C_3P_2 (84 vol%) and PW (14 vol%) and contain nearly no water, which goes in line with the driving force of the SC effect, *i.e.* the thermodynamically favorable dehydration of the nano-ion and the solute (or surface).

Table 3.3. Composition of the colloid $[PW]_m[C_3P_2]_n$ estimated by the simultaneous fit of the SAXS/SANS spectra. Φ_C^i and N_C^i are the volume fractions and the numbers of *i*th components of the colloids.

i	Φ_C^i	N_C^i
PW	0.14	4.5
C_3P_2	0.84	30.4
H_2O	0.02	7.8

The total volume fraction of the colloids, Φ_C, is around 2 vol% which is small compared to volume fraction of C_3P_2 (10 wt% ≈ 9 vol%), indicating that a large quantity of C_3P_2 remains outside the colloids in surrounding solvent as monomers. The fraction of PW and C_3P_2 aggregated in the colloids can be further calculated:

$$c_{aggregated,\ i} = \frac{\Phi_C^i \Phi_C}{\Phi_{total}^i} \cdot c_{initial,\ i} \tag{3.9}$$

This gives $c_{aggregated,\ PW}$ = 13 mmol kg^{-1} and $c_{aggregated,\ C_3P_2}$ = 1.8 wt% = 102 mmol kg^{-1}, compared to the total concentrations 50 mmol kg^{-1} of PW and 10 wt% C_3P_2, meaning that approximately 1/4 of the PW and 1/5 of C_3P_2 participates to the colloids. It is highly noteworthy that $c_{aggregated,\ PW}$ = 13 mmol kg^{-1} corresponds well with the boarder of regime (I) and (II) and supports the hypothesis of a saturation, where a maximum number of colloids are formed as stated above. Therefore, the free or excess PW can screen the electrostatic repulsions between the colloids promoting a decrease in the CP upon further increase in the PW concentrations as proposed above by considering the DLVO theory.

Further quantitative information on the self-assembly of POMs are obtained by discussing the position of the correlation peaks in the SAXS spectra, informing on the average colloid-colloid distance, $d_{C-C} = \frac{2\pi}{q_{C-C}}$, see Fig. 3.4b. Indeed, the average aggregation number of POM in the colloids, N_C^{PW}, can be estimated, by assuming a distribution of the colloids in a cubic lattice and from $d_{C\text{-}C}$, with the following equation:

$$d_{C-C} = \left(\frac{2\pi}{q_{C-C}}\right) = \sqrt[3]{\frac{N_C^{PW}}{c_{aggregated,\ PW} \cdot 6.02 \cdot 10^{-4}}} \tag{3.10}$$

The peak position for 10 wt% C_3P_2 and 50 mmol kg^{-1} is at $q_{C\text{-}C}$ = 0.85 nm^{-1} which gives N_C^{PW} = 3.2 if we consider $c_{aggregated,\ PW}$ = 13 mmol kg^{-1}. Note that a detailed treatment of all peak positions in the measured SAXS spectra is given in Table S6 (ESI). Moreover, we can calculate N_C^{PW} from the number of charges of the colloids from the fitting results, *i.e.* 10.9. By assuming full dissociation of the counterion of PW, meaning that the effective charge of PW is 3-, then N_C^{PW} = 10.9/3 = 3.6. Therefore, the three independent methods used here to estimate the number of PW in the colloids are in relatively good agreement, giving in average four PW in a colloid: N_C^{PW} (from the fitting procedure) = 4.5, N_C^{PW} (from $q_{C\text{-}C}$) = 3.2 and N_C^{PW} (from n_{charge}) = 3.6. Moreover, this validates the assumption that the counterions of the PW are mostly dissociated. Summarized, these treatments inform on the composition of $[POM]_m[C_3P_2]_n$ and lead us to the conclusion that m = 4 and n = 30, *i.e.* $[POM]_4[C_3P_2]_{30}$.

3.4.3 Effect of POMs on concentrated C_3P_2 solution

In the following, the effect of POMs is further investigated at high C_3P_2 content, x(C_3P_2) = 55 wt%, which is the composition at the LCST.[23] Figure 3.6a shows the evolution of the CP upon the addition of POMs. The CP of 55 wt% C_3P_2 is at 14 °C, which is in agreement with the LCST value in the literature.[23,24] PW, PMo and SiW also produce here a strong increase in the CP at low POM concentrations, up to around 25 mmol kg^{-1}. Upon further addition of POM, two distinct behaviors appear:

(i) SiW produces a continuous increase of the CP, in a nearly linear fashion, up to 120 mmol kg^{-1}. For higher SiW concentrations, the CP keeps increasing up to above 100 °C.

(ii) PW/PMo produce a significantly less pronounced increase in the CP, reaching a maximum CP value of 29 and 30 °C, respectively for PMo and PW at c(POM) = 100 mmol kg^{-1}. Then the CP decreases for higher POM concentrations.

The general trend of the CP evolution is comparable to the CP evolution of 10 wt% C_3P_2 upon addition of POMs, *cf.* Fig. 3.3. Nevertheless, the stronger SC of PW (or PMo) over SiW, which was obtained at 10 wt% C_3P_2 and previously with many other systems,[2,14] was not observed here at any POM concentration. Note that the CP evolution of 55 wt% C_3P_2 was investigated upon the addition of several additives, see Fig. S9 and Table S7 (ESI). At low C_3P_2 concentrations (10 wt%) the origin for the lower CP of PW compared to SiW in regime (II) (see Fig. 3.3) was clearly attributed to the formation of $[POM]_m[C_3P_2]_n$ colloids, which is related to the stronger binding of PW with C_3P_2. Therefore, SAXS was performed here, in order to investigate if supramolecular assembly appears and if it can also help to explain the lower CP produced by PW compared to SiW.

Figure 3.6b shows the SAXS spectra of 40 mmol kg^{-1} and 140 mmol kg^{-1} SiW in water and in 55 wt% C_3P_2. The SAXS spectrum of 40 mmol kg^{-1} SiW in 55 wt% C_3P_2 shows nearly no difference with the SAXS spectrum of 40 mmol kg^{-1} SiW in water. This indicates that C_3P_2 at such high concentrations does not produce assembly (colloids) of several SiW anions. Moreover, this suggests that, if there is a local change in the solvation sphere of SiW, this does not produce a noticeable difference in the SAXS pattern of the SiW, presumably due to a weak contrast between the solvation shell and the solvent (here C_3P_2/H_2O 55 wt%/45 wt%). However, the strong CP increase suggests that strong interaction between SiW and C_3P_2 takes place in solution, as it was shown by ^{1}H-NMR at lower C_3P_2 concentrations (2 wt%) above, see Fig. S2 (ESI). For 140 mmol kg^{-1} SiW in 55 wt% C_3P_2, the SAXS spectrum shows an intense peak, at q = 3 nm^{-1}, which arises from the SiW-SiW structure factor and provides information on the average SiW-SiW distance (around $2\pi/q \approx 2.1$ nm). This correlation peak is at the same position as in the SAXS spectrum of 140 mmol kg^{-1} SiW in water but its shape is slightly different. Indeed, the peak is thinner in 55 wt% C_3P_2 than in water, which can be related to stronger SiW-SiW electrostatic repulsions, as expected from the lower permittivity of 55 wt% C_3P_2 compared to water. The presence of the peak in the SAXS spectrum arises from the first maximum in the structure factor and its position, at q_{max}, can be related here to the average POM-POM (or

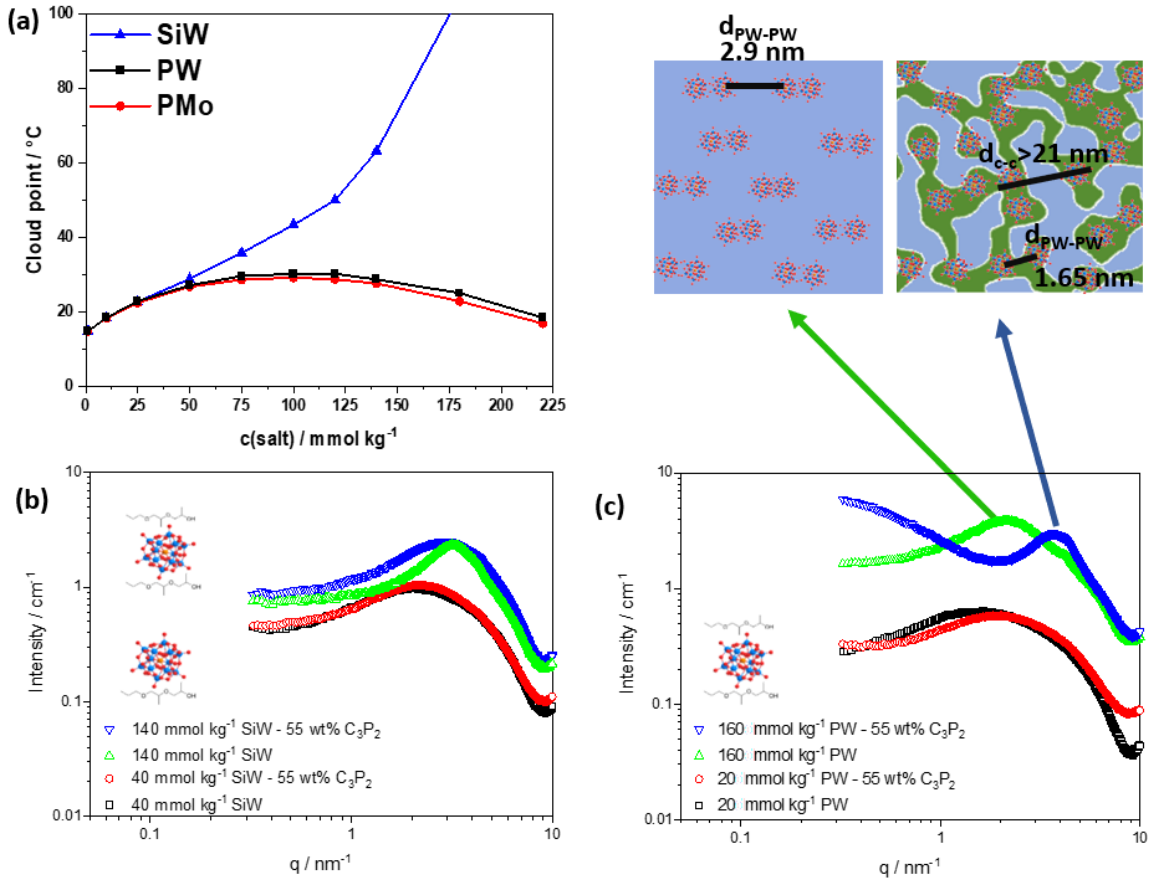

Figure 3.6. (a) Cloud point evolution of 55 wt% C_3P_2 upon addition of POM. SAXS spectra, measured at room temperature, of (b) SiW in water and in 55 wt% C_3P_2 and (c) PW in water and in 55 wt% C_3P_2.

aggregate-aggregate) distance in solution, which corresponds to the first neighbor distance between scattering objects. This is only true if the form factor, *P(q)*, has a negligible effect on the peak position, visible in the scattered intensity spectrum, *I(q)*, which results from the product (or convolution) of *P(q)* and *S(q)*. The expected average SiW-SiW distance for a fully dispersed SiW solution, *i.e.* without SiW aggregation for a molecular solution, can be simply expressed from the SiW concentration, via equation 3.10 by considering a cubic arrangement of POM in solution. Therefore, $d_{SiW\text{-}SiW}$ at 140 mmol kg^{-1} is expected to be around 2.3 nm which is close to the value obtained from the peak position in the SAXS spectrum, *i.e.* 2.1 nm, confirming that SiW is not aggregated in pure water nor in C_3P_2/water (55 wt%/45 wt%) mixture.

For PW 20 mmol kg^{-1}, the general scattering patterns of the PW at $q > 2$ nm^{-1}, arising mainly from the PW form factor (sphere), are comparable in water and in 55 wt% C_3P_2, see Fig. 3.6c. At lower *q* values, a shift of the maximum in the scattered intensity is observed from 2 nm^{-1} in pure water down to 1.2 nm^{-1} in 55 wt% C_3P_2. The maximum in the scattered intensity can be related to the first order PW-PW correlation peak (structure factor), as discussed above. However, the peak is here too weak for further interpretation, in terms of the evaluation of the average PW-PW distance, as it is likely that its position may not be directly resulting from the first maximum in the structure factor. Indeed, a change in the solvent permittivity, water compared to C_3P_2/water (55 wt%/45 wt%), and a change in the local electron density of the PW, due to a different solvation, may affect respectively the structure factor (PW-PW) and the form factor of the solvated PW.

For 160 mmol kg^{-1} PW, the SAXS spectrum shows a significantly different scattering pattern in water and in 55 wt% C_3P_2. In water, a distinct scattering peak is observed at 2.2 nm^{-1}, which corresponds to 2.9 nm in real space. If we assume monomers of PW, *i.e.* unaggregated form which are isotropically distributed in water, the PW-PW distance, $d_{PW\text{-}PW}$, is expected to be 2.2 nm (calculated from equation 3.10 with N_C^{PW} = 1) and the peak position is therefore expected at 2.9 nm^{-1}. This indicates that the correlation peak corresponds to correlation between aggregates, and not between PW anions. Therefore, PW at 160 mmol kg^{-1} is already aggregated in water with an average aggregation number (N_C^{POM}) of 2.2, as calculated from the peak position, at 2.2 nm^{-1} ($d_{PW\text{-}PW}$ = 2.9 nm) from equation 3.10.

This result is in good agreement with the previous work of Bera *et. al.* that has shown, by synchrotron SAXS experiments at high *q* range and by molecular dynamics (MD) simulation, the general tendency of PW to self-assemble in water at high concentrations.[28] Indeed, these authors have shown that PW forms aggregates constituted of several PW anions (dimers, trimers, *etc.*) and that these aggregates turn into larger percolating structures by increasing PW concentration. The presence of these large scattering objects was also detected by using DLS.[27] Therefore, it appears here that PW at 160 mmol kg^{-1} is mostly present as dimers in water, as sketched in Fig. 3.6c (left

sketch).

The spectrum for PW at 160 mmol kg^{-1} is very much different in 55 wt% C_3P_2, compared to the spectrum in pure water, as it shows a correlation peak at higher *q* values and a large scattering excess at low *q*, see Fig. 3.6c. The peak at higher *q* is observed at 3.8 nm^{-1}, which corresponds to 1.65 nm in real space. Considering that the PW dimension is around 1 nm, this latter peak can be attributed to an internal structure factor, *i.e.* to PW-PW correlations inside the aggregates. Indeed, the presence of POM aggregates is confirmed in the low *q*-regime, for $q < 2$ nm^{-1}, where a strong excess scattering is observed. Therefore, PW self-aggregates in mesoscopic structures in 55 wt% C_3P_2. The size of these aggregates is larger than 21 nm, *cf.* Eq. S4 (ESI). It can be noted that the PW-PW distance in the aggregates (1.65 nm) is larger than the expected PW-PW distance at close contact, which is around the size of PW, *ca.* 1 nm. Therefore, it is likely that the aggregates contain C_3P_2 molecules between the PWs. To investigate these objects further, SAXS measurements should be performed at lower angles in order to find out if the aggregates have a finite size, as in the case of the composition 10 wt% C_3P_2 and 50 mmol kg^{-1} of PW. Note that several more SAXS measurements at different POM concentrations in water and in 55 wt% C_3P_2 are shown in Fig. S10 and S11 (ESI).

Nevertheless, here no aggregate-aggregate peak is visible in the spectrum, probably because it appears at *q* lower than 0.3 nm^{-1}. Consequently, we can conclude that the PW aggregation number is larger than 885 (calculated from a peak position of 0.3 nm^{-1} from equation 3.10). This result suggests that the PW aggregates have no finite size, such as encountered in microemulsions with a bicontinuous structure or with an interconnected cylinder network or surfactant-free microemulsions. This hypothesis is further supported by the large concentrations of the three components: water, C_3P_2 and PW, which favours such interconnected structures. If we assume that such infinite size structures form, two pseudo phases should be present: a water-rich and a C_3P_2-rich phase, *i.e.* the PW aggregated phase or the pseudo-phase where PW accumulates. A sketch representing a hypothetical bicontinuous-like mesoscale structure is given as an example in Fig. 3.6c (right). PW is likely to accumulate in the C_3P_2 pseudo-phase, as it was shown by NMR that POMs and C_3P_2 strongly interact and obtained in Fig. S12 (ESI). In such a case, the peak position, here at 3.8 nm^{-1}, informs on the PW concentration in the C_3P_2 rich pseudo phase. By considering evenly distributed PW in a cubic pattern, with $d_{PW\text{-}PW}$ = 1.65 nm, the PW concentration in the C_3P_2 phase can be roughly estimated by using equation 3.10, by taking N_C^{PW} = 1, which gives 357 mmol kg^{-1}. This concentration is then around two times larger than the bulk PW concentration in the whole sample (160 mmol kg^{-1}). This is well in agreement with our hypothesis of the formation of two pseudo phases, where PW accumulates in the C_3P_2 pseudo phase. Indeed, C_3P_2 in the C_3P_2/water mixture is around 55 wt%, therefore the concentration of PW accumulated in a C_3P_2 pseudo phase,

which is probed by the PW-PW peak position observed in SAXS, is expected to be around two times larger than the total bulk PW concentration.

As a conclusion here, the decrease in the CP observed with PW at high concentration (> 100 mmol kg^{-1}, see Fig. 3.6a), is concomitant with the appearance of mesoscale structuration (aggregation of many PW with C_3P_2). This is comparable to the conclusion made at lower C_3P_2 content in water (at 10 wt%), that has also shown that the appearance of aggregates, *i.e.* in this case $[POM]_m[C_3P_2]_n$ colloids with $m \approx 4$ and $n \approx 30$, led to the decrease in the CP. On the contrary, SiW does not self-aggregate in small colloids or mesoscale structures, and lead to a continuous increase in the CP upon POM addition. This different tendency for self-assembly between PW/PMo and SiW seems to be related to the properties of these POMs in water. Indeed, the tendency of PW to self-assemble, compared to SiW, was already observed in pure water.[27,28]

In the following, the effect of POM is investigated over a large range of C_3P_2/water ratios in order to give an overview of the SC effect of Keggin POMs on the evolution of the phase diagram of this short chain amphiphilic molecule in water. Figure 3.7 shows the binary water-C_3P_2 phase diagram and the influence of a constant concentration of c(additive) = 100 mmol kg^{-1} SiW, PW and NaSCN, which can be considered as a classical chaotropic ion. As previously stated, the system water-C_3P_2 shows a LCST, 14 °C, at x(C_3P_2) = 55 wt%, see the green curve in Fig. 3.7. Upon the addition of NaSCN, *i.e.* 100 mmol kg^{-1}, the biphasic region is shifted to higher temperatures. The LCST increases by 10 °C,

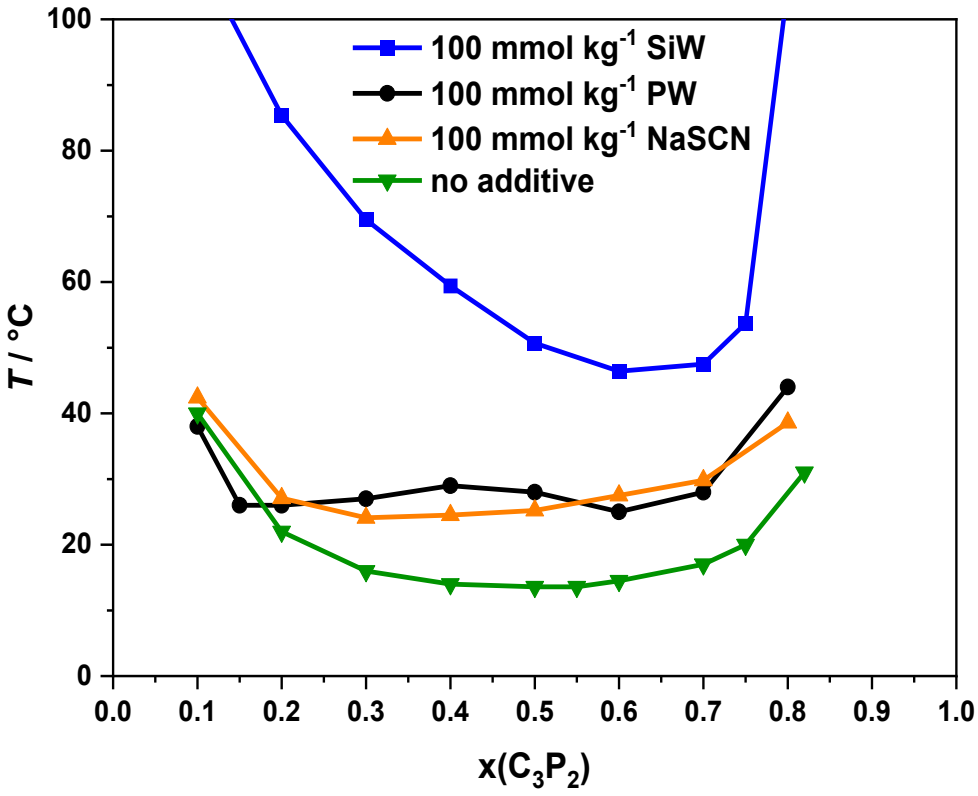

Figure 3.7. Influence of PW, SiW and NaSCN on the binary phase diagram water-C_3P_2. The lines represent the liquid-liquid phase demixion line. Above these lines the system phase separates into two macroscopic liquid phases, one water-rich and one C_3P_2-rich phase.

up to 24 °C. This fact arises due to the salting-in ability of the chaotropic SCN^- and was already intensively investigated.[24,25] Upon the addition of 100 mmol kg^{-1} SiW the phase boundary is shifted to even higher temperatures, *i.e.* the LCST is raised to 46 °C. This is caused by the strong interaction of the superchaotropic SiW with C_3P_2. The influence of PW in contrast causes both: *(i)* an increase of the co-miscibility of water-C_3P_2 ($x(C_3P_2) > 0.2$) and also *(ii)* a decrease of the co-miscibility ($x(C_3P_2) < 0.2$). On the one hand, the increase in co-miscibility for ($x(C_3P_2) > 0.2$) can be explained by the general ability of PW to interact strongly with C_3P_2. On the other hand, the decrease in solubility for ($x(C_3P_2) < 0.2$) can be explained by the formation of C_3P_2/PW co-assemblies, which promote macroscopic liquid-liquid phase separation upon increasing temperature.

It is remarkable that the interaction of common proteins (*e.g.* human serum albumin (HSA)) with surfaces (either charged or uncharged) is not only dictated by electrostatic interactions either.[36,37] For example, the protein adsorption on uncharged surfaces such as polytetrafluorethylene (PTFE) was described by a sum of various components, *e.g.* dispersion forces and Lifshitz-van der Waals forces.[38] POMs also interact via a combination of diverse intermolecular forces, electrostatic, hydration forces, hydrophobic effect and dispersion forces. Therefore, POMs are, in that sense, comparable to proteins. As POMs are known to be catalytically active[39] they may be called artificial enzymes or nanozyme, as already investigated by several research groups.[40–42]

3.5 Conclusion

In this contribution, we showed that the Keggin-type POMs, SiW and PW/PMo, interact strongly in water with a short-chain non-ionic amphiphile, C_3P_2, that is too short to form micelles in water compared to classical surfactants. The strong POM-C_3P_2 interaction (or binding) results from the thermodynamically favorable dehydration of POM and C_3P_2, *i.e.* the superchaotropic effect. This effect was observed here through the significant increase in the CP of C_3P_2 and by NMR measurements. At low POM concentrations (below 15 mmol kg^{-1}) and at 10 wt% C_3P_2, a stronger superchaotropic behavior was observed for PW (and PMo) over SiW, resulting from the lower charge density of PW (3-) over SiW (4-). Lower charge density nano-ions have a weaker hydration and, therefore, their dehydration is easier (or more favorable). This trend in the superchaotropicity of Keggin POMs, PW ≈ PMo > SiW, was observed previously with many other systems: non-ionic surfactants (polyethoxylated and glucose based),[1,2] PEG oligomers,[3] PNiPAM,[14] lipid monolayers,[43] γ-CD[4].

At higher POM concentrations (> 15 mmol kg^{-1}), SiW shows a continuous increase in the CP as a result of strong SiW-C_3P_2 attractive interactions. The combination of SAXS/SANS/NMR shows that SiW forms small nano-assemblies, such as $[SiW][C_3P_2]_{1\text{-}2}$. On the contrary, PW leads to a decrease in the CP which is concomitant with the formation of larger aggregates: *(i)* containing many PW anions

and C_3P_2, with the general formula $[PW]_m[C_3P_2]_n$ at 10 wt% C_3P_2, with $m \approx 4$ and $n \approx 30$, and *(ii)* percolated (interconnected, bicontinuous-like) structures at 55 wt% C_3P_2. This latter structure shows the thermodynamically stable coexistence of two pseudo phases: a water-rich phase and a C_3P_2-rich phase where PW accumulates (*i.e.* the percolated-like structure). In this C_3P_2-rich phase, the average PW-PW distance is around 1.65 nm and the size domain of this structure is > 21 nm.

It seems that the formation of PW aggregates, *i.e.* $[PW]_m[C_3P_2]_n$ and interconnected structure, is related to the intrinsic tendency of PW (or PMo) to self-assemble in water, as shown previously by Bera *et al.*[28] On the contrary, SiW does not form self-assembled colloids containing many SiW anions in water, presumably because of too strong SiW-SiW electrostatic repulsions preventing their self-assembly. However, due to the superchaotropic effect SiW interacts strongly with C_3P_2, as inferred by the continuous increase in the CP upon increasing SiW concentration, whereas PW only leads to an increase in the CP at low concentrations, *i.e.* where it does not self-assemble. The decrease in the CP by further increasing PW concentration is proposed to be due to the screening of the electrostatic repulsions between the $[PW]_m[C_3P_2]_n$, by the excess PW increasing the ionic strength. This screening effect leads to the destabilization of the $[PW]_m[C_3P_2]_n$ colloids and to the phase demixion, and consequently to the decrease in the CP. This process is comparable to the destabilization mechanism of charged colloidal suspensions that is well understood by the DLVO theory.

As a conclusion, we show here for the first time that:

(i) PW induces the self-assembly of a short amphiphilic molecule with hydrophobic character, here an oligopropylene glycol alkylether, in water, and that

(ii) SiW, at high concentrations, has a stronger salting-in property, *i.e.* a stronger increase in the CP of C_3P_2, compared to PW, because of the formation of $[PW]_m[C_3P_2]_n$ colloids (lower Coulomb repulsion of PW clusters compared to SiW clusters).

This stronger salting-in effect of SiW over PW results therefore in a drastic enhancement of the co-miscibility of C_3P_2 and water, up to reaching full co-miscibility at room temperature, see the phase diagram in Fig. 3.7. Considering that POMs are photo-catalytically active, the present results open new opportunities in the design of stimuli-responsive (water-organic) solvent media with controlled nano-structures to perform photochemical reactions.

3.6 Bibliography

[1] B. Naskar, O. Diat, V. Nardello-Rataj, P. Bauduin, *J. Phys. Chem. C* **2015**, *119*, 20985–20992.

[2] T. Buchecker, P. Schmid, S. Renaudineau, O. Diat, A. Proust, A. Pfitzner, P. Bauduin, *Chem. Commun.* **2018**, *54*, 1833–1836.

[3] T. Buchecker, X. LeGoff, B. Naskar, A. Pfitzner, O. Diat, P. Bauduin, *Chem. - A Eur. J.* **2017**, *23*, 8434–8442.

[4] K. I. Assaf, M. S. Ural, F. Pan, T. Georgiev, S. Simova, K. Rissanen, D. Gabel, W. M. Nau, *Angew. Chem. - Int. Ed.* **2015**, *54*, 6852–6856.

[5] S. Yao, C. Falaise, A. A. Ivanov, N. Leclerc, M. Hohenschutz, M. Haouas, D. Landy, M. A. Shestopalov, P. Bauduin, E. Cadot, *Inorg. Chem. Front.* **2021**, *8*, 12–25.

[6] K. I. Assaf, W. M. Nau, *Angew. Chem. - Int. Ed.* **2018**, *57*, 13968–13981.

[7] W. Kunz, *Specific Ion Effects*, World Scientific, Singapore **2010**.

[8] W. Kunz, J. Henle, B. W. Ninham, *Curr. Opin. Colloid Interface Sci.* **2004**, *9*, 19–37.

[9] L. Pérez-Fuentes, D. Bastos-González, J. Faraudo, C. Drummond, *Soft Matter* **2018**, *14*, 7818–7828.

[10] M. Christoforou, E. Leontidis, G. Brezesinski, *J. Phys. Chem. B* **2012**, *116*, 14602–14612.

[11] M. Hohenschutz, I. Grillo, O. Diat, P. Bauduin, *Angew. Chem. - Int. Ed.* **2020**, *59*, 8084–8088.

[12] P. Bauduin, S. Prevost, P. Farràs, F. Teixidor, O. Diat, T. Zemb, *Angew. Chem. - Int. Ed.* **2011**, *50*, 5298–5300.

[13] C. Drummond, L. Pérez-Fuentes, D. Bastos-González, *J. Phys. Chem. C* **2019**, *123*, 28744–28752.

[14] T. Buchecker, P. Schmid, I. Grillo, S. Prévost, M. Drechsler, O. Diat, A. Pfitzner, P. Bauduin, *J. Am. Chem. Soc.* **2019**, *141*, 6890–6899.

[15] A. Misra, K. Kozma, C. Streb, M. Nyman, *Angew. Chem. - Int. Ed.* **2019**, *59*, 596–612.

[16] C. Falaise, M. A. Moussawi, S. Floquet, P. A. Abramov, M. N. Sokolov, M. Haouas, E. Cadot, *J. Am. Chem. Soc.* **2018**, *140*, 11198–11201.

[17] D. Stoye, in *Ulmann`s Encycl. Ind. Chemsitry*, Wiley-VCH Verlag GmbH & Co. KGaA, Weinheim **2012**, 619–688.

[18] W. Kunz, K. Holmberg, T. Zemb, *Curr. Opin. Colloid Interface Sci.* **2016**, *22*, 99–107.

[19] S. E. Friberg, *Curr. Opin. Colloid Interface Sci.* **1997**, *2*, 490–494.

[20] T. K. Hodgdon, E. W. Kaler, *Curr. Opin. Colloid Interface Sci.* **2007**, *12*, 121–128.

[21] D. Evans, H. Wennerström, *The Colloidal Domain*, Wiley, New York City **1999**.

[22] T. Buchecker, S. Krickl, R. Winkler, I. Grillo, P. Bauduin, D. Touraud, A. Pfitzner, W. Kunz, *Phys. Chem. Chem. Phys.* **2017**, *19*, 1806–1816.

[23] P. Bauduin, L. Wattebled, S. Schrödle, D. Touraud, W. Kunz, *J. Mol. Liq.* **2004**, *115*, 23–28.

[24] G. Grundl, M. Müller, D. Touraud, W. Kunz, *J. Mol. Liq.* **2017**, *236*, 368–375.

[25] P. Bauduin, L. Wattebled, D. Touraud, W. Kunz, *Zeitschrift für Phys. Chemie* **2004**, *218*, 631–641.

[26] C. D. Dewhurst, I. Grillo, D. Honecker, M. Bonnaud, M. Jacques, C. Amrouni, A. Perillo-Marcone, G. Manzin, R. Cubitt, *J. Appl. Crystallogr.* **2016**, *49*, 1–14.

[27] A. Malinenko, A. Jonchère, L. Girard, S. Parrès-Maynadié, O. Diat, P. Bauduin, *Langmuir* **2018**, *34*, 2026–2038.

[28] M. K. Bera, B. Qiao, S. Seifert, B. P. Burton-Pye, M. Olvera De La Cruz, M. R. Antonio, *J. Phys. Chem. C* **2016**, *120*, 1317–1327.

[29] M. R. Antonio, M. K. Bera, *Eur. J. Inorg. Chem.* **2019**, *2019*, 367–373.

[30] J. Isrealachvili, *Intermolecular and Surface Forces*, Academic Press, London, **2011**.

[31] J. A. Molina-Bolívar, F. Galisteo-González, R. Hidalgo-Alvarez, *Colloids Surfaces B Biointerfaces* **1999**, *14*, 3–17.

[32] R. M. Pashley, *J. Colloid Interface Sci.* **1981**, *83*, 531–546.

[33] Y. Zhang, S. Furyk, D. E. Bergbreiter, P. S. Cremer, *J. Am. Chem. Soc.* **2005**, *127*, 14505–14510.

[34] J. B. Hayter, J. Penfold, *Mol. Phys.* **1981**, *42*, 109–118.

[35] J. Hansen, J. B. Hayter, *Mol. Phys.* **1982**, *46*, 651–656.

[36] C. M. Roth, A. M. Lenhoff, *Langmuir* **1993**, *9*, 962–972.

[37] W. Norde, *Macromol. Symp.* **1996**, *103*, 5–18.

[38] C. J. Van Oss, R. J. Good, M. K. Chaudhury, *J. Colloid Interface Sci.* **1986**, *111*, 378–390.

[39] S. Krickl, T. Buchecker, A. U. Meyer, I. Grillo, D. Touraud, P. Bauduin, B. König, A. Pfitzner, W. Kunz, *Phys. Chem. Chem. Phys.* **2017**, *19*, 23773–23780.

[40] B. Zhang, M. Zhao, Y. Qi, R. Tian, B. B. Carter, H. Zou, C. Zhang, C. Wang, *Sci. Rep.* **2019**, *9*, 1–12.

[41] Y. He, X. Li, X. Xu, J. Pan, X. Niu, *J. Mater. Chem. B* **2018**, *6*, 5750–5755.

[42] N. Gao, K. Dong, A. Zhao, H. Sun, Y. Wang, J. Ren, X. Qu, *Nano Res.* **2016**, *9*, 1079–1090.

[43] D. Kobayashi, H. Nakahara, O. Shibata, K. Unoura, H. Nabika, *J. Phys. Chem. C* **2017**, *121*, 12895–12902.

4 Counterion effect on α-Keggin polyoxometalates in water: the peculiar role of H^+ on their salting-in effect and co-assembly with organics

4.1 Preface and Abstract

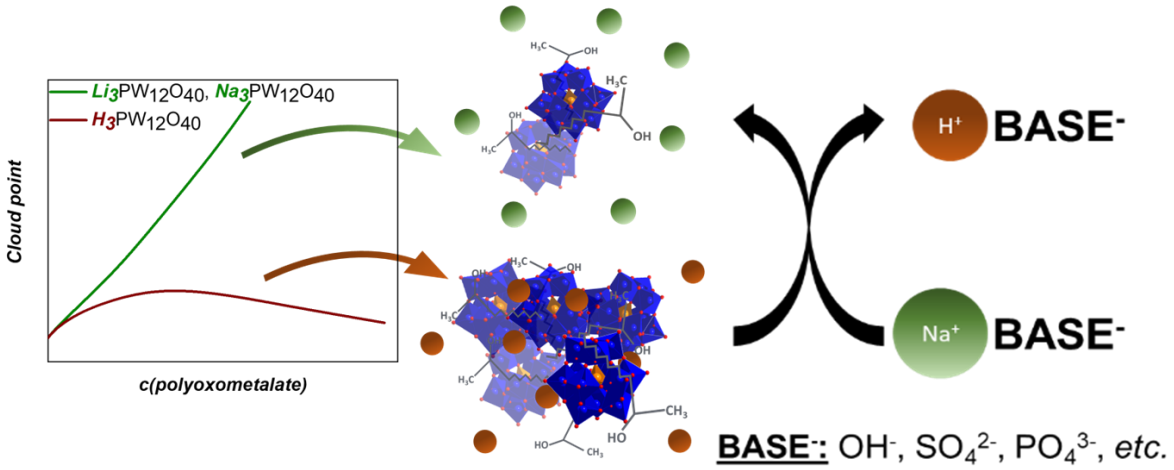

Figure 4.1. Graphical Abstract of the published article in *Journal of Molecular Liquids*.

This chapter was published in the peer-reviewed *Journal of Molecular Liquids* of the publisher Elsevier (DOI: doi.org/10.1016/j.molliq.2022.119214). At this place also the electronic supplementary information (ESI) can be found. Reproduced with permission from Elsevier. Figures and text may differ from the published version. Several other people contributed to this work:

- Dr. Max Hohenschutz performed cloud point and pH measurements in the C_8E_4 system, measured and fitted SAXS spectra, contributed to the original draft of the manuscript and is equal first author.
- Xaver Graß and Michael Witzmann performed a part of cloud point and conductivity experiments.
- Dr. Didier Touraud and Dr. Olivier Diat contributed with fruitful discussions and improved the manuscript.
- Prof. Dr. Arno Pfitzner supervised the project, contributed with fruitful discussion, provided resources and improved the manuscript.
- Dr. Pierre Bauduin supervised the project, conceptualized experiments, contributed with fruitful discussion, wrote and improved the manuscript and is corresponding author.
- Philipp Schmid conceptualized and performed cloud point, NMR and titration (cloud point and conductivity) experiments, prepared samples for SAXS measurements, fitted SAXS spectra, designed the figures and wrote and improved the manuscript.

Abstract: Hofmeister effects of ions in aqueous solution strongly affect chemical and biological systems. High and low charge density anions, such as SO_4^{2-} and SCN^- respectively, decrease (salting-out) or increase (salting-in) the solubility of organic solutes in water. Due to their very low charge density, nanometric anions, *e.g.* polyoxometalates (POMs), increase the solubility of organic solutes tremendously (highly salting-in) as they bind to neutral hydrated solutes strongly – a property that is attributed to the (super-)chaotropic effect. Here, we show that salting-out anions can be turned into salting-in anions in the presence of a superchaotropic POM, α-$PW_{12}O_{40}^{3-}$. The effect of salts composed of salting-out anions, *e.g.* SO_4^{2-}, was investigated on the cloud point (CP) of an ethoxylated surfactant (C_8E_4) and a propoxylated co-solvent (C_3P_2) in the presence of $SiW_{12}O_{40}^{4-}$ and $PW_{12}O_{40}^{3-}$ with different counter-cations (H^+, Li^+, Na^+, K^+). $SiW_{12}O_{40}^{4-}$ and $PW_{12}O_{40}^{3-}$ lead to a monotonic strong CP increase regardless of the counterion, except for $PW_{12}O_{40}^{3-}$ combined with H^+. Indeed, $H_3PW_{12}O_{40}$ shows a CP decrease at high POM concentrations. This peculiar behavior is attributed to the formation of large $H_3PW_{12}O_{40}$-C_3P_2 (and $H_3PW_{12}O_{40}$-C_8E_4) co-assemblies, as shown by SAXS. The formation of these co-assemblies results from the "bridging" effect of H^+ and the lower charge density of $PW_{12}O_{40}^{3-}$ compared to $SiW_{12}O_{40}^{4-}$. The addition of (basic) salting-out anions leads to *(i)* the consumption of H^+, then to *(ii)* the disruption of the large $H_3PW_{12}O_{40}$-C_3P_2 (and $H_3PW_{12}O_{40}$-C_8E_4) co-assemblies and subsequently to *(iii)* a CP increase. In the peculiar case, this shows how commonly used salting-out anions can become apparently salting-in.

4.2 Introduction

Specific ion effects of salts on aqueous solutions of organic solutes are well-known since pioneering work of Franz Hofmeister who studied protein solubility.[1] Commonly, high charge density ions, referred to as kosmotropes, *e.g.* SO_4^{2-}, decrease the solubility of hydrocarbon based solutes in water, a phenomenon called salting-out effect.[2] On the contrary, chaotropes, which are low charge density ions, *e.g.* SCN^-, produce an increase in the solubility of organic matter in water and are therefore called salting-in agents.[3] This general distinction between salting-out (kosmotropes) and salting-in (chaotropes) effect is known to be valid for a broad spectrum of solutes, ranging from proteins[4] and non-ionic micellar systems[5] over polymers[6,7] to small[8] (amphiphilic[9]) molecules and many more.[3] Interestingly, it was found that the effects of mixtures of salting-in and salting-out anions are not additive, *i.e.* a salting-out anion does not necessarily compensate the effect of a salting-in anion.[10]

In the recent years, it was shown that nanometer sized ions ("nano-ions" or NIs) with very low charge density, compared to classical salting-in ions, have a remarkable propensity to adsorb/bind to non-ionic organic solutes in aqueous solution. For example, polyoxometalates (POMs) were shown to adsorb to non-ionic oligo- and polymers,[11,12] surfactant self-assemblies,[13–17] or the

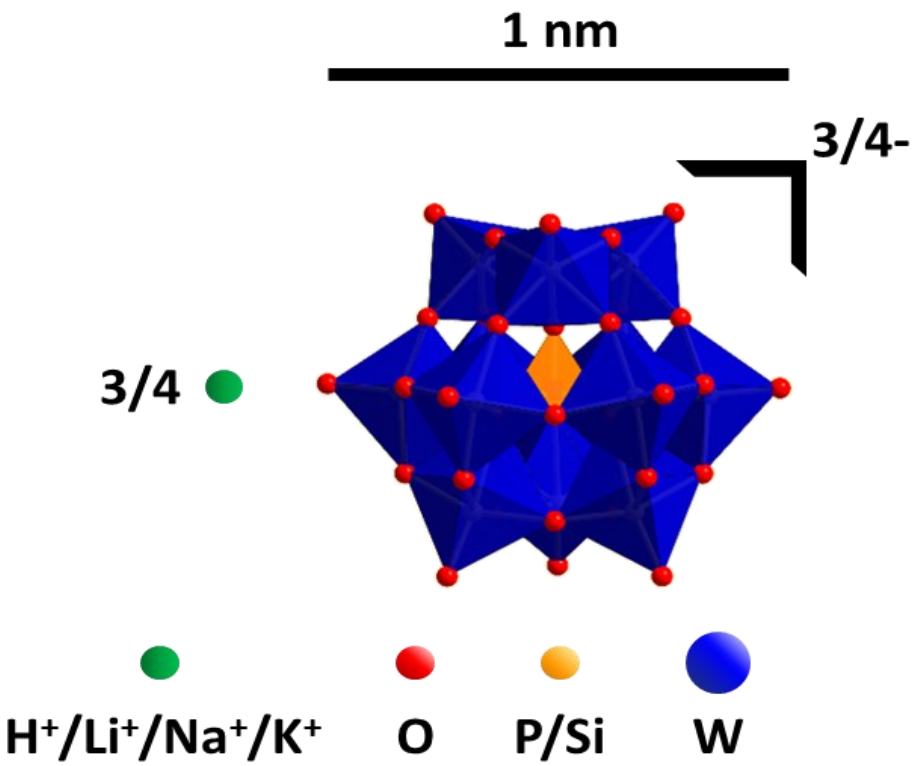

Figure 4.2. Molecular representation of the α-Keggin type POMs: phosphotungstic and silicotungstic acid (HPW and HSiW) and alkali metal-phosphotungstate and -silicotungstate (LiPW, NaPW and LiSiW, NaSiW, KSiW). Atom radii are not drawn to scale.

surfactant-covered air/water interface,[17,18] to bind to macrocyclic molecules,[13,19–21] and to self-assemble with short-chain amphiphiles or co-solvents.[22] Similar strong binding affinity was also observed between anionic boron clusters and non-ionic interfaces/solutes/macrocycles.[15,23–26] Typically, the binding of these NIs with non-ionic solutes occurs at micro- to millimolar concentrations and is driven by a thermodynamically favorable release of hydration water as the NI and the solute bind, resulting in a high gain in enthalpy accompanied by an entropic penalty.[24] This water-mediated driving force – known as the chaotropic effect – causes weak association of classical chaotropic ions in the Hofmeister series, *e.g.* I^- or SCN^-, with non-ionic surfaces[25,27] and is much more pronounced for NIs, which were therefore called superchaotropes.[17,24] Upon association, a superchaotropic ion conveys its charge to the non-ionic solute impacting its phase behavior strongly. Thus, thermo-sensitive non-ionic solutes, which exhibit a thermally induced liquid/liquid phase separation, called a cloud point (CP), manifest a strongly increased CP in the presence of a superchaotropic ion. The extent in the CP increase of the non-ionic surfactant tetraethylene glycol *n*-octylether (C_8E_4) upon addition of a nano-ion informs on its superchaotropicity which scales inversely with the (nano)ion's volume charge density, *i.e.* the lower the charge density, the more chaotropic the ion, and the more strongly the ion binds to non-ionic solutes.[13,14] Hence, in the series of the isostructural α-Keggin POMs: $H_2W_{12}O_{40}^{6-}$, $BW_{12}O_{40}^{5-}$,

$SiW_{12}O_{40}^{4-}$ (SiW) and $PW_{12}O_{40}^{3-}$ (PW), see Fig. 4.2, the chaotropicity increases strongly from Keggin^{6-} to Keggin^{3-}.[13,14,17,28] Interestingly, when considering the effect of POMs on the CPs of the short-chain amphiphile dipropylene glycol *n*-propylether (C_3P_2) or of the poly-*N*-isopropylacrylamide (PNiPAM) polymer, this series was found to be valid only at low POM concentrations. On the contrary, at high POM concentrations, HPW induced a pronounced CP decrease which becomes lower than the CP of HSiW-C_3P_2 or of HSiW-PNiPAM, causing therefore an unexpected reversal in the ordering of HPW and HSiW.[12,22] Reversal of the Hofmeister series as a function of salt concentration was also observed on the CP evolution of *e.g.* lysozyme by increasing salt concentrations of classical chaotropic anions.[29–31] Furthermore, reversal of Hofmeister series was also reported on the binding of ions to the *N*-terminus of uncapped oligopeptides[32] or carboxylate groups depending on pH.[33]

In the particular case of the HPW-C_3P_2 (or HPW-PNiPAM) system, where protons are counterions of PW, it was suggested that the CP decrease observed at high HPW concentration is related to the formation of $[HPW]_m[C_3P_2]_n$ (or $[HPW]_m[PNiPAM]_n$) aggregates/co-assemblies induced by strong short-range attraction between PW clusters and reinforced by the superchaotropic effect. This later interpretation is supported by the general tendency of HPWs to self-aggregate which was observed experimentally at high concentrations in pure water. This self-assembly tendency of HPW was proposed to be due to the presence of "bridging" H^+ between PW clusters.[34–36] HPW self-assemblies are presumably less polar (compared to single PW clusters) as suggested by their preferential distribution in the organic phase in biphasic media (*e.g.* towards the organic phase in water/1-octanol systems). NaPW/LiPW, on the contrary, mainly distribute to the aqueous phase in 1-octanol/water biphasic systems, highlighting again the peculiarity of H^+ as a counterion of $PW_{12}O_{40}^{3-}$.[37] Such counterion effects of α-Keggin POMs are generally often neglected,[38] even though counterions influence strongly the self-assembly behavior of superchaotropic POMs[39] and ionic boron clusters.[40] Moreover, addition of H^+, *i.e.* acidification, was shown to control the complexation of superchaotropic dodecaborate clusters with macrocyclic guests.[41]

Here, we examine first the impact of different monovalent counterions (H^+, Li^+, Na^+, K^+) on the superchaotropic effect of POMs: $SiW_{12}O_{40}^{4-}$ and $PW_{12}O_{40}^{3-}$ via CP measurements of an ethoxylated surfactant (C_8E_4) and a propoxylated co-solvent (C_3P_2). Then, the effect of counterion exchange of H^+ versus alkali cations is performed by titration with classical inorganic bases (NaOH, LiOH) or basic salting-out salts (SO_4^{2-}, PO_4^{3-}, $P_2O_7^{4-}$, $P_3O_{10}^{5-}$). Moreover, the counterion effect was investigated on the aggregation of POMs and C_3P_2 by using small angle X-ray scattering (SAXS) and the speciation of $PW_{12}O_{40}^{3-}$ was followed by ^{31}P-nuclear magnetic resonance (^{31}P-NMR).

4.3 Experimental section

Materials. Phosphotungstic acid hydrate ($H_3PW_{12}O_{40}$, MW = 2880 g/mol, 99.995% purity) and silicotungstic acid hydrate ($H_4SiW_{12}O_{40}$, MW = 2878 g/mol) were purchased from Sigma Aldrich and used without further purification. Sodium phosphotungstate ($Na_3PW_{12}O_{40}$, MW = 2946 g/mol) was also purchased from Sigma Aldrich and used as obtained for SAXS and CP measurements. The other cation-POM were synthesized by an *in-situ* titration of phosphotungstic or silicotungstic acid with an appropriate base, *i.e.* LiOH (powder, purity = 98 %), NaOH (pellets, purity = 97 %), KOH (pellets, purity = 89 %) or *N*-methyl ethanol amine (NMEA, purity = 99 %). All used bases and salts were purchased from Sigma Aldrich. The non-ionic solutes tetraethylene glycol *n*-octyl ether (C_8E_4, $C_{16}H_{34}O_5$, purity > 99%) and dipropylene glycol *n*-propylether (C_3P_2, $C_9H_{20}O_3$, purity > 95%) were purchased from Santa Cruz chemicals and Sigma Aldrich, respectively. Milli-Q water was used with a conductivity lower than 10.5 µS/cm and a total organic carbon content of 400 ppb.

Cloud point (CP) measurements. For CP measurements, 2 g of (pseudo-)ternary (water, C_3P_2/C_8E_4, POM (+ salt/base)) mixtures were prepared into screwable tubes of borosilicate glass. The tubes were put into tube holders set into a thermostat (Thermomix_1460, B. Braun AG, Melsungen). The thermostat was heated with a heating rate of approximately 1 °C min^{-1} and the phase separation was detected visually by the appearance of a white clouding in the sample. Hysteresis of the CP was not obtained for any sample. The expected precision of the measurements is ± 1 °C.

Small angle X-ray scattering (SAXS). SAXS measurements, using Mo-$K_{\alpha1}$ radiation (λ = 0.071 nm), were performed on a bench built by XENOCS. The scattered beam was recorded using a large online scanner detector (diameter: 345 mm, from MAR Research). A large *q*-range (0.2 to 35 nm^{-1}) was covered with an off-center detection. The collimation was applied using a 12:∝ multilayer Xenocs mirror (for Mo radiation) coupled to two sets of scatter less FORVIS slits providing a 0.8 mm × 0.8 mm X-ray beam at the sample position. Pre-analysis of data was performed using the FIT2D software. The scattered intensities, Intensity or *I(q)*, are expressed versus the magnitude of scattering vector $q = [(4\pi)/\lambda]\sin(\vartheta/2)$, where λ is the wavelength of incident radiation and ϑ the scattering angle. 2 mm quartz capillaries were used as sample containers for the solutions. Usual corrections for background (empty cell and detector noise) subtractions and intensity normalization using a high-density polyethylene film as a standard were applied. Experimental resolution was $\Delta q/q$ = 0.05. Silver behenate in a sealed capillary was used as the scattering vector calibration standard. All experiments were performed at 22 ± 2 °C.

Conductivity. Conductivity measurements were carried out in a thermostated measurement cell (22 ± 0.2 °C) under permanent stirring using a low-frequency WTW inoLab Cond 730 conductivity meter connected with a WTW TetraCon 325 electrode (Weilheim, Germany). 20 g of each sample (fixed concentration of C_3P_2 and C_8E_4 in the presence of a fixed concentration of HPW) were filled

in the measurement cell and the additive (base or salt) was successively added. After each addition step, the obtained conductivity was noted.

pH measurements. pH measurements were performed with a conventionally calibrated pH meter from Schott Instruments Analytics (ProLab 2000). The titration procedure was copied from conductivity measurements. Experiments were performed at room temperature.

^{31}P-nuclear magnetic resonance (^{31}P-NMR). Solution ^{31}P-NMR spectra were recorded (at room temperature) with an Avance400 (Bruker) spectrometer using 85 % phosphoric acid as an internal standard. Chemical shifts (δ) are provided in parts per million (ppm) and coupling constants (J) are reported in Hertz (Hz). D_2O was used as solvent.

4.4 Results and Discussion

4.4.1 CP evolution upon POM addition and inhibition of POM-hydrolysis

Figure 4.3a shows schematically the CP measurement of C_8E_4 or C_3P_2 in the presence of different POMs. Figure 4.3b shows the CP evolution of 60 mmol kg^{-1} C_8E_4 as a function of POM concentration, for the phosphotungstates HPW, LiPW, NaPW and the silicotungstates HSiW, LiSiW, NaSiW, KSiW.

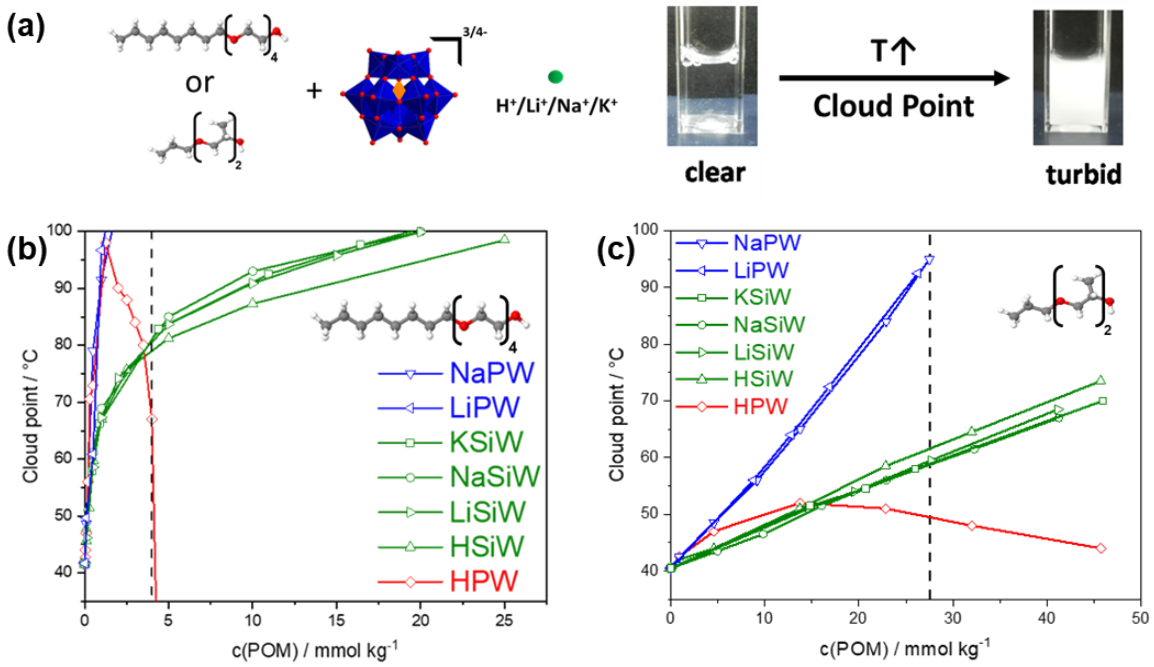

Figure 4.3. (a) Schematic representation of a CP measurement of aqueous C_8E_4 or C_3P_2 solutions upon the addition of POMs. (b) CP of 60 mmol kg^{-1} C_8E_4 as a function of c(POM) and (c) CP of 570 mmol kg^{-1} (10 % (w:w)) C_3P_2 as a function of c(POM). Molecular representations of C_8E_4 and C_3P_2 are provided in the corresponding graphs. The CP increases similarly upon the addition of KSiW, NaSiW, LiSiW or HSiW in both systems, whereas a significant difference occurs by comparing HPW with LiPW and NaPW. HPW leads to a decrease of the CP at high POM concentrations. Dashed dark lines indicate compositions used for titration experiments, see Fig. 4.4.

Note that KPW was not investigated as it shows a limited solubility in aqueous solution. The CP increases identically in the presence of SiW regardless of the counterion up to 2.5 mmol kg^{-1}, while above 2.5 mmol kg^{-1}, HSiW causes a slightly less pronounced CP increase than the alkali cation SiW. For PW, the CP evolution for HPW, LiPW and NaPW overlap up to 1.5 mmol kg^{-1}. At higher PW concentrations, HPW drastically differs from LiPW and NaPW. NaPW or LiPW causes a CP increase beyond 100 °C, while with HPW a sharp drop of the CP occurs, indicating the peculiarity of H^+ with $PW_{12}O_{40}^{3-}$.

For the CP of 10 % (w:w) C_3P_2 (570 mmol kg^{-1}), see Fig. 4.3c, similar conclusions are drawn on the general CP evolution with the different POMs and different counterions. The CP of C_3P_2 increases linearly upon addition of HSiW, LiSiW, NaSiW and KSiW. In this system the CP is slightly higher for the addition of HSiW compared to other silicotungstates, whereas the opposite was obtained in 60 mmol kg^{-1} C_8E_4. Nevertheless, in both systems the CP curves in presence of silicotungstate with different counterions differ only slightly. However, a strong difference occurs again between HPW and the alkali cation phosphotungstates: NaPW and LiPW. NaPW and LiPW lead to a monotonic increase in the CP with a higher slope compared to silicotungstates, while HPW induces a decrease in the CP above 14 mmol kg^{-1}.

The general stronger CP increase for LiPW/NaPW over HSiW/LiSiW/NaSiW/KSiW arises from the higher superchaotropicity of PW compared to SiW, as the charge density of PW is lower compared to SiW. The CP decrease upon the addition of HPW was previously attributed to the formation of $[HPW]_m[C_3P_2]_n$ aggregates and their coalescence at high HPW concentrations.[22,42] In summary, the CP evolutions for both, C_8E_4 and C_3P_2, in Fig. 4.3 show:

(i) HSiW, LiSiW, NaSiW and KSiW exhibit similar effects on the CP of C_8E_4 and C_3P_2 and thus behave alike in the two systems regardless of the counter-cation.

(ii) HPW, LiPW and NaPW increase the CPs similarly only at low concentrations, while at high POM concentrations, only HPW causes a CP decrease. The counterion type (H^+ or Li^+, Na^+) strongly impacts the CP evolution here.

These results unveil the peculiar character of HPW in the series of α-Keggin POMs and highlight the special role of the proton as the counterion of PW.

To investigate further the peculiarity of the proton, the CP (and electrical conductivity) at a fixed HPW concentration, in the region where the CP decrease is observed with HPW (represented by the dark dashed lines in Fig. 4.3b&c), was measured upon addition of a base: the strong inorganic base NaOH (Fig. 4.4) and the weak organic base *N*-methyl ethanolamine (NMEA), pK_b (NMEA) = 4.36 at 20 °C[43], see Fig. S1 (ESI).

For 60 mmol kg^{-1} C_8E_4 with 4 mmol kg^{-1} HPW (dark dashed line in Fig. 4.3b), NaOH addition causes a steep CP increase beyond 100 °C at c(NaOH) < 2.5 mmol kg^{-1}, see Fig. 4.4a&c (blue squares,

regime (I)). Then, at c(NaOH) ≥ 15 mmol kg^{-1} the CP drops again strongly, even below the initial CP of 71 °C in absence of NaOH (blue squares, regime (II)). The CP evolution of 10 % (w:w) C_3P_2 - 27.4 mmol kg^{-1} HPW (dark dashed line in Fig. 4.3c) as a function of c(NaOH) is shown in Fig. 4.4b, blue squares. Similar to the measurements performed on the C_8E_4 system, we observe a strong CP increase at c(NaOH) < 80 mmol kg^{-1} (regime (I)). At higher NaOH concentrations, again a decrease in the CP occurs (regime (II)).

As $H_3PW_{12}O_{40}$ is a strong acid,[44,45] all three protons of HPW are titrated in one step with strong or weak bases.[46,47] Titration of HPW with NaOH results in the POM counterion exchange from H^+ to Na^+ up to the equivalence point (EP) as

$$H_3PW_{12}O_{40} + 3\ NaOH \rightarrow Na_3PW_{12}O_{40} + 3\ H_2O. \quad (4.1)$$

However, it should be noted that PW is well-known to become hydrolyzed in pure water at pH > 2.5, *i.e*. before reaching the EP.[47,48]

The general CP increase (regime (I) in Fig. 4.4a-c and also Fig. S1 (ESI)) is likely to be due to the POM counterion exchange (H^+ to Na^+), as expected from the CP results presented in Fig. 4.3. The CP decrease at higher NaOH concentrations (regime (II) in Fig. 4.4a-c and Fig. S1 (ESI)) is likely to arise from the degradation/hydrolysis of PW into other tungstate species at high pH.[49,50] Indeed, in pure water $PW_{12}O_{40}^{3-}$ decomposes gradually at pH > 2.5. At 2.5 < pH < 9, lacunary POM-species, such as the mono-lacunary $PW_{11}O_{39}^{7-}$ (PW_{11}), form and at pH > 9 orthotungstate, WO_4^{2-}, and phosphate are the major species. We investigated here the PW speciation using ^{31}P-NMR in the presence of 10 % (w:w) C_3P_2 along titration with NaOH, see Fig. 4.4d. The sample compositions for ^{31}P-NMR shown in Fig. 4.4d are indicated by the colored stars in Fig. 4.4b. The composition without added NaOH, 27.4 mmol kg^{-1} HPW in 10 % (w:w) C_3P_2, produces a singlet at -14.8 ppm (dark star symbol in Fig. 4.4d, bottom spectrum) indicating the presence of the plenary $PW_{12}0_{40}^{3-}$ anion. After titration with NaOH (75 mmol kg^{-1}) close to the EP, the NMR spectrum shows no evolution indicating the full integrity of the plenary PW with Na^+ as counterions up to the EP in regime (I), see Fig. 4.4d red (middle) spectrum. Far above the EP (200 mmol kg^{-1} NaOH), the intensity of the singlet at -14.8 ppm is decreased and a second peak occurs at -10.1 ppm showing the partial decomposition of PW to the monolacunary PW_{11} at rather neutral conditions, see Fig. 4.4d green (top) spectrum. It is worth to note that at such high base concentrations, a large portion of plenary PW is still present in solution. Fig. 4.4e summarizes schematically the HPW reactions in the regimes (I) and (II) along titration with NaOH. In regime (I) only a POM-cation exchange from H^+ to Na^+ occurs (according to Eq. 4.1) and in regime (II) the Keggin POM is degraded/hydrolyzed due to the high alkalinity in solution. Importantly, all known decomposition products of PW, *i.e.* lacunary POMs, phosphate and tungstate, exhibit much higher charge densities than PW (Table S1 (ESI)) and are therefore expected

to exhibit less chaotropic or even kosmotropic behavior. Indeed, tungstate[17] and phosphate[9,51] are well-known salting-out anions. Therefore, the CP decrease in regime (II) can be attributed to the salting-out effect of decomposition products of PW (most likely tungstate and phosphate). Interestingly, we show here that the plenary α-Keggin structure of PW is strongly stabilized against hydrolysis in basic conditions (addition of NaOH) by C_3P_2 (10% (w:w)), see Fig. 4.4d and Fig. S2 (ESI). The addition of large quantities of co-solvents (typically around 50 % (w:w)), such as acetone or 1,4-dioxane, is well-known to extend the stability of PW towards neutral pH.[47,48] However, 10 % (w:w) C_3P_2 is much more efficient, compared to these common co-solvents, in stabilizing PW because plenary PW can be observed at neutral pH (here pH ≈ 5-6). At such low contents of organic

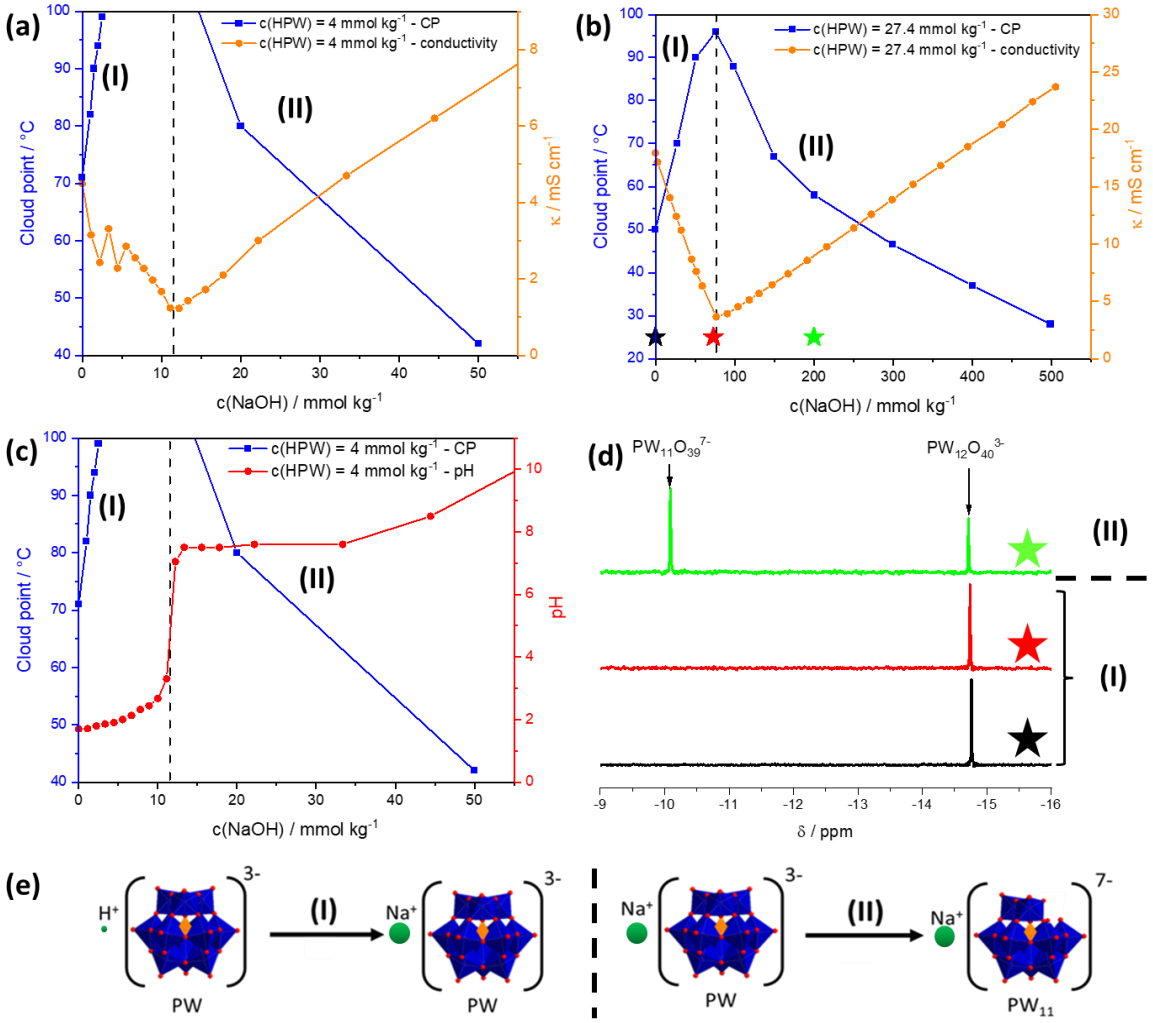

Figure 4.4. CP and conductivity measurements of (a) 60 mmol kg^{-1} C_8E_4 - 4 mmol kg^{-1} HPW and (b) 10 % (w:w) C_3P_2 - 27.4 mmol kg^{-1} HPW as a function of c(NaOH). (c) CP and pH measurements of 60 mmol kg^{-1} C_8E_4 - 4 mmol kg^{-1} HPW. The dark dashed lines indicate that the CP maximum coincides with the equivalence point (EP) which separates two regimes (I) and (II). (d) shows ^{31}P-NMR spectra of HPW in the C_3P_2 - NaOH system (see corresponding-colored stars in (b)) indicating that in regime (I) the plenary PW structure remains intact, whereas in regime (II) the POM is degraded to lacunary species. (e) schematic representations of the chemical reactions in regime (I): only counterion exchange and regime (II): degradation of the Keggin-structure. pH, conductometry and ^{31}P-NMR were performed at room temperature.

co-solvents PW is fully decomposed in water/acetone or water/1,4-dioxane mixtures. Therefore, it seems here that C_3P_2 is more efficient in stabilizing PW than acetone and 1,4-dioxane. This over-stabilization of PW against basic hydrolysis observed with C_3P_2 is likely to be due to the strong association of C_3P_2 with PW as a result of the superchaotropic effect. Very recently, Yao *et al.* showed a similar over-stabilization effect of PW driven by the superchaotropic effect.[48] They have demonstrated that the binding of PW with γ-cyclodextrin (γ-CD) in a stoichiometric PW:γ-CD (1:2) ratio extends the stabilization of PW against hydrolysis from pH < 2.5 in pure water to pH < 5 for PW:γ-CD (1:2) mixtures in aqueous solution, which is fully in line with our findings here.

In parallel, the titrations of HPW-C_8E_4 and HPW-C_3P_2 by NaOH were monitored by conductivity (Fig. 4.4a&b). By titrating 60 mmol kg^{-1} C_8E_4 - 4 mmol kg^{-1} HPW with NaOH, the conductivity decreases linearly from 0 to 12 mmol kg^{-1} NaOH, followed by a linear increase at higher NaOH concentrations, see Fig. 4.4a, orange circles. Here, the initial conductivity decrease is due to the consumption of H^+ (which has a very high specific ion conductivity[52]) being replaced by Na^+ (with a much lower specific ion conductivity than H^+). In regime (II), excess of NaOH leads to a strong increase in conductivity. Therefore, the EP (12 mmol kg^{-1}) is here indicated by a minimum in the conductivity along titration with NaOH (dark dashed line in Fig. 4.4a). In Fig. 4.4b, the EP of the titration of 10 % (w:w) C_3P_2 - 27.4 mmol kg^{-1} HPW with NaOH is detected at around 80 mmol kg^{-1} NaOH (dark dashed line) which coincides precisely with the maximum in the CP (orange circles).

The EP in the C_8E_4 system, determined by conductivity in Fig. 4.4a, was confirmed by a classical pH titration (Fig. 4.4c, red circles). The pH evolution shows a typical sigmoidal shape of a titration of a strong acid by a strong base, with an EP determined at the inflexion point, here at around 12 mmol kg^{-1} NaOH which agrees with the conductivity results in Fig. 4.4a. pH measurements were not possible in the C_3P_2 system due to the large amount (10 % (w:w)) of organic C_3P_2.

In order to further investigate and generalize the apparent correlation between the maximum in the CP and the EP, titration was performed with a weak base, NMEA, in the 10 % (w:w) C_3P_2 system, see Fig. S1 (ESI). The HPW concentration was fixed to 32 mmol kg^{-1}. Here, we observe again that the CP increases strongly between 0 and 100 mmol kg^{-1} NMEA and drops down for higher base concentrations. The CP maximum coincides well with the EP indicated by the conductivity minimum. Further supporting CP results are given in the supporting information, see Figs. S3-S6 (ESI). CP and conductivity titration curves of HPW in 10 % (w:w) C_3P_2 performed at different HPW concentrations (Fig. S3, ESI) are fully in agreement with the results presented here. The CP of C_3P_2 or C_8E_4 (without POM) upon addition of a base shows a much smaller effect compared to the titration in the presence of POM (Fig. S4, ESI). Therefore, the effect of the base on the CP of the pure thermosensitive compounds can be neglected. In a next step, we investigated the reversibility of the salting-in/-out effect of HPW upon successive base/acid titration. Fig. S6 (ESI) shows three

salting-in/-out cycles of the CP of 10 % (w:w) C_3P_2 - 32 mmol kg^{-1} HPW demonstrating the reversibility of the process.

4.4.2 Counterion effects on POM/C_3P_2 assembly

In the following we elucidate the effects of the POM counterions on POM-C_3P_2 self-assembly at the nanometer scale using small angle X-ray scattering (SAXS). For this purpose, we focus on the C_3P_2 system because it constitutes the simpler system without inherent self-assembly[22] compared to the non-ionic surfactant C_8E_4, forming micelles. Thus, we compare exemplary the SAXS spectra of 32 mmol kg^{-1} HPW and 32.1 mmol kg^{-1} NaPW in water and in 10 % (w:w) C_3P_2 with and without HCl and NaCl respectively, see Fig. 4.5. X-rays scatter due to electron density (expressed here as scattering length density, ρ) differences within a sample. Correspondingly, the scattering length density of PW (ρ_{PW} = 74 · 10^{10} cm^{-2}) exceeds largely the one of the dispersing medium composed of water (ρ_{H_2O} = 9.4 · 10^{10} cm^{-2}) and C_3P_2 ($\rho_{C_3P_2}$ = 8.7 · 10^{10} cm^{-2}). Therefore, PW in 10 % (w:w) C_3P_2 produces a large scattering contrast ($\Delta\rho = |\rho_{PW} - \rho_{medium}|$), and consequently the SAXS spectra show exclusively the scattering of PW clusters and their assemblies. The SAXS spectra of 32 mmol kg^{-1} HPW or 32.1 mmol kg^{-1} NaPW in water are identical (dark squares in Fig. 4.5a&b and also see Fig. S7a (ESI)) and show the characteristic scattering of repulsive spheres. The decrease in intensity in the low q regime (q < 1.7 nm^{-1}) here informs on electrostatic repulsions between PWs in solution. The position of the broad maximum at q = 1.7 nm^{-1} informs on the mean PW-PW

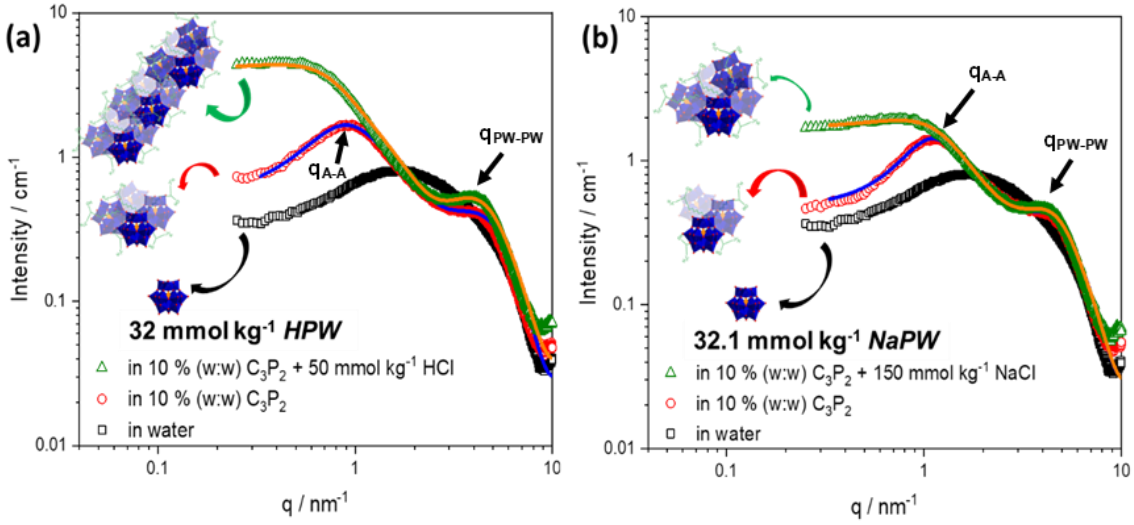

Figure 4.5. SAXS spectra of (a) 32 mmol kg^{-1} HPW in 10 % (w:w) C_3P_2 and in the presence of 10 % (w:w) C_3P_2 + 50 mmol kg^{-1} HCl and (b) 32.1 mmol kg^{-1} NaPW in 10 % (w:w) C_3P_2 and in the presence of 10 % (w:w) C_3P_2 + 150 mmol kg^{-1} NaCl. 32 mmol kg^{-1} HPW and 32.1 mmol kg^{-1} NaPW in water are shown as references. q_{A-A} depicts the correlation peak of the mean aggregate-aggregate distance, whereas q_{PW-PW} indicates the correlation peak of the mean PW-PW distance inside the aggregates. Corresponding sketches of fitting models are provided in the graphs. The spectra were collected at 22 ± 2 °C.

distance of d_{PW-PW} = 3.6 nm. By setting PWs into a cubic lattice, d_{PW-PW} = 3.6 nm, corresponds to a PW concentration of 32 mmol kg^{-1}, which agrees with the experimental PW concentration. Therefore, the peak position attests that the PW clusters are not aggregated in solution, *i.e.* they are dispersed isotopically. A more detailed description of SAXS spectra of aqueous α-Keggin POM solutions is given elsewhere.[34,35,53]

Upon changing the medium from water to 10 % (w:w) C_3P_2 (dark squares to red circles in Fig. 4.5a&b), the SAXS spectra of 32 mmol kg^{-1} HPW and 32.1 mmol kg^{-1} NaPW still show the characteristic intensity increase of individual PW, *i.e.* form factor of the PW, at q > 5 nm^{-1}, while the spectra change drastically at lower q values showing:

(i) a correlation peak at q_{PW-PW} = 4.0 nm^{-1} attributed to PW-PW correlations informs on the average PW-PW distance, d_{PW-PW} = 1.57 nm, and

(ii) an excess scattering at lower q, which can be attributed to aggregates (A), here assembly of PW clusters. The maximum in scattered intensity (correlation peak) is observed at q_{A-A}(HPW) = 0.87 nm^{-1} (Fig. 4.5a) and q_{A-A}(NaPW) = 1.12 nm^{-1} (Fig. 4.5b) and correspond to aggregate-aggregate correlations.

As C_3P_2 itself does not produce any measurable scattering in water, the emergence of excess scattering (point (ii)) at low q occurs due to C_3P_2-induced aggregation of HPW or NaPW. These aggregates are strongly repulsive as indicated by the pronounced intensity decrease at $q < q_{A-A}$. The q_{PW-PW} peak corresponds to the mean POM-POM distance, d_{PW-PW}, within the aggregates. For NaPW as well as for HPW, d_{PW-PW} = 1.57 nm. Considering an approximate PW-diameter of 0.96 nm,[14] the gaps between the PW molecules are 0.61 nm. The aggregates are composed of PW and C_3P_2 (and a negligible number of water molecules) as shown previously by small-angle neutron scattering.[22] Therefore the gaps between the PW clusters within the aggregates are made of nearly pure C_3P_2. These aggregates are denoted as $[PW]_m[C_3P_2]_n$ aggregates.

As stated above, the spectra with HPW and NaPW differ in the positions of q_{A-A} as well as in the maximum intensity (red circles in Fig. 4.5a&b and see also Fig. S7b (ESI)). To simplify the spectra, salt was added to screen the electrostatic repulsions and suppress the q_{A-A} correlation peak. Thus, 50 mmol kg^{-1} HCl (Fig. 4.5a green triangles) and 150 mmol kg^{-1} NaCl (Fig. 4.5b green triangles) were respectively added to 32 mmol kg^{-1} HPW and 32.1 mmol kg^{-1} NaPW in 10 % (w:w) C_3P_2 avoiding counterion mixtures of Na^+/H^+. NaCl/HCl were chosen because Cl^- ions have no pronounced effect on the CP, *i.e.* they are neither salting-out nor salting-in, see Fig. S11 (ESI). Interestingly, HCl (Fig. 4.5a) is much more efficient than NaCl (Fig. 4.5b) in screening the electrostatic repulsion, see also Fig. S5a (ESI). The resulting higher intensity at low q for HPW + HCl compared to NaPW + NaCl suggests that $[PW]_m[C_3P_2]_n$ aggregates are larger and contain more POMs with HPW compared to NaPW (if the volume fractions of the aggregates are assumed to be the same in both cases).

To quantify the aggregation of HPW and NaPW with and without salt, the SAXS spectra were fitted using appropriate theoretical models, see Fig. 4.5 solid lines. A precise description of the fitting procedure is given in section S4.2 and Fig. S8 (ESI). The key results from the fits are shown in Table 4.1.

Table 4.1. Fitting parameters of the PW-aggregates A from the SAXS fits with their volume fraction Φ_A, number of PW-molecules in an aggregate N_A^{PW} and aggregate charge Z_A.

Sample composition in 10 % (w:w) C_3P_2	$\boldsymbol{\Phi_A}$	$\boldsymbol{N_A^{PW}}$	$\boldsymbol{Z_A}$
32 mmol kg^{-1} HPW	0.0182	3.7	9
32.1 mmol kg^{-1} NaPW	0.0176	2.6	11
32 mmol kg^{-1} HPW - 50 mmol kg^{-1} HCl	0.0181	13.4	14
32.1 mmol kg^{-1} NaPW - 150 mmol kg^{-1} NaCl	0.0181	4.5	16

The scattering curve fittings reveal that regardless of the counterion (H^+ or Na^+) of PW or the addition of salt, the volume fraction of the aggregates, Φ_A, stays around 0.018, *i.e.* 1.8 % (v:v). This result indicates that the affinity of PW to aggregate with C_3P_2 is independent of the counterion or added electrolyte, *i.e.* the POM`s superchaotropicity remains strong. However, the volume of the aggregates (Table S4 (ESI)) and the number of PWs per aggregate, N_A^{PW}, changes significantly depending on the type of counterion and added salt. Thus, around 4 (3.7) PWs constitute the aggregates for 32 mmol kg^{-1} HPW ($[PW]_{3.7}[C_3P_2]_n$), while for 32.1 mmol kg^{-1} NaPW, only 3 (2.6) PW molecules ($[PW]_{2.6}[C_3P_2]_n$) make up each aggregate. Addition of HCl or NaCl respectively then further promotes aggregation to 13.4 PWs for 32 mmol kg^{-1} HPW + 50 mmol kg^{-1} HCl ($[PW]_{13.4}[C_3P_2]_n$) or to 4.5 PWs for 32.1 mmol kg^{-1} NaPW + 150 mmol kg^{-1} NaCl ($[PW]_{4.5}[C_3P_2]_n$). Thus, screening with an acid, here HCl, is found to be much more effective at promoting the self-assembly of PW, which is already more pronounced for 32 mmol kg^{-1} HPW than for 32.1 mmol kg^{-1} NaPW in absence of salt/acid. These results corroborate the difference in the behavior of the counterions H^+ and Na^+ on the CP (Fig. 4.3). A look into the charge of the aggregates, Z_A, from the Hayter-MSA structure factor[54,55] hints at the underlying mechanism. In the aggregates of HPW in the presence of HCl, the electrostatic charge is very low considering the number of aggregated POMs, *i.e.* an aggregate of 13.4 PW molecules carries the charge of only 14 whereas it is expected to be around 42 (if full dissociation of HPW is considered). Therefore, HPW in the aggregates is not fully dissociated as previously suggested by molecular dynamics simulations.[36] In contrast, the charge of the NaPW aggregates in the presence of NaCl is found to be very high, *i.e.* 16 charges for an aggregate of 4.5 PW molecules. In the presence of Na^+ counterions, PW therefore seems to be fully dissociated, and the fitting procedure here results even in a reasonable overestimation of the charge of the aggregate.

In summary, the SAXS spectra and their quantitative analysis suggest that H^+ (compared to Na^+) as the counterion of PW, promotes strongly the self-assembly of PW anions with C_3P_2 in aggregates $[PW]_m[C_3P_2]_n$. This is related to the general propensity of HPW to self-assemble in pure water[22,34] and the proton`s location in the close vicinity of the PW anion,[34,36] leading to a screening of the electrostatic repulsions and therefore a gluing of PW anions by protons.

Considering previous publications on PW in pure water, H^+ shows theoretically, by density functional theory (DFT) and molecular dynamics (MD) simulation, a shorter cation-POM distance compared to alkali cations (see section S5 (ESI)). This is paradoxical as HPW is usually considered as a superacid, *i.e.* it tends to be fully dissociated also in lower permittivity medium.[44] However, it is in agreement with the promoting role of H^+ for self-assembly in pure water and observed here with HPW and C_3P_2. In light of these conclusions, the stepwise addition of the base NMEA up to the EP of 32 mmol kg^{-1} HPW in 10 % (w:w) C_3P_2 causes a decrease in SAXS intensity, *i.e.* a decrease in size of the $[PW]_m[C_3P_2]_n$ aggregates, which can be readily understood as the self-assembly promoting proton is consumed by NMEA, see Fig. S9 (ESI).

4.4.3 How to turn salting-out anions into salting-in anions?

The influence of several (Na-)salts on bare C_3P_2 solutions was the topic of previous investigations.[9,51] Note that the effect of several classical Na-salts on 10 % (w:w) C_3P_2 is shown in Fig. S11 (ESI). As observed for many other systems,[2,4,7] salting-out ions (such as SO_4^{2-}, PO_4^{3-}, $P_2O_7^{4-}$ or $P_3O_{10}^{5-}$) lead to a pronounced decrease in the CP. Here, we probe the influence of classical salting-out sodium salts on the CP of 10 % (w:w) C_3P_2 in the presence of 32 mmol kg^{-1} HPW, see Fig. 4.6. Aside from their strong salting-out character, the investigated anions are also (weak) bases (*e.g.* $pK_a(SO_4^{2-}/HSO_4^-) \approx 1.9$ or $pK_a(PO_4^{3-}/HPO_4^{2-}) \approx 12.3$[56], pH of 32 mmol kg^{-1} HPW: pH ≈ 1). Therefore, a comparable CP increase upon addition of kosmotropic Na-salts is expected as observed with NaOH (Fig. 4.4b) or NMEA (Fig. S1 (ESI)). Indeed, a strong CP increase followed by a CP decrease, with a maximum in CP at around 100 mmol kg^{-1} Na_2SO_4, and 20 mmol kg^{-1}, 50 mmol kg^{-1} and 20 mmol kg^{-1} for Na_3PO_4, $Na_4P_2O_7$ and $Na_5P_3O_{10}$ respectively, is observed. Notably, these CP maxima are close to 100 °C and highlight, how efficiently salting-out anions can be turned into salting-in anions here. Moreover, conductometry results are shown as an example for the addition of Na_2SO_4 in Fig. S19 and Fig. S20 (ESI). Indeed, minima in the conductivity titration curves are observed upon the addition of a Na_2SO_4 for different HPW concentrations. Here, compared to the bases investigated previously (NaOH or NMEA), the maximum in the CP and minimum in conductivity are not at the same base/salt concentration because SO_4^{2-} *(i)* is a weaker base and it *(ii)* does not only neutralize

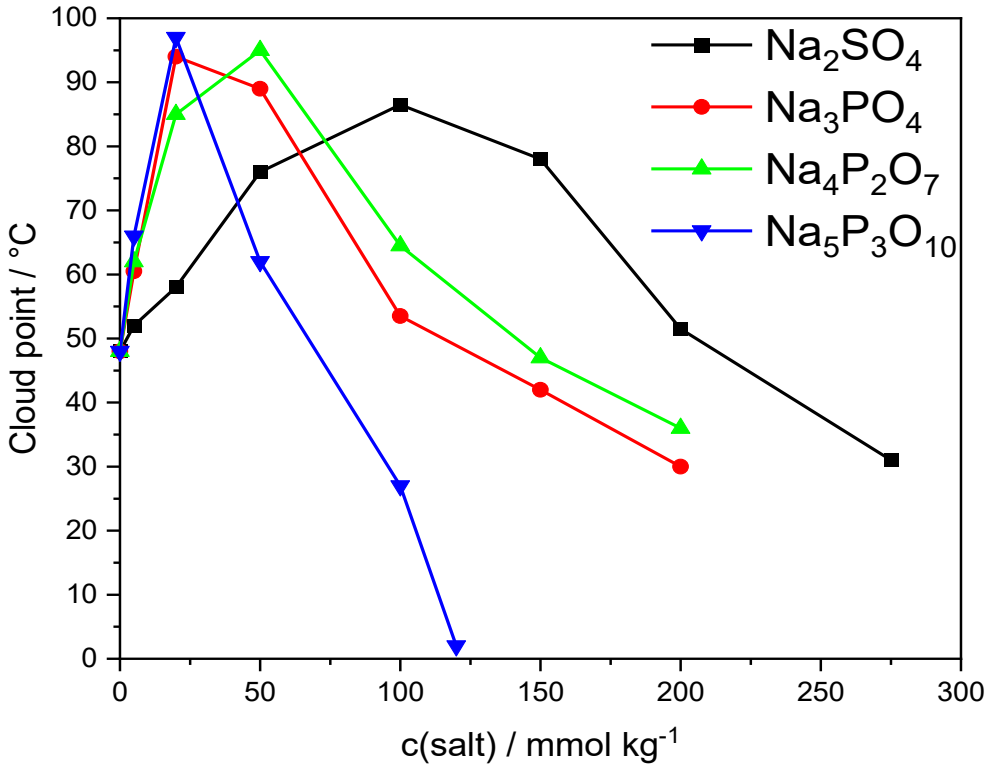

Figure 4.6. CP evolution of 10 % (w:w) C_3P_2 - 32 mmol kg^{-1} HPW upon the addition of kosmotropic Na-salts showing the apparent salting-in property of commonly strong salting-out anions.

HPW but also participates strongly to the ionic strength. Supporting results are shown in section S6 (ESI) on a broad spectrum of salting-out sodium salts. The present results point out that the basic character of classical salting-out anion may play a decisive role on the salting-in/salting-out behavior of salts and therefore on the reversal of Hofmeister series.

4.5 Conclusion

We show here, how PW in its acidic form can turn classical salting-out salts into highly salting-in salts and therefore (partially) invert the classical Hofmeister series, as previously observed by addition of classical salt on the CP of proteins like lysozyme.[29,57,58]

The often overlooked counterion effects of POMs have a strong effect on the solubility of POMs.[38] Nevertheless, it was found here that the type of alkali counterion (Li^+, Na^+, K^+) of α-Keggin type POMs $PW_{12}O_{40}^{3-}$ (PW) and $SiW_{12}O_{40}^{4-}$ (SiW) does not change their (superchaotropicity-driven) association with the non-ionic surfactant C_8E_4 and short-chain amphiphile C_3P_2. In both systems, SiW and PW produced a strong CP increase with alkali counter-cations (Li^+, Na^+, K^+). A steeper CP increase was observed for PW compared to SiW as expected from its lower charge density, *i.e.* stronger (super)chaotropic effect. A peculiarity was found for PW with protons as counterions. Indeed, HPW forms large co-assemblies with C_3P_2, (C_8E_4 and in a previous investigation PNiPAM[12]) phase-demix at lower temperatures. Addition of a base, *e.g.* NaOH or salting-out, basic salts, such

as Na_2SO_4, leads to the consumption of the proton counterions which results in the counterion exchange (H^+ by Na^+) and therefore in the formation of NaPW that strongly increases CP compared to HPW.

The larger size of the aggregates formed with HPW is likely to be related to the location of the proton, *i.e.* in the close vicinity of PW anions compared to SiW, as suggested by Chaumont *et al.* and Bera *et al.*[34,36] Bera *et al.* proposed that the (hydrated) proton H^+, under the form of H_3O^+ or $H_5O_2^+$ (next to other cations such as Cs^+, UO_2^{2+}, Eu^{3+} or tetrabutylammonium according to Chaumont *et al.*) acts as a bridging cation between PW clusters, which promotes self-assembly of HPW in water (compared to HSiW), or in our case PW-C_3P_2 (or PW-C_8E_4) co-assembly. Interestingly, the formation of PW-C_3P_2 aggregates was shown to stabilize superchaotropic α-Keggin PW species against hydrolysis up to pH = 5, while in pure water PW is hydrolyzed, *e.g.* into lacunary species, at pH > 2.5. Consumption of (hydrated) protons by a base leads to decrease the tendency of PW to co-assemble with C_3P_2 and to an increase CP. Therefore, classical salting-out anions (with a basic character, *e.g.* SO_4^{2-}) produce here a strong salting-in effect, *i.e.* inverting the Hofmeister effect of classical salts. The present study thus provides some hints on another mechanism leading to inversion of Hofmeister series, that is well known in the literature for other systems [29–31].

The basicity of salting-out (kosmotropic) anions is usually not considered and overlooked in the investigations of Hofmeister effects in colloidal systems, while it is expected to have a substantial effect especially on pH dependent systems *e.g.* on proteins.[59] In the present work, the strong salting-in behavior of POM is “hidden” by the proton counterion and then released by consuming H^+ and exchanging it by another cation (upon addition of a salt containing a basic/salting-out anion). Therefore, we show here that salt effects with superchaotropic POMs can be non-additive, as previously observed for classical Hofmeister salts.[10] It is worth to note that another indirect Hofmeister series reversal was observed by Klaus *et al.*[60] The authors showed that divalent salting-out anions such as SO_4^{2-} or CO_3^{2-} push isotropically distributed sodium xylene sulfonate (SXS, strong salting-in agent) into micelles of a thermosensitive surfactant. As a consequence, SO_4^{2-} or CO_3^{2-} indirectly produce a CP increase.

Such general conclusion on specific ion effects highlights the peculiar role of the proton, which is already known to have a special place among monovalent cations. For example the proton shows surface activity, while all other cations have the opposite tendency on the surface tension of water.[61,62]

4.6 Bibliography

[1] F. Hofmeister, *Arch. Exp. Pathol. Pharmakol.* **1888**, *25*, 1–30.

[2] W. Kunz, P. Lo Nostro, B. W. Ninham, *Curr. Opin. Colloid Interface Sci.* **2004**, *9*, 1–18.

[3] W. Kunz, *Specific Ion Effects*, World Scientific, Singapore **2010**.

[4] H. I. Okur, J. Hladilkova, K. B. Rembert, Y. Cho, J. Heyda, J. Dzubiella, P. S. Cremer, P. Jungwirth, *J. Phys. Chem. B* **2017**, *121*, 1997–2014.

[5] P. Parekh, U. R. Yerramilli, P. Bahadur, *Indian J. Chem.* **2013**, *52A*, 1284–1290.

[6] Y. Zhang, S. Furyk, D. E. Bergbreiter, P. S. Cremer, *J. Am. Chem. Soc.* **2005**, *127*, 14505–14510.

[7] Y. Zhang, S. Furyk, L. B. Sagle, Y. Cho, D. E. Bergbreiter, P. S. Cremer, *J. Phys. Chem. C* **2007**, *111*, 8916–8924.

[8] E. A. Algaer, N. F. A. van der Vegt, *J. Phys. Chem. B* **2011**, *115*, 13781–13787.

[9] G. Grundl, M. Müller, D. Touraud, W. Kunz, *J. Mol. Liq.* **2017**, *236*, 368–375.

[10] E. E. Bruce, P. T. Bui, B. A. Rogers, P. S. Cremer, N. F. A. van der Vegt, *J. Am. Chem. Soc.* **2019**, *141*, 6609–6616.

[11] T. Buchecker, X. LeGoff, B. Naskar, A. Pfitzner, O. Diat, P. Bauduin, *Chem. - A Eur. J.* **2017**, *23*, 8434–8442.

[12] T. Buchecker, P. Schmid, I. Grillo, S. Prévost, M. Drechsler, O. Diat, A. Pfitzner, P. Bauduin, *J. Am. Chem. Soc.* **2019**, *141*, 6890–6899.

[13] S. Yao, C. Falaise, A. A. Ivanov, N. Leclerc, M. Hohenschutz, M. Haouas, D. Landy, M. A. Shestopalov, P. Bauduin, E. Cadot, *Inorg. Chem. Front.* **2021**, *8*, 12–25.

[14] T. Buchecker, P. Schmid, S. Renaudineau, O. Diat, A. Proust, A. Pfitzner, P. Bauduin, *Chem. Commun.* **2018**, *54*, 1833–1836.

[15] M. Hohenschutz, I. Grillo, O. Diat, P. Bauduin, *Angew. Chem. - Int. Ed.* **2020**, *59*, 8084–8088.

[16] L. Girard, B. Naskar, J. F. Dufrêche, J. Lai, O. Diat, P. Bauduin, *J. Mol. Liq.* **2019**, *293*, 111280.

[17] B. Naskar, O. Diat, V. Nardello-Rataj, P. Bauduin, *J. Phys. Chem. C* **2015**, *119*, 20985–20992.

[18] M. Hohenschutz, I. Grillo, C. D. Dewhurst, P. Schmid, L. Girard, A. Jonchère, O. Diat, P. Bauduin, *J. Colloid Interface Sci.* **2021**, *603*, 141–147.

[19] Y. Wu, R. Shi, Y. Wu, J. M. Holcroft, Z. Liu, M. Frasconi, M. R. Wasielewski, H. Li, J. F. Stoddart, *J. Am. Chem. Soc.* **2015**, *137*, 4111–4118.

[20] M. A. Moussawi, M. Haouas, S. Floquet, W. E. Shepard, P. A. Abramov, M. N. Sokolov, V. P. Fedin, S. Cordier, A. Ponchel, E. Monflier, J. Marrot, E. Cadot, *J. Am. Chem. Soc.* **2017**, *139*, 14376–14379.

[21] C. Falaise, M. A. Moussawi, S. Floquet, P. A. Abramov, M. N. Sokolov, M. Haouas, E. Cadot, *J. Am. Chem. Soc.* **2018**, *140*, 11198–11201.

[22] P. Schmid, T. Buchecker, A. Khoshsima, D. Touraud, O. Diat, W. Kunz, A. Pfitzner, P. Bauduin, *J. Colloid Interface Sci.* **2021**, *587*, 347–357.

[23] A. T. Merhi, A. Jonchère, L. Girard, O. Diat, M. Nuez, C. Viñas, P. Bauduin, *Chem. - A Eur. J.* **2020**, *26*, 13935–13947.

[24] K. I. Assaf, M. S. Ural, F. Pan, T. Georgiev, S. Simova, K. Rissanen, D. Gabel, W. M. Nau, *Angew. Chem. - Int. Ed.* **2015**, *54*, 6852–6856.

[25] K. I. Assaf, W. M. Nau, *Angew. Chem. - Int. Ed.* **2018**, *57*, 13968–13981.

[26] K. I. Assaf, B. Begaj, A. Frank, M. Nilam, A. S. Mougharbel, U. Kortz, J. Nekvinda, B. Grüner, D. Gabel, W. M. Nau, *J. Org. Chem.* **2019**, *84*, 11790–11798.

[27] W. Kunz, J. Henle, B. W. Ninham, *Curr. Opin. Colloid Interface Sci.* **2004**, *9*, 19–37.

[28] D. Kobayashi, H. Nakahara, O. Shibata, K. Unoura, H. Nabika, *J. Phys. Chem. C* **2017**, *121*, 12895–12902.

[29] Y. Zhang, P. S. Cremer, *Proc. Natl. Acad. Sci.* **2009**, *106*, 15249–15253.

[30] M. Boström, D. F. Parsons, A. Salis, B. W. Ninham, M. Monduzzi, *Langmuir* **2011**, *27*, 9504–9511.

[31] A. Salis, F. Cugia, D. F. Parsons, B. W. Ninham, M. Monduzzi, *Phys. Chem. Chem. Phys.* **2012**, *14*, 4343–4346.

[32] J. Paterová, K. B. Rembert, J. Heyda, Y. Kurra, H. I. Okur, W. R. Liu, C. Hilty, P. S. Cremer, P. Jungwirth, *J. Phys. Chem. B* **2013**, *117*, 8150–8158.

[33] N. Schwierz, D. Horinek, R. R. Netz, *Langmuir* **2015**, *31*, 215–225.

[34] M. K. Bera, B. Qiao, S. Seifert, B. P. Burton-Pye, M. Olvera De La Cruz, M. R. Antonio, *J. Phys. Chem. C* **2016**, *120*, 1317–1327.

[35] M. R. Antonio, M. K. Bera, *Eur. J. Inorg. Chem.* **2019**, *2019*, 367–373.

[36] A. Chaumont, G. Wipff, *Phys. Chem. Chem. Phys.* **2008**, *10*, 6940–6953.

[37] P. Schmid, G. Jost, X. Grass, D. Touraud, O. Diat, A. Pfitzner, P. Bauduin, *Green Chem.* **2022**, *24*, 2516–2526.

[38] A. Misra, K. Kozma, C. Streb, M. Nyman, *Angew. Chem. - Int. Ed.* **2019**, *59*, 596–612.

[39] P. Yin, D. Li, T. Liu, *Chem. Soc. Rev.* **2012**, *41*, 7368–7383.

[40] Z. Medos, B. Hleli, Z. Tosner, P. Ogrin, T. Urbic, K. Kogej, M. Bester-Rogac, P. Matejicek, *J. Phys. Chem. C* **2022**, *126*, 5735–5742.

[41] W. Wang, X. Wang, C. Xiang, X. Zhou, D. Gabel, W. M. Nau, K. I. Assaf, H. Zhang, *ChemNanoMat* **2019**, *5*, 124–129.

[42] J. Isrealachvili, *Intermolecular and Surface Forces*, Academic Press, London, **2011**.

[43] R. J. Littel, M. Bos, G. J. Knoop, *J. Chem. Eng. Data* **1990**, *35*, 276–277.

[44] I. V Kozhevnikov, *Chem. Rev.* **1998**, *98*, 171–198.

[45] J. J. Borrás-Almenar, E. Coronado, A. Müller, M. Pope, *Polyoxometalate Molecular Science*, Springer, Netherlands, Dondrecht, **2003**.

[46] B. J. Smith, V. A. Patrick, *Aust. J. Chem.* **2004**, *57*, 261–268.

[47] Z. Zhu, R. Tain, C. Rhodes, *Can. J. Chem.* **2003**, *81*, 1044–1050.

[48] S. Yao, C. Falaise, N. Leclerc, C. Roch-Marchal, M. Haouas, E. Cadot, *Inorg. Chem.* **2022**, *61(9)*, 4193-4203.

[49] N. I. Gumerova, A. Rompel, *Chem. Soc. Rev.* **2020**, *49*, 7568–7601.

[50] R. I. Maksimovskaya, G. M. Maksimov, *Coord. Chem. Rev.* **2019**, *385*, 81–99.

[51] P. Bauduin, L. Wattebled, D. Touraud, W. Kunz, *Zeitschrift für Phys. Chemie* **2004**, *218*, 631–641.

[52] C. A. Reed, *Acc. Chem. Res.* **2013**, *46*, 2567–2575.

[53] A. Malinenko, A. Jonchère, L. Girard, S. Parrès-Maynadié, O. Diat, P. Bauduin, *Langmuir* **2018**, *34*, 2026–2038.

[54] J. B. Hayter, J. Penfold, *Mol. Phys.* **1981**, *42*, 109–118.

[55] J. Hansen, J. B. Hayter, *Mol. Phys.* **1982**, *46*, 651–656.

[56] C. E. Mortimer, U. Müller, *Chemie - Das Basiswissen Der Chemie*, Thieme, Stuttgart, **2014**.

[57] N. Schwierz, D. Horinek, R. R. Netz, *Langmuir* **2010**, *26*, 7370–7379.

[58] N. Schwierz, D. Horinek, U. Sivan, R. R. Netz, *Curr. Opin. Colloid Interface Sci.* **2016**, *23*, 10–18.

[59] P. Yuan, Z. Ruan, L. Liu, T. Li, T. Jing, L. Yan, *Macromol. Chem. Phys.* **2017**, *219*, 1–10.

[60] A. Klaus, G. J. T. Tiddy, R. Rachel, A. P. Trinh, E. Maurer, D. Touraud, W. Kunz, *Langmuir* **2011**, *27*, 4403-4411.

[61] S. I. Mamatkulov, C. Allolio, R. R. Netz, D. J. Bonthuis, *Angew. Chem. - Int. Ed.* **2017**, *56*, 15846-15851.

[62] S. Das, M. Bonn, E. H. G. Backus, *Angew. Chem. - Int. Ed.* **2019**, *58*, 15636–15639.

5 The potential role of chaotropic polyoxometalates in the origin of life

5.1 Preface and Abstract

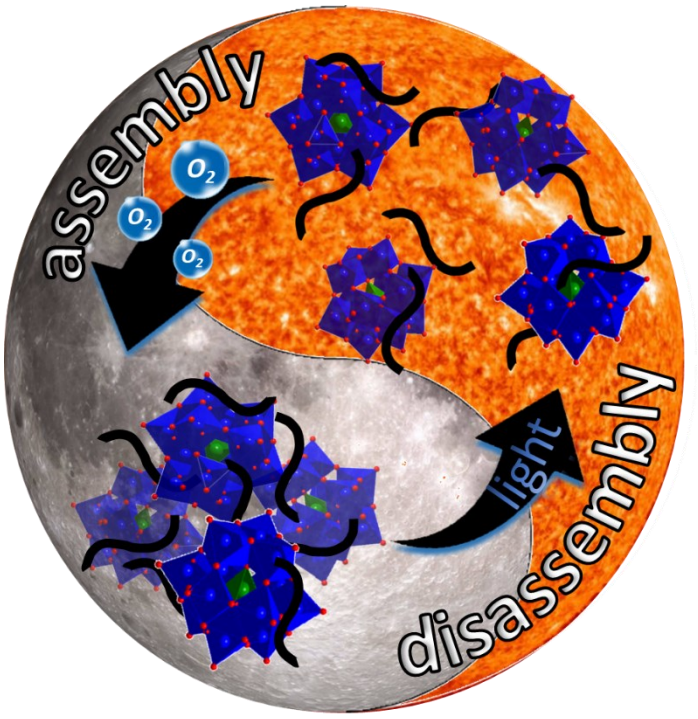

Figure 5.1. Graphical Abstract of the prepared article.

This chapter is prepared as a letter for the peer-reviewed Journal *Nature Chemistry*. Several other people contributed to this work:

- Dr. Didier Touraud contributed with fruitful discussions.
- Dr. Max Hohenschutz assisted with the simulation of SAXS spectra and contributed with fruitful discussion.
- Dr. Olivier Diat contributed with fruitful discussion and improved the manuscript.
- Prof. Dr. Arno Pfitzner supervised the project, provided resources, contributed with fruitful discussions and improved the manuscript.
- Dr. Pierre Bauduin supervised the project, initiated the link between the chaotropic effect and the origin of life with a crucial literature research, measured one SAXS spectrum, wrote and improved the manuscript and is corresponding author.
- Philipp Schmid conceptualized and performed all experiments, designed the figures, wrote and improved the manuscript.

Abstract: Self-assembly, leading to supramolecular arrangements, played a crucial role in the evolution of life.[1–3] Metal ions are fundamental elements for the maintenance of living systems to control, for example, the electrochemical environment.[4] It was proposed that the association of

large, poorly solvated ions (radius about 0.2 nm) – known as chaotropes – in water could be a first step towards the origin of life.[5] However, the role of the chaotropic effect in self-assembling life was never demonstrated experimentally. Here, we present a photoredox-responsive inorganic-organic hybrid system, based on a highly chaotropic polyoxometalate[6] (radius about 0.5 nm) and an oligomeric propylene glycol, as a model for prebiotic self-assembly. Indeed, the assembly-disassembly of this system synchronizes with day/night cycle. Therefore, these supramolecular aggregates adapt to environmental conditions and subsequently display properties, characteristic of emerging life.[3] The availability of oxometalate- or thiometalate-ion species (*i.e.* WO_4^{2-} and WS_4^{2-}),[7] forming polyoxometalates or polythiometalates under acidic conditions, and oligomeric organic biomolecules (oligonucleotides or oligopeptides)[8] in the prebiotic ocean suggests that a similar scenario may have taken place in early life evolution. Our findings show how the chaotropic effect could have played a role for the origin of life on earth.

5.2 Introduction

Investigating chemical evolution and its contribution to the origin of life is still a huge challenge as it requires knowledge in diverse scientific disciplines and the imagination of scientists.[9–12] A crucial stage for emerging life was the hierarchical construction of cellular constituents from small molecules (*e.g.* lipids and sugars) or oligomers (*e.g.* oligopeptides and oligonucleotides).[13–15] Covalent linkage of these molecular subunits and multiple non-covalent interactions forming supramolecular assemblies were both decisive for the emergence of life.[14,16] Such supramolecular self-assemblies in living systems are known to respond to external stimuli and adapt to environmental conditions.[3]

During the evolution of life, metal ions were incorporated into organic systems to control the redox environment and to perform chemical syntheses.[17] For instance, ferredoxin – a redox-protein – was shown to be one of the first proteins on earth.[18,19] Recently, self-assembly of inorganic ions, *e.g.* CN^- or SCN^-, was suggested as a driving force for the synthesis of nucleobases in the prebiotic ocean.[5] The formation of such assemblies emerges from the chaotropic character of large, weakly hydrated anions as SCN^- ($r_{SCN^-} \approx 0.2$ nm).[20] Indeed, chaotropes may associate with each other or adsorb to organic solutes by stripping off their hydration shell – a phenomenon called chaotropic effect.[21–23] SCN^- was proposed as the most weakly hydrated and therefore the most chaotropic anion in the prebiotic environment.[5]

In 2015, nanometric anions, *e.g.* polyoxometalates (POMs) and anionic boron clusters (halogenated dodecaborates), were shown to bind orders of magnitude more strongly to organic matter than SCN^-, due to their "superchaotropicity".[6,24,25] POMs are water soluble metal oxides, which consist

of metal-oxo units (most commonly tungstate (WO_4^{2-}) and molybdate (MoO_4^{2-})).[26] POMs find their applications mostly in catalysis due to their redox-activity.[27–30]

In the prebiotic era, metalates such as WO_4^{2-} and thiotungstate, WS_4^{2-}, (and later MoO_4^{2-}) and phosphate (PO_4^{3-}) or silicate (SiO_4^{4-}) were available.[7,31] It is well-known that WO_4^{2-} and MoO_4^{2-} readily form α-Keggin POMs in the presence of PO_4^{3-} or SiO_4^{4-} in acidic environment.[32–34] Therefore, it is likely that Keggin POMs, such as α-$PW_{12}O_{40}^{3-}$ (PW^{3-}) and α-$SiW_{12}O_{40}^{4-}$ (SiW^{4-}) have formed during the prebiotic era.

5.3 Experimental section

Materials. Phosphotungstic acid hydrate ($H_3PW_{12}O_{40} \cdot xH_2O$, HPW, MW = 2898 g/mol, 99.995% purity) and silicotungstic acid ($H_4SiW_{12}O_{40} \cdot xH_2O$, HSiW, MW = 2878 g/mol) were purchased from Sigma Aldrich. Concentration calculations were done with x_{HPW} = 17 and x_{HSiW} = 25 based on thermogravimetric measurements of HPW and HSiW. Dipropylene glycol *n*-propylether (C_3P_2) was purchased from Sigma Aldrich and used as obtained. Milli-Q water was used with a conductivity lower than 10.5 µS/cm and a total organic carbon content of 400 ppb.

Cloud point (CP) measurements/phase diagrams. For CP measurements, 2 g of ternary (water, C_3P_2 and POM) mixtures were prepared into screwable tubes of borosilicate glass. The tubes were put into a thermostat (Thermomix_1460, B. Braun Melsungen AG) in special tube holders. The thermostat was heated with a heating rate of 1 °C min^{-1} and the phase separation (turbidity) was detected with the naked eye. Note that an external precision thermometer was used for temperature determination. The expected precision of the measurements is approximately ± 1 °C. In case of the CP measurements of illuminated samples following procedure was applied: 2 g of the ternary solution was filled in a glass tube (Flachbodenglas N8, 1. Hydrolytic class) from Macherey/Nagel GmbH & Co. KG, which was sealed with a polyethylene plug and parafilm. The cylindrical tubes have an approximate diameter of 8.2 mm and a height of 4 cm. These tubes were set under a UV lamp (6 W, λ = 365 nm, Herolab GmbH) and in certain time steps the CP was measured. Due to the strong coloring of the solution (reduced POM) the approximated error is ± 2.5 °C. These steps were repeated for several times. For solutions exposed to air the procedure was as follows: The illuminated, sealed glass tube was opened (without stirring or shaking) and exposed to air. In certain time steps, the CP was measured with an accuracy of ± 2.5 °C. The described steps were repeated several times.

^{31}P-nuclear magnetic resonance (^{31}P-NMR). Solution ^{31}P-NMR spectra were recorded (at room temperature) with an Avance400 (Bruker) spectrometer using 85 % phosphoric acid as an internal standard. Chemical shifts (δ) are provided in parts per million (ppm) and coupling constants (J) are reported in Hertz (Hz). D_2O was used as solvent.

^{1}H-nuclear magnetic resonance (^{1}H-NMR). Solution ^{1}H-NMR spectra were recorded (at room temperature) with an Avance300 (Bruker) spectrometer using tetramethyl silane as an internal standard. Chemical shifts (δ) are provided in parts per million (ppm) and coupling constants (J) are reported in Hertz (Hz). D_2O was used as solvent.

Small angle X-ray scattering (SAXS). SAXS measurements, using Mo-$K_{\alpha1}$ radiation (λ = 0.071 nm), were performed on a bench built by XENOCS. The scattered beam was recorded using a large online scanner detector (diameter: 345 mm, from MAR Research). A large q-range (0.2 to 40 nm^{-1}) was covered with an off-center detection. The collimation was applied using a 12:∝ multilayer Xenocs mirror (for Mo radiation) coupled to two sets of scatter less FORVIS slits providing a 0.8 mm × 0.8 mm X-ray beam at the sample position. Pre-analysis of data was performed using FIT2D software. The scattered intensities are expressed versus the magnitude of scattering vector $q = [(4\pi)/\lambda]\sin(\vartheta/2)$, where λ is the wavelength of incident radiation and ϑ the scattering angle. 2 mm quartz capillaries were used as sample containers for the solutions. Usual corrections for background (empty cell and detector noise) subtractions and intensity normalization using a high-density polyethylene film as a standard were applied. Experimental resolution was $\Delta q/q$ = 0.05. Silver behenate in a sealed capillary was used as the scattering vector calibration standard. All experiments were performed at 22 ± 2 °C. In case of SAXS measurements of irradiated samples, a sample of freshly prepared solution was filled into a sealed measurement capillary. Afterwards the sealed capillary was irradiated with UV light (6 W, λ = 365 nm, Herolab GmbH) and the SAXS pattern was collected.

SAXS fitting. SAXS-fits were performed using SASfit version 0.94.11,[35] where the scattered intensity, $I(q)$, of an isotropic sample containing identical and randomly oriented particles is expressed as $I(q) = n \cdot V^2 \cdot \Delta\rho^2 \cdot P(q) \cdot S(q)$ with n the number density of the scattering object, V its volume, the scattering contrast $\Delta\rho=\rho_{particle}-\rho_{solvent}$, the form factor $P(q)$ and the structure factor $S(q)$. SAXS spectra of $[PW^{3-}]_m[C_3P_2]_n$ were fitted with a $P(q)$ representing an ellipsoid.

UV/VIS measurements. UV/VIS measurements were carried out (at room temperature) on an Infinite M Nano+ from Tecan Trading AG. The measurements were performed in 1 cm quartz glass cuvettes and 1 wt% C_3P_2 was automatically subtracted as a background from all measured samples.

5.4 Results and Discussion

Here, we present a {PW^{3-}/oligomer} redox-responsive self-assembled system, that is adaptable to changes in environmental conditions, *i.e.* sunlight and access to oxygen during day/night cycles. Fig. 5.2a shows PW^{3-}, which can undergo reduction to $PW_{12}O_{40}^{4-}$ (PW^{4-}) upon light-mediated oxidation of an organic compound, and the oligomeric dipropylene glycol *n*-propylether (C_3P_2). We choose C_3P_2 as a model oligomer, as it exhibits a simple molecular structure and allows tracking the

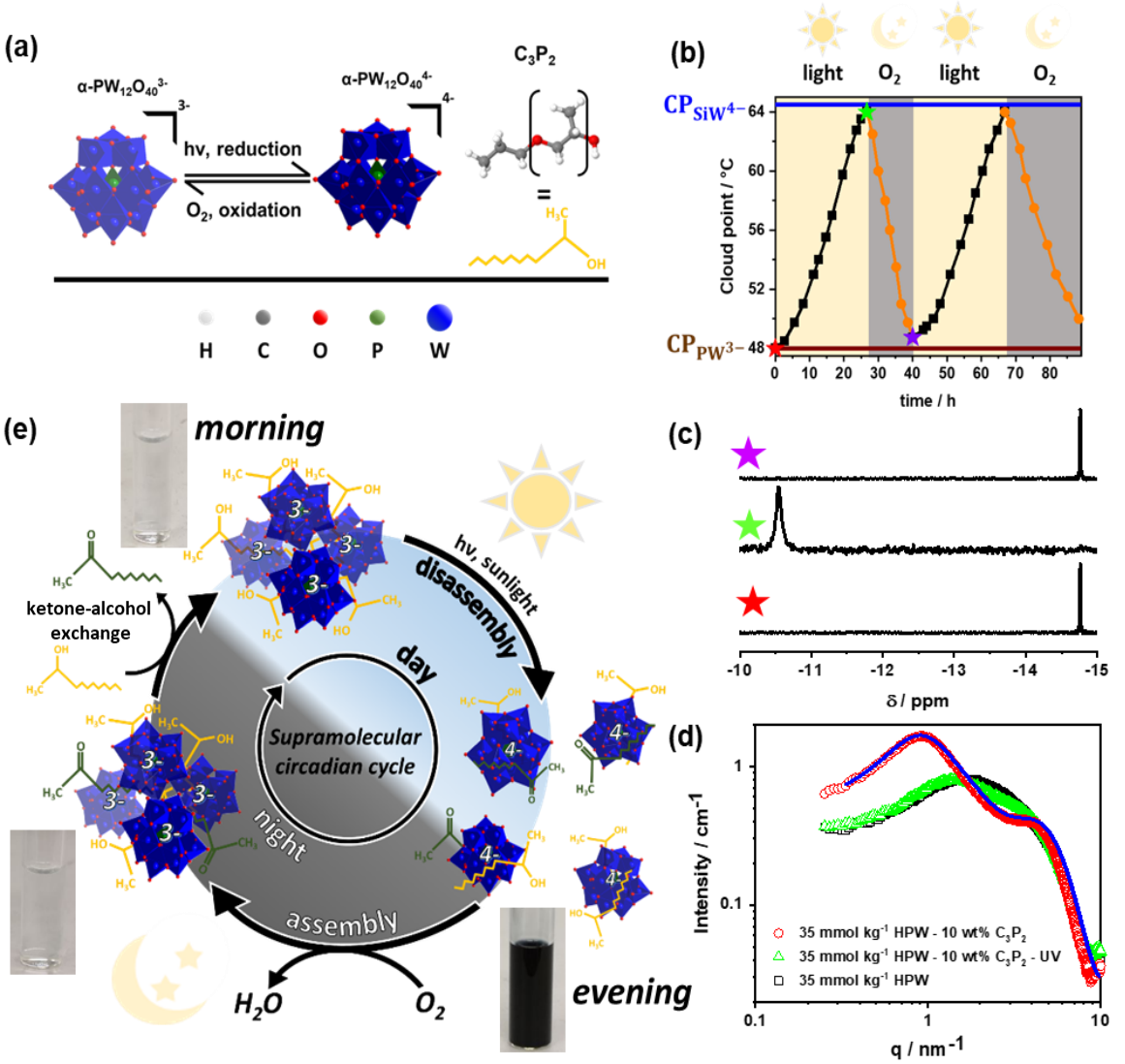

Figure 5.2. (a) Molecular representation of the α-Keggin type POM phosphotungstate and its redox-responsive change, *i.e.* reversible transition between PW^{3-} and PW^{4-}. Molecular and schematic representation of the dipropylene glycol *n*-propyl ether (C_3P_2). (b) CP evolution of 10 wt% C_3P_2 in the presence of 35 mmol kg^{-1} HPW under UV-irradiation (λ = 365 nm) (black) and subsequent exposure to air (orange). As a reference the CP of 10 wt% C_3P_2 - 35 mmol kg^{-1} HPW/HSiW is indicated respectively by the brown and blue horizontal lines. (c) ^{31}P-NMR spectra of the samples (but D_2O used instead of H_2O) indicated with colored stars in (b). The spectra show the reversible reaction of $PW^{3-} \leftrightarrow PW^{4-}$. (d) SAXS spectra of 35 mmol kg^{-1} HPW in water as a reference and in 10 wt% C_3P_2 after fresh preparation and after 16 hours of UV-irradiation (in a 2 mm glass capillary). NMR and SAXS spectra were collected at room temperature. (e) Schematic illustration of the adaptation of the system to day/night cycle including a ketone-alcohol exchange in order to avoid ketone accumulation due to the irreversible alcohol oxidation.

redox state of POM owing to its thermosensitive property. Indeed, C_3P_2, similarly to more complex oligo- and polymers and some proteins,[36,37] phase-separates at a characteristic temperature, called cloud point (CP).[38] The CP was shown to be highly sensitive to the presence of chaotropic species and to enable the classification of nanometric anions according to their (super-)chaotropicity.[39,40]

PW^{3-} and SiW^{4-}, in their acidic forms $H_3PW_{12}O_{40}$ (HPW) and $H_4SiW_{12}O_{40}$ (HSiW), associate with C_3P_2 upon the chaotropic effect. The less superchaotropic SiW^{4-} binds weakly to C_3P_2 and forms small "stoichiometric" complexes such as $[SiW^{4-}][C_3P_2]_{1-2}$, while the stronger superchaotrope PW^{3-} assembles into larger aggregates with the general formula $[PW^{3-}]_m[C_3P_2]_n$ ($m \approx 4$ and $n \approx 30$).[41] Here, the CPs of C_3P_2 (10 wt% ≈ 570 mmol kg^{-1}) in the presence of HPW/HSiW (35 mmol kg^{-1}) are $CP_{PW^{3-}}$ = 48 °C and $CP_{SiW^{4-}}$ = 64.5 °C, respectively, see Fig. 5.2b brown and blue horizontal lines. To investigate the effect of illumination, a 35 mmol kg^{-1} HPW - 10 wt% C_3P_2 solution was irradiated by UV-light (λ = 365 nm) in a sealed glass tube. The CP increases continuously towards the CP of 35 mmol kg^{-1} HSiW - 10 wt% C_3P_2 (blue line) within 27 h, see Fig. 5.2b dark squares. Thereafter, UV-irradiation was stopped and the glass container was opened. During 14 h exposition to air, the CP continuously decreased down to the initial CP of 35 mmol kg^{-1} HPW - 10 wt% C_3P_2 (brown line), see Fig. 5.2b orange circles. UV-irradiation and subsequent exposure to air was repeated in a second cycle (from 40 to 88 h) to show the reversibility of this phenomenon, see Fig. 5.2b.

^{31}P-NMR spectra and UV/VIS measurements presented in Fig. 5.2c and section 5.6.1, were used to identify the oxidation states of the phosphotungstate anion. The ^{31}P-NMR spectrum after fresh preparation shows a singlet peak at -14.8 ppm characteristic of the fully oxidized PW^{3-} (red star, bottom spectrum).[42] After 27 h UV-irradiation, a broad singlet is present at -10.5 ppm, while the peak at -14.8 ppm completely disappeared, indicating full conversion of PW^{3-} to the one-electron reduced species PW^{4-} (green star, middle spectrum).[43] After subsequent exposure to air during 13 h, only one singlet at -14.8 ppm is observed, which confirms full recovery of PW^{3-} (violet star, top spectrum). The reversible $PW^{3-} \leftrightarrow PW^{4-}$ conversion is easily detected visually by the transition from transparent to blue, see images in Fig. 5.2e. During reduction of PW^{3-}, a small portion of C_3P_2 (around 3 %) is partially oxidized as confirmed by ^{1}H-NMR, see section 5.6.2, with the release of a proton.

The self-assembly of PW^{3-}/PW^{4-} with C_3P_2 was investigated before (red circles) and after (green triangles) UV-irradiation by small angle X-ray scattering (SAXS), see Fig. 5.2d. The SAXS spectrum of 35 mmol kg^{-1} HPW in water (dark squares) is given as a reference and shows the scattering pattern of repulsive spherical scattering objects, typical of individually dispersed Keggin ions in water.[44] In 10 wt% C_3P_2, a large excess scattering, due to the presence of $[PW^{3-}]_m[C_3P_2]_n$ aggregates, is observed at low scattering angles, expressed here as a wavevector q [nm^{-1}]. Fitting of the SAXS spectrum (Fig. 5.2d, blue solid line) reveals that $[PW^{3-}]_4[C_3P_2]_{25}$ aggregates are present, see section 5.6.3. After UV-irradiation (green triangles in Fig. 5.2d), the SAXS spectrum overlaps almost entirely with the spectrum of HPW in water. Therefore, the $[PW^{3-}]_4[C_3P_2]_{25}$ aggregates disassembled upon the photo-reduction $PW^{3-} \rightarrow PW^{4-}$. PW^{4-} with C_3P_2 gives a similar SAXS spectrum as SiW^{4-} which could be

expected as PW^{4-} and SiW^{4-} have the same size and charge, see Fig. S5.6. This agrees with the CP evolution oscillating between $CP_{PW^{3-}}$ and $CP_{SiW^{4-}}$.

This reversible assembly-disassembly auto-synchronizes with the day/night cycle, see Fig. 5.2e and section 5.6.4. The images in Fig. 5.2e show the visual aspect of a tube containing a sample of 35 mmol kg^{-1} HPW - 10 wt% C_3P_2 solution. In the morning, the solution appears transparent, as expected for the fully oxidized PW^{3-} within $[PW^{3-}]_4[C_3P_2]_{25}$ aggregates. During the day, the exposure to sunlight drives the $PW^{3-} \rightarrow PW^{4-}$ photo-reduction and the solution turns deeply blue, indicating the presence of PW^{4-}. Therefore, $[PW^{3-}]_4[C_3P_2]_{25}$ disassembles along the day. Through the night, PW^{4-} is oxidized by diffusion of atmospheric O_2 and the solution appears transparent again, which suggests the formation of $[PW^{3-}]_4[C_3P_2]_{25}$ assemblies. Such self-assembly adaptation to a day/night cycle reminds of a circadian cycle, which is an intrinsic property of most living systems.[45,46]

5.5 Conclusion

As a conclusion (Fig. 5.3), metalate ions (MQ_4^{2-} with M: W or Mo and Q: O or S), originated from the leaching of rocks, were available in the prebiotic ocean.[7,33] Under acidic conditions in the presence of phosphate or silicate, POMs with a strong chaotropic character (*i.e.* high affinity for binding to organic molecules) may have formed as suggested in literature.[47,48] POMs are prone to form molecular assemblies with soluble organic matter containing diverse chemical moieties (sugars,

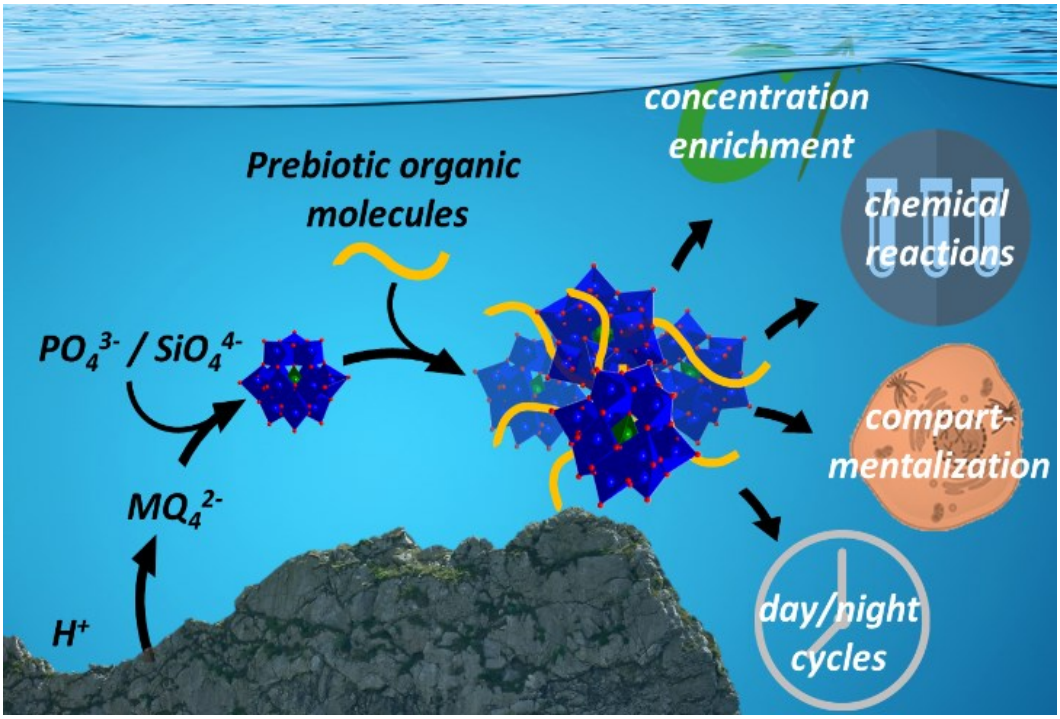

Figure 5.3. In the prebiotic era, POMs may have been formed and assembled with organic prebiotic soup molecules to promote concentration enrichment, chemical reactions, compartmentalization and day/night cycles.

amides, glycol ethers).[6,25,39,49–52] As suggested in this article, POMs also associate with synthetic oligomers and presumably prebiotic soup molecules.[53] $[POM]_m[oligomer]_n$ assemblies may have promoted the evolution in early biology by stimulating concentration enrichment, chemical reactions, compartmentalization and adapting to day/night cycles.

To increase concentrations locally is a fundamental principle in the evolution of life as it enables the contact of chemical substances on a molecular scale.[54] Such small distances between highly concentrated molecules promote chemical reactions and syntheses. $[POM]_m[oligomer]_n$ assemblies are well-defined aggregates of a fixed size, *i.e.* delimited self-assembled aggregates. These small association colloids may have participated to the formation of larger compartmentalized aggregates, such as coacervates, which were recently proposed as the missing link between chemistry and biology in the origin of life.[55] Adaptation to the day/night cycle, stimulated by environmental conditions, is a key property in an evolutionary process to enhance the evolutionary fitness. Here, a day/night cycle was controlled by (sun)light and oxygen diffusion. POMs have been shown to produce O_2 from water via a photocatalytic oxidation reaction.[30,56] Consequently, $[POM]_m[oligomer]_n$ assembly-disassembly may already have adapted to the day/night cycle in the prebiotic era, even before the great oxygen event (*ca.* 2.4 billion years ago).

We suggest that our study provides new insights in ancient chemistry that may have contributed to emerging life. Driven by the chaotropic effect, POMs (inorganic) associate with oligomeric molecules (organic). Such self-assemblies may have been present in the prebiotic era and were discussed to exhibit diverse essential properties for emerging life (redox-environment control, concentration enrichment, compartmentalization, “microreactors” for chemical reactions and adaptation to environmental conditions). The next obvious step to investigate the role of the chaotropic effect of POMs in emerging life would be to explore their supramolecular assemblies with out-of equilibrium, dissipative conditions.[3]

5.6 Supporting Information

5.6.1 Investigations on phosphotungstate speciation

^{31}P-NMR

Figure S5.1 recalls and discusses ^{31}P-NMR spectra from Fig. 5.2c. After (a) fresh preparation, a sample of 35 mmol kg^{-1} HPW - 10 wt% C_3P_2 (in D_2O) gives two singlet peaks at *(i)* -14.8 ppm and *(ii)* 0.6 ppm. Peak *(i)* can be assigned to the $PW_{12}O_{40}^{3-}$ anion, whereas peak *(ii)* may be attributed to uncondensed $H_{3-x}PO_4^{x-}$ (x =]0; 3]) species. After (b) irradiating this sample for 27 hours with UV-light (λ = 365 nm), ^{31}P-NMR shows singlets at *(i)* -10.6 ppm and *(ii)* 0.5 ppm. Peak *(i)* is attributed to the

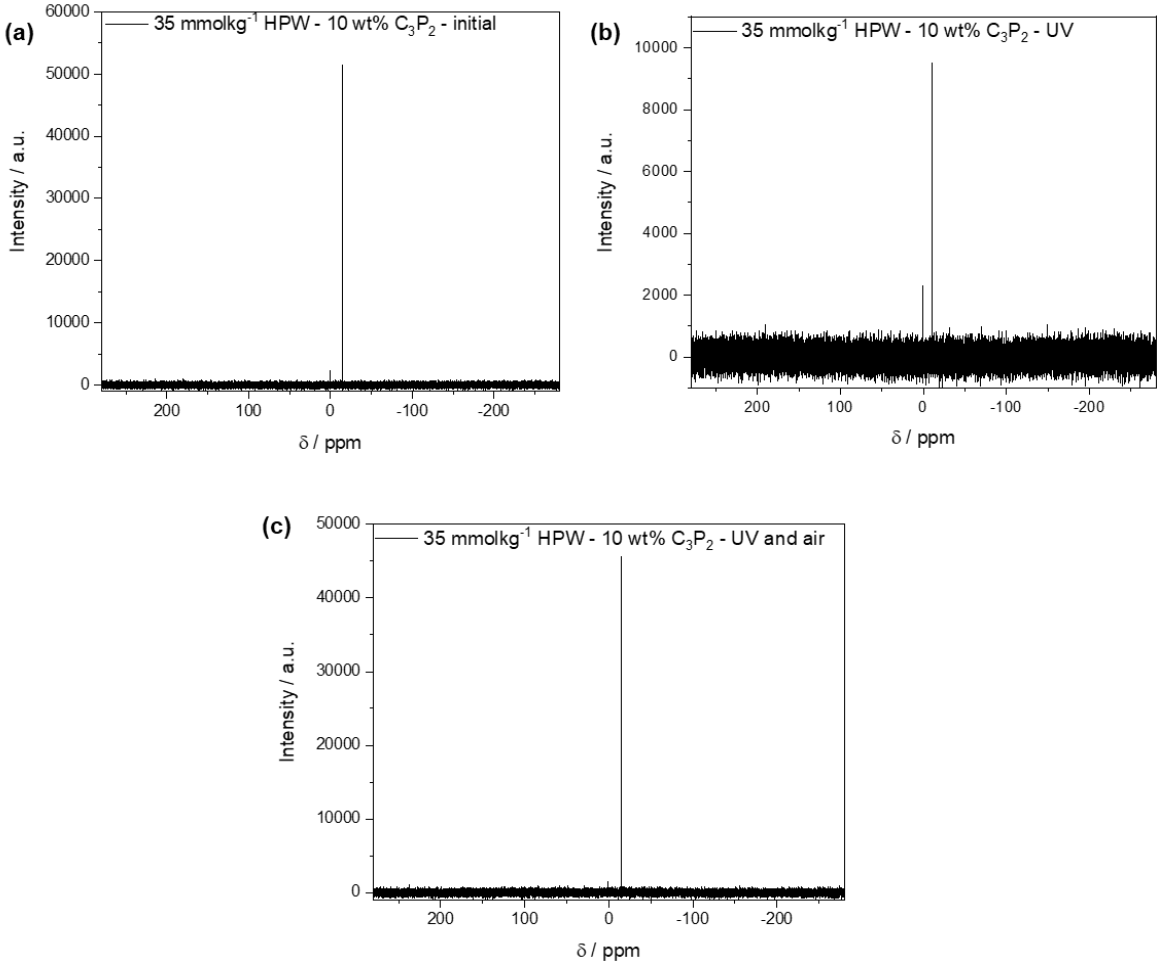

Figure S5.1. Full ^{31}P-NMR spectra of 35 mmol kg^{-1} HPW - 10 wt% C_3P_2 (in D_2O) after (a) fresh preparation, (b) 27 hours of UV illumination and (c) 27 hours of UV illumination and subsequent exposure to air for 14 hours.

one-electron reduced species of phosphotungstate, *i.e.* PW^{4-}. Peak *(ii)* arises again due to $H_{3-x}PO_4^{x-}$ species. By (c) UV-irradiation for 27 h and consecutive exposure to air for 14 h, ^{31}P-NMR shows singlets at *(i)* -14.8 ppm and *(ii)* 0.6 ppm. This clearly indicates that PW^{3-} is reformed. Table S5.1 summarizes the obtained signals and attributes them to the species in solution. Table S5.2 shows the different signals and the relative amount of each species in solution deduced from NMR spectrum integration.

Table S5.1. Summary of the obtained ^{31}P-NMR signals and their attribution to the different species present in aqueous solution.

^{31}P-NMR	**signal *(i)* / ppm**	**attribution**	**signal *(ii)* / ppm**	**attribution**
initial	-14.8	PW^{3-}	0.6	$H_{3-x}PO_4^{x-}$
UV light	-10.6	PW^{4-}	0.5	$H_{3-x}PO_4^{x-}$
UV light and air exposure	-14.8	PW^{3-}	0.6	$H_{3-x}PO_4^{x-}$

Table S5.2. Relative amounts of the different species present in solution provided in %. The relative amounts were calculated by integrating the signals of the ^{31}P-NMR spectra in Fig. S5.1.

^{31}P-NMR	attribution	rel. amount / %	attribution	rel. amount / %
initial	PW^{3-}	96.2	$H_{3-x}PO_4^{x-}$	3.8
UV light	PW^{4-}	96.9	$H_{3-x}PO_4^{x-}$	3.1
UV light and air exposure	PW^{3-}	96.2	$H_{3-x}PO_4^{x-}$	3.8

UV/VIS measurements

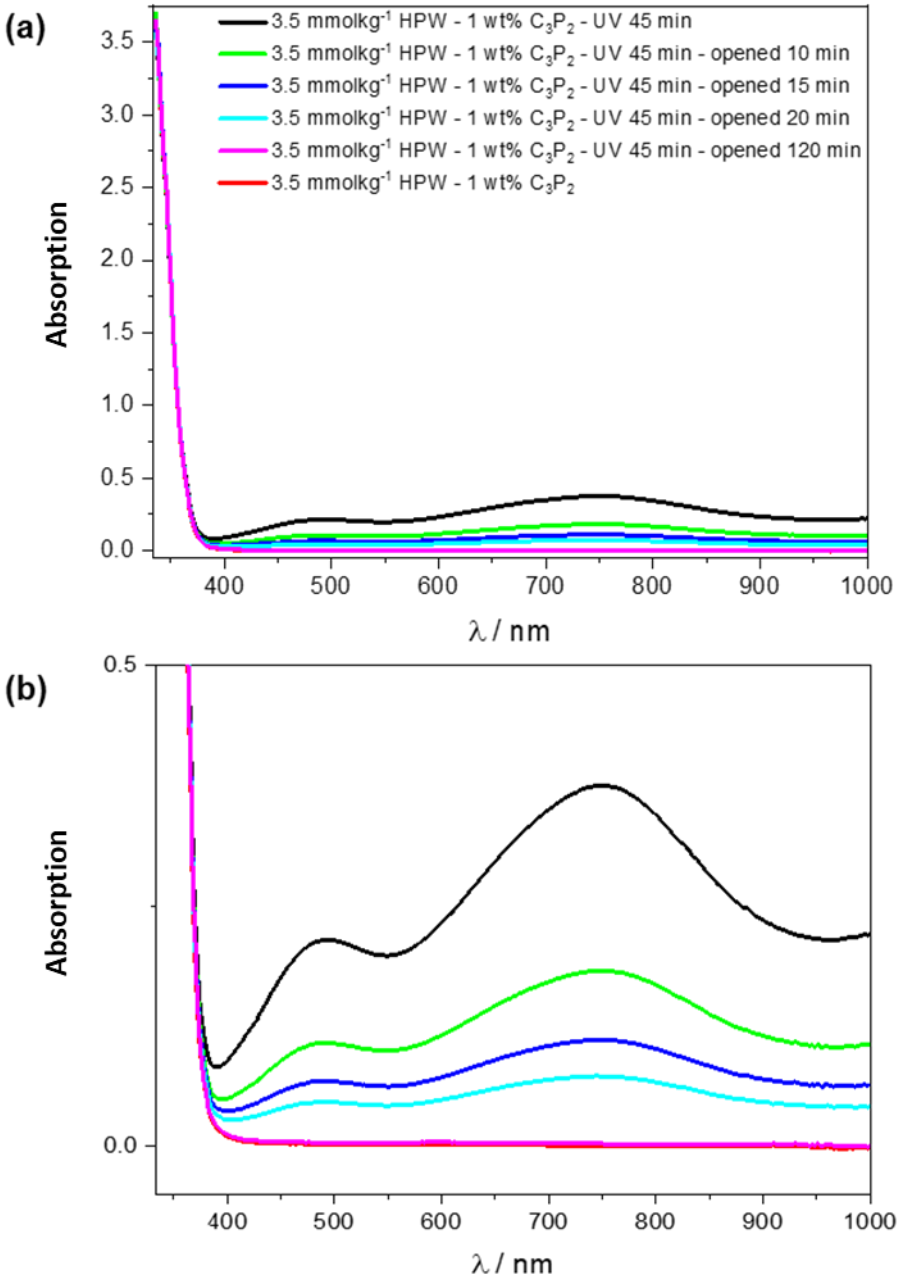

Figure S5.2. (a) UV/VIS spectra of 3.5 mmol kg^{-1} HPW in 1 wt% C_3P_2 after UV-irradiation and exposure to air. (b) shows an enlargement of the spectra in (a).

For UV/VIS experiments, initial samples (35 mmol kg^{-1} HPW - 10 wt% C_3P_2) were diluted with water by a factor of ten which gives 3.5 mmol kg^{-1} HPW in 1 wt% C_3P_2. This step was done due to the intense color of concentrated heteropoly blue species leading to (unreliable) absorptions > 1.5.
The UV/VIS spectrum of 3.5 mmol kg^{-1} HPW in 1 wt% C_3P_2 after fresh preparation shows a strong absorption in the UV part and no absorption in the VIS part, which is reasonable as the solution appears visually colorless, see Fig. S5.2. After irradiating the sample for 45 minutes with UV-light two maxima appear in the VIS range: at 490 and 750 nm. These maxima are characteristic for the one-electron reduced PW^{4-} molecule.[57] Upon exposing the sample to air, the maxima in the VIS range disappear and the UV/VIS spectrum perfectly coincides to the spectrum of the initial sample.

5.6.2 Oxidation of C_3P_2 as counter reaction of phosphotungstate reduction

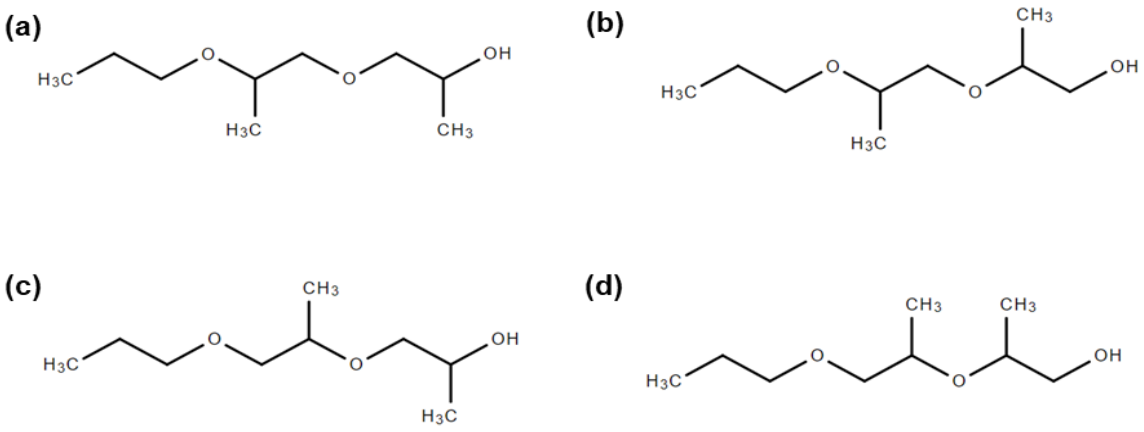

Figure S5.3. Different isomers in commercially sold C_3P_2.

Commercially available C_3P_2, *i.e.* dipropylene glycol *n*-propylether, is composed of four different isomers, see Fig. S5.3. Bauduin reported the approximate distribution of these four isomers in commercially sold C_3P_2, see Table S5.3. Moreover, impurities (0.2 to 0.3 %) of dipropylene glycol *n*-butylether are present in the mixture.[58]

Table S5.3. Distribution of the four main isomers, (a) - (d) shown in Fig. S5.3, in commercially sold C_3P_2.

Isomer	Relative amount of isomer in an industrial mixture / %
(a)	7.5
(b)	0.3
(c)	88.7
(d)	3.1

The ^{1}H-NMR spectrum of 10 wt% C_3P_2 in D_2O is shown in Fig. S5.4. A triplet (t) arises at 0.73 ppm stemming from the protons of the terminal methyl group of the *n*-propyl moiety (marked blued).

This t was integrated with 3 equivalents of H. A doublet (d) is present at 0.98 ppm due to protons of the CH_3 groups in the propylene glycol moieties giving 5.99 equivalents of protons (marked green). A multiplet (m) is located at 1.42 ppm (integrated 1.99 equivalents H) which is attributed to the protons of the intermediate CH_2 group of the *n*-propyl group (marked red). Around 3.32 ppm an extremely broad m is recorded stemming from the CH_2 groups next to an O atom (marked orange). Here, the integration leads to a reasonable value of 6.01. At 3.58 and 3.78 ppm m signals stemming from the two quaternary protons are present which lead to integrals of 1.03 and 0.96.

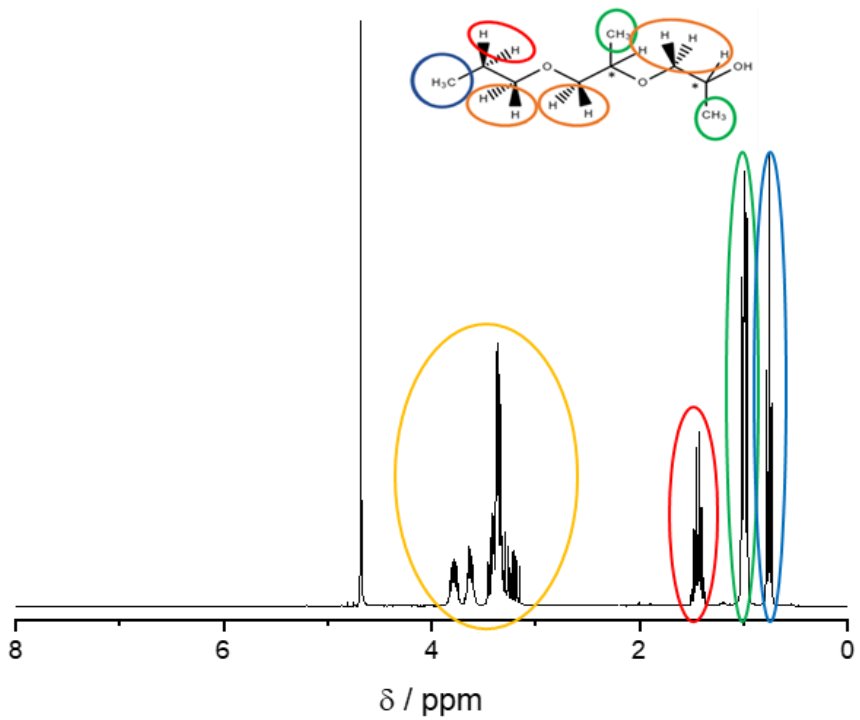

Figure S5.4. ^{1}H-NMR spectrum of 10 wt% C_3P_2 in D_2O. The signals stemming from the different protons are marked in colored ellipses. These colors correspond to the colors in the molecular representation of C_3P_2, see inlet.

The photo-oxidation of C_3P_2 (being an alcohol with the general formula R-CH_2-OH) by $PW_{12}O_{40}^{3-}$ (PW^{3-}) obeys following reaction equation

Ox.:	R-CH_2-OH → R-CHO + 2 e^- + 2H^+
Red.:	2 $PW_{12}O_{40}^{3-}$ + 2 e^- → 2 $PW_{12}O_{40}^{4-}$
Redox:	R-CH_2-OH + 2 $PW_{12}O_{40}^{3-}$ → R-CHO + 2 $PW_{12}O_{40}^{4-}$ + 2H^+

We concluded from CP measurements and ^{31}P-NMR that PW^{3-} is fully transferred into $PW_{12}O_{40}^{4-}$ (PW^{4-}). According to the reaction equation shown above, ½ of the initial c(PW^{3-}) = $c_{oxidized}(C_3P_2)$ is needed for full PW^{3-}→PW^{4-} photoreduction, *i.e.* ½ · 35 mmol kg^{-1} = 17.5 mmol kg^{-1}. Considering the initial C_3P_2 concentration (10 wt% = 570 mmol kg^{-1}), < 3 % C_3P_2 are required for full PW^{3-}→PW^{4-} photoreduction.

Figure S5.5 shows excerpts of ^{1}H-NMR spectra of 35 mmol kg^{-1} HPW - 10 wt% C_3P_2 in D_2O, freshly prepared (dark spectra) and after UV-irradiation (27 h, red spectra). Due to different isomers of C_3P_2 (see Fig. S5.3), ketones and aldehydes can be formed upon its (photo-)oxidation. By forming a ketone, a signal of the terminal methyl group (singlet), next to the ketone functional group, arises around 1.90 ppm, see Fig. S5.5a. By forming an aldehyde, a signal (singlet) of the proton bound to the aldehyde functional group, arises around 9.52 ppm, see Fig. S5.5b.

Note that also multiplicities (in propylene glycol) change upon oxidation. Nevertheless, we focus here qualitatively on emerging signals rather than changing multiplicities, as only small portions (around 3 %) of C_3P_2 are oxidized, which prohibits to identify multiplicity changes easily.

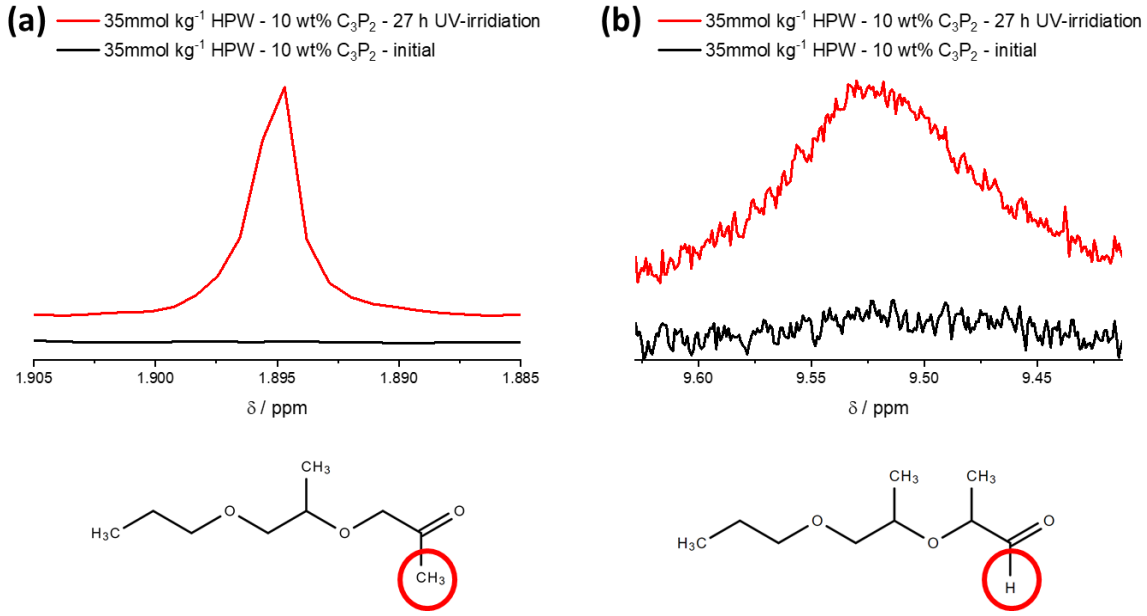

Figure S5.5. Excerpts of ^{1}H-NMR spectra of 35 mmol kg^{-1} HPW - 10 wt% C_3P_2 in D_2O after fresh preparation (dark curves) and 27 h UV-irradiation (red curves) showing the formation of signals characteristic for oxidation products of C_3P_2. These products (ketone (a) and aldehyde (b)) are shown below the spectra. Groups in the molecular structure, producing these characteristic ^{1}H-NMR signals for C_3P_2 oxidation products are marked in red circles.

5.6.3 SAXS spectra and data processing

SAXS fitting of 35 mmol kg^{-1} HPW - 10 wt% C_3P_2

In the following subsection the fully oxidized phosphotungstate (PW^{3-}) is abbreviated PW. All SAXS fits were performed using SASfit version 0.94.11[35], where the scattered intensity, *I(q)*, of an isotropic sample containing identical and randomly oriented particles is expressed by Eq. 5.1.

$$I(q) = n \cdot V^2 \cdot \Delta\rho^2 \cdot P(q) \cdot S(q) \qquad (5.1)$$

with n the number density of the scattering object, *V* its volume, the scattering contrast $\Delta\rho = \rho_{particle} - \rho_{solvent}$, the form factor *P(q)* and the structure factor *S(q).* The form factor *P(q)* describes the shape of the scattering object, while the structure factor *S(q)* describes the higher order arrangement of the scattering objects.

Determination of electron densities

In order to determine the scattering contrast, the individual electronic densities $\rho_{particle}$ and $\rho_{solvent}$ were calculated by Eq. 5.2.

$$\rho_i = \frac{\sum_j b_j}{v_i} \cdot l_{Thomson} \tag{5.2}$$

with b_j being the number of electrons in the *j*th atom, v_i the scattering objects volume and $l_{Thomson}$ the Thomson length ($l_{Thomson}$ = 2.82 × 10^{-13} m). The thereby calculated electron densities of $PW_{12}O_{40}^{3-}$, H_2O and C_3P_2 are shown in Table S5.4.

Table S5.4. Molecular volumes, number of electrons and electron densities (ρ) of the used compounds.

Compound	Molecular volume / nm³	Number of electrons	ρ^{SAXS} / 10^{10} cm^{-2}
$PW_{12}O_{40}^{3-}$	0.46[#]	1223	74.9
H_2O	0.03[+]	10	9.4
C_3P_2	0.318[+]	98	8.65

[#]taken from Buchecker *et al.*[40]

[+]calculated from the respective pure liquid densities

Fit of the SAXS spectrum

The SAXS spectrum (Fig. 5.2d) of 35 mmol kg^{-1} HPW - 10 wt% C_3P_2 (without UV-irradiation!) shows two contributions:

(i) individual $PW_{12}O_{40}^{3-}$ molecules at q > 4 nm^{-1}

(ii) $[PW]_m[C_3P_2]_n$, aggregates (A) at q < 4 nm^{-1}.

To model this superposition, the individual POMs as well as the $[PW]_m[C_3P_2]_n$ aggregates were modeled individually with form and structure factors. The scattered intensity $I(q)$ is then expressed as shown in Eq. 5.3.

$$\begin{aligned} I(q) = {} & n_{POM} \cdot V_{POM}^2 \cdot \Delta\rho_{POM}^2 \cdot P_{POM}^{sphere}(q,r) \cdot S_{POM}^{HS}(q, r_{HS}, \phi) + \\ & + n_A \cdot V_A^2 \cdot \Delta\rho_A^2 \cdot P_A^{ellipsoid}(q, r_{eq}, r_{pol}) \cdot S_A^{HMSA}(q, r_{HS}, q_e, I) \end{aligned} \tag{5.3}$$

A spherical form factor $P_{POM}^{sphere}(q,r)$ here describes the shape of $PW_{12}O_{40}^{3-}$ and a Hard Sphere (HS) structure factor $S_{POM}^{HS}(q,r_{HS},\phi)$ approximates PW^{3-}-PW^{3-}-interactions. To describe the shape of the aggregates (A), an ellipsoidal form factor $P_A^{ellipsoid}(q,r_{eq},r_{pol})$ was used and the electrostatic inter-aggregate repulsion was modelled with a Hayter Rescaled Mean Sphere Approximation (HMSA) structure factor $S_A^{HMSA}(q,r_{HS},q_e,I)$.[59,60] As a starting point in the fitting procedure, we refer to our previous publication, where $[PW^{3-}]_m[C_3P_2]_n$ aggregates were characterized with SAXS and SANS on a sample containing 50 mmol kg^{-1} HPW and 10 wt% C_3P_2. The combination of SAXS and SANS therein lead to a robust global fit of the $[PW^{3-}]_m[C_3P_2]_n$.[41]

The SAXS fit were done using a fixed contrast of the solvent and of $PW_{12}O_{40}^{3-}$ (see Table S5.4) and of the aggregates ($\rho_A = 20 \cdot 10^{10}$ cm^{-2}). All other parameters were fit parameters, which were adapted within the range of physical meaning. The obtained parameters are shown in Table S5.5.

Table S5.5. Fit (output) parameters for fit procedures assuming an ellipsoidal scattering object (here $[PW]_m[C_3P_2]_n$).

P(q)				*S(q)*			
r_{eq} / nm	r_{pol} / nm	V_A^{-1} / nm^{-3}	ρ_A / 10^{10} cm^{-2}	r_{HMSA} / nm	$n_{charge}(A)$ / e^-	Φ_A	c(salt) / mM
1.05	2.2	0.00183	20	1.35	9	0.02	5

The following lists the used parameter abbreviations: r_{eq}: equatorial radius of the aggregates, r_{pol}: polar radius of the aggregates, V_A^{-1}: particle number density of the aggregates in solution, ρ_A: scattering length density of the aggregates, r_{HMSA}: Hayter-MSA radius, $n_{charge}(A)$: charge of the aggregates, Φ_A: volume fraction of the aggregates used for calculation of the structure factor, c(salt): concentration of the screening salt.

As a next step, the volume of the aggregate can be calculated via

$$V_A = 4/3\pi \cdot r_{pol} \cdot r_{eq}^2. \quad (5.4)$$

Moreover, we can calculate the volume fraction from the particle number density and the particle volume

$$\Phi_A = V_A V_A^{-1} \quad (5.5)$$

Table S5.6. Volume and volume fraction of the self-assembled $[PW^{3-}]_m[C_3P_2]_n$ aggregates.

V_A / nm^3	Φ_A
9.9	0.0182

The scattering length density of the aggregates can be calculated via

$$\rho_A^{SAXS} = \Phi_A^{PW}\rho_{PW}^{SAXS} + \Phi_A^{H_2O}\rho_{H_2O}^{SAXS} + \Phi_A^{C_3P_2}\rho_{C_3P_2}^{SAXS} = \Phi_A^{PW}\rho_{PW}^{SAXS} + (1-\Phi_A^{PW})\,\rho_{C_3P_2}^{SAXS} \quad (5.6)$$

if we assume

$$\rho_{C_3P_2}^{SAXS} \approx \rho_{H_2O}^{SAXS}. \quad (5.7)$$

Consequently, we can calculate the volume fraction of PW molecules in the colloid with

$$\Phi_A^{PW} = \frac{\rho_A^{SAXS} - \rho_{C_3P_2}^{SAXS}}{\rho_{PW}^{SAXS} - \rho_{C_3P_2}^{SAXS}}. \quad (5.8)$$

From the PW volume fraction, we can conclude on the aggregation number of PW^{3-} molecules per aggregate, N_A^{PW} with

$$N_A^{PW} = \frac{\Phi_A^{PW} V_A}{V_{PW}}. \quad (5.9)$$

V_{PW} is calculated with a POM radius of 0.48 nm which gives V_{PW} = 0.46 nm^3.[40] Hence, the aggregation number of PW per aggregate is: $N_A^{PW} = 3.7 \approx 4$.

From V_A = 9.9 nm^3, $N_A^{PW} = 4$ and V_{PW} = 0.46 nm^3 we can conclude on the volume of C_3P_2 within the colloids, which is $V_{A,\ C_3P_2}$ = 8.06 nm^3. If it is assumed that the aggregates are fully "dry", *i.e.* free of water, as we found previously,[41] the remaining volume of 8.06 nm^3 is exclusively made up by C_3P_2. With its molecular volume of 0.318 nm^3 we obtain 25.3 ≈ 25 C_3P_2 molecules in the aggregates. This calculation leads to the aggregate formula $[PW^{3-}]_4[C_3P_2]_{25}$.

Further SAXS spectra

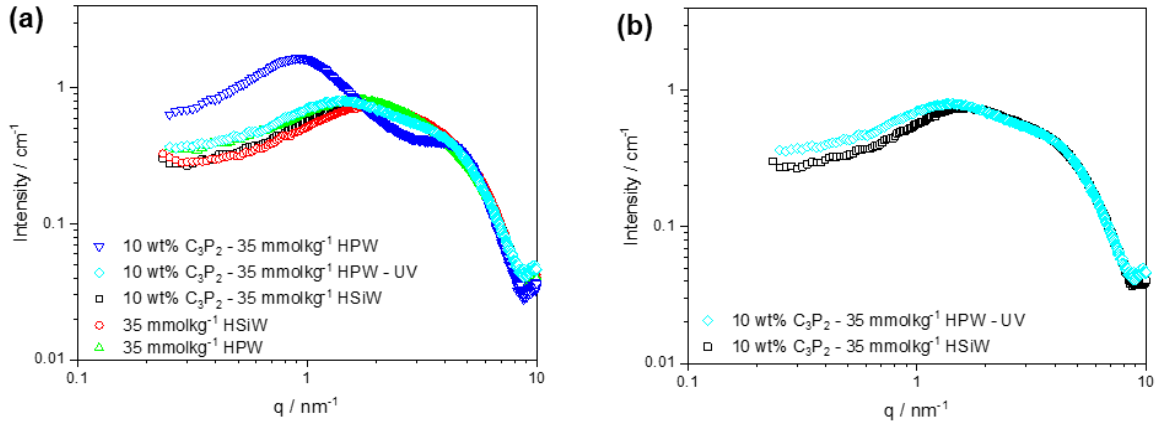

Figure S5.6. (a) SAXS spectra of 35 mmol kg^{-1} HPW and HSiW in water and in 10 wt% C_3P_2 and SAXS spectrum of 35 mmol kg^{-1} HPW in 10 wt% C_3P_2 (UV-irradiated). (b) highlights the strong similarity of SiW^{4-}-C_3P_2 nano-assemblies and PW^{4-}-C_3P_2 nano-assemblies. The spectra were measured at room temperature.

Figure S5.6a shows SAXS spectra of 35 mmol kg^{-1} HPW/HSiW in water and in the presence of 10 wt% C_3P_2. Additionally, the SAXS spectrum of 35 mmol kg^{-1} HPW - 10 wt % C_3P_2 after 16 hours UV-irradiation is provided. The shown curves, except for 35 mmol kg^{-1} HSiW - 10 wt % C_3P_2 are already discussed in the manuscript. Figure S5.6b highlights the similarity of 35 mmol kg^{-1} HSiW - 10 wt % C_3P_2 and 35 mmol kg^{-1} HPW - 10 wt % C_3P_2 after UV-irradiation.

5.6.4 Adaption to day/night cycle

In a last experiment, the stimuli-responsive POM assembly was synchronized with the rhythm of a day, *i.e.* the day/night cycle, see Fig. S5.7.

At the beginning (left, in the morning, 06.30 a.m.), the solution, 35 mmol kg^{-1} HPW - 10 wt% C_3P_2, appears colorless due to the presence of PW^{3-}. Evaluation of SAXS experiments (see section 5.6.3)

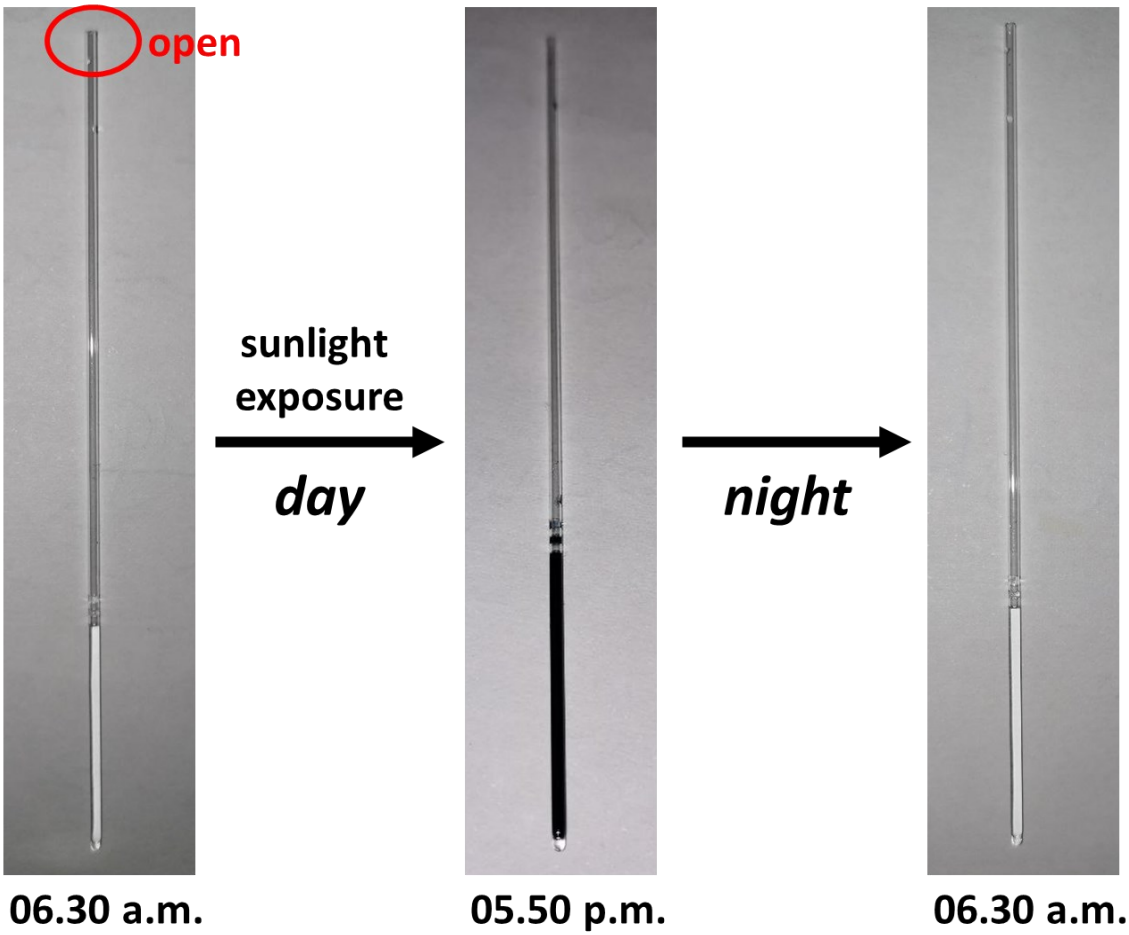

Figure S5.7. Documentation of the day/night cycle of 35 mmol kg^{-1} HPW - 10 wt% C_3P_2. After fresh preparation, the solution occurs colorless indicating the presence of fully oxidized PW^{3-} (left). Here, the initial state is present: $[PW^{3-}]_4[C_3P_2]_{25}$ assemblies. After the sunlight exposure (middle) the solution turns deeply blue which was related to the reduction of the PW anion to PW^{4-} and consecutively the disassembly of $[PW]_4[C_3P_2]_{25}$. During the night, PW^{4-} is reoxidized by oxygen leading to a color transition from deeply blue to colorless. Therefore, the system regenerates and $[PW]_4[C_3P_2]_{25}$ is formed.

revealed that $[PW^{3-}]_4[C_3P_2]_{25}$ aggregates are present. After exposure to sunlight (middle, evening, at 05.50 p.m.), $PW^{3-} \rightarrow PW^{4-}$ photo-reduction occurs as the solution turns deeply blue/black (reduced POM species). Therefore, the aggregates disassemble. During the night, the color turns back to colorless (right, 06.30 a.m., on the consecutive day), which was attributed to the $PW^{4-} \rightarrow PW^{3-}$ reoxidation. Consequently, $[PW^{3-}]_4[C_3P_2]_{25}$ assemble again. We show with this experiment that the presented switchable POM self-assembly can be easily controlled by the day/night cycle.

The experiment shown in Fig. S5.7 was performed from 28.02.2021 (06.30 a.m.) to 01.03.2021 (06.30 a.m.) in Waldmünchen, Bavaria, Germany. The sample (35 mmol kg^{-1} HPW - 10 wt% C_3P_2) was sucked into a glass capillary (outer diameter 1 mm, inner diameter 0.8 mm, filling height approximately 1.6 cm) and one end of the capillary was sealed. The other end of the capillary remained open ensuring the contact of air/oxygen with the sample. At 06.30 a.m. of the first experiment day, the capillary was set close to a window (*ca.* 10 cm distance, window alignment south-east, ambient conditions, bright room) and remained untouched for the whole experiment, except for taking images. Meteorological data of 28.02.2021 are as follows: sunrise: 06.54 a.m. sunset: 5.50 p.m., which delimit the irradiation-/"day" time.

A similar experiment was simulated in a larger scale (*ca.* 4 mL) under laboratory conditions. UV-irradiation (365 nm) was used instead of sunlight. Similarly, to the experiment explained above, the experiment duration was 28.02.2021 (06.30 a.m.) to 01.03.2021 (06.30 a.m.). Furthermore, the UV-irradiation time was synchronized with the meteorological data of this day, here: "artificial sunrise": 06.54 a.m. "artificial sunset": 5.50 p.m. This procedure also leads to an artificial circadian cycle, see Fig. S5.8. Here, a 7 mL glass vial served as sample container. A needle provided continuous access to oxygen.

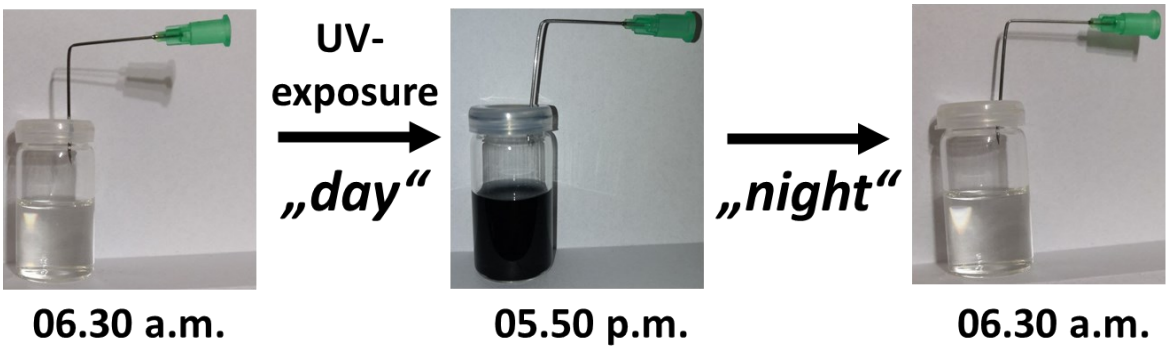

Figure S5.8. Artificial adaptation to day/night cycle under laboratory conditions. The sunlight was simulated with UV light (λ = 365 nm). The 35 mmol kg^{-1} HPW - 10 wt% C_3P_2 system shows also here an artificial circadian cycle: initial state (left), reduced POM state (middle) and reformed initial state (right).

5.7 Bibliography

[1] C. P. Brangwynne, C. R. Eckmann, D. S. Courson, A. Rybarska, C. Hoege, J. Gharakhani, F. Jülicher, A. A. Hyman, *Science* **2012**, *324*, 1729–1732.

[2] P.-A. Monnard, D. W. Deamer, *Anat. Rec.* **2002**, *268*, 196–207.

[3] Editorial, *Nat. Nanotechnol.* **2016**, *11*, 909.

[4] A. Sigel, H. Sigel, R. Sigel, *Metal Ions in Biological Systems - Volume 44*, CRC Press, Boca Raton, **2005**.

[5] B. C. Gibb, *Nat. Chem.* **2018**, *10*, 997–998.

[6] B. Naskar, O. Diat, V. Nardello-Rataj, P. Bauduin, *J. Phys. Chem. C* **2015**, *119*, 20985–20992.

[7] A. Sigel, H. Sigel, R. Sigel, *Metallomics and the Cell (Metal Ions in Life Sciences Book 12)*, Springer, Dondrecht, **2013**.

[8] J. P. Ferris, A. R. Hill, R. Liu, L. E. Orgel, *Nature* **1996**, *381*, 59–61.

[9] R. Krishnamurthy, N. V. Hud, *Chem. Rev.* **2020**, *120*, 4613–4615.

[10] G. Wächtershäuser, *J. Theor. Biol.* **1997**, *187*, 483–494.

[11] C. Sherrington, *Man on His Nature*, Cambridge University Press, Cambridge, **1951**.

[12] B. M. Bizzarri, R. Saladino, I. Delfino, J. M. Garcia-Ruiz, E. Di Mauro, *Int. J. Mol. Sci.* **2021**, *22*, 917.

[13] A. Navrotsky, R. Hervig, J. Lyons, D.-K. Seo, E. Shock, A. Voskanyan, *Proc. Natl. Acad. Sci.* **2021**, *118*, e2021117118.

[14] M. Frenkel-Pinter, M. Samanta, G. Ashkenasy, L. J. Leman, *Chem. Rev.* **2020**, *120*, 4707–4765.

[15] L. Cronin, S. I. Walker, *Science* **2016**, *352*, 1174–1175.

[16] S. B. Gould, *Curr. Biol.* **2018**, *28*, R381–R385.

[17] M. Faustini, L. Nicole, E. Ruiz-Hitzky, C. Sanchez, *Adv. Funct. Mater.* **2018**, *28*, 1704158.

[18] R. Östberg, *Nature* **1974**, *249*, 382–383.

[19] D. O. Hall, R. Cammack, K. K. Rao, *Nature* **1971**, *233*, 136–138.

[20] F. Hofmeister, *Arch. Exp. Pathol. Pharmakol.* **1888**, *25*, 1–30.

[21] W. Kunz, *Specific Ion Effects*, World Scientific, Singapore, **2010**.

[22] W. Kunz, *Curr. Opin. Colloid Interface Sci.* **2010**, *15*, 34–39.

[23] W. Yao, K. Wang, A. Wu, W. F. Reed, B. C. Gibb, *Chem. Sci.* **2020**, *12*, 320–330.

[24] K. I. Assaf, M. S. Ural, F. Pan, T. Georgiev, S. Simova, K. Rissanen, D. Gabel, W. M. Nau, *Angew. Chem. - Int. Ed.* **2015**, *54*, 6852–6856.

[25] Y. Wu, R. Shi, Y. Wu, J. M. Holcroft, Z. Liu, M. Frasconi, M. R. Wasielewski, H. Li, J. F. Stoddart, *J. Am. Chem. Soc.* **2015**, *137*, 4111–4118.

[26] M. T. Pope, A. Müller, *Angew. Chem. - Int. Ed.* **1991**, *30*, 34–48.

[27] S.-S. Wang, G.-Y. Yang, *Chem. Rev.* **2015**, *115*, 4893–4962.

[28] C. Streb, K. Kastner, J. Tucher, *Phys. Sci. Rev.* **2019**, *4*, 1–10.

[29] S. Yao, C. Falaise, S. Khilfi, N. Leclerc, M. Haouas, D. Landy, E. Cadot, *Inorg. Chem.* **2021**, *60*, 7433–7441.

[30] M. Martin-Sabi, J. Soriano-López, R. S. Winter, J. Chen, L. Vilà-Nadal, D. Long, J. R. Galán-Mascarós, L. Cronin, *Nat. Catal.* **2018**, *1*, 208–213.

[31] N. J. Planavsky, O. J. Rouxel, A. Bekker, S. V Lalonde, K. O. Konhauser, C. T. Reinhard, T. W. Lyons, *Nature* **2010**, *467*, 1088–1090.

[32] J. J. Borrás-Almenar, E. Coronado, A. Müller, M. Pope, *Polyoxometalate Molecular Science*, Springer, Netherlands, Dondrecht, **2003**.

[33] X. Chen, Q. Chen, F. Guo, Y. Liao, Z. Zhao, *Hydrometallurgy* **2018**, *175*, 326–332.

[34] N. I. Gumerova, A. Rompel, *Chem. Soc. Rev.* **2020**, *49*, 7568–7601.

[35] J. Kohlbrecher, A. F. Thu, *J. Appl. Crystallogr.* **2015**, *48*, 1587–1598.

[36] M. Iqbal, Y. Tao, S. Xie, Y. Zhu, D. Chen, X. Wang, L. Huang, D. Peng, A. Sattar, M. S. B. Abu, H. I. Hussain, S. Ahmed, Z. Yuan, *Biol. Proced. Online* **2016**, *18*, 1–18.

[37] Y. Zhang, S. Furyk, D. E. Bergbreiter, P. S. Cremer, *J. Am. Chem. Soc.* **2005**, *127*, 14505–14510.

[38] P. Bauduin, L. Wattebled, S. Schrödle, D. Touraud, W. Kunz, *J. Mol. Liq.* **2004**, *115*, 23–28.

[39] M. Hohenschutz, I. Grillo, O. Diat, P. Bauduin, *Angew. Chem. - Int. Ed.* **2020**, *59*, 8084–8088.

[40] T. Buchecker, P. Schmid, S. Renaudineau, O. Diat, A. Proust, A. Pfitzner, P. Bauduin, *Chem. Commun.* **2018**, *54*, 1833–1836.

[41] P. Schmid, T. Buchecker, A. Khoshsima, D. Touraud, O. Diat, W. Kunz, A. Pfitzner, P. Bauduin, *J. Colloid Interface Sci.* **2021**, *587*, 347–357.

[42] R. I. Maksimovskaya, G. M. Maksimov, *Coord. Chem. Rev.* **2019**, *385*, 81–99.

[43] M. Kozik, C. F. Hammer, L. C. W. Baker, *J. Am. Chem. Soc.* **1986**, *108*, 7627–7630.

[44] M. K. Bera, B. Qiao, S. Seifert, B. P. Burton-Pye, M. Olvera De La Cruz, M. R. Antonio, *J. Phys. Chem. C* **2016**, *120*, 1317–1327.

[45] J. Abe, T. B. Hiyama, A. Mukaiyama, S. Son, T. Mori, S. Saito, M. Osako, J. Wolanin, E. Yamashita, T. Kondo, S. Akiyama, *Science* **2015**, *349*, 4908–4913.

[46] S. E. Cohen, S. S. Golden, *Microbiol. Mol. Biol. Rev.* **2015**, *79*, 373–385.

[47] M. Nyman, *Polyoxometalates and Other Metal-Oxo Clusters in Nature*, Springer, Cham, **2018**.

[48] S. Krivovichev, *Acta Crystallogr. B* **2020**, *76*, 618–629.

[49] K. I. Assaf, W. M. Nau, *Angew. Chem. - Int. Ed.* **2018**, *57*, 13968–13981.

[50] T. Buchecker, P. Schmid, I. Grillo, S. Prévost, M. Drechsler, O. Diat, A. Pfitzner, P. Bauduin, *J. Am. Chem. Soc.* **2019**, *141*, 6890–6899.

[51] C. Falaise, M. A. Moussawi, S. Floquet, P. A. Abramov, M. N. Sokolov, M. Haouas, E. Cadot, *J. Am. Chem. Soc.* **2018**, *140*, 11198–11201.

[52] T. Buchecker, X. LeGoff, B. Naskar, A. Pfitzner, O. Diat, P. Bauduin, *Chem. - A Eur. J.* **2017**, *23*, 8434–8442.

[53] B. A. Rogers, H. I. Okur, C. Yan, T. Yang, J. Heyda, P. S. Cremer, *Nat. Chem.* **2022**, *14*, 40–45.

[54] S. Oehler, B. Müller-Hill, *J. Mol. Biol.* **2010**, *395*, 242–253.

[55] M. Matsuo, K. Kurihara, *Nat. Commun.* **2021**, *12*, 5487.

[56] H. Lv, Y. V Geletii, C. Zhao, J. W. Vickers, G. Zhu, Z. Luo, J. Song, T. Lian, D. G. Musaev, C. L. Hill, *Chem. Soc. Rev.* **2012**, *41*, 7572–7589.

[57] E. Papaconstantinou, *Chem. Soc. Rev.* **1989**, *18*, 1–31.

[58] P. Bauduin, Characterization of Short Polypropylene Glycol Monoalkylethers and Design of Enzymatic Reaction Media - Dissertation, University of Regensburg, **2005**.

[59] J. Hansen, J. B. Hayter, *Mol. Phys.* **1982**, *46*, 651–656.

[60] J. B. Hayter, J. Penfold, *Mol. Phys.* **1981**, *42*, 109–118.

6 A paradox: Hydrophilic molecular metal-oxides are selective solubilizers for moderately hydrophobic compounds

6.1 Preface and Abstract

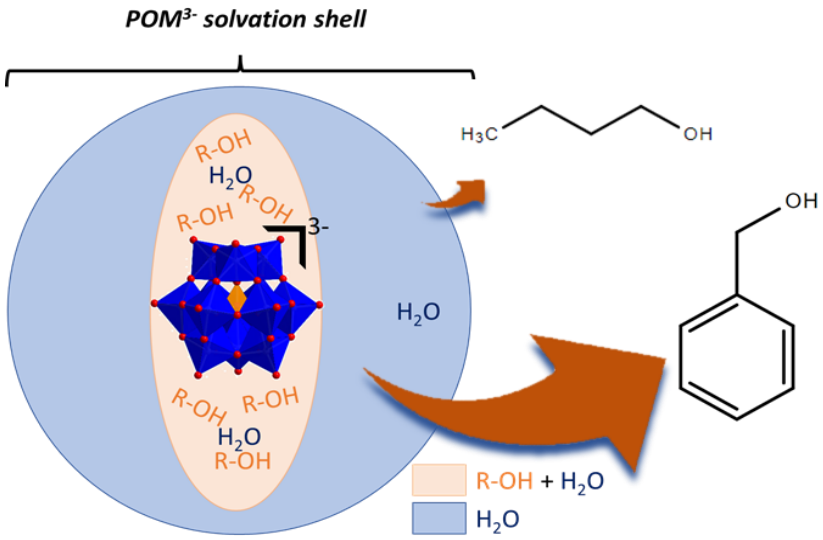

Figure 6.1. Graphical Abstract of the prepared article.

This chapter is prepared as a communication for the peer-reviewed Journal *Chemical Communications*. Several other people contributed to this work:

- Xaver Graß contributed with experiments on ternary phase diagrams.
- Dr. Didier Touraud contributed with fruitful discussions.
- Prof. Dr. Arno Pfitzner supervised the project, provided resources and contributed with fruitful discussions.
- Dr. Pierre Bauduin supervised the project, provided resources, contributed with fruitful discussion, improved the manuscript and is corresponding author.
- Philipp Schmid conceptualized and performed all experiments, designed the figures, wrote and improved the manuscript.

Abstract: Hydrophilic molecular metal-oxides, namely chaotropic α-Keggin Polyoxometalates (POMs) are used here as solubilizers for moderately hydrophobic organic compounds, *e.g.* water-immiscible short-chain alcohols. POM-mediated solubilization is selective to aromatic over aliphatic alcohols presumably due to a combination of the chaotropic effect and specific POM-π-electron attractions.

6.2 Introduction

Solubilizing hydrophobic organic molecules in water is a challenge in research and applications, such as for bioavailability of drugs,[1,2] extraction processes[3] or water purification.[4] Four main solubilization techniques have evolved:[5] *(i)* co-solvency,[6,7] solubilization with *(ii)* surfactants[8,9] or *(iii)* hydrotropes,[10–13] and *(iv)* inclusive or chelating complexation with (highly) soluble guest molecules.[14,15] While co-solvency represents a bulk solubilization technique,[16] surfactants (micellar aggregates) solubilize hydrophobic molecules inside aggregates (in the hydrophobic core of the micelles), as well as at the water-aggregate interface. For hydrotropes, that are short chained amphiphilic molecules, the solubilization of hydrophobic compound is generally admitted to result from a solute-hydrotrope aggregation (ill-defined mesoscopic aggregates), presumably with the hydrophobic effect playing a major role.[4,17,18] In contrast to all these solubilization processes, solubilization by complexation is fully driven by a host-guest association/binding.[19] Often, these solubilization techniques demand the use of non-green solvents, hazardous, toxic surface active agents or expensive chemicals though,[20–23] and therefore alternative techniques and solubilizers are constantly searched for.

A substance class which is currently intensively investigated in different fields of (solution) chemistry is the class of polyoxometalates (POMs),[24] such as α-Keggin POMs, see Fig. 6.2 inlets. POMs are molecular metal-oxides of nanometric size. They consist of early transition metal-oxo units, especially group V and VI metals (V, Nb, Ta, Mo, W), and often incorporate heteroatoms (*e.g.* P, Si, Al, B).[25,26] Due to their architectural versatility (structural and electronic), POMs find diverse applications as photocatalysts and in materials science.[27–29] More recently, low charge density POMs and other nanometric ions, such as anionic boron clusters, were shown to bind strongly to non-ionic, hydrated (molecular) surfaces, *e.g.* to oligo- and polymers,[30,31] foams[32,33] and macrocyclic guest molecules.[34–37] These association phenomena are driven by the so-called superchaotropic (SC) effect. The SC effect is based on the partial dehydration of both, the POM and the non-ionic (molecular) surface, leading to a high gain in enthalpy, accompanied by an entropic penalty.[38–40] The term SC effect is derived from classical chaotropic ions (*e.g.* SCN^-), which are known to associate with different solutes since late 19th century.[41–43] SC POMs have an association constant with neutral solutes/surfaces which is usually three orders of magnitude higher compared to classical chaotropes.[34,44]

SC ions were shown to drastically increase the cloud point (CP), a temperature-dependent liquid-liquid phase demixion, of thermo-responsive neutral solutes in aqueous solution.[44] Due to their binding, SC POMs convey their charge to non-ionic solutes and subsequently increase their temperature-dependent solubility in water, *e.g.* for surfactants,[24,33,40] thermo-responsive polymers[31] and short amphiphiles.[45] As a consecutive step, based on these latter promising

findings, we investigate here how SC POMs can be generally used as solubilizers for hydrophobic molecules.

6.3 Experimental section

Materials. Phosphotungstic and silicotungstic acid ($H_3PW_{12}O_{40}$, HPW (99 %) and $H_4SiW_{12}O_{40}$, HSiW (99 %)) and sodium phosphotungstate ($Na_3PW_{12}O_{40}$, NaPW (99.9 %)) were purchased from Sigma Aldrich. Sodium dodecyl sulfate (SDS, 99 %) and sodium xylene sulfonate (SXS, 90 %) were purchased from Sigma Aldrich. 1-butanol (99.8 %), 2-butanol (> 99 %), 2-methyl-1-propanol (99.5 %), 1-pentanol (> 99 %), benzyl alcohol (> 99 %), cyclohexyl methanol (> 99 %), toluene (99.5 %) and benzaldehyde (> 99 %) were obtained from Sigma Aldrich. 1-hexanol (> 99 %) was purchased from Merck. Milli-Q water was used with a conductivity lower than 10.5 µS/cm and a total organic carbon content of 400 ppb. All chemicals were used without further purification.

Solubilization measurements/phase diagrams. Phase diagrams were recorded using a dynamic and static process according to Clausse *et al.*[46] Accordingly, 2 g of a binary mixture (water-POM) were prepared into screwable tubes of borosilicate glass. The third component was added gradually until the solution turned turbid and the turbid phase remained after three minutes. The measurements were carried out at 22 ± 1 °C and the phase transition was detected with the naked eye. Weight fractions and molar fractions were calculated from the mass of all individual components derived from weight measurements.

^{31}P-nuclear magnetic resonance (^{31}P-NMR). Solution ^{31}P-NMR spectra were recorded (at room temperature) with an Avance400 (Bruker) spectrometer using 85 % phosphoric acid as an internal standard. Chemical shifts (δ) are provided in parts per million (ppm) and coupling constants (J) are reported in Hertz (Hz). D_2O was used as solvent.

^{1}H-nuclear magnetic resonance (^{1}H-NMR). Solution ^{1}H-NMR spectra were recorded with an Avance300 (Bruker) spectrometer using tetramethyl silane as an internal standard. Chemical shifts (δ) are provided in parts per million (ppm) and coupling constants (J) are reported in Hertz (Hz). D_2O was used instead of H_2O.

UV/VIS measurements. UV/VIS measurements were carried out (at room temperature) on an Infinite M Nano+ from Tecan Trading AG. The measurements were performed in 1 cm quartz glass cuvettes and water (or aqueous POM solutions) was automatically subtracted as a background from all measured samples.

Small angle X-ray scattering (SAXS). SAXS measurements, using Mo-$K_{\alpha1}$ radiation (λ = 0.071 nm), were performed on a bench built by XENOCS. The scattered beam was recorded using a large online scanner detector (diameter: 345 mm, from MAR Research). A large q-range (0.2 to 40 nm^{-1}) was covered with an off-center detection. The collimation was applied using a 12:∝ multilayer Xenocs

mirror (for Mo radiation) coupled to two sets of scatter less FORVIS slits providing a 0.8 mm × 0.8 mm X-ray beam at the sample position. Pre-analysis of data was performed using FIT2D software. The scattered intensities are expressed versus the magnitude of scattering vector $q = [(4\pi)/\lambda]\sin(\vartheta/2)$, where λ is the wavelength of incident radiation and ϑ the scattering angle. 2 mm quartz capillaries were used as sample containers for the solutions. Usual corrections for background (empty cell and detector noise) subtractions and intensity normalization using a high-density polyethylene film as a standard were applied. Experimental resolution was $\Delta q/q = 0.05$. Silver behenate in a sealed capillary was used as the scattering vector calibration standard. All experiments were performed at 22 ± 2 °C.

SAXS fitting. SAXS fits were performed with the SasView 5.0.3 fitting software.[47] All fits were made with a core-shell ellipsoid form factor model. Therefore, the POM was considered to be the core (with fixed spherical geometry and scattering length density) and the surrounding ellipsoid was assumed to consist of a mixture of H_2O and a corresponding alcohol. Consequently, the ellipsoid dimension (equatorial and polar radii) and its constitution (scattering length density) were fitting parameters. A Hayter-mean spherical approximation (Hayter-MSA) structure factor was applied to take into account for the electrostatic repulsion between the POM-alcohol assemblies.[48,49]

6.4 Results and Discussion

Figure 6.2a shows solubility measurements of five aliphatic alcohols, *i.e.* 2-butanol (2-BuOH), 1-butanol (1-BuOH), 2-methyl-1-propanol (2-Me-1-PrOH), 1-pentanol (1-PentOH), 1-hexanol (1-HexOH) and the aromatic compounds benzyl alcohol (BnOH) and toluene with increasing concentration of $Na_3PW_{12}O_{40}$ (NaPW). The compounds can be classified according to their solubility in pure water as:

1-HexOH ≈ toluene < 1-PentOH < BnOH < 2-Me-1-PrOH ≈ 1-BuOH < 2-BuOH,

being in good agreement with literature,[50,51] see also Table S6.1a. Addition of NaPW has effectively no influence on the solubility of 1-HexOH. The solubility of toluene increases from 0.09 mol kg^{-1} to 0.69 mol kg^{-1} by adding 200 mmol kg^{-1} NaPW. For 1-PentOH (from 0.4 mol kg^{-1} to 1.67 mol kg^{-1} at 200 mmol kg^{-1} NaPW) and BnOH (from 0.49 mol kg^{-1} to 2.65 mol kg^{-1} at 200 mmol kg^{-1} NaPW) the solubility also increases for the addition of NaPW. For 2-Me-1-PrOH (from 1.05 mol kg^{-1} to 3.93 mol kg^{-1} at 200 mmol kg^{-1} NaPW) and 1-BuOH (from 1.12 mol kg^{-1} to 5.69 mol kg^{-1} at 200 mmol kg^{-1} NaPW) a strong solubility increase is observed upon adding NaPW. A drastic solubility increase appears for 2-BuOH (from 2.43 mol kg^{-1} in pure water to 7.16 mol kg^{-1} at 30 mmol kg^{-1} NaPW, reaching full water:2-BuOH co-miscibility at c(NaPW) > 30 mmol kg^{-1}).

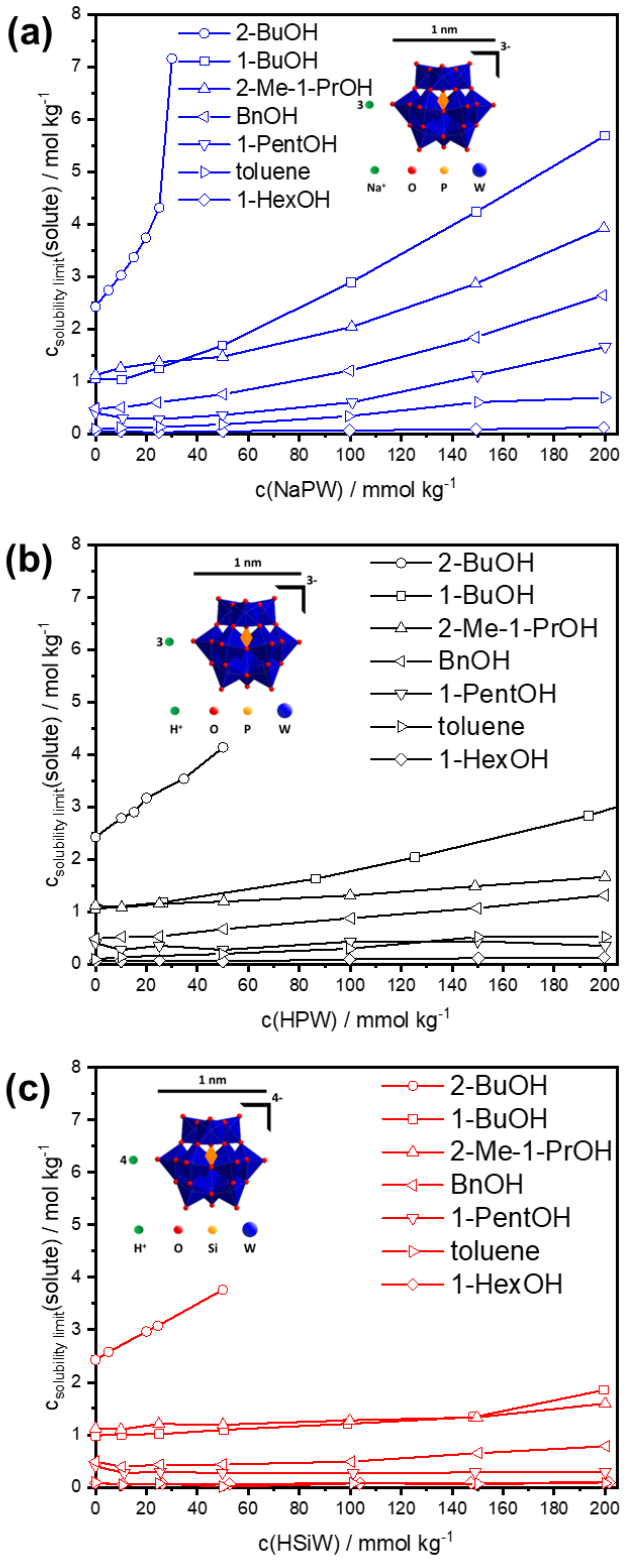

Figure 6.2. Solubilization measurements of five different short-chain aliphatic alcohols, *i.e.* 2-BuOH, 1-BuOH, 2-Me-1-PrOH, 1-PentOH and 1-HexOH and the aromatic compounds BnOH and toluene. Areas above the solid lines indicate biphasic regions. The POMs (a) NaPW, (b) HPW and (c) HSiW were used. All measurements were conducted at 22 ± 1 °C. Schematic representations of the used POMs are shown in figure inlets.

In the case of $H_3PW_{12}O_{40}$ (HPW), similar phase diagrams are observed as for NaPW, see Fig. 6.2b. Nevertheless, the solubilization is less efficient with HPW compared to NaPW. $H_4SiW_{12}O_{40}$ (HSiW)

produces even smaller solubility increases than HPW, see Fig. 6.2c.

As a first approximation, phase diagrams in Fig. 6.2 were fitted (linear fits), which allows to obtain roughly the ratio of solubilized organic molecules per one POM, *i.e.* the solubilization efficiency of the POM, see Table 6.1. These results are compared to data obtained for the model surfactant sodium dodecyl sulfate (SDS) and hydrotrope sodium xylene sulfonate (SXS). Details on the fitting procedure are given in section 6.6.1.

Table 6.1. Number of solubilized substrate molecules per single POM obtained from fits of the phase diagrams in Fig. 6.2. The results are compared to results for the model surfactant SDS and hydrotrope SXS. Highlighted values indicate the most efficient solubilizer for a given substrate. Values in brackets represent the coefficient of determination, R^2.

Substrate	NaPW	HPW	HSiW	SDS	SXS
2-BuOH	129.7 (76 %)	33.6 (99 %)	26.6 (100 %)	120 (83 %)	32.3 (84 %)
1-BuOH	23.7 (99 %)	10.5 (98 %)	3.8 (88 %)	22.9 (96 %)	8.5 (96 %)
2-Me-1-PrOH	13.4 (96 %)	2.8 (98 %)	2.1 (90 %)	11.6 (98 %)	7.5 (94 %)
BnOH	10.6 (97 %)	4.2 (99 %)	1.7 (84 %)	2.4 (99 %)	-0.4 (26 %)
1-PentOH	6.5 (90 %)	0.3 (14 %)	-0.2 (12 %)	7.2 (92 %)	2.5 (80 %)
toluene	3.2 (96 %)	2.3 (95 %)	0.05 (2 %)	0.6 (84 %)	0.1 (12 %)
1-HexOH	0.4 (82 %)	0.2 (60 %)	0.1 (62 %)	1.6 (97 %)	-0.2 (14 %)

Interestingly, NaPW (M(NaPW) = 2945 g · mol^{-1}) is a better solubilizer compared to SDS (M(SDS) = 288 g · mol^{-1}) for 2-BuOH, 1-BuOH, 2-Me-1-PrOH and especially BnOH and toluene (Table 6.1). On the contrary, SDS is more efficient in solubilizing longer chained alcohols 1-PentOH and 1-HexOH, presumably because SDS forms micelles enabling solubilization in the micellar core and surface. Therefore, SDS micelles may accommodate more efficiently longer alcohols compared to POMs, which do not self-assemble and therefore do not form clearly defined hydrophobic regions.

The hydrotrope SXS (M(SXS) = 208 g · mol^{-1}) appears to be a much less efficient solubilizing agent with even negative solubilized molecules per SXS ratios for BnOH and 1-HexOH (SXS leads to decreased solubility). The most efficient solubilizers are highlighted (green background color) in Table 6.1. As already concluded from the qualitative evaluation of the phase diagrams, HPW and especially HSiW are less efficient in solubilizing the investigated hydrophobic compounds compared to NaPW and SDS. From fitting results, five different criteria for hydrophobic substrates promoting the solubilization efficiency of POMs can be identified:

(i) Moderate solubility (*ca.* 0.3 mol kg^{-1} or 2 % (w:w)) in water (*cf.* 1-HexOH).

(ii) Shorter chain length of aliphatic moieties, < C_6 (*cf.* 1-HexOH).

(iii) Branching of the aliphatic moieties decreases solubilization efficiency (2-Me-1-PrOH *vs.* 1-BuOH).

(iv) Hydroxylation enhances the solubilization (BnOH *vs.* toluene).

(v) π-electron containing moieties enhance the solubilization (toluene *vs.* 1-HexOH).

Moreover, the nature of the POM affects the solubilization efficiency: *(i)* the charge density of the POM (NaPW/HPW *vs.* HSiW) and *(ii)* the counter-cation of the POM (NaPW *vs.* HPW) are decisive features. It was shown previously that the binding strength of SC POMs with non-ionic organic molecules scales inversely with the POM charge density, *i.e.* the lower the charge density, the stronger the association to non-ionic molecules (stronger SC effect).[33,40,44] Hence, it is likely that more SC POMs associate more strongly with alcohols (and toluene), and subsequently lead to a higher solubilization efficiency (NaPW/HPW *vs.* HSiW). Indeed, it was shown experimentally by using ^{1}H-NMR that NaPW/HPW binds more strongly to the solubilized molecules compared to HSiW, see Figs. S6.4 and S6.5.

Recently, the counterion of POMs was shown to have a strong impact on the self-assembly of POMs with organic matter (chapter 4). H^{+} as a POM counter-cation has a peculiar role among monovalent cations. Due to its location in the close vicinity of the POM anion, it reduces the apparent charge of the POM and therefore promotes (hybrid) self-assembly.[52,53] It is also known that such large self-assemblies are less thermodynamically stable leading to phase demixion.[31,45]

Small angle X-ray scattering (SAXS) was performed to investigate the POM/hydrophobic compound self-assemblies here, see section 6.6.3. For all three POMs, no clustering of POMs was found upon association with alcohols. Nevertheless, small differences in the scattering were observed suggesting that the solvation of POMs changes upon addition of the hydrophobic solutes. This was confirmed by fitting/simulation of the SAXS spectra. For HSiW, nearly no influence on the solvation shell was observed by comparing HSiW in pure water and in water-alcohol (*i.e.* 2-BuOH, 1-BuOH, 2-Me-1-PrOH and BnOH) mixtures. Note that only weak HSiW-alcohol interactions were also confirmed by ^{1}H-NMR, see section 6.6.2. For NaPW, an ellipsoidal solvation shell, composed of alcohol and water (*e.g.* equatorial shell thickness, r_{eq} = 0.9 nm for 50 mmol kg^{-1} NaPW - 1.08 mol kg^{-1} 1-BuOH) was used to fit the scattering data. It suggests then that alcohol molecules assemble around the POM due to the SC effect. In the context of solubilization techniques, the solubilization with SC POMs can therefore be referred to as an association solubilization. Compared to NaPW, HPW nucleates the formation of larger ellipsoidal water-alcohol solvation shells (*e.g.* r_{eq} = 1.4 nm for 50 mmol kg^{-1} HPW - 1.08 mol kg^{-1} 1-BuOH). This enhanced self-assembly behavior is likely to arise from self-assembly promoting protons, which “glue” POMs with organic molecules (or other POMs).[31,45,52,53] It appears here that such growing self-assemblies provoke phase demixion, leading to a decreased solubilization efficiency, as previously observed in refs [31,45].

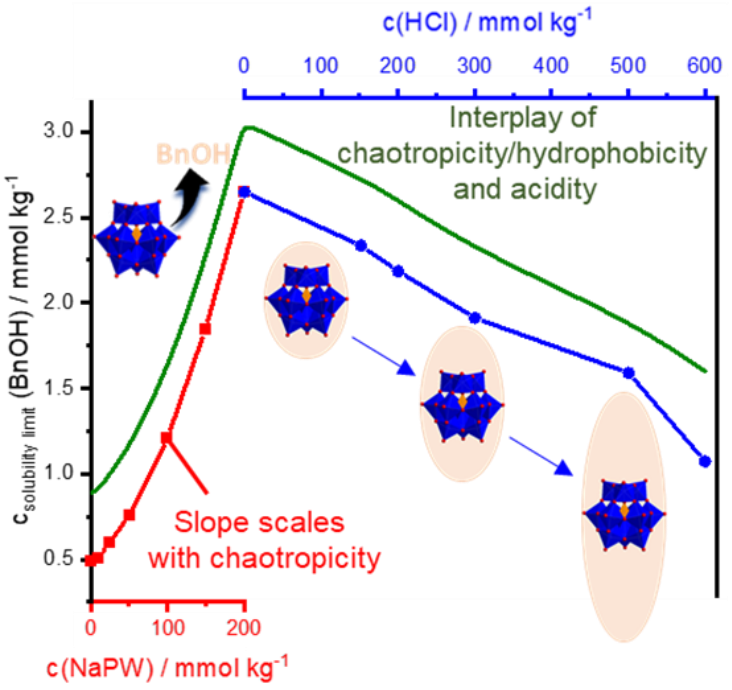

Figure 6.3. Illustration of the influence of chaotropicity (low charge density), see red squares, and acidity, blue circles, on the solubilization efficiency of POMs.

Figure 6.3 summarizes the two different POM features contributing to the solubilization efficiency. The addition of SC POMs (here NaPW, red squares) leads to a strong increase of the solubility of hydrophobic substrates (here BnOH). The slope of the solubility increase is related to the POM`s charge density and therefore to its SC character. Upon acidification, the solubility of BnOH decreases (blue circles). This solubility decrease is explained by growing POM-BnOH nano-assemblies which lead to phase separation (as found in chapter 4).

During the investigations here, it was noticed that solutions, containing SC POMs and aromatic molecules (π-electrons), such as toluene or BnOH, appear colored, see Fig. 6.4a photographs. Neither NaPW/HPW/HSiW, nor toluene/BnOH alone absorb visible light. Therefore, the binding of POM with aromatic compounds can explain the appearance of color by mixing. This effect was characterized by UV/VIS spectroscopy showing a strong bathochromic shift in the UV absorption spectrum of POMs, see Fig. 6.4a for NaPW upon addition of BnOH. ^{31}P- and ^{1}H-NMR informed that no chemical reaction occurred (*i.e.* the POM and the organic compounds did not react) and it therefore confirmed that the color change is due to their non-covalent binding, see Fig. S6.11. Further photographs of solutions containing different SC POMs and aromatic alcohols are shown in Fig. S6.12 to demonstrate this phenomenon visually.

UV/VIS spectra of 10 mmol kg^{-1} POM (NaPW, HPW and HSiW) were recorded for increasing concentrations of BnOH to quantify the bathochromic shift on the absorption spectrum of POMs. α-Keggin POMs have a very high molar extinction coefficient (around 10^4 L · mol^{-1} · cm^{-1})[54] in the UV region and consequently it is impossible to track absorption maxima of POMs at millimolar

concentrations in standard UV/VIS setups. Therefore, we followed the bathochromic shift by plotting the wavelength giving a fixed absorbance value (absorbance (A) = 0.2), this value is noted $\lambda_{A>0.2}$ hereafter, see Fig. 6.4b. $\lambda_{A>0.2}$ of 10 mmol kg^{-1} HSiW increases nearly linearly from 380 nm to 399 nm by increasing the BnOH concentration from 0 to 320 mmol kg^{-1} (close to solubility limit of BnOH in 10 mmol kg^{-1} POM solution). The red dashed line indicates $\lambda_{A>0.2}$ of HSiW in pure BnOH (409 nm). For NaPW and HPW $\lambda_{A>0.2}$ shifts from 374 nm to 441 nm, and 442 nm respectively, by increasing BnOH concentration to 320 mmol kg^{-1}. These curves follow rather a saturation shape. $\lambda_{A>0.2}$ is more red-shifted for NaPW/HPW, compared to HSiW, confirming that NaPW/HPW interacts more strongly with BnOH. Interestingly, $\lambda_{A=0.2}$ of NaPW/HPW in 320 mmol kg^{-1} BnOH is similar to $\lambda_{A=0.2}$ obtained for 10 mmol kg^{-1} NaPW/HPW in pure BnOH (see dashed blue and dark line, respectively). Hence, we conclude here that the solvation of NaPW/HPW in 320 mmol kg^{-1} BnOH is comparable to the solvation in pure BnOH, *i.e.* the POM is fully solvated by BnOH.

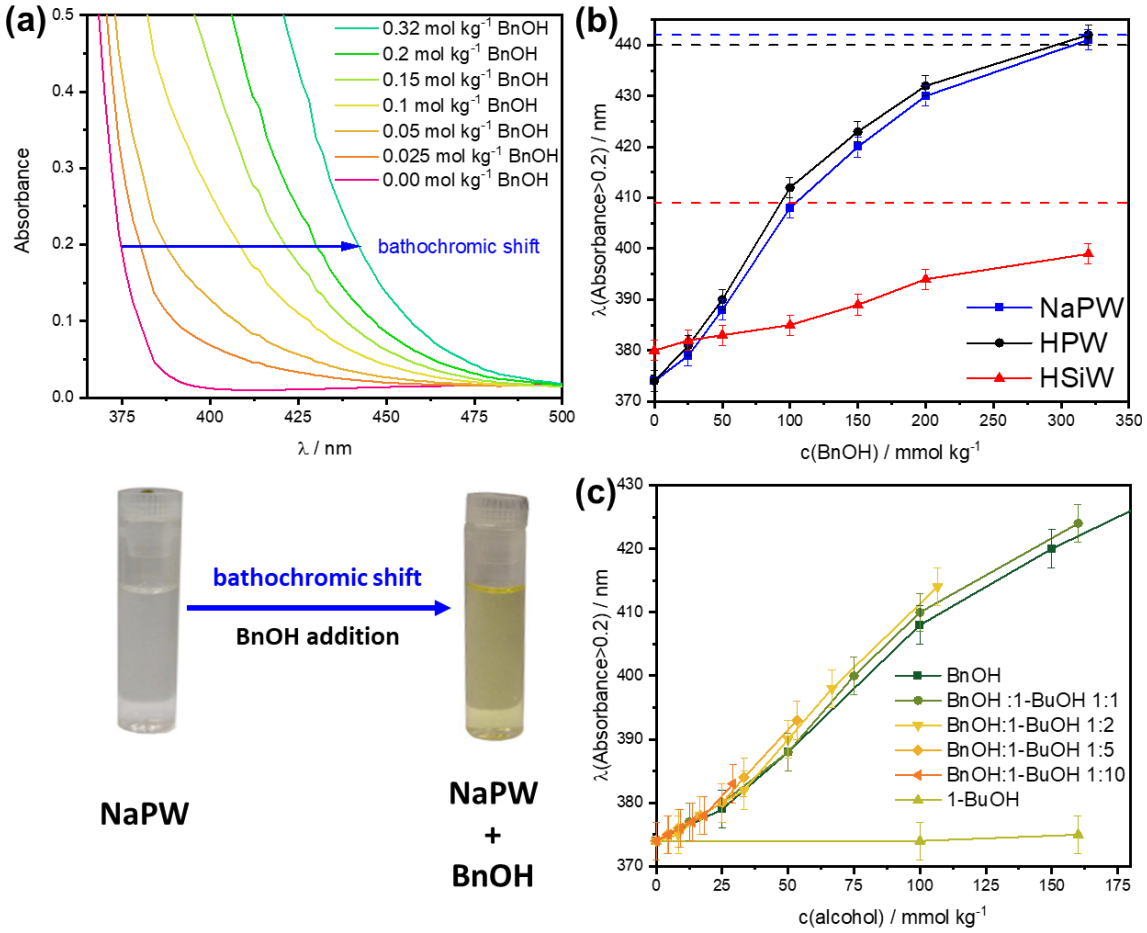

Figure 6.4. (a) Bathochromic shift of 10 mmol kg^{-1} NaPW upon the addition of an increasing amount of BnOH with sketches at the bottom. (b) Shift of $\lambda_{A>0.2}$ of 10 mmol kg^{-1} POM (NaPW, HPW, HSiW) as a function of BnOH concentration. (c) Evolution of $\lambda_{A>0.2}$ of 10 mmol kg^{-1} NaPW as a function of the concentration of BnOH, 1-BuOH and competitive BnOH:1-BuOH mixtures. For competitive mixtures, the x-axis represents the BnOH concentration. The overlap of the evolution of $\lambda_{A>0.2}$ as a function of BnOH and competitive mixtures suggests the selective binding of NaPW to BnOH.

As a next step, we probe the association of NaPW (most efficient solubilizing POM) with BnOH in dilute solutions of mixtures of aromatic BnOH and aliphatic 1-BuOH. We followed $\lambda_{A>0.2}$ as a function of different BnOH:1-BuOH ratios, ranging from pure BnOH and pure 1-BuOH to mixtures of BnOH:1-BuOH in molar ratios from 1:1 to 1:10 (high 1-BuOH excess) in aqueous solution, see Fig. 6.4c. The alcohol concentration is plotted on the x-axis. For competitive media (mixtures of BnOH and 1-BuOH), the x-axis gives the concentration of BnOH. Upon increasing the BnOH concentration (for pure BnOH addition), a strong bathochromic shift of $\lambda_{A>0.2}$ of NaPW (10 mmol kg^{-1}) is observed. On the contrary, the presence of 1-BuOH does not affect $\lambda_{A>0.2}$ of NaPW. This observation underlines the peculiarity and strength of specific POM-π interactions, compared to POM-aliphatic interactions. For the addition of alcohol mixtures, the shift of $\lambda_{A>0.2}$ perfectly overlaps with the evolution for pure BnOH addition. The association of NaPW and BnOH in competitive media (BnOH:1-BuOH) remains similarly strong, compared to the association of NaPW with BnOH in aqueous BnOH solution. In summary, NaPW binds highly selective to BnOH (aromatic) over 1-BuOH (aliphatic) in dilute solutions. Such a high affinity of SC POMs for aromatic molecules was recently reported by Liu and colleagues.[55] They explained the strong association of POMs with aromatic molecules as an enhanced macro-ion recognition due to a combination of the SC effect and short-range POM-π attractions.

In a last experiment, the selectivity of NaPW for aromatic molecules was combined with its solubilizing property, see Fig. 6.5a. Dark squares show the expected ratio of BnOH:1-BuOH as a function of c(NaPW) in solution, saturated with a 1:1 (BnOH:1-BuOH) mixture. These data are calculated from the single-compound solubilization data in Fig. 6.2a, *i.e.* the ratio of $c_{solubility\ limit}$(BnOH) and $c_{solubility\ limit}$(1-BuOH) is calculated at given NaPW concentrations. The BnOH:1-BuOH ratio remains constant around 0.45 (corresponding reasonably exactly to the ratio of *m*(BnOH):*m*(1-BuOH) = 10.6/23.7 = 0.45, see Table 6.1) for increasing NaPW concentrations, *i.e.* from the single-compound solubilization data no selectivity is expected. The red circles give experimental values for the ratio BnOH:1-BuOH solubilized in NaPW solution. Therefore, aqueous NaPW solutions were mixed with a BnOH:1-BuOH (1:1) solution at two times the solubility limit of the BnOH:1-BuOH (1:1) mixture. After equilibration and centrifugation, phase analysis allowed to determine the ratio BnOH:1-BuOH in aqueous solution. The ratio BnOH:1-BuOH increases nearly linearly with increasing NaPW concentration (from 0.53 to 1.03 for 200 mmol kg^{-1} NaPW), *i.e.* approximately two times more BnOH is solubilized as expected. On the contrary, SXS is a promising selective solubilizer considering its single-compound solubilizations, see Fig. 6.5b, black data. It can be expected that mainly 1-BuOH is solubilized from BnOH:1-BuOH mixtures. Nevertheless, it is shown experimentally (approximately constant BnOH:1-BuOH ratio by increasing SXS

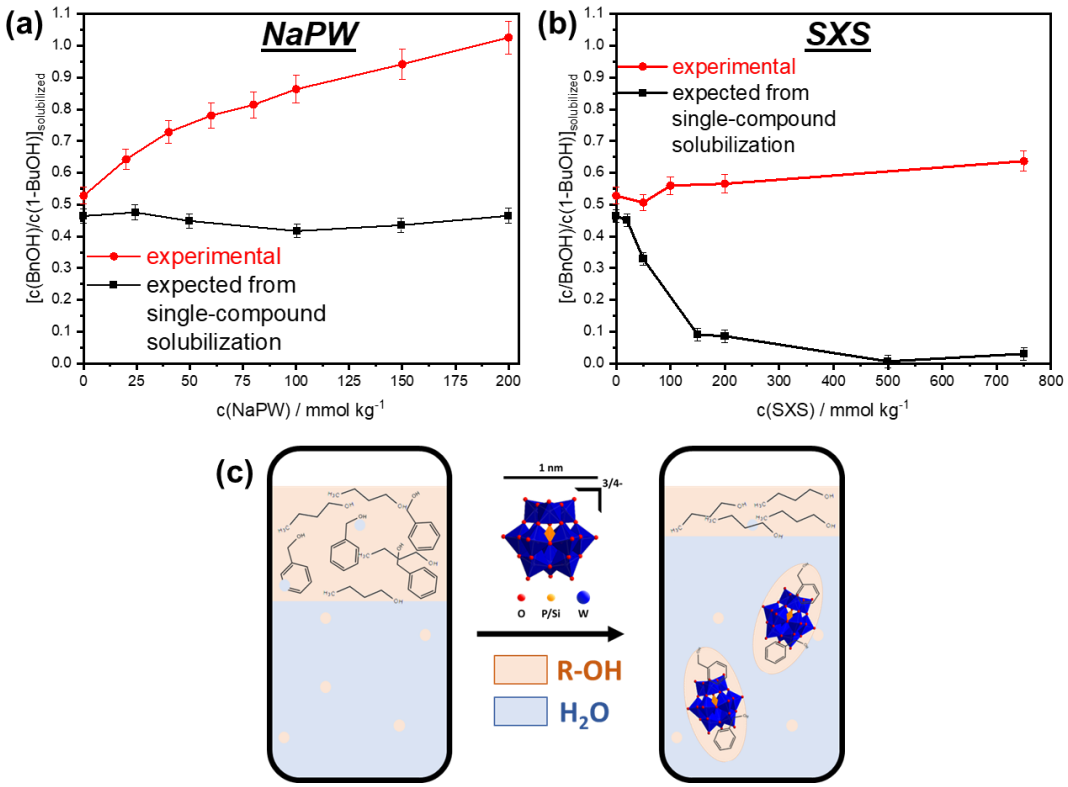

Figure 6.5. Ratio of solubilized BnOH:1-BuOH versus the concentration of (a) NaPW and (b) SXS. Dark data are calculated from the single compound solubilization data (see Fig. 6.2a, Fig. S6.1c respectively). Red data give the alcohol ratio in the aqueous solution of a biphasic system (two times solubility limit of BnOH:1-BuOH (1:1)) at given NaPW/SXS concentrations. (c) Schematic representation of the selective solubilization mechanism of POMs.

concentration, see Fig. 6.5b, red data) that SXS does not act as a selective solubilizer here. As a conclusion, NaPW is a selective solubilizer, see scheme in Fig. 6.5c, for aromatic alcohols over aliphatic alcohols, even though the selectivity is lower compared to dilute aqueous solutions, *cf.* Fig. 6.4c.

6.5 Conclusion

We showed here that SC α-Keggin POMs NaPW, HPW and HSiW solubilize moderately hydrophobic molecules in water. We find especially NaPW to be similarly, or even more, efficient in solubilizing hydrophobic short-chain alcohols and aromatic molecules respectively, as the model surfactant SDS and much more efficient than the model hydrotrope SXS. Their high solubilization efficiency was explained by the strong association of POMs with solubilized substrate molecules. These molecules substitute a part of the solvation shell of the POM compared to the POM hydration in pure water, driven by the SC effect. Therefore, water-soluble non-covalent POM-substrate complexes are formed. Five qualitative criteria concerning the substrate (hydrophobic compounds), that influence the solubilization efficiency of SC POM were evaluated: *(i)* moderate water solubility is required

(around 2 % (w:w)), *(ii)* chain length of aliphatic alcohols must be $<C_6$, *(iii)* branching of aliphatic moieties decreases solubilization efficiency, *(iv)* hydroxylation and *(v)* π-electron containing moieties enhance solubilization efficiency. The influence of these five parameters is recalled in Fig. S6.14 and Table S6.6. Moreover, a stronger chaotropic character (lower charge density) of the POM enhances the solubilization of the POM. On the contrary, protons as POM counter-cations promote the formation of large POM-substrate nano-assemblies, leading to a decreased solubilization efficiency.

In dilute competitive solutions of aromatic (BnOH) and aliphatic (1-BuOH) alcohols, NaPW exclusively associates with BnOH. The preferential binding of NaPW to BnOH (over 1-BuOH) arises due to a combination of the SC effect and short-range POM-π attractions. These specific interactions allow the selective solubilization of BnOH from BnOH:1-BuOH mixtures in aqueous solution. This selective solubilization of a single alcohol from alcohol mixtures is unique by comparing it to the selectivity of SXS. We imagine this work to be the starting point for POMs as selective solubilizers and anticipate applications in directed POM-mediated reactions in water, such as photocatalysis with visible light, by combining the selective solubilization of POMs with their catalytic activity.

6.6 Supporting Information

6.6.1 Additional solubilization measurements and data treatment

Figure S6.1 shows solubilization measurements of eight hydrophobic molecules (2-Butanol (2-BuOH), 1-Butanol (1-BuOH), 2-Methyl-1-Propanol (2-Me-1-PrOH), benzyl alcohol (BnOH), 1-Pentanol (1-PentOH), toluene, cyclohexyl methanol and 1-Hexanol (1-HexOH)) as a function of the concentration of (a) the α-Keggin POM $Na_3PW_{12}O_{40}$ (NaPW), (b) the surfactant sodium dodecyl sulfate (SDS) and (c) the hydrotrope sodium xylene sulfonate (SXS) in water.

In case of (a) NaPW addition the solubility limit can be increased for 2-BuOH, 1-BuOH, 2-Me-1-PrOH, 1-PentOH, BnOH and toluene. For the aliphatic alcohols cyclohexyl methanol and 1-HexOH the solubility limit remains untouched upon the addition of NaPW. Upon the addition of (b) SDS the solubility is increased for 2-BuOH, 1-BuOH, 2-Me-1-PrOH, 1-PentOH, whereas the solubility is not significantly increased for BnOH, toluene, cyclohexyl methanol and 1-HexOH. In case of (c) SXS, solubility increases are only observed at higher concentrations (c(SXS) > 200 mmol kg^{-1}), except for 2-BuOH. In summary, SXS acts here as a less efficient solubilizer compared to NaPW and SDS.

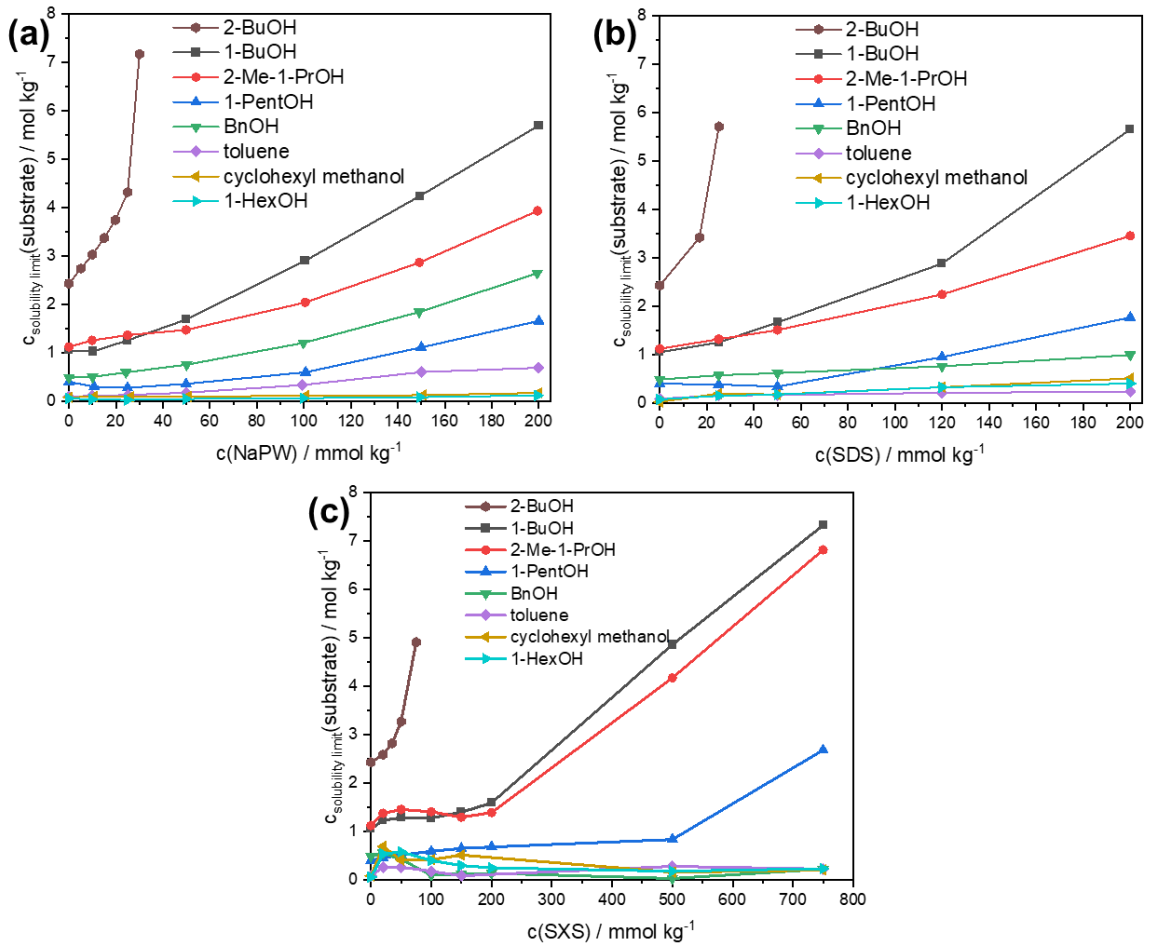

Figure S6.1. Solubilization diagrams of several hydrophobic molecules as a function of the concentration of (a) the α-Keggin POM $Na_3PW_{12}O_{40}$ (NaPW), (b) the surfactant sodium dodecyl sulfate ($Na(SO_4)$-$C_{12}H_{25}$, SDS) and (c) sodium xylene sulfonate (SXS). The solubilization measurements show already on the first view that the solubilization efficiency of NaPW compares to the one of SDS for most of the hydrophobic molecules.

In order to provide a quantitative comparison of the solubilization efficiency of the different solubilizers, POMs: NaPW, HPW and HSiW, surfactant: SDS and hydrotrope: SXS, a simple fitting procedure was applied to the phase diagrams in Fig. S6.1 and Fig. 6.2. As described in the manuscript, a linear fit was used with the general equation

$$c_{solubility\ limit}(alcohol) = m \cdot c(POM, SDS, SXS) + t. \quad (6.1)$$

The parameter *m* (slope of the curve) represents the number of hydrophobic molecules which are solubilized per one molecule of solubilizer. The y-axis intercept *t* informs on the solubility limit of the hydrophobic compound in pure water. In Fig. S6.2, we show an example of such a fit which was applied to the solubilization diagram of BnOH with NaPW as a solubilizer. As the y-axis is typically given in mol kg^{-1} and the x-axis in mmol kg^{-1} the parameter *m* needs to be multiplied by a factor of 10^3 in order to obtain the number of solubilized BnOH molecules per one POM/SDS/SXS molecule. Accordingly, a convenient approach to compare the solubilization efficiency of the

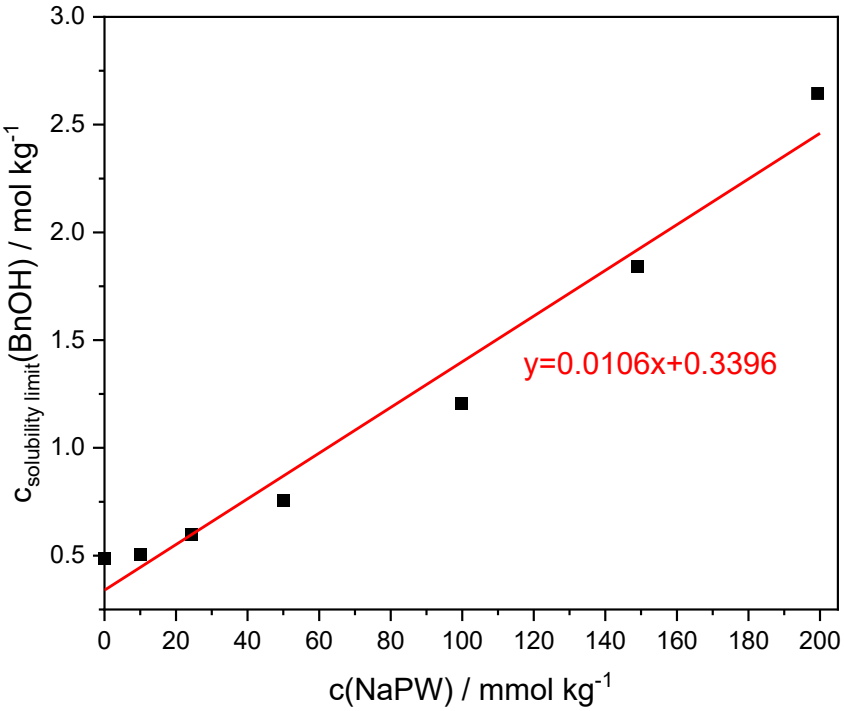

Figure S6.2. Example of a fitting graph of solubilization measurements (benzyl alcohol (BnOH) solubilization as a function of NaPW concentration). The solubilization measurements were fitted with a linear fit, *i.e.* $y = m \cdot x + t = c_{solubility\ limit}(molecule) = m \cdot c(POM/surfactant) + + c_{solubility\ limit\ in\ water}(molecule)$. Therefore, the slope *m* informs on the number of molecules which are solubilized per POM/surfactant/hydrotrope.

different solubilizers is to consider the *m* parameters, which are summarized in Table S6.1b, while Table S6.1a shows the comparison of experimentally determined aqueous solubilities with literature data.

Table S6.1a. Comparison of the experimentally determined solubility limit of the investigated organic solutes in pure water with literature data.

Substrate	$c_{experimental}$ / mol kg^{-1}	$c_{literature}$ / mol kg^{-1}[50,51]
2-BuOH	2.30	2.43
1-BuOH	1.01	1.05
2-Me-1-PrOH	1.02	1.12
BnOH	0.37	0.49
1-PentOH	0.26	0.40
toluene	0.01	0.09
1-HexOH	0.06	0.06

Table S6.1b. *m* (× 10^3) parameter for NaPW/HPW/HSiW/SDS/SXS determined from linear fits of solubilization measurements. The highest *m* parameters (most efficient solubilizers) are indicated in light green. If the *m* parameter of the best solubilizer exceeds those of the second best by a factor of ≥ 1.5, the parameter is marked dark green. Values in brackets represent the coefficient of determination, R^2.

Substrate	NaPW	HPW	HSiW	SDS	SXS
2-BuOH	129.7 (76 %)	33.6 (99 %)	26.6 (100 %)	120 (83 %)	32.3 (84 %)
1-BuOH	23.7 (99 %)	10.5 (98 %)	3.8 (88 %)	22.9 (96 %)	8.5 (96 %)
2-Me-1-PrOH	13.4 (96 %)	2.8 (98 %)	2.1 (90 %)	11.6 (98 %)	7.5 (94 %)
BnOH	10.6 (97 %)	4.2 (99 %)	1.7 (84 %)	2.4 (99 %)	-0.4 (26 %)
1-PentOH	6.5 (90 %)	0.3 (14 %)	-0.2 (12 %)	7.2 (92 %)	2.5 (80 %)
toluene	3.2 (96 %)	2.3 (95 %)	0.05 (2 %)	0.6 (84 %)	0.1 (12 %)
1-HexOH	0.4 (82 %)	0.2 (60 %)	0.1 (62 %)	1.6 (97 %)	-0.2 (14 %)
cyclohexyl methanol	0.4 (92 %)	0.09 (27 %)	0.5 (54 %)	2.2 (95 %)	-0.3 (20 %)

The evaluation of the linear fits suggests that *ca.* 130 molecules of 2-BuOH can be solubilized by per single NaPW. Remarkably, this number even exceeds the one of SDS, *i.e.* one molecule of NaPW solubilizes more 2-BuOH than one molecule of the surfactant SDS. With 33.6 and 26.6 the solubilization efficiency is less pronounced for HPW and HSiW, respectively. A similar observation (comparable solubilization efficiency of NaPW and SDS and lower efficiency for HPW/HSiW) is drawn for the solubilization of 1-BuOH, 2-Me-1-PrOH and 1-PentOH. In case of the longer chained aliphatic alcohols 1-HexOH and cyclohexyl methanol the highest *m* parameters were found for SDS followed by NaPW, HPW and HSiW. Interestingly, for the aromatic compounds BnOH and toluene the *m* parameters are the highest for NaPW followed by HPW, SDS and HSiW. Here, especially NaPW is a much more efficient solubilizer than the model surfactant SDS.

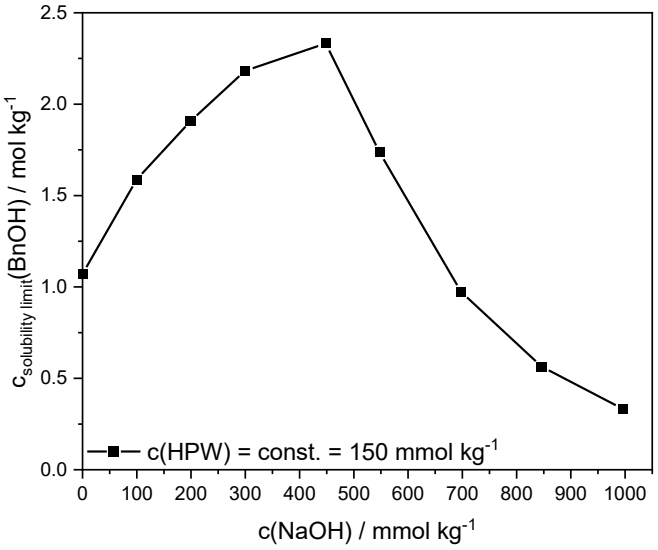

Figure S6.3. Solubilization of BnOH at a fixed HPW concentration (150 mmol kg^{-1}) as a function of c(NaOH). The solubilization increases strongly until all protons are exchanged for Na^+ (around 450 mmol kg^{-1} NaOH and decreases again due to the decomposition of the POM (alkaline pH).

Figure S6.3 shows the solubility limit of BnOH in water at a fixed $H_3PW_{12}O_{40}$ (HPW) concentration of 150 mmol kg^{-1} as a function of NaOH concentration, *i.e.* as a function of the pH. At 0 mmol kg^{-1} NaOH the solubility limit of BnOH is around 1.1 mol kg^{-1}. Up to 450 mmol kg^{-1} NaOH the solubility limit increases drastically to 2.3 mol kg^{-1} BnOH. At higher NaOH concentrations the solubility limit decreases again, even below the initial solubility limit (< 0.5 mol kg^{-1}).

Up to 450 mmol kg^{-1} NaOH the solubility limit of BnOH strongly increases, as the counter-cation of HPW (150 mmol kg^{-1}) is exchanged for Na^+ according to following titration equation

$$H_3PW_{12}O_{40} + 3\ NaOH \rightarrow Na_3PW_{12}O_{40} + 3\ H_2O. \quad (6.2)$$

As shown in the manuscript, NaPW is a better solubilizer compared to HPW. At even higher NaOH concentrations (> 450 mmol kg^{-1}), the pH turns neutral to alkaline, as the EP of Eq. 6.2 is crossed. It is known that at such high pH, the POM gradually decomposes towards tungstate, WO_4^{2}, and phosphate, PO_4^{3-}.[56] These, high charge density anions (kosmotropic) are not expected to produce a solubility increase of hydrophobic molecules in water. On the contrary, they are known to favor a decreased solubility of hydrophobic compounds in aqueous solution.[41,57]

6.6.2 ^{1}H-NMR experiments

As superchaotropic POMs have been shown to be efficient solubilizers for moderately hydrophobic alcohols in water, we want to understand the solubilization mechanism. Hence, ^{1}H-NMR spectra are recorded to investigate the local environment of the solubilized alcohols. It is worth to note that ^{1}H-NMR already appeared as a powerful tool to probe next-neighbor interactions arising from the superchaotropic effect.[30,31,35,36,40,45,58,59] As an example, we investigate the ^{1}H-NMR spectrum of 10 mmol kg^{-1} 1-BuOH as a function of increasing POM concentrations (NaPW, HPW and HSiW) and HCl concentration as a reference.

Figure S6.4a shows the ^{1}H-NMR spectrum of 10 mmol kg^{-1} 1-BuOH in D_2O. According to Shoolery`s rules,[60] 1-BuOH produces four different signals. Around 0.74 ppm a triplet arises which can be assigned to the protons of the terminal CH_3 group (signal 1). At 1.18 ppm a multiplet emerges due to multiple coupling of protons of the CH_2 moiety next to the terminal CH_3 group (signal 2). At 1.36 ppm another multiplet arises, stemming from the centered CH_2 group (signal 3). Around 3.45 ppm a triplet is present, stemming from protons of the CH_2 moiety next to the -OH functional group (signal 4). Figure S6.4b depicts the shift of the chemical shift, Δδ, of the four ^{1}H-NMR signals of 1-BuOH as a function of the concentration of NaPW (blue), HPW (dark) and HSiW (red). Note that plotting Δδ, deduced from NMR, was already used to probe the superchaotropic effect, *i.e.* the adsorption of POMs (or nano-ions in general) on organic matter, in diverse systems.[30,34,35,40]

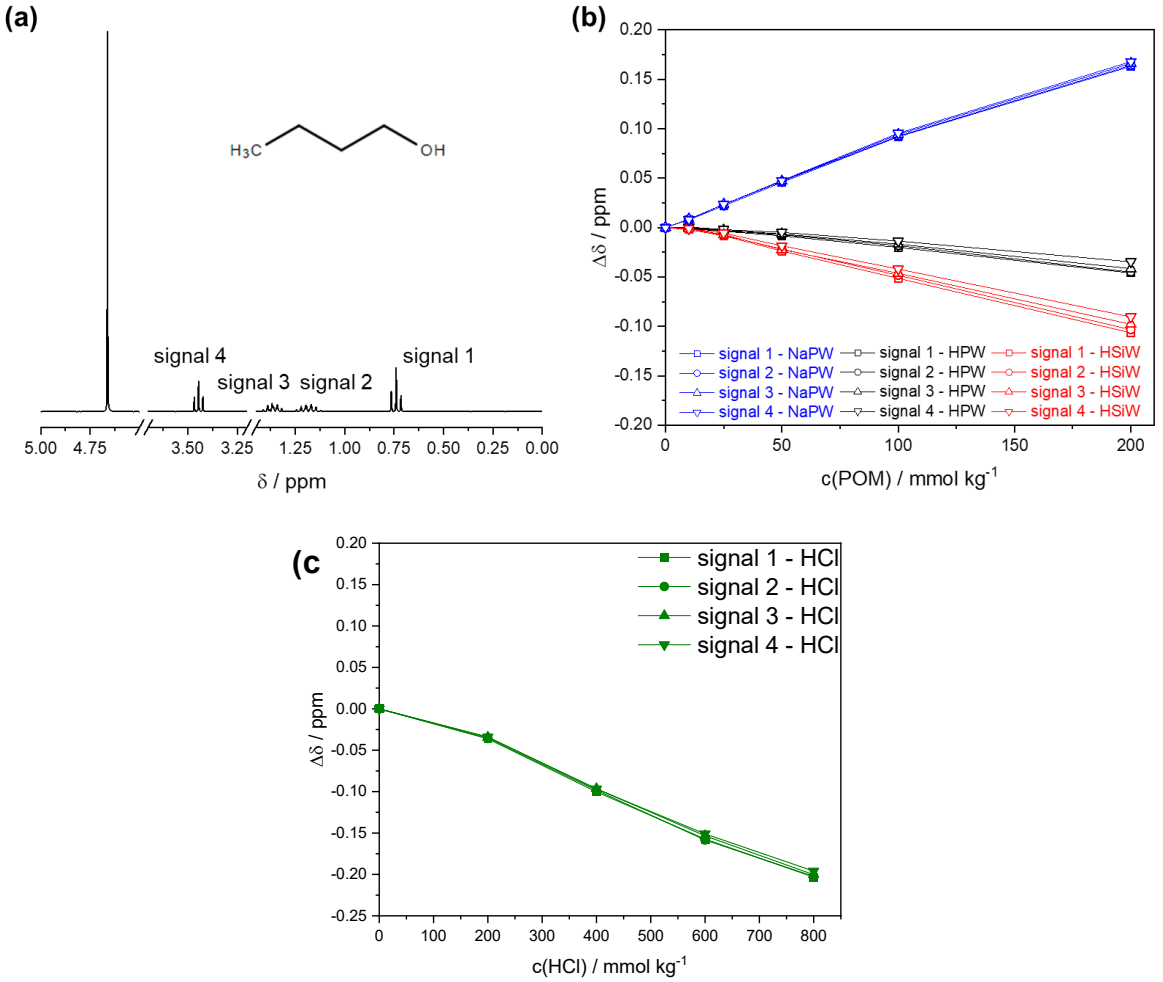

Figure S6.4. (a) ^{1}H-NMR spectrum of 10 mmol kg^{-1} 1-BuOH in D_2O. Four different signals can be identified (signal 1: terminal CH_3 group, signal 2 and 3: CH_2 moieties located in the center of 1-BuOH and signal 4: CH_2 moiety next to the OH group). (b) Shift of the chemical shift of the four 1-BuOH signals as a function of the NaPW, HPW and HSiW concentration. (c) Reference shifts of the chemical shifts of the four signals of 1-BuOH as a function of c(HCl).

Interestingly, all four signals of 1-BuOH are shifted similarly. Hence, it is likely that 1-BuOH has no preferential orientation around the POMs. For example, the addition of 200 mmol kg^{-1} NaPW leads to a positive shift of +0.17 ppm for all signals. In case of 200 mmol kg^{-1} HPW the signals are shifted -0.04 ppm and -0.10 ppm for 200 mmol kg^{-1} HSiW, respectively. The downfield-shift upon the addition of NaPW arises due to the close contact of 1-BuOH with the electron rich PW anion. The upfield-shift upon the addition of HPW and HSiW is likely to arise from a combination of a downfield-shift (superchaotropic effect) and an upfield-shift owing to the high acidity in solution. Therefore, Fig. S6.4c shows the evolution of the four 1-BuOH signals upon the addition of HCl, which leads to strong upfield shifts with increasing HCl concentration, as a comparison.

Figure S6.5 shows a similar experiment as shown in Fig. S6.4, but BnOH was the investigated molecule instead of 1-BuOH. 10 mmol kg^{-1} BnOH in D_2O produce two signals in ^{1}H-NMR: a singlet at 4.49 ppm arising from the CH_2 group (signal 1) and a multiplet around 7.28 ppm stemming from the protons in the aromatic C_6H_5 moiety (signal 2), see Fig. S6.5a. Again, both signals show a similar shift of the chemical shift, Δδ, as a function of increasing POM concentration, *i.e.* BnOH shows no preferential orientation on the POM surface, see Fig. S6.5b. In the case of the addition of NaPW, the signals are shifted by +0.15 ppm at 200 mmol kg^{-1} POM. For HPW a shift of -0.01 ppm is observed and -0.08 ppm for HSiW, respectively at 200 mmol kg^{-1}. Again, the downfield-shift (upon NaPW addition) can be explained by the close contact of BnOH with the electron rich POM, whereas the overall upfield-shift (observed for HPW and HSiW) arises from a combination of a down field-

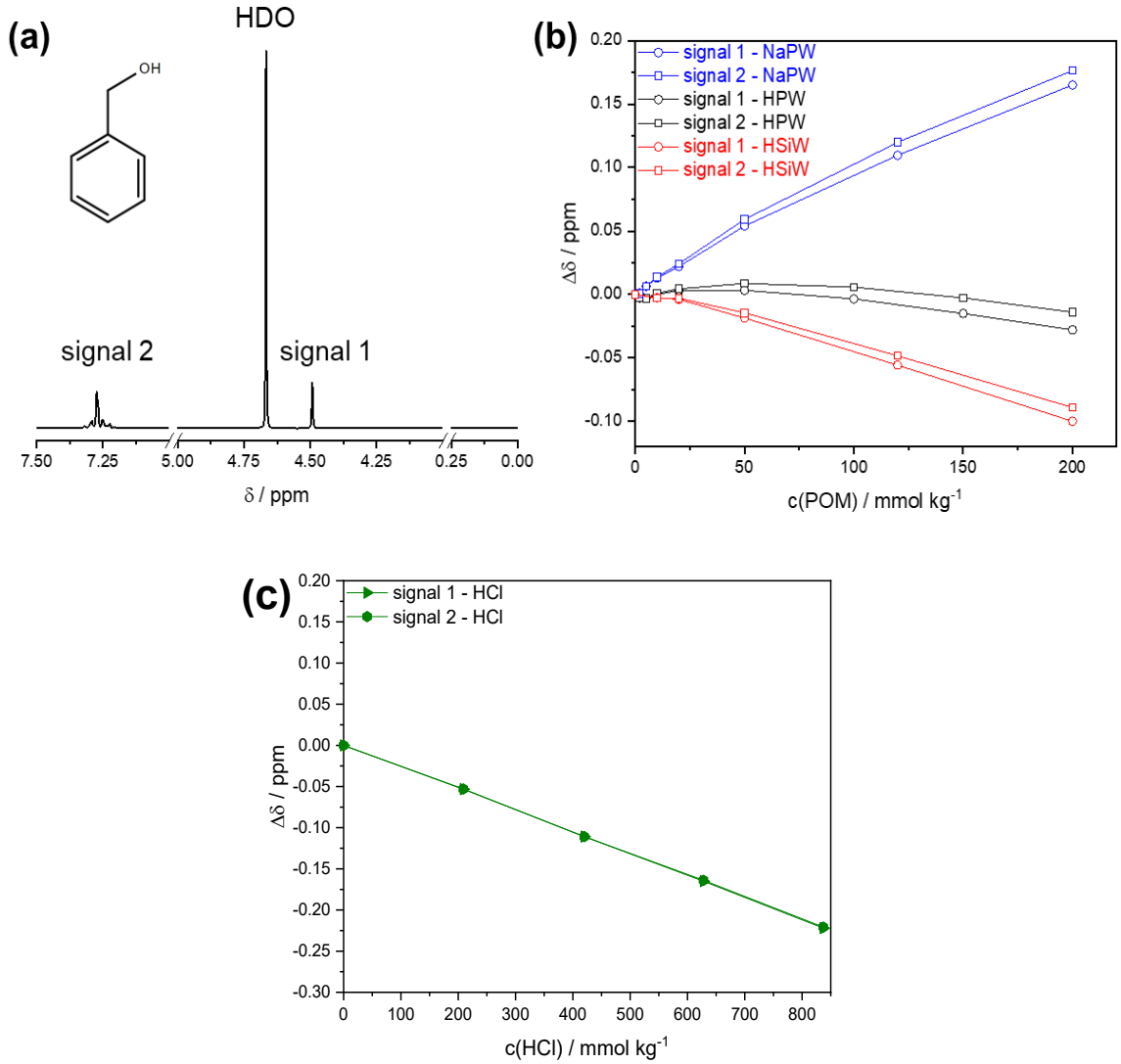

Figure S6.5. (a) ^{1}H-NMR spectrum of 10 mmol kg^{-1} BnOH in D_2O. Two different signals can be identified (signal 1: CH_2 group next to the OH group, signal 2: aromatic protons). (b) Shift of the chemical shift of the two BnOH signals as a function of NaPW, HPW and HSiW concentration. (c) Reference shifts of the chemical shift of the two signals of BnOH as a function of c(HCl).

shift (superchaotropic effect) and the strong solution acidity, *cf.* strong negative shifts upon HCl addition, see Fig. S6.5c.

In summary, ^{1}H-NMR experiments confirm strong interactions of superchaotropic POMs with 1-BuOH and BnOH. It is most likely that these alcohol molecules assemble around the POMs on their surface.

6.6.3 SAXS spectra and data fitting

Fundamentals

All SAXS-fits were performed using SasView version 5.0.3,[47] where the scattered intensity, *I(q)*, of an isotropic sample containing identical and randomly oriented particles is expressed by Eq. 6.3.

$$I(q) = n \cdot V^2 \cdot \Delta\rho^2 \cdot P(q) \cdot S(q) \tag{6.3}$$

with n the number density of the scattering object, V its volume, the scattering contrast $\Delta\rho = \rho_{particle} - \rho_{solvent}$, the form factor $P(q)$ and the structure factor $S(q)$. The form factor $P(q)$ describes the shape of the scattering object, while the structure factor $S(q)$ describes the higher order arrangement of the scattering objects.

Determination of electron densities

In order to determine the scattering contrast, the individual electronic densities $\rho_{particle}$ and $\rho_{solvent}$ were calculated by Eq. 6.4.

$$\rho_i = \frac{\sum_j b_j}{v_i} \cdot l_{Thomson} \tag{6.4}$$

with b_j being the number of electrons in the *j*th atom, v_i the scattering objects volume and $l_{Thomson}$ the Thomson length ($l_{Thomson}$ = 2.82 × 10^{-13} m). The thereby calculated electron densities of $PW_{12}O_{40}^{3-}$, H_2O and the alcohols 1-BuOH, 2-BuOH, 2-Me-1-PrOH and BnOH are shown in Table S6.2.

Table S6.2. Molecular volumes, number of electrons and scattering length densities (ρ) of the used compounds.

Compound	Molecular volume / nm³	Number of electrons	ρ^{SAXS} / 10^{10} cm^{-2}
$PW_{12}O_{40}^{3-}$	0.46[1]	1223	74.9
$SiW_{12}O_{40}^{3-}$	0.46[1]	1222	74.9
H_2O	0.03[2]	10	9.4
1-BuOH	0.15[2]	50	7.8
2-BuOH	0.15[2]	50	7.8
2-Me-1-PrOH	0.15[2]	50	7.7
BnOH	0.165[2]	64	9.5

[1] taken from Buchecker *et al.*[44]

[2] calculated from the respective pure liquid densities

Fits of the SAXS spectra

All fits were performed using an ellipsoidal core-shell model. Therefore, the POM was considered to be the core with a radius of approximately 0.45 nm.[44] To represent the spherical shape of the POM, the ratio of polar and equatorial radii, x_core (r_polar/r_equatorial), was set to 1. The overall scattering length density (SLD or ρ) is dominated by the SLD of the POM, given in Table S6.2 with a fitting freedom of ±5 %. The shell was considered as a mixture of water and a corresponding alcohol. To do so, the SLD was considered as a linear combination of the SLD of water and the SLD of the alcohol. Moreover, the shell thickness and expansion, x_polar_shell (shell_polar/shell_equator), were fitting parameters. To reproduce repulsive interactions of these aggregates, a Hayter-MSA structure factor[48,49] was applied including the aggregate`s charge, the salinity of the sample, the dielectric constant and temperature of the medium.

Fits were performed for the three different POMs NaPW, HPW and HSiW in water and in the presence of 1-BuOH, 2-BuOH, 2-Me-1-PrOH and BnOH. The spectra with their fits are shown in Figs. S6.6-S6.9. The fitting parameters are shown in Table S6.3-S6.5.

General discussion of the SAXS spectra

Whereas in ^{1}H-NMR the focus is made on the organic matter, SAXS investigates the local environment of POMs as in X-ray scattering, POMs give a strong signal (> 1200 e^- per POM) compared to water and the solubilized alcohol. Figure S6.7 shows the SAXS spectra of NaPW (c(NaPW) = 50 mmol kg^{-1}) in (a) 1-BuOH, (b) 2-BuOH, (c) 2-Me-1-PrOH and (d) BnOH below and above the solubility limit of the alcohols in pure water. The reference spectrum of 50 mmol kg^{-1}

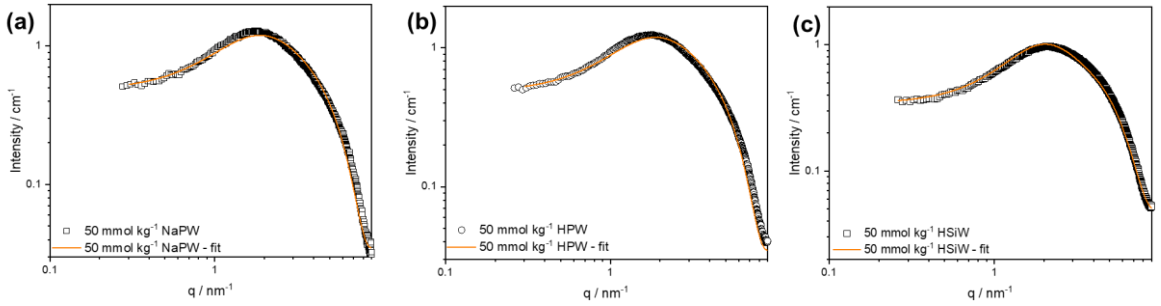

Figure S6.6. Reference SAXS spectra of 50 mmol kg^{-1} (a) NaPW, (b) HPW and (c) HSiW in water including fits.

NaPW in aqueous solution gives the characteristic spectrum of a spherical scattering object, see Fig. S6.6a. At $q > 2$ nm^{-1} the scattered intensity strongly increases due to the form factor, *P(q)*, of the spherical POM. Around $q = 2$ nm^{-1} a maximum scattered intensity is reached leading to a slightly pronounced peak. The peak position informs on the mean POM-POM distance and therefore correlates with the experimental POM concentration. At $q < 2$ nm^{-1}, the scattered intensity decreases due to the structure factor, *S(q)*. Decreased *S(q)* usually arise from electrostatic repulsions in (colloidal) solutions, *i.e.* the decreased *S(q)* can be attributed to electrostatic repulsions between the isotropically dispersed POM clusters. Accordingly, the intensity is lower at low *q* for HSiW (POM^{4-}) compared to NaPW/HPW (POM^{3-}), see Fig S6.6a-c. Note that a more detailed description of aqueous POM solutions is given elsewhere.[52,61,62]

By changing the solvent medium from water to water-alcohol mixtures, the SAXS spectra of the POMs are generally changed/modified: In case of *e.g.* NaPW (Fig. S6.7) *(i)* a pronounced modulation occurs at *q* around 4 nm^{-1}, *(ii)* an intensity depletion between *q* around 4 nm^{-1} and $q = 1.5$ nm^{-1} appears and *(iii)* a correlation peak occurs at *q* around 1.5 nm^{-1}. At $q < 1.5$ nm^{-1} the spectrum overlaps with the reference of 50 mmol kg^{-1} NaPW in water. Interestingly, the absence of pronounced excess scattering at low *q* suggests that NaPW clusters are not self-assembled and are still homogeneously dispersed. It is worth to note that typical SAXS spectra of assembled POM clusters in the presence of organic solutes were reported in previous works.[24,31,44,45,59] Hence, it is likely that the change in the SAXS spectrum only arises from a change in the local environment (solvation) of NaPW, as the scattered intensity arises from a change in the scattering length density, ρ,

$$I(q) \propto \Delta\rho^2 = |\rho_{solvated\ POM} - \rho_{solvent}|^2 \qquad (6.5)$$

It is worth to note that alcohols (*e.g.* 1-BuOH: $7.8 \cdot 10^{10}$ cm^{-2}) and water ($9.4 \cdot 10^{10}$ cm^{-2}) have different scattering length densities. In case of aqueous POM solutions, the solvation of the POM is water and therefore the equation simplifies to

$$I(q) \propto \Delta\rho^2 = |\rho_{POM} - \rho_{water}|^2 \quad (6.6)$$

and effects in the solvation of the POM remain invisible. In order to access deeper understanding on the environment of POMs, a convenient method is to fit the collected SAXS spectra. Therefore, a core-shell model was used with the POM being the core and a mixture of alcohol and water the shell. An ellipsoidal *P(q)* was applied, as core-shell sphere simulations do not lead to proper fitting results in general.

In case of 50 mmol kg^{-1} NaPW - 1.08 mol kg^{-1} 1-BuOH the fit revealed an equatorial radius of 1.33 nm and a polar radius of 0.48 nm for the solvation shell. If a radius of 0.46 nm of POMs,[44] being in the center of this ellipsoid, is assumed, the shell thickness is 0.87 nm (equatorial) and 0.02 nm (polar). For 50 mmol kg^{-1} HPW - 1.08 mol kg^{-1} 1-BuOH, see Fig. S6.8a, the fit gives an equatorial radius of 1.82 nm and a polar radius of 0.47 nm (much larger compared to NaPW case). Accordingly, the shell size thickness is 1.36 nm (equatorial) and 0.01 nm (polar). Fitting the spectrum of 50 mmol kg^{-1} HSiW - 1.08 mol kg^{-1} 1-BuOH, see Fig. S6.9a, reveals an equatorial radius of 0.69 nm and a polar radius of 0.69 nm, *i.e.* the solvation can be described as a sphere with a shell thickness of 0.22 nm. Further fitting results on the different alcohol-water mixtures are summarized in Tables S6.3-S6.5 and Figs. S6.7-S6.9.

As a summary, we observe *(i)* in pure water, the POM is fully solvated by water, whereas an ellipsoidal solvation sphere, made up with alcohol and water forms around *(ii)* NaPW and *(iii)* HPW in the presence of alcohol (which are much larger for HPW compared to NaPW). In case of *(iv)* HSiW a solvation sphere forms around HSiW with a small amount of alcohol and a high amount of water. We attribute the strong solubilization power of the investigated POMs to the partial substitution of their water hydration by alcohol molecules, which form a solvation ellipsoid(/sphere) together with water molecules around the POM. The partial substitution of the POM solvation shell was already observed for the interaction of POMs with diverse substrates in the context of the superchaotropic effect.[30,40] Hence, the solubilization of hydrophobic alcohols by POMs can be discussed as an effect arising from the POM`s superchaotropicity. This manifests in the strong impact of the POM`s charge density (PW compared to SiW) and of the POM`s counter-cation (Na^+ compared to H^+) on the interaction strength with the hydrophobic alcohol and subsequently their different solubilization efficiencies for these alcohols. Interestingly, HPW exhibit larger alcohol solvation shells around the POM compared to NaPW, due to the self-assembly promoting role of H^+. These larger aggregates are likely to coalesce and therefore HPW is a less efficient solubilizer than NaPW.

NaPW

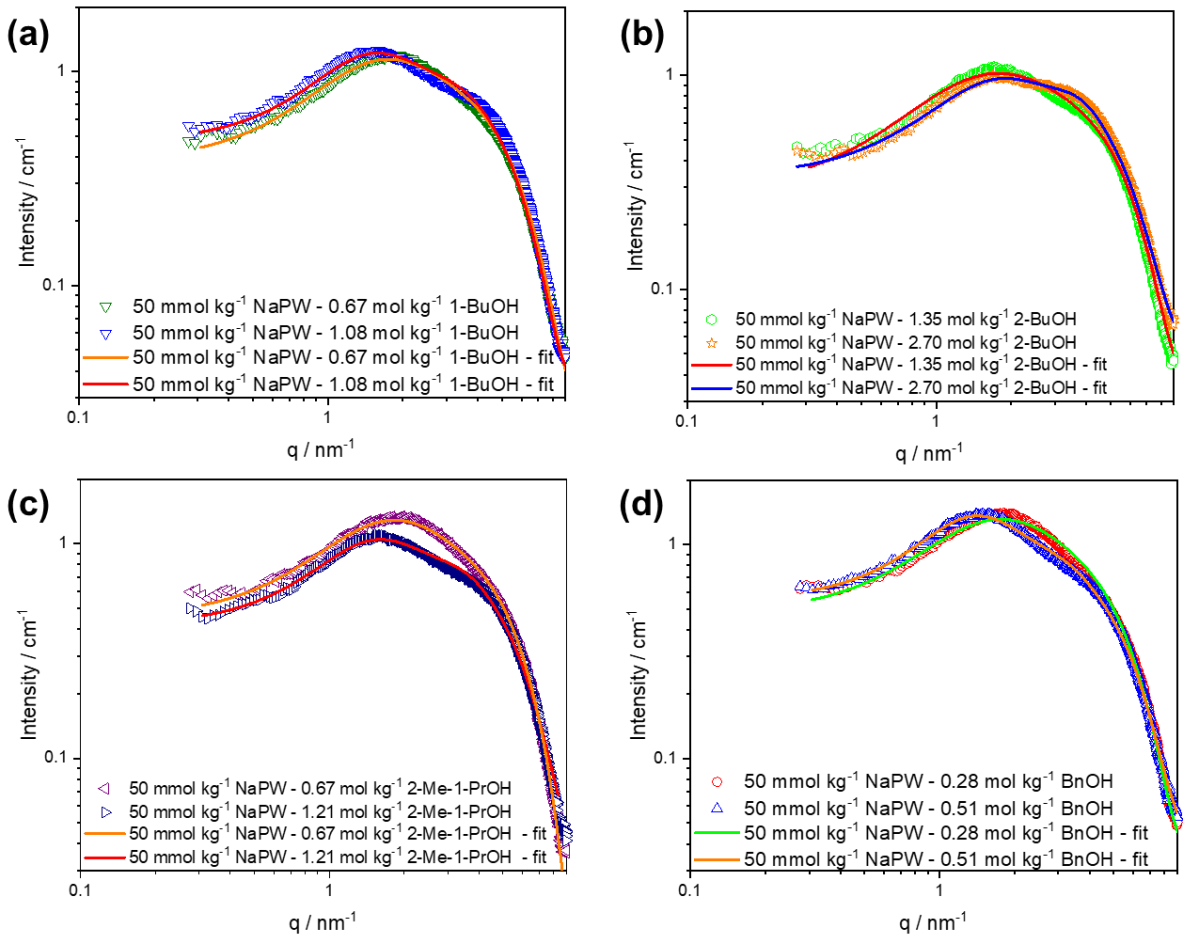

Figure S6.7. SAXS spectra including fits of 50 mmol kg^{-1} NaPW in the presence of (a) 0.67 and 1.08 mol kg^{-1} 1-BuOH, (b) 1.35 and 2.70 mol kg^{-1} 2-BuOH, (c) 0.67 and 1.21 mol kg^{-1} 2-Me-1-PrOH and (d) 0.28 and 0.51 mol kg^{-1} BnOH.

Table S6.3. Fit parameters of the SAXS spectra in Fig. S6.7. M is here used as an abbreviation for mol kg^{-1}.

	50 mM NaPW 0.67 M 2-Me-1-PrOH	**50 mM NaPW 1.21 M 2-Me-1-PrOH**	**50 mM NaPW 0.67 M 1-BuOH**	**50 mM NaPW 1.08 M 1-BuOH**	**50 mM NaPW 1.35 M 2-BuOH**	**50 mM NaPW 2.70 M 2-BuOH**	**50 mM NaPW 0.28 M BnOH**	**50 mM NaPW 0.51 M BnOH**
scale	1	1	1	1	1	1	1	1
background	0.011929	0.043641	0.0325433	0.04	0.043223	0.062471	0.03615	0.049279
r_effective_model	max outer radius	max outer radius	max outer radius	max outer radius	max outer radius	max outer radius	max outer radius	max outer radius
r_equatorial_core / Å	4.5	4.5	4.5	4.7	4.5	4.5	4.6	4.5
x_core (r_polar/r_equatorial_core)	1	1	1	1	1	1	1	1
thick_shell (shell thickness equator) / Å	4.1245	10.934	3.379	8.6221	5.8661	10.706	3.8	11.265
x_polar_shell (shell_polar/shell_equator)	0.036439	0.026584	0.00017165	0.026584	0.11085	1.67E-07	0.039862	0.03
sld_core / 10^{10} cm^{-2}	83.527	81.055	86.131	81.5	77.154	79	81.391	86
sld_shell / 10^{10} cm^{-2}	8.8011	8.8695	8.5	8.7	8.688	7.8665	9.5	10.024
sld_solvent / 10^{10} cm^{-2}	9.2402	9.3074	9.4	9.3	9.4	9.3	9.4	9.4
$r_{effective}$ / Å	8.6245096	15.4344704	7.879	13.3222	10.36	15.2	8.3999999	15.765339
Volume fraction	0.02686	0.07406	0.017586	0.051404	0.041757	0.078154	0.023551	0.07
Charge / q	3.9131	4.7185	4.1	5.4909	3	3	3.5	5.8
Temperature / K	293	293	293	293	293	293	293	293
c(salt) / M	0.023345	0.059865	0.014643	0.054216	0.02	0.02158	0.02	0.060579
dielectric constant	75.5	72	71	72	68	65	71	70

HPW

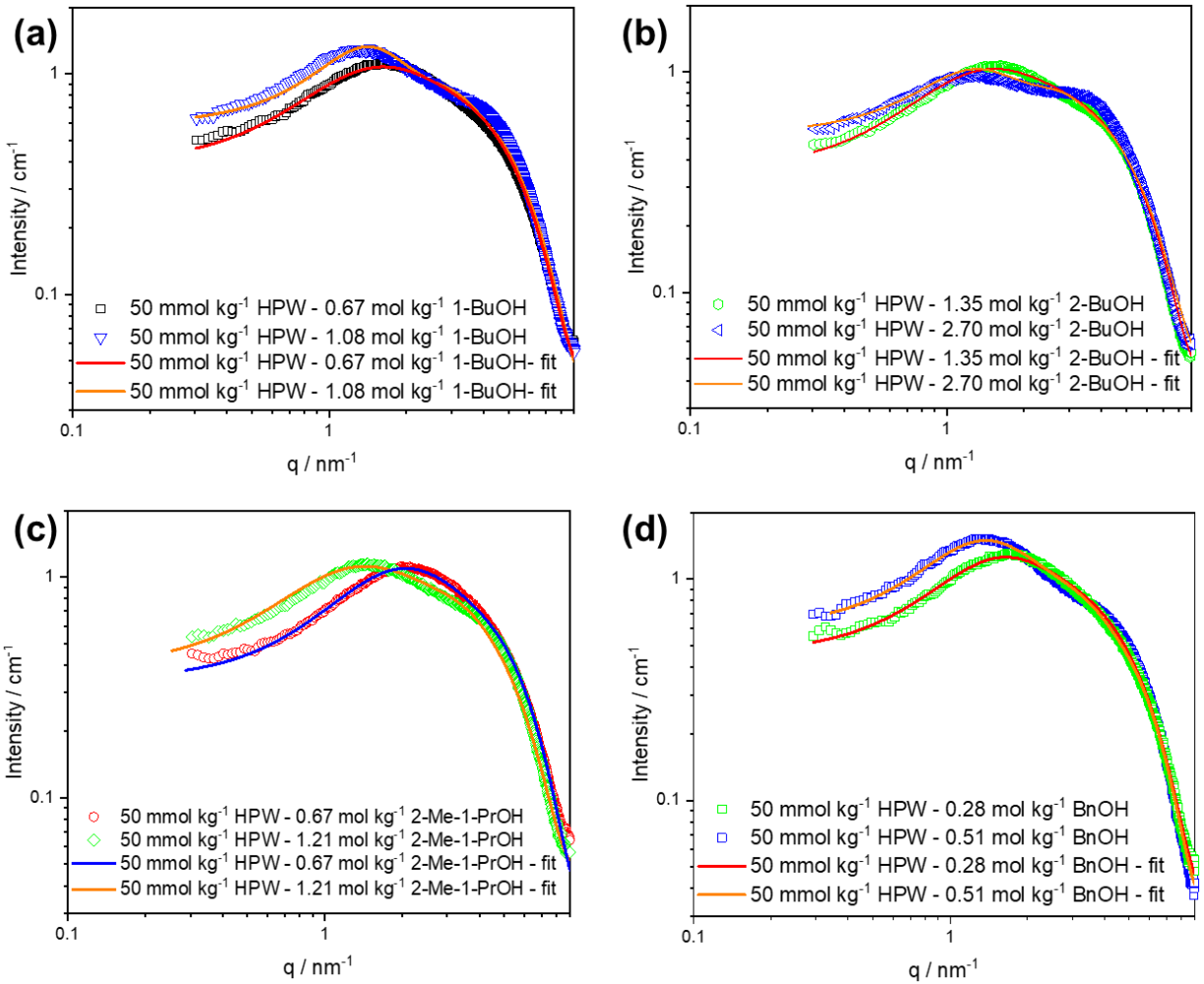

Figure S6.8. SAXS spectra including fits of 50 mmol kg^{-1} HPW in the presence of (a) 0.67 and 1.08 mol kg^{-1} 1-BuOH, (b) 1.35 and 2.70 mol kg^{-1} 2-BuOH, (c) 0.67 and 1.21 mol kg^{-1} 2-Me-1-PrOH and (d) 0.28 and 0.51 mol kg^{-1} BnOH.

Table S6.4. Fit parameters of the SAXS spectra in Fig. S6.8. M is here used as an abbreviation for mol kg^{-1}.

	50 mM HPW 0.67 M 2-Me-1-PrOH	50 mM HPW 1.21 M 2-Me-1-PrOH	50 mM HPW 0.67 M 1-BuOH	50 mM HPW 1.08 M 1-BuOH	50 mM HPW 1.35 M 2-BuOH	50 mM HPW 2.70 M 2-BuOH	50 mM HPW 0.28 M BnOH	50 mM HPW 0.51 M BnOH
scale	1	1	1	1	1.3029	1.3029	1	1
background	0.035891	0.05	0.048319	0.05	0.047168	0.05	0.03959	0.035
r_effective_model	max outer radius	max outer radius	max outer radius	max outer radius	max outer radius	max outer radius	max outer radius	max outer radius
r_equatorial_core / Å	4.4	4.7	4.6	4.8023	4.5	4.4	4.5042	4.5
x_core (r_polar/r_equatorial_core)	1	1	1	0.9	1	1	1	1
thick_shell (shell thickness equator) / Å	5.2972	11.229	4.1481	13.554	6.7948	16.109	5.2906	11.506
x_polar_shell (shell_polar/shell_equator)	0.79879	0.05	2.1397E-09	2.0918E-08	0.0002	0.00002	6.4933E-08	1.7478E-09
sld_core / 10^{10} cm^{-2}	85	86	86	86	86	90	84.243	86
sld_shell / 10^{10} cm^{-2}	9.25	9.3	9.35	9.4	9.1686	9.3746	10.067	10.418
sld_solvent / 10^{10} cm^{-2}	9.5	9.5	9.5	9.5	9.4	9.5	9.4	9.4
$r_{effective}$ / Å	9.69723975	15.92905	8.7841	18.356651	11.29479	20.5089	9.794864	16.006
Volume fraction	0.06	0.06	0.018	0.075053	0.030492	0.074186	0.027816	0.07
Charge / q	3.3945	3.7696	3.2818	3.5598	4	5.3422	4.5	5
Temperature / K	293	293	293	293	293	293	293	293
c(salt) / M	0.014482	0.012	0.014557	0.024961	0.012405	0.12	0.025599	0.0409
dielectric constant	71	71	71	68	71.08	64	71	70

HSiW

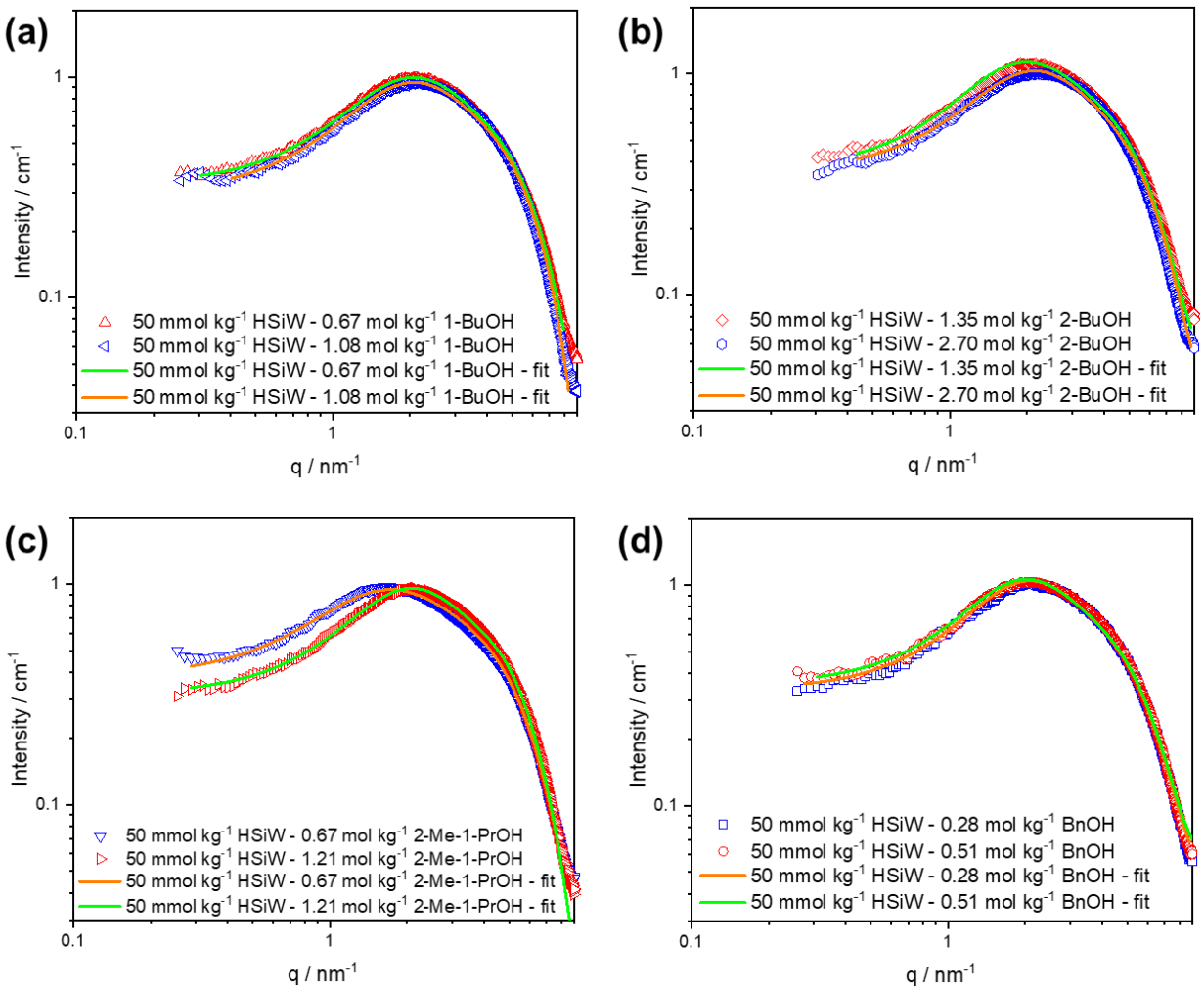

Figure S6.9. SAXS spectra including fits of 50 mmol kg^{-1} HSiW in the presence of (a) 0.67 and 1.08 mol kg^{-1} 1-BuOH, (b) 1.35 and 2.70 mol kg^{-1} 2-BuOH, (c) 0.67 and 1.21 mol kg^{-1} 2-Me-1-PrOH and (d) 0.28 and 0.51 mol kg^{-1} BnOH.

Table S6.5. Fit parameters of the SAXS spectra in Fig. S6.9. M is here used as an abbreviation for mol kg^{-1}.

	50 mM HSiW 0.67 M 2-Me-1-PrOH	**50 mM HSiW 1.21 M 2-Me-1-PrOH**	**50 mM HSiW 0.67 M 1-BuOH**	**50 mM HSiW 1.08 M 1-BuOH**	**50 mM HSiW 1.35 M 2-BuOH**	**50 mM HSiW 2.70 M 2-BuOH**	**50 mM HSiW 0.28 M BnOH**	**50 mM HSiW 0.51 M BnOH**
scale	1	1	1	1	1	1	1	1
background	0.021191	0.014012	0.028085	0.0095921	0.058144	0.041098	0.057302	0.059902
r_effective_model	max outer radius	max outer radius	outer radius	outer radius	outer radius	outer radius	unconstrained	outer radius
r_equatorial_core / Å	4.5	4.4627	4.5	4.5	4.5	4.4	4.5	4.5
x_core (r_polar/r_equatorial_core)	1	1	1	1	1	1	1	1
thick_shell (shell thickness equator) / Å	2.6336	6.6754	1.7332	2.2415	3.9127	3.8806	0.79121	1.3611
x_polar_shell (shell_polar/shell_equator)	0.01125	0.9994	1	1	1	1	1	1
sld_core / 10^{10} cm^{-2}	86	86	80.922	80.922	87	80	76	80.665
sld_shell / 10^{10} cm^{-2}	9.0992	8.9527	9.1237	9.1846	9.0552	9.3	9.7	9.8362
sld_solvent / 10^{10} cm^{-2}	9.3566	9.2551	9.4	9.4	9.2774	9.4	9.46	9.7
$r_{effective}$ / Å	7.133598	11.1380776	6.233163	6.74151559	8.41268	8.280641	5.29121	5.86107944
Volume fraction	0.011748	0.081551	0.016637	0.020932	0.035779	0.044042	0.011	0.013105
Charge / q	4.4932	4	4.4373	4.3103	4.3906	4	4.8908	5.0601
Temperature / K	293	293	293	293	293	293	293	293
c(salt) / M	0.031047	0.062598	0.023479	0.023479	0.023018	0.034618	0.014961	0.022347
dielectric constant	75	75	74.848	74.848	71.08	71.08	71	71

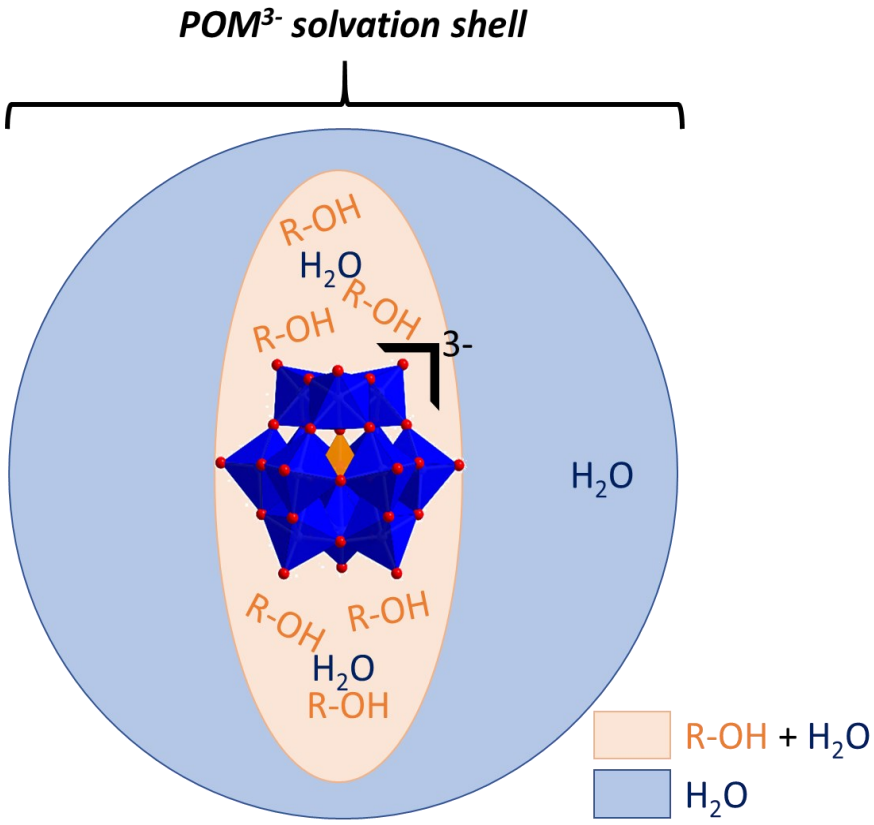

Figure S6.10. Schematic sketch of the POM solvation in the presence of a hydrophobic alcohol.

Figure S6.10 shows a schematic sketch of the POM solvation in mixtures of H_2O and a hydrophobic alcohols. This sketch is deduced from the SAXS fits shown above. The POM (NaPW and HPW) is surrounded by an ellipsoidal solvation shell which is made up from water and the hydrophobic alcohol.

6.6.4 Bathochromic shift of POM-aromatic molecules solutions

Figure S6.11 shows representative ^{1}H- and ^{31}P-NMR spectra of mixtures of NaPW/HPW (100 mmol kg^{-1}) and BnOH (100 mmol kg^{-1}) in aqueous solution (D_2O). Additionally, reference spectra of 100 mmol kg^{-1} NaPW/HPW and 100 mmol kg^{-1} BnOH in D_2O were recorded separately. As described in the manuscript, mixtures of POM and aromatic compounds (here BnOH), lead to a bathochromic shift of the POM absorption spectrum, *e.g.* colorless POM solutions turn yellowish in the presence of BnOH. Hence, the spectra shown in Fig. S6.11 serve here to probe if this color transition is exclusively due to a physical phenomenon (POM-BnOH interaction) and does not emerge due to a chemical reaction. Fig. S6.11a shows the ^{31}P-NMR spectrum of 100 mmol kg^{-1} NaPW in water (dark spectrum) and 100 mmol kg^{-1} NaPW - 100 mmol kg^{-1} BnOH (red spectrum). Indeed, the ^{31}P-NMR spectrum indicates that the POM structure remains intact, as no change in the spectrum of NaPW is obtained by adding BnOH. Figure S6.11b depicts the corresponding ^{1}H-NMR

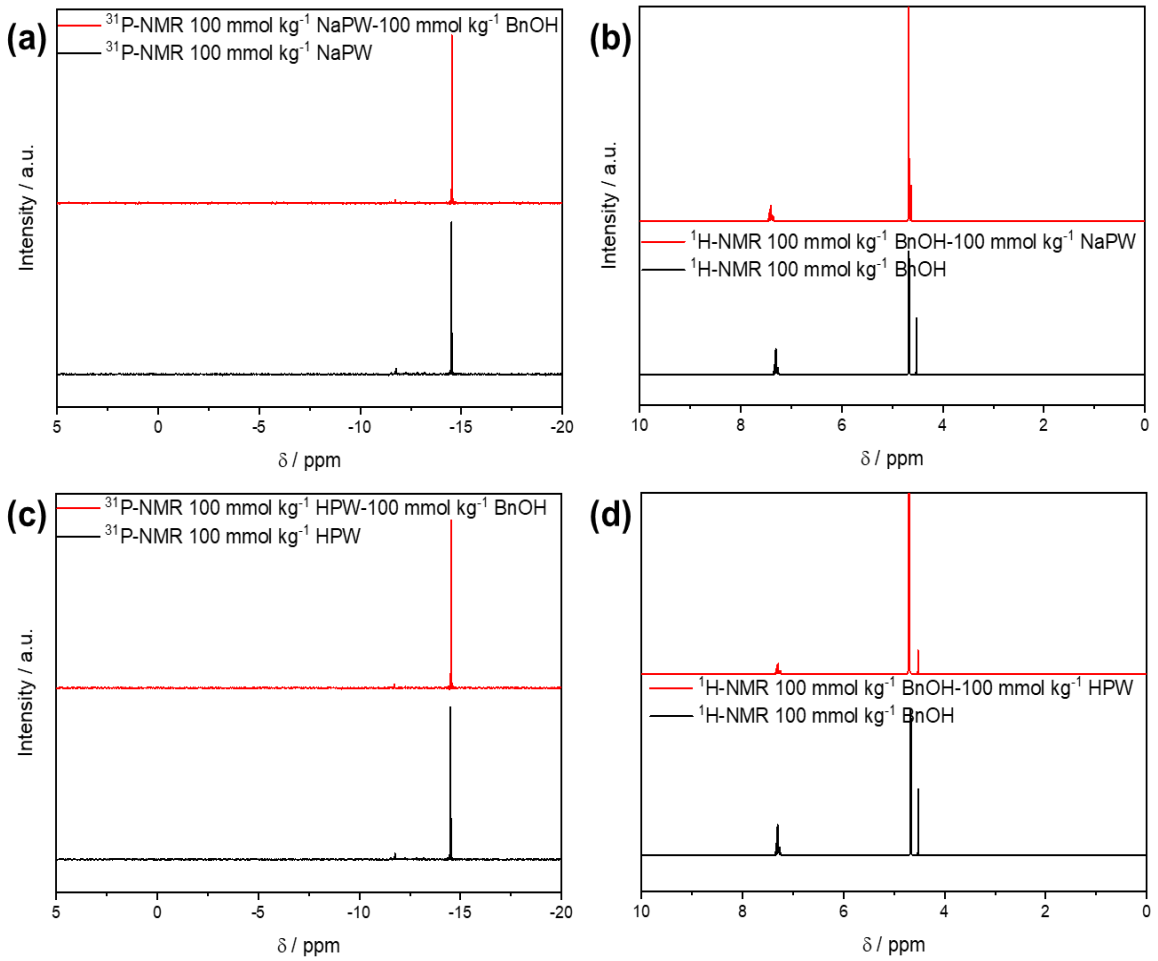

Figure S6.11. (a) ^{31}P-NMR and (b) ^{1}H-NMR spectra of 100 mmol kg^{-1} NaPW - 100 mmol kg^{-1} BnOH with reference spectra, indicating that molecular structures of NaPW and BnOH remain unchanged. (c) ^{31}P-NMR and (d) ^{1}H-NMR spectra of 100 mmol kg^{-1} HPW - 100 mmol kg^{-1} BnOH with reference spectra, indicating that molecular structures of HPW and BnOH remain unchanged. As the molecular structures remain unchanged, we can conclude that the obtained bathochromic shift is only due to the association of the POM with the aromatic alcohol BnOH.

spectra. Also here, the structure of BnOH remains intact upon the addition of NaPW. The same situation is observed for HPW mixtures with BnOH, see Fig. S6.11c (^{31}P-NMR spectra) and Fig. S6.11d (^{1}H-NMR spectra). Finally, we conclude that the bathochromic shift of the POM absorption spectrum is exclusively observed due to a physical phenomenon, *i.e.* the binding of the POM with BnOH.

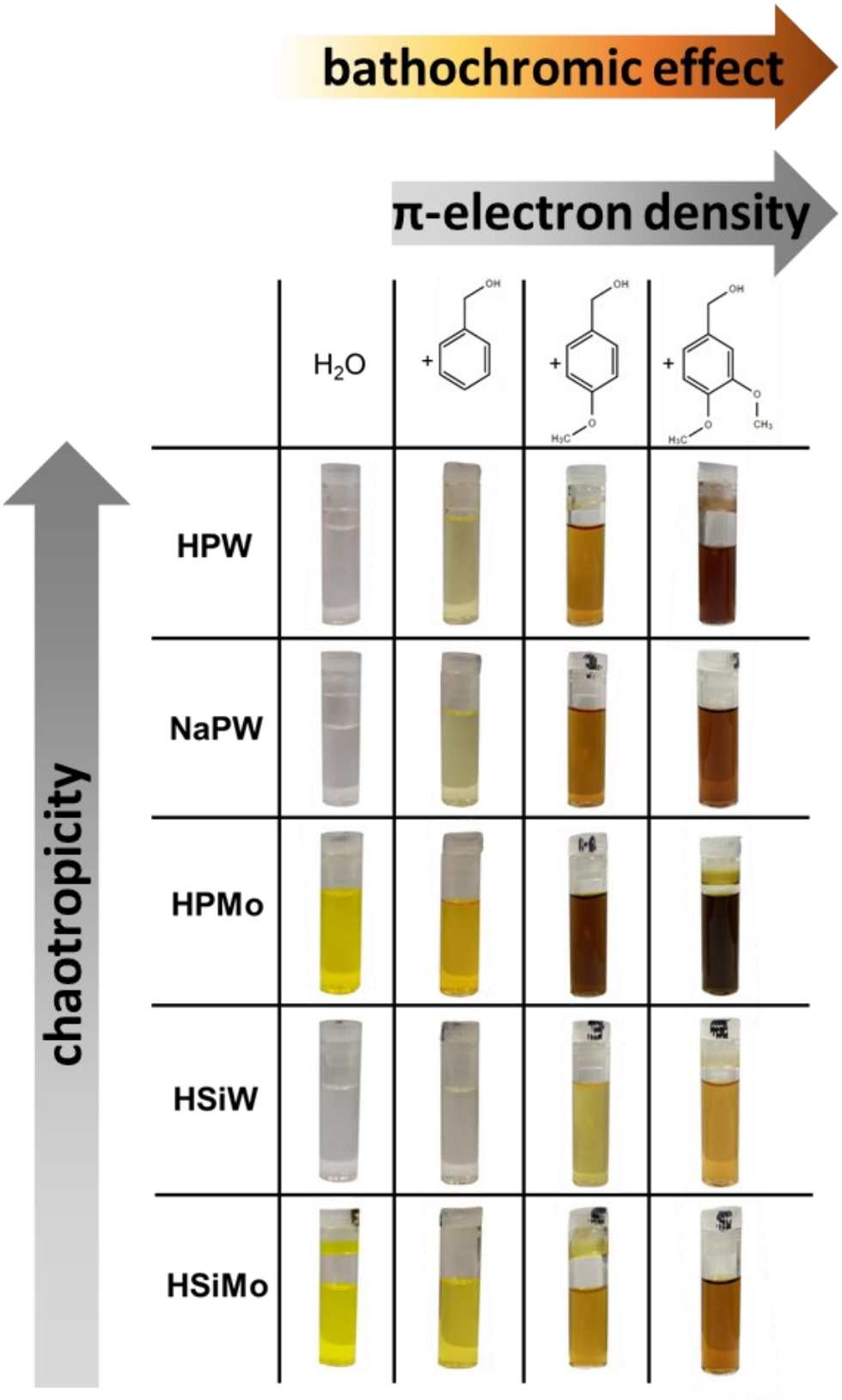

Figure S6.12. Photographs of solutions containing 100 mmol kg^{-1} POM ($H_3PW_{12}O_{40}$ (HPW), $Na_3PW_{12}O_{40}$ (NaPW), $H_3PMo_{12}O_{40}$ (HPMo), $H_4SiW_{12}O_{40}$ (HSiW) and $H_4SiMo_{12}O_{40}$ (HSiMo)) and 100 mmol kg^{-1} of an aromatic alcohol (BnOH, 4-methoxy-BnOH and 3,4-dimethoxy-BnOH) showing the bathochromic effect visually as a function of the chaotropicity of the POM and the π-electron density of the aromatic alcohol.

Figure S6.12 shows photographs of aqueous solutions of 100 mmol kg^{-1} POM ($H_3PW_{12}O_{40}$ (HPW), $Na_3PW_{12}O_{40}$ (NaPW), $H_3PMo_{12}O_{40}$ (HPMo), $H_4SiW_{12}O_{40}$ (HSiW) and $H_4SiMo_{12}O_{40}$ (HSiMo)) in the presence of 100 mmol kg^{-1} of an aromatic alcohol (BnOH, 4-methoxy-BnOH and 3,4-dimethoxy-BnOH) or in water (reference). Therefore, we vary the charge (density) of the POMs: HPW, NaPW and HPMo as threefold negative anions and HSiW and HSiMo as fourfold negative anions, as well as the POM`s polarizability: HPW, NaPW and HSiW with 12 · 74 e^- from W and HPMo and HSiMo with 12 · 42 e^- from Mo. Moreover, we vary the electron density of the aromatic alcohol as methoxy groups (-OMe) are known to be strongly electron-donating. Consequently, the aromatic electron density increases from BnOH over 4-methoxy-BnOH to 3,4-dimethoxy-BnOH.

As an example, the series of HPW is described here: The pure 100 mmol kg^{-1} HPW solution appears colorless. Upon the addition of 100 mmol kg^{-1} BnOH the solution turns yellowish. Adding 100 mmol kg^{-1} 4-methoxy-BnOH leads to an orange color and the addition of 100 mmol kg^{-1} 3,4-dimethoxy-BnOH gives a red to brownish color. Similar conclusions can be drawn for all investigated POMs. Nevertheless, it appears that the bathochromic effect is less pronounced for fourfold charged POMs compared to threefold charged POMs (HSiW/HSiMo *vs.* HPW, NaPW, HPMo) which is likely to arise from their less pronounced superchaotropic character. As a conclusion, we find that the bathochromic shift depends on both, the POM`s charge density, as well as the charge density of the aromatic alcohol. Interestingly, the combination of low charge density POMs and high aromatic charge density leads to the strongest bathochromic shifts.

In the manuscript, we only mentioned that the addition of aromatic alcohols (or in general aromatic molecules, such as toluene) leads to a bathochromic shift of the POM absorption spectrum. Nevertheless, a bathochromic shift can also be obtained by adding an increasing concentration of

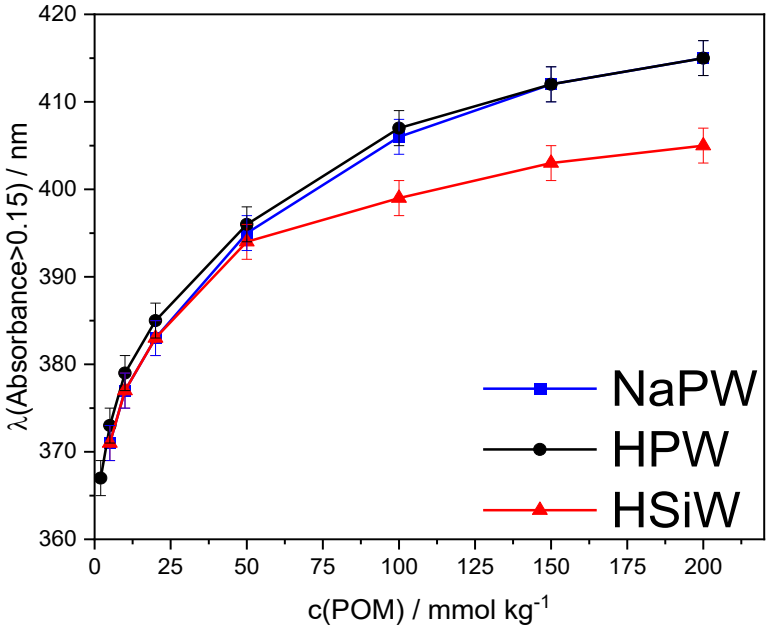

Figure S6.13. Bathochromic shift of 10 mmol kg^{-1} BnOH as a function of POM concentration, *i.e.* NaPW, HPW and HSiW.

POM to a 10 mmol kg^{-1} BnOH solution, see Fig. S6.13. Here, we show that the addition of POM shifts $\lambda_{A>0.15}$ of BnOH towards the visible region, *i.e.* a bathochromic effect appears. Again, the shift is less pronounced for the less superchaotropic HSiW compared to NaPW/HPW. In conclusion, the bathochromic shift of the absorption spectra in solution appears to be additive, *i.e.* as well the addition of BnOH to POM solutions leads to a bathochromic effect as the addition of POM to BnOH solutions.

In a last step, we have chosen four model molecules whose structure is based on toluene, see Fig. S6.14 right. These molecules are toluene, the alcohol benzyl alcohol (BnOH), the aldehyde benzaldehyde and the alcohol cyclohexyl methanol. The solubility limits of this organic compounds in pure water are 0.08 mol kg^{-1} for cyclohexyl methanol, 0.09 mol kg^{-1} for toluene, 0.15 mol kg^{-1} for benzaldehyde and 0.37 mol kg^{-1} for BnOH. In case of cyclohexyl methanol only 0.17 mol kg^{-1} can be solubilized in 200 mmol kg^{-1} NaPW, *i.e.* the solubilization curve remains flat. In case of toluene the solubility increases linearly with increasing NaPW concentrations (0.69 mol kg^{-1} for 200 mmol kg^{-1} NaPW). The solubilization measurement of benzaldehyde shows a similar shape with a solubility limit of 0.94 mol kg^{-1} at 196 mmol kg^{-1} NaPW. In case of BnOH the solubility increases even more drastically with increasing NaPW concentration, leading to 2.65 mol kg^{-1} benzyl alcohol in 200 mmol kg^{-1} NaPW solution. Again, we evaluated the number of solubilized molecules per NaPW (see section 6.6.1, *m* parameter). For cyclohexyl methanol we find 0.4, 3.2 for toluene, 4.1 for benzaldehyde and 10.6 for BnOH, respectively. Consequently, the following trend in the solubilization efficiency of NaPW (or in general a POM) appears: BnOH > benzaldehyde > toluene > cyclohexyl methanol. Therefore, we find several criteria that a hydrophobic molecule must fulfil to be properly solubilized by a POM, *i.e.* heteroatoms (in BnOH and benzaldehyde), π-electron systems

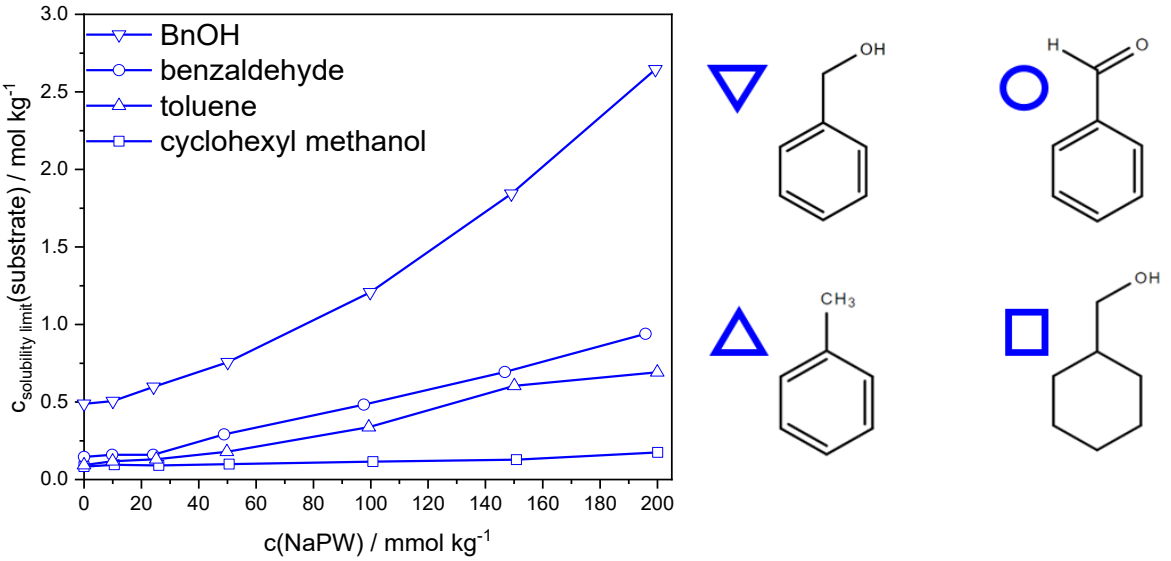

Figure S6.14. Solubilization measurements of benzyl alcohol (BnOH), benzaldehyde, toluene and cyclohexyl methanol as a function of NaPW concentration. The chemical structure formulae are shown on the right and the associated symbol (down-triangle, circle, up-triangle, square) correspond to the symbols in the solubilization measurement graph.

(solubility of toluene), a high solubility of the molecule in pure water (BnOH compared to benzaldehyde or cyclohexyl methanol).

Table S6.6 shows an overview of these four hydrophobic molecules, with several parameters that influence the solubilization performance of POM (here NaPW) and the *m* parameter which represents the solubilization efficiency of the POM. The parameters found in this work, influencing the solubilization efficiency of a certain POM, are the solubility limit of the hydrophobic compound in pure water (the higher the better), the presence of heteroatoms and conjugated π-electron systems. Benzyl alcohol, having a high water solubility, a hetero atom (-OH group) and a conjugated π-system (aromatic) shows the highest solubility increase upon the addition of NaPW, *cf. m* = 10.6. In case of benzaldehyde, the *m* parameter is lower (4.1) as its water solubility is much lower compared to benzyl alcohol. For toluene the *m* parameter is even smaller (3.2) as the solubility in water is smaller (compared to benzyl alcohol and benzaldehyde) and it does not provide a heteroatom. For cyclohexyl methanol the *m* parameter is the smallest (0.4) as it provides low water solubility and no π-system.

Table S6.6. Schematic overview of POM and molecule parameters in order to predict the solubility increase of a molecule upon the addition of NaPW.

substrate	solubility in water / wt%	heteroatom	conjugated π-system	parameter *m*	solubility increase with POMs
benzyl alcohol	5.3	+	+	10.6	very strong
benzaldehyde	1.6	+	+	4.1	strong
toluene	0.9	-	+	3.2	low
cyclohexyl methanol	0.9	+	-	0.4	negligible

6.7 Bibliography

[1] C. A. Lipinski, *J. Pharmacol. Toxicol. Methods* **2000**, *44*, 235–249.

[2] D. F. Veber, S. R. Johnson, H. Cheng, B. R. Smith, K. W. Ward, K. D. Kopple, *J. Med. Chem.* **2002**, *45*, 2615–2623.

[3] P. Degot, V. Huber, E. Hofmann, M. Hahn, D. Touraud, W. Kunz, *Food Chem.* **2021**, *336*, 127660.

[4] A. Shah, S. Shahzad, A. Munir, M. N. Nadagouda, G. S. Khan, D. F. Shams, D. D. Dionysiou, U. A. Rana, *Chem. Rev.* **2016**, *116*, 6042–6074.

[5] K. T. Savjani, A. K. Gajjar, J. K. Savjani, *Int. Sch. Res. Not. ISRN Pharm. Hindawi* **2012**, *2012*, 1–10.

[6] Y. Miyako, N. Khalef, K. Matsuzaki, R. Pinal, *Int. J. Pharm.* **2010**, *393*, 48–54.

[7] M. Yeh, L. Chang, A. H. Chiou, *AAPS PharmSciTech* **2009**, *10*, 166–171.

[8] E. Söderlind, M. Wollbratt, C. Von Corswant, *Int. J. Pharm.* **2003**, *252*, 61–71.

[9] A. Dogra, A. K. Rakshit, *J. Phys. Chem. B* **2004**, *108*, 10053–10061.

[10] W. Kunz, K. Holmberg, T. Zemb, *Curr. Opin. Colloid Interface Sci.* **2016**, *22*, 99–107.

[11] J. Mehringer, W. Kunz, *Adv. Colloid Interface Sci.* **2021**, *294*, 102476.

[12] T. N. Zemb, M. Klossek, T. Lopian, J. Marcus, S. Schöettl, D. Horinek, S. F. Prevost, D. Touraud, O. Diat, S. Marčelja, W. Kunz, *Proc. Natl. Acad. Sci.* **2016**, *113*, 4260–4265.

[13] S. Friberg, *J. Am. Oil Chem. Soc.* **1971**, *48*, 578–581.

[14] K. Uekama, F. Hirayama, T. Irie, *Chem. Rev.* **1998**, *2665*, 2045–2076.

[15] L. W. Doner, G. Bécard, *Biotechnol. Tech.* **1991**, *5*, 28–31.

[16] Chad T. Jafvert, *Technol. Eval. Rep.* **1996**, 1–45.

[17] T. Buchecker, S. Krickl, R. Winkler, I. Grillo, P. Bauduin, D. Touraud, A. Pfitzner, W. Kunz, *Phys. Chem. Chem. Phys.* **2017**, *19*, 1806–1816.

[18] B. Zhu, X. Zhao, T. Gu, *J. Chem. Soc. Faraday Trans.* **1988**, *84*, 3951–3960.

[19] T. Loftsson, A. Magnusdottir, M. Masson, J. Sigurjonsdottir, *J. Pharm. Sci.* **2002**, *91*, 2307–2316.

[20] F. P. Byrne, S. Jin, G. Paggiola, T. H. M. Petchey, J. H. Clark, T. J. Farmer, A. J. Hunt, C. R. Mcelroy, J. Sherwood, *Sustain. Chem. Process.* **2016**, *4*, 1–24.

[21] T. R. Tephlyl, *Life Sci.* **1991**, *48*, 1031–1041.

[22] Y. Wang, Y. Zhang, X. Li, M. Sun, Z. Wei, Y. Wang, A. Gao, *Sci. Rep.* **2015**, *5*, 10107.

[23] M. Lechuga, M. Fernández-serrano, E. Jurado, F. Ríos, *Ecotoxicol. Environ. Saf.* **2016**, *125*, 1–8.

[24] M. Hohenschutz, I. Grillo, O. Diat, P. Bauduin, *Angew. Chem. - Int. Ed.* **2020**, *59*, 8084–8088.

[25] J. J. Borrás-Almenar, E. Coronado, A. Müller, M. Pope, *Polyoxometalate Molecular Science*, Springer, Netherlands, Dondrecht, **2003**.

[26] M. T. Pope, A. Müller, *Angew. Chem. - Int. Ed.* **1991**, *30*, 34–48.

[27] C. Streb, K. Kastner, J. Tucher, *Phys. Sci. Rev.* **2019**, *4*, 1–10.

[28] H. N. Miras, J. Yan, D.-L. Long, L. Cronin, *Chem. Soc. Rev.* **2012**, *41*, 7403–7430.

[29] G. Izzet, F. Volatron, A. Proust, *Chem. Rec.* **2017**, *17*, 250–266.

[30] T. Buchecker, X. LeGoff, B. Naskar, A. Pfitzner, O. Diat, P. Bauduin, *Chem. - A Eur. J.* **2017**, *23*, 8434–8442.

[31] T. Buchecker, P. Schmid, I. Grillo, S. Prévost, M. Drechsler, O. Diat, A. Pfitzner, P. Bauduin, *J. Am. Chem. Soc.* **2019**, *141*, 6890–6899.

[32] M. Hohenschutz, I. Grillo, C. D. Dewhurst, P. Schmid, L. Girard, A. Jonchère, O. Diat, P. Bauduin, *J. Colloid Interface Sci.* **2021**, *603*, 141–147.

[33] B. Naskar, O. Diat, V. Nardello-Rataj, P. Bauduin, *J. Phys. Chem. C* **2015**, *119*, 20985–20992.

[34] K. I. Assaf, M. S. Ural, F. Pan, T. Georgiev, S. Simova, K. Rissanen, D. Gabel, W. M. Nau, *Angew. Chem. - Int. Ed.* **2015**, *54*, 6852–6856.

[35] C. Falaise, M. A. Moussawi, S. Floquet, P. A. Abramov, M. N. Sokolov, M. Haouas, E. Cadot, *J. Am. Chem. Soc.* **2018**, *140*, 11198–11201.

[36] K. I. Assaf, B. Begaj, A. Frank, M. Nilam, A. S. Mougharbel, U. Kortz, J. Nekvinda, B. Grüner, D. Gabel, W. M. Nau, *J. Org. Chem.* **2019**, *84*, 11790–11798.

[37] K. I. Assaf, O. Suckova, N. Al Danaf, V. Von Glasenapp, D. Gabel, W. M. Nau, *Org. Lett.* **2016**, *18*, 932–935.

[38] K. I. Assaf, W. M. Nau, *Angew. Chem. - Int. Ed.* **2018**, *57*, 13968–13981.

[39] Y. Wu, R. Shi, Y. Wu, J. M. Holcroft, Z. Liu, M. Frasconi, M. R. Wasielewski, H. Li, J. F. Stoddart, *J. Am. Chem. Soc.* **2015**, *137*, 4111–4118.

[40] S. Yao, C. Falaise, A. A. Ivanov, N. Leclerc, M. Hohenschutz, M. Haouas, D. Landy, M. A. Shestopalov, P. Bauduin, E. Cadot, *Inorg. Chem. Front.* **2021**, *8*, 12–25.

[41] F. Hofmeister, *Arch. Exp. Pathol. Pharmakol.* **1888**, *25*, 1–30.

[42] W. Kunz, J. Henle, B. W. Ninham, *Curr. Opin. Colloid Interface Sci.* **2004**, *9*, 19–37.

[43] Y. Zhang, P. S. Cremer, *Curr. Opin. Chem. Biol.* **2006**, *10*, 658–663.

[44] T. Buchecker, P. Schmid, S. Renaudineau, O. Diat, A. Proust, A. Pfitzner, P. Bauduin, *Chem. Commun.* **2018**, *54*, 1833–1836.

[45] P. Schmid, T. Buchecker, A. Khoshsima, D. Touraud, O. Diat, W. Kunz, A. Pfitzner, P. Bauduin, *J. Colloid Interface Sci.* **2021**, *587*, 347–357.

[46] M. L. Dekker, M. Clausse, H. L. Rosano, A. Zradba, *Microemulsion Systems, Surfactant Science Ser.*, New York, **1987**.

[47] M. Doucet, J. H. Cho, G. Alina, Z. Attala, J. Bakker, W. Bouwman, P. Butler, K. Campbell, T. Cooper-Benun, C. Durniak, L. Forster, M. Gonzales, R. Heenan, A. Jackson, S. King, P. Kienzle, J. Krzywon, T. Nielsen, L. O'Driscoll, W. Potrzebowski, S. Prescott, R. Ferraz Leal, P. Rozycko, T. Snow, A. Washington, **2020**, doi.org/10.5281/zenodo.3930098.

[48] J. Hansen, J. B. Hayter, *Mol. Phys.* **1982**, *46*, 651–656.

[49] J. B. Hayter, J. Penfold, *Mol. Phys.* **1981**, *42*, 109–118.

[50] G. L. Amidon, S. H. Yalkowsky, S. Leung, *J. Pharm. Sci.* **1974**, *63*, 1858–1866.

[51] S. Banerjee, *Environ. Sci. Technol.* **1984**, *18*, 587–591.

[52] M. K. Bera, B. Qiao, S. Seifert, B. P. Burton-Pye, M. Olvera De La Cruz, M. R. Antonio, *J. Phys. Chem. C* **2016**, *120*, 1317–1327.

[53] A. Chaumont, G. Wipff, *Phys. Chem. Chem. Phys.* **2008**, *10*, 6940–6953.

[54] C. Streb, *Dalt. Trans.* **2012**, *41*, 1651–1659.

[55] B. Qi, S. An, J. Luo, T. Liu, Y.-F. Song, *Chem. - A Eur. J.* **2020**, *26*, 16802–16810.

[56] N. I. Gumerova, A. Rompel, *Chem. Soc. Rev.* **2020**, *49*, 7568–7601.

[57] W. Kunz, *Specific Ion Effects*, World Scientific, Singapore, **2010**.

[58] S. Yao, C. Falaise, S. Khilfi, N. Leclerc, M. Haouas, D. Landy, E. Cadot, *Inorg. Chem.* **2021**, *60*, 7433–7441.

[59] C. Falaise, S. Khilfi, P. Bauduin, P. Schmid, W. E. Shepard, A. A. Ivanov, M. N. Sokolov, M. A. Shestopalov, P. A. Abramov, S. Cordier, J. Marrot, M. Haouas, E. Cadot, *Angew. Chem. - Int. Ed.* **2021**, *60*, 14146–14153.

[60] J. Mohan, *Organic Spectroscopy: Principles and Applications*, Alpha Science, Paris, **2004**.

[61] M. R. Antonio, M. K. Bera, *Eur. J. Inorg. Chem.* **2019**, *2019*, 367–373.

[62] A. Malinenko, A. Jonchère, L. Girard, S. Parrès-Maynadié, O. Diat, P. Bauduin, *Langmuir* **2018**, *34*, 2026–2038.

7 {2-phases 2-reactions 1-catalyst} concept for the sustainable performance of coupled reactions

7.1 Preface and Abstract

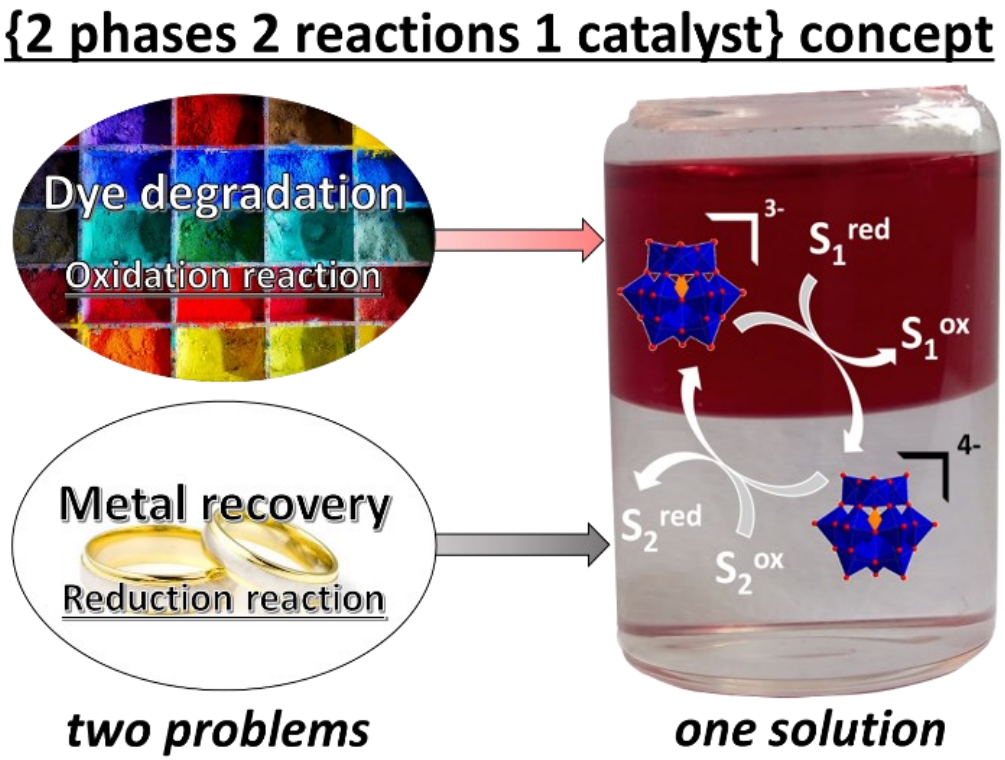

Figure 7.1. Graphical Abstract of the published article in *Green Chemistry*.

This chapter was published in the peer-reviewed Journal *Green Chemistry* of the publisher The Royal Society of Chemistry (RSC, DOI: doi.org/10.1039/D1GC04265C). At this place also the electronic supplementary information (ESI) can be found. Reproduced with permission from RSC. Figures and text may differ from the published version. Several other people contributed to this work:

- Gašper Jošt performed a part of ICP-OES measurements.
- Xaver Graß performed a part of reaction analyses with UV/VIS measurements.
- Dr. Didier Touraud and Dr. Olivier Diat contributed with fruitful discussions and improved the manuscript.
- Prof. Dr. Arno Pfitzner supervised the project, contributed with fruitful discussion, provided resources and improved the manuscript.
- Dr. Pierre Bauduin supervised the project, conceptualized experiments, contributed with fruitful discussion, wrote and improved the manuscript and is corresponding author.
- Philipp Schmid conceptualized experiments, developed an ICP-OES method, performed and analyzed reactions, designed the figures and wrote and improved the manuscript.

Abstract: In the recent years, photoredox chemistry has been intensively investigated due to its sustainability and low energy-cost. Here, we propose a physicochemical concept – called {2-phases 2-reactions 1-catalyst} – to perform two chemical reactions simultaneously with only one catalyst using a liquid-liquid biphasic system. The well-known and commercially available α-Keggin polyoxometalate (POM), $PW_{12}O_{40}^{3-}$, was used as a photocatalyst for oxidizing a hydrophobic compound in an organic phase. The reduced POM, $PW_{12}O_{40}^{4-}$, being more hydrophilic, diffuses then in the aqueous phase where it reduces a hydrophilic compound. After this step, the re-oxidized POM migrates back to the organic phase closing the catalytic cycle. We applied this concept to several basic reactions: oxidations of organic compounds (*e.g.* alcohol to aldehyde), degradation of organic dyes, metal recovery by reduction of metal ions, and *in-situ* metal-organic complexation reactions. This concept is proposed as a powerful, simple and sustainable tool to couple diverse photo-oxidation/reduction reactions. As an example, oxidative dye degradation/metal (silver) recovery were performed using this general methodology. The main advantage of the {2-phases 2-reactions 1-catalyst} concept is the economy of one reactor and one catalyst, including its self-regeneration by another useful reaction.

7.2 Introduction

Polyoxometalates (POMs) are nanometric anionic metal-oxo clusters which consist of condensed polyhedral transition metal-oxo (mainly group V and VI metals) units and often incorporate a (centered) heteroatom-oxo (*e.g.* B, Al, Si, Ge, P, *etc.*) unit.[1,2] Owing to their electronic and architectural versatility, they are widely used in diverse research fields and applications, such as biology,[3,4] protein crystallography,[5] medicine[6] and molecular and composite materials.[7–9] Additionally, POMs are well-known catalysts in diverse catalysis processes, ranging from acid- and redox-catalysis to multifunctional catalysis.[10,11] Especially photocatalysis – initiated by (visible) light – has gained high interest in the recent years owing to its simplicity and low energy cost.[12] Indeed, POMs (in aqueous solution) are also widely used as photocatalysts, as they can be transferred into redox-active species by excitation with a photo-stimulus, see scheme 7.1.[13,14] Typically, excitation of fully oxidized POMs is achieved with light between 200-500 nm.[15] Irradiation leads to an intramolecular charge transfer from the O^{2-}-based highest occupied molecular orbital (HOMO) to the W^{6+}-based lowest unoccupied molecular orbital (LUMO).[16] The excited POM can consecutively initiate oxidation of a substrate ($Substrate^1_{red}$ to $Substrate^1_{ox}$) by being reduced. This reduced POM species, on the contrary, can catalyze a reduction reaction ($Substrate^2_{ox}$ to $Substrate^2_{red}$), while the POM is re-oxidized in order to close the catalytic cycle.[17] A detailed description of catalytic POM-cycles is given by *e.g.* Papaconstantinou *et al.*[18]

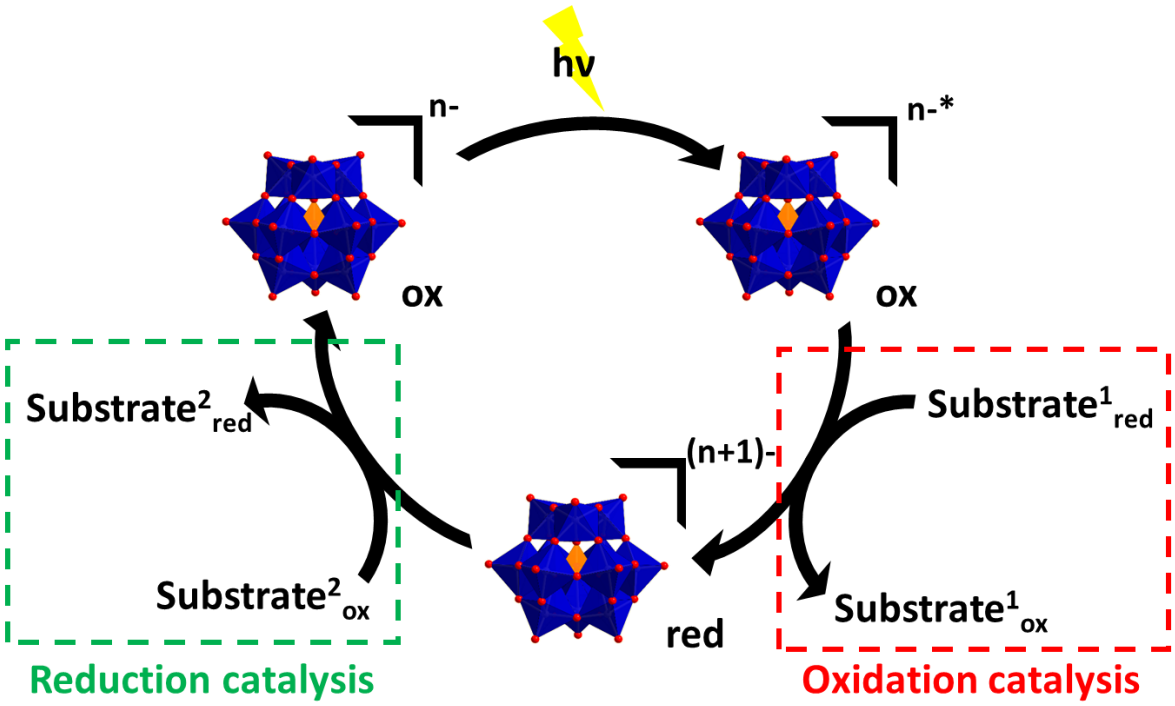

Scheme 7.1. Classical photocatalytic cycle of an α-Keggin POM. By irradiation with *hv*, the fully oxidized POM turns into an exited state, which can catalyze an oxidation reaction, while it is reduced. The reduced POM can consecutively catalyze a reduction, while the POM itself is re-oxidized closing the catalytic cycle.

Low charge density POMs were recently found to interact strongly with (hydrated) macroscopic polar surfaces in foams,[19,20] oligo- and polymers,[21,22] macrocyclic molecules,[23–26] non-ionic surfactants[27,28] and small aromatic molecules[29] in aqueous solution. This phenomenon was proposed to arise from the dehydration of the POM as well as the (molecular) surface of the interacting molecule – a phenomenon called the (super-)chaotropic effect.[19,30,31] It is worth to note that similar observations have also been made for low charge density anionic boron cluster.[28,32–35] Interestingly, Nau and colleagues classified threefold negatively charged α-Keggin POMs, such as $PW_{12}O_{40}^{3-}$ (PW), to be on the border between superchaotropic and hydrophobic anions.[36] Indeed, PW, and other very low charge density POMs, were found to enter the hydrophobic cavity of cyclodextrin cages in aqueous solution.[23–25] Our group proposed that PW mainly distributes to the hydrophobic pseudo-phase of a bicontinuous microemulsion.[37] The hydrophobic character of PW manifests in its ability to self-assemble in pure water, analogously to surfactants and hydrophobic ions.[38–42] It is noteworthy that the higher charged homologue, $SiW_{12}O_{40}^{4-}$ (SiW), compared to PW, does not self-assemble in water as a result of its less pronounced hydrophobic character.

Here, we exploit the photocatalytic activity of POMs to change their global charge and therefore their distribution in a liquid-liquid water:hydrophobic alcohol (1-hexanol, 1-octanol and 2-methyl-2-hexanol) system. We show that oxidized PW distributes mainly in the organic phase in a biphasic system whereas its reduced form, $PW_{12}O_{40}^{4-}$, mainly distributes in the water phase. This opposite

distribution of $PW_{12}O_{40}^{3-}$ and $PW_{12}O_{40}^{4-}$ between the water and alcohol phases enables to perform separately oxidation and reduction in the two phases with only one common catalyst. Accordingly, a {2-phases 2-reactions 1-catalyst} concept is here established and exemplified with different chemical reactions: oxidations of organic compounds (*e.g.* alcohol to aldehyde), degradation of organic dyes, metal recovery by reduction of metal ions, and metal-organic complexation reactions. We monitor the POM-distribution with inductively coupled plasma-optical emission spectroscopy (ICP-OES) and investigate the PW oxidation state by ^{31}P-nuclear magnetic resonance (^{31}P-NMR). Reactions are followed by ultraviolet-visible (UV-VIS) and ^{1}H-NMR spectroscopy.

7.3 Experimental section

Materials. Phosphotungstic acid hydrate ($H_3PW_{12}O_{40}$, MW = 2880 g/mol, 99.995% purity), silicotungstic acid hydrate ($H_4SiW_{12}O_{40}$, MW = 2878 g/mol) and sodium phosphotungstate ($Na_3PW_{12}O_{40}$, MW = 2946 g/mol) were purchased from Sigma Aldrich and used without further purification. Hydrochloric acid was purchased from Fischer Scientific. The hydrophobic alcohols 1-Hexanol, 1-Octanol and 2-Methyl-2-Hexanol were also purchased from Sigma Aldrich. The reaction chemicals benzyl alcohol, Disperse Red-13, $AgNO_3$ and $FeSO_4$ were obtained from Sigma Aldrich and used without further purification. $FeCl_3$ was purchased from Merck. (1,10)-phenanthroline was obtained from TCI Chemicals. ICP-OES standards were purchased from Bernd Kraft, Laborchemikalien. Milli-Q water was used with a conductivity lower than 10.5 µS/cm and a total organic carbon content of 400 ppb.

Sample preparation and distribution/reaction processes. The preparation of samples to determine the distribution coefficient followed a systematic procedure:

1) Aqueous stock solutions (concentration between 0 and 20 mmol L^{-1}) of POM (+ additive) have been prepared. In order to precisely determine the POM concentration, a sample was taken, properly diluted and the concentration was analyzed with inductively coupled plasma-optical emission spectroscopy (ICP-OES).
2) 0.5 mL of the stock solutions were prepared into a 2 g reaction container (safe-lock Eppendorf cone).
3) 0.5 mL of an organic alcohol (1-hexanol, 1-octanol, 2-methyl-2-hexanol) were added to the reaction container.
4) In order to increase the interface of the aqueous phase and the alcohol phase, the samples were shaken vigorously for three minutes.
5) The samples were set on the laboratory bench for five minutes to achieve macroscopic phase separation.

6) A sample of the aqueous phase was taken, properly diluted and the concentration was analyzed with ICP-OES.

The preparation of all syntheses followed a systematic procedure:

1) Aqueous stock solutions (concentration: 10 or 5 mmol L^{-1}) of POM (+ hydrophilic starting material for reactions) have been prepared.
2) 0.5 mL of the stock solutions were prepared into a lockable 7 g reaction glass container.
3) Stock solutions of an alcohol (+ hydrophobic starting material for reaction) have been prepared.
4) 0.5 mL of the organic alcohol stock solution were added to the reaction container.
5) A magnetic stirring bar was set into the glass container and the glass container was put on a magnetic stirrer (*ca.* 400 rpm).
6) A UV analysis lamp from Herolab GmbH, with a power of 6 W was used to initiate the different reactions. The excitation wavelength was in the near UV-region, *i.e.* with a monochromatic wavelength of 365 nm. The cylindrical lamp (length approximately 25 cm) was fixed in a special lamp holder. The lamp holder, including the lamp, were set close to the samples in a distance of approximately 2.5 cm. The length of 25 cm allows to perform multiple reactions (*ca.* 10) simultaneously in the used 7 g reaction glass container, guaranteeing the same flux of photons hitting a sample.
7) After fixed reaction times, samples were taken and the reactions were analyzed via UV/VIS spectrometry (DR-13 recovery, Ag recovery, ferroin formation), ^{1}H-NMR (benzyl alcohol oxidation) or XRPD (dried Ag).

Quantitative analyses.

Extraction process (Distribution coefficient determination)

The distribution coefficient $log\ (K_D^X)$ of a compound *X* between an aqueous phase (aq.) and an organic phase (org.) can be described as

$$log\ (K_D^X)\ =\ log\ (\frac{c_{X,org.}}{c_{X,aq.}}). \tag{7.1}$$

As we only analyzed the concentrations in the aqueous phase this term is extended to

$$log\ (K_D^X) = log\ (\frac{c_{0X} - c_{X,aq,after\ extraction.}}{c_{X,aq,after\ extraction.}}) \tag{7.2}$$

with c_{0X} being the initial concentration of X in the aqueous phase. All distribution coefficients in the manuscript and the supporting information were calculated with equation 7.2.

Reaction analyses

All performed reactions were analyzed (semi-)quantitatively. Here, we describe the analysis progress step by step.

(i) Benzyl alcohol oxidation

In a first reaction we oxidized benzyl alcohol to benzaldehyde. Benzyl alcohol and benzaldehyde produce a characteristic multiplet (arising from the protons in the benzyl moiety) around 7.3 ppm in ^{1}H-NMR. Moreover, benzyl alcohol gives a singlet (stemming from the CH_2 group around 4.6 ppm, whereas benzaldehyde produces a singlet (stemming from the H bound to the aldehyde functional group) around 10 ppm. ^{1}H-NMR allows to quantify the concentration of different protons by integrating NMR signals. Hence, samples were taken after certain reaction times, the characteristic peaks at 4.6 ppm (benzyl alcohol) and 10 ppm (benzaldehyde) were integrated and the quotient

$$\frac{c_{10\ ppm}}{c_{4.6\ ppm} + c_{10\ ppm}} = \frac{c_{benzaldehyde}}{c_{benzyl\ alcohol,initial}} \quad (7.3)$$

was calculated and informed quantitatively on the generation of benzaldehyde from benzyl alcohol.

(ii) DR-13 degradation

DR-13 produces a λ_{max} around 520 nm in UV/VIS spectroscopy. UV/VIS spectroscopy is known to follow Lambert-Beer`s law and we can conclude on the DR-13 degradation by following the decreasing absorbance at λ_{max} with time. Consequently, we tracked the absorbance at 520 nm and calculated the degradation of DR-13.

(iii) Ag recovery

As proposed by Troupis *et al.* the recovery of Ag from Ag^{+} leads to an increased solution turbidity, as Ag particles are formed.[43] Next to specialized turbidimetry, classical UV/VIS spectrometry serves well to follow turbidity, as the basic absorbance level is elevated due to scattering and absorption. Absorbances were recalculated with dilution factors of the measured samples. Next to this semi-quantitative analysis XRPD was carried out on the dried Ag.

(iv) Ferroin complexation

Owing to its red color (with Fe^{2+} as metal center), ferroin produces a λ_{max} around 526 nm in UV/VIS spectroscopy. UV/VIS spectroscopy is known to follow Lambert-Beer`s law and we can conclude on the ferroin formation by following the increasing absorbance at λ_{max} with time. Consequently, we tracked the absorbance at 526 nm and calculated the formation of ferroin. The total conversion (100 % formation) was established by using 0.5 mmol kg^{-1} (1,10)-phenanthroline in the organic phase (1-OctOH) and 2 mmol L^{-1} $Fe^{II}SO_4$.

^{1}H-nuclear magnetic resonance (^{1}H-NMR). Solution ^{1}H-NMR spectra were recorded (at room temperature) with an Avance300 (Bruker) spectrometer using tetramethyl silane as an internal standard. Chemical shifts (δ) are provided in parts per million (ppm) and coupling constants (J) are reported in Hertz (Hz). $CDCl_3$ was used as solvent.

^{31}P-nuclear magnetic resonance (^{31}P-NMR). Solution ^{31}P-NMR spectra were recorded (at room temperature) with an Avance400 (Bruker) spectrometer using 85 % phosphoric acid as an internal

standard. Chemical shifts (δ) are provided in parts per million (ppm) and coupling constants (J) are reported in Hertz (Hz). D_2O and $CDCl_3$ were used as solvent.

UV/VIS measurements. UV/VIS measurements were carried out (at room temperature) on an Infinite M Nano+ from Tecan Trading AG. The measurements were executed in 1 cm quartz glass cuvettes and the samples were appropriately diluted with acetone (organic phase analysis) and water (aqueous phase analysis) and the absorption was therefore recalculated. Appropriate background samples were automatically subtracted.

Inductively coupled plasma-optical emission spectroscopy (ICP-OES). An ICP spectrometer, Ametek, Spectro, Spectroblue, was used to determine metal concentrations in aqueous solution. Therefore, calibration curves were established using ICP-OES standards from Bernd Kraft, Laborchemikalien. The samples were appropriately diluted with milli-Q water or HNO_3 solution and measured.

X-ray powder diffraction (XRPD). XRPD measurements were carried out with a STOE Stadi P diffractometer with monochromatic Cu-$K_{\alpha1}$ radiation (λ = 0.154 nm, Ge monochromator, Mythen 1K detector). The Ag-sample was measured at room temperature in a sealed glass capillary (1 mm) in a 2Θ range from 10 to 80 °.The WinXPow software was used to process the data.[44]

pH measurements. pH measurements were performed with a conventionally calibrated pH meter from Schott Instruments Analytics (ProLab 2000). Recalculation of $c(H^+)$ allowed to determine the distribution of H^+ in a biphasic system.

7.4 Results and Discussion

7.4.1 Distribution of α-Keggin POMs in biphasic water:alcohol systems

Different biphasic systems were investigated, with water being one phase and a water-immiscible alcohol the second phase. We use 1-hexanol (1-HexOH), 1-octanol (1-OctOH) and 2-methyl-2-hexanol (2-Me-2-HexOH) as a second phase. The solubility of these alcohols in water is very small: 0.6 % (w:w) 1-HexOH, 0.05 % (w:w) 1-OctOH[45] and 0.8 % (w:w) 2-Me-2-HexOH (experimentally determined according to a procedure of Clausse *et al.*[46]). The solubility of water in the most hydrophilic alcohol 1-HexOH is 6.8 % (w:w) and therefore the mutual solubility of water with these alcohols is limited.[47]

Figure 7.2a shows the distribution coefficient of PW, $log\ (K_D^{PW})$ = $log\ (\frac{c(PW)_{org.}}{c(PW)_{aq.}})$, as a function of the initial PW (in its acidic form ($H_3PW_{12}O_{40}$, HPW)) concentration in the aqueous phase, called c_0. The concentration of PW in each phase was determined at equilibrium after extraction with ICP-OES. As the $log\ (K_D^{PW})$ is presented logarithmically, a negative $log\ (K_D^{PW})$ indicates the

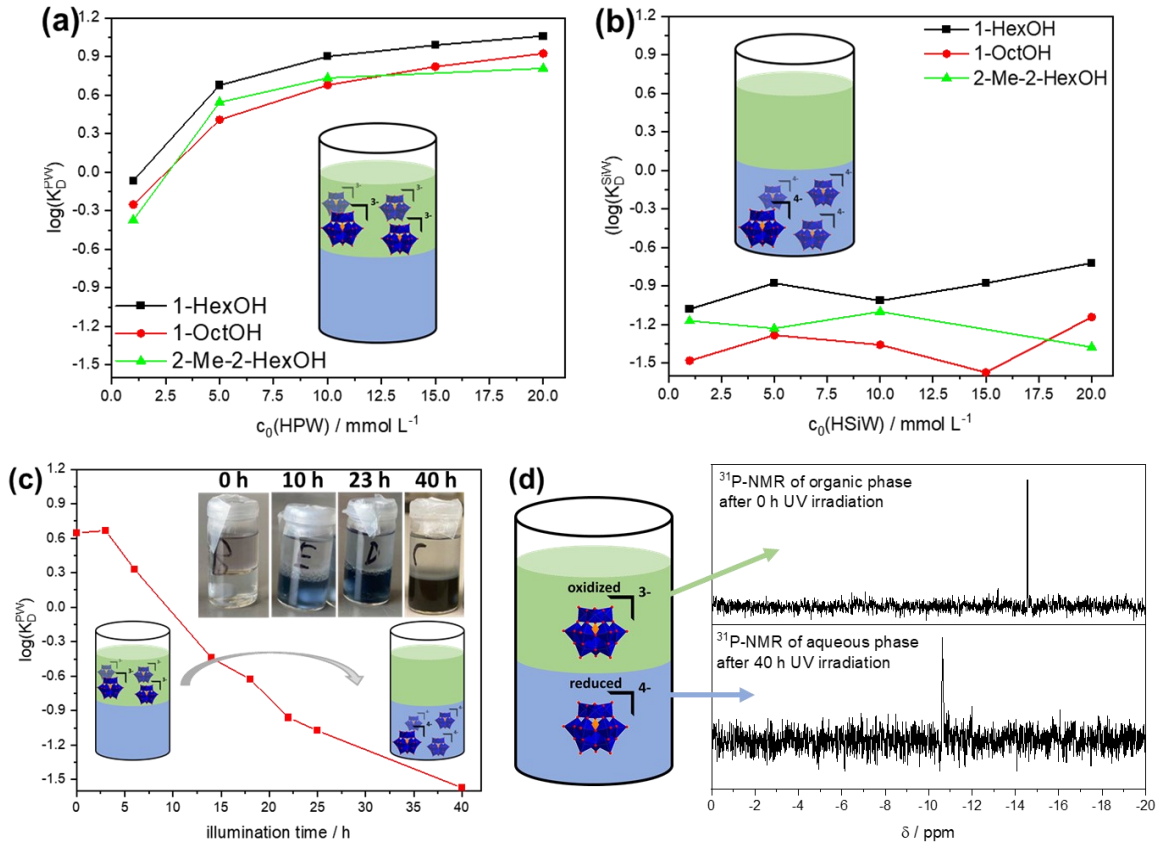

Figure 7.2. Distribution of (a) $H_3PW_{12}O_{40}$ (HPW) and (b) $H_4SiW_{12}O_{40}$ (HSiW) between water and an organic alcohol phase. HPW (POM^{3-}) shows a high affinity for the organic phase whereas HSiW (POM^{4-}) mainly distributes in the aqueous phase. (c) Evolution of 10 mmol L^{-1} HPW distribution in water:1-OctOH as a function of UV illumination (λ = 365 nm). The inlet shows photographs of the water:alcohol system after 0, 10, 23 and 40 h UV illumination. The deep blue color of the aqueous phase indicates the presence of the one-electron reduced $PW_{12}O_{40}^{4-}$. (d) Illustration of the separation of oxidized $PW_{12}O_{40}^{3-}$ in the organic phase and reduced $PW_{12}O_{40}^{4-}$ in the aqueous phase and the corresponding ^{31}P-NMR spectra.

preferred distribution in the aqueous phase, whereas a positive $log\ (K_D^{PW})$ indicates the preferred distribution to the organic phase. The distribution coefficient of HPW to 1-HexOH increases strongly up to 0.67 for c_0(HPW) up to 5 mmol L^{-1}. For c_0(HPW) > 5 mmol L^{-1} the distribution remains rather constant between 0.67 and 1.06. Similar conclusions can be drawn for the distribution of HPW with 1-OctOH and 2-Me-2-HexOH, as the curves nearly overlap with the data obtained for 1-HexOH. As a summary, PW (in its acidic form) distributes mostly in the organic phase, see sketch in Fig. 7.2a. The increase of the distribution coefficient as a function of c_0 is attributed here to the increase of the solution`s acidity, as HPW is a strong acid. This is confirmed in Fig. S1 (ESI), which shows the distribution of 10 mmol L^{-1} HPW to the 1-OctOH phase as a function of inorganic strong acid/base (HCl/LiOH, NaOH) concentration. Interestingly, the addition of HCl strongly promotes the PW distribution in the organic phase: ($log\ (K_D^{PW})$ increases from 0.67 to 1.6 upon the addition of 200 mmol L^{-1} HCl), whereas adding LiOH/NaOH leads to a strong decrease in the distribution coefficient (from 0.67 to approximately -1.25 upon the addition of 100 mmol L^{-1} LiOH/NaOH). Even

though HPW acts as a strong acid in water,[1] it was proposed that in highly acidic media, protons are in the close environment of PW, *i.e.* they form (partially) condensed ion-pairs.[38,40] This counter-cation condensation suggests that the PW`s effective charge decreases, leading to a stronger hydrophobic character. The addition of a base, in contrast, is known to lead to the PW`s decomposition as PW is only stable at high acidities (pH < 2.5).[48,49] The decomposition products of PW (*e.g.* lacunary POMs, PO_4^{3-} and WO_4^{2-}) exhibit a higher charge density with a higher hydrophilicity and consequently a lower distribution coefficient to hydrophobic alcohols.

The distribution coefficient of SiW, $log\ (K_D^{SiW})$, in its acidic form ($H_4SiW_{12}O_{40}$, HSiW), is shown in Fig. 7.2b for the different alcohols. SiW mainly distributes in the water phase, with distribution coefficients between -0.7 < $log\ (K_D^{SiW})$ < -1.6 for 0 ≤ c_0(HSiW) ≤ 20 mmol L^{-1}, see sketch in Fig. 7.2b. As a conclusion, PW (POM^{3-}) mainly distributes in the organic phase ($log\ (K_D^{PW})$ around 0.7), whereas SiW (POM^{4-}) mainly distributes in the aqueous phase ($log\ (K_D^{SiW})$ around -1.2). The type of alcohol (1-HexOH, 1-OctOH, 2-Me-2-HexOH) has here no significant effect on the POM distribution coefficient.

As a next step, we investigate the effect of UV-illumination on the distribution coefficient of PW. The $log\ (K_D^{PW})$ for c_0(HPW) = 10 mmol L^{-1} with 1-OctOH for different illumination times with a UV-lamp (λ = 365 nm), is shown in Fig. 7.2c. In the starting system (t = 0 h), PW distributes mostly in the 1-OctOH phase ($log\ (K_D^{PW})$ = 0.67). After a first period of 4 h, where $log\ (K_D^{PW})$ remains constant, $log\ (K_D^{PW})$ decreases continuously down to -1.6 within around 40 h. Therefore, PW is nearly fully transferred to the aqueous phase upon UV-illumination. As stated in the introduction, PW is known to photo-catalyze the oxidation of primary and secondary alcohols, here 1-OctOH.[50] By illuminating the biphasic system, a part of 1-OctOH (being in large excess) is oxidized and PW, *i.e.* $PW_{12}O_{40}^{3-}$, is reduced to $PW_{12}O_{40}^{4-}$. Note that the samples were kept in closed vials to avoid reoxidation of $PW_{12}O_{40}^{4-}$ by air/oxygen. At initial conditions (t = 0 h), ^{31}P-NMR reveals a singlet peak at -14.6 ppm which is the characteristic chemical shift of phosphorus in $PW_{12}O_{40}^{3-}$,[51] see top spectra in Fig. 7.2d (spectrum taken from organic phase). After 40 h, one peak is observed at -10.6 ppm in the ^{31}P-NMR spectrum of the aqueous phase indicating the presence of the one-electron reduced species, $PW_{12}O_{40}^{4-}$, see bottom spectrum in Fig. 7.2d.[51,52] The formation of $PW_{12}O_{40}^{4-}$ is further supported as the aqueous phase appears deeply blue after 40 h, see Fig. 7.2c inlet. The distribution coefficient of $PW_{12}O_{40}^{4-}$ (POM^{4-}) to the alcohol phase is around -1.6. Therefore, the distribution coefficient of $PW_{12}O_{40}^{4-}$ is comparable as for $SiW_{12}O_{40}^{4-}$, $log\ (K_D^{SiW})$ = -1.4 at c_0(HSiW) = 10 mmol L^{-1}, see Fig. 7.2b, which is not surprising as $SiW_{12}O_{40}^{4-}$ and $PW_{12}O_{40}^{4-}$ have the same charge and (nearly) the same size.

The kinetics is rather slow (full phase transfer within 40 h). Here, the kinetics are composed of two contributions: *(i)* the photoreduction of $PW_{12}O_{40}^{3-}$ to $PW_{12}O_{40}^{4-}$ and *(ii)* the phase migration of

$PW_{12}O_{40}^{4-}$. The reduction of $PW_{12}O_{40}^{3-}$ is mainly controlled by the flux of photons, which are exposed to the sample and taken up by the POM. In our case the UV-source is a standard UV-lamp, see section S7 (ESI). Hence, the reaction kinetics are slow compared to the usage of high-power UV-lamps. Moreover, $PW_{12}O_{40}^{3-}$ is well-known to show rather slow reaction kinetics. The phase migration of $PW_{12}O_{40}^{4-}$ is proportional to the surface area of 1-OctOH and water interface, which is very small in a macroscopically demixed system as presented here. Combining both, *(i)* the reaction kinetics and *(ii)* the migration flux, leads to a slow overall kinetic process.

In summary, the fully oxidized $PW_{12}O_{40}^{3-}$ distributes mostly in the organic phase whereas $PW_{12}O_{40}^{4-}$ distributes in the aqueous phase. This allows to separate oxidizing POM species and reducing POM species in two macroscopic phases, see Fig. 7.2d.

7.4.2 Oxidation in the organic phase: Organic synthesis

At this point, we have a system that enables us to separate oxidizing and reducing environments with only one catalyst. In the following, we use this system to exemplify our {2-phases 2-reactions 1-catalyst} concept with several standard chemical reactions.

As a first reaction, the oxidation of benzyl alcohol (initial concentration $c_{org.\ phase}$(benzyl alcohol) = 20 mmol kg^{-1}) to benzaldehyde, in the organic phase is probed. To avoid a competitive reaction, 2-Me-2-HexOH, a tertiary alcohol, is chosen as organic solvent. The moderate hydrophobicity of benzyl alcohol guarantees its preferential distribution in the organic phase.[53] c_0 = 10 mmol L^{-1} of the catalyst HPW was used. Reoxidation of $PW_{12}O_{40}^{4-}$ in the aqueous phase was

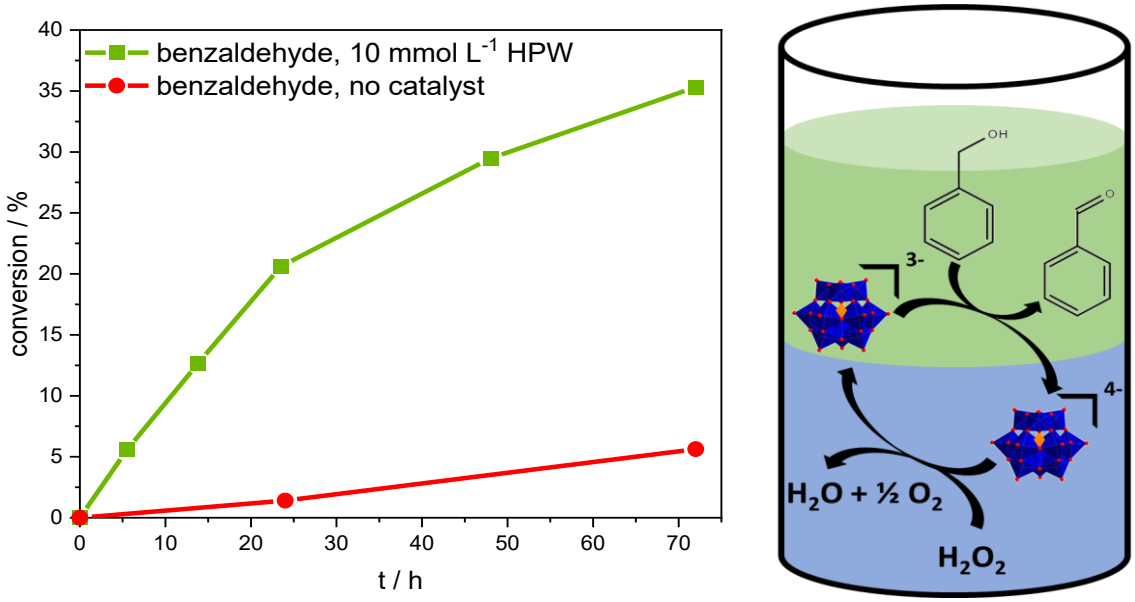

Figure 7.3. Photooxidation of benzyl alcohol to benzaldehyde in the organic phase (2-Me-2-HexOH) as a function of illumination time. The catalytic cycle is closed by H_2O_2 reduction in the aqueous phase.

performed by using H_2O_2 (100 mmol L^{-1}, highly hydrophilic[54]) in order to close the catalytic cycle, shown in the sketch in Fig. 7.3. The equation of the reaction is presented below (with Ph being the phenyl moiety C_6H_5):

Ox.:	$PhCH_2\text{-}OH \rightarrow PhCHO + 2e^- + 2H^+$
Red.:	$H_2O_2 + 2H^+ + 2e^- \rightarrow 2H_2O$
Redox:	$PhCH_2\text{-}OH + H_2O_2 \rightarrow PhCHO + 2H_2O$

The conversion of benzyl alcohol to benzaldehyde in the organic phase is shown as a function of UV-illumination (λ = 365 nm) time in Fig. 7.3, green data. Within 72 h, a conversion of 35 % can be achieved. For details on the conversion calculation see section S2 (ESI). The oxidation of benzyl alcohol with POMs is known to be rather slow.[55] It is noteworthy that In absence of HPW, on the contrary, only 5 % benzyl alcohol can be converted within 72 h, see Fig. 7.3, red data. As a conclusion, oxidation of an aromatic alcohol to the corresponding aldehyde is performed in the organic phase using H_2O_2 in the aqueous phase. It is likely that diverse POM-mediated organic syntheses, such as epoxidations, oxidation of alkanes, arenes and sulfur-containing compounds and many more[50] can be similarly executed.

7.4.3 Oxidation in the organic phase: Degradation of dyes

Dyes may be harmful to living systems, as they may be toxic, mutagenic and carcinogenic.[56] Consequently, the degradation of dyes is a challenging problem, that we tackle in the present biphasic reaction system. In the present study we neglect that in certain cases the degradation

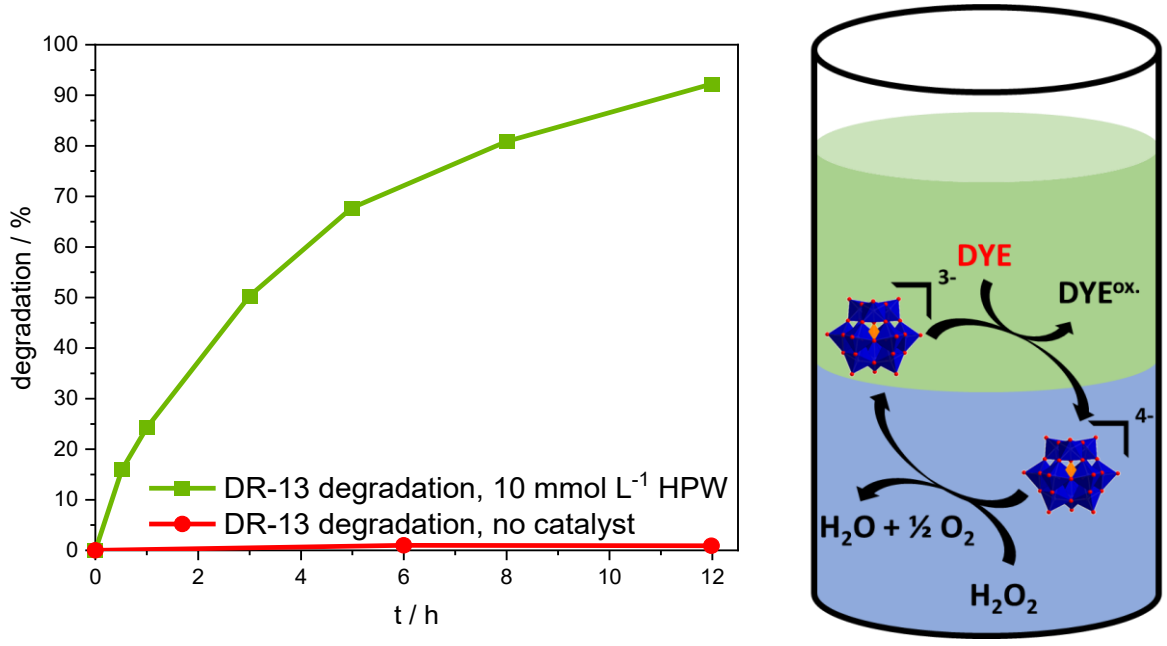

Figure 7.4. Photodegradation of DR-13 via oxidation in the organic phase (2-Me-2-HexOH) as a function of illumination time. The catalytic cycle is closed by H_2O_2 reduction in the aqueous phase.

products of dyes may be even more toxic than the dye itself. As an example, the oxidative degradation of the hydrophobic azo-dye Disperse Red-13 (DR-13)[57] is investigated here. The oxidation of the functional azo group cleaves a C-N- or N-N-bond, leading to diverse non-VIS absorbing products.[58] It is worth to note that azo-dyes may also be degraded reductively by POMs.[59,60]

Here, the initial DR-13 concentration was $c_{org.\ phase}$(DR-13) = 1 mmol kg^{-1}. Again, we have chosen HPW as a catalyst (c_0 = 10 mmol L^{-1}). H_2O_2 at 100 mmol L^{-1} in the aqueous phase was used to close the catalytic cycle. 2-Me-2-HexOH was used as organic phase to avoid competitive oxidation reactions. The reaction container was illuminated with UV-light (λ = 365 nm). The reaction cycle is schematically shown in Fig. 7.4, sketch and see the reaction equation:

Ox.:	"Dye → Dye^{ox} (diff. products) + $2H^+$ + $2e^-$"
Red.:	H_2O_2 + $2H^+$ + $2e^-$ → $2H_2O$
Redox:	Dye + H_2O_2 → Dye^{ox} + $2H_2O$

Figure 7.4 shows the degradation of DR-13 as a function of illumination time, see Fig. S3 (ESI). The degradation yield (defined as the decrease in DR-13 concentration deduced from the decrease in the absorption at λ_{max} of DR-13) is 93 % after 12 h reaction time (Fig. 7.4, green data). As a reference, the same experiment was performed in absence of HPW leading to only 2 % degradation of DR-13 after 12 h. Moreover, without UV illumination no change in the color of the organic phase was observed. In conclusion, the oxidative degradation of a dye in the organic phase can be performed using H_2O_2 in the aqueous phase. Similarly, the degradation of a broad spectrum of azo-dyes could be performed as proposed in literature.[61–64]

7.4.4 Reduction in the aqueous phase: Metal recovery

Photoreduced PW and other POMs have been shown to enable the reduction of diverse metal ions and to recover metals from solution.[65] Here, we show the recovery of silver by reducing Ag^+ to elemental Ag^0 in the aqueous phase.

We used the initial concentration $c_{aq.\ phase}$ ($AgNO_3$) = 25 mmol L^{-1} and HPW (c_0 = 5 mmol L^{-1}) as a catalyst. At these concentrations, Ag^+ is mainly distributed in the aqueous phase ($log\left(K_D^{Ag}\right)$ = -0.9), see Fig. S4 (ESI). The catalytic cycle was closed by the oxidation of 1-OctOH which was used as the organic phase. The reaction cycle is schematically shown in Fig. 7.5, sketch and the equation for reactions are presented below:

Ox.:	(C_8H_{17})-OH → (C_7H_{15})-CHO + $2e^-$ + $2H^+$
Red.:	$2Ag^+$ + $2e^-$ → $2Ag^0$
Redox:	$2Ag^+$ + (C_8H_{17})-OH → $2Ag^0$ + (C_7H_{15})-CHO +$2H^+$

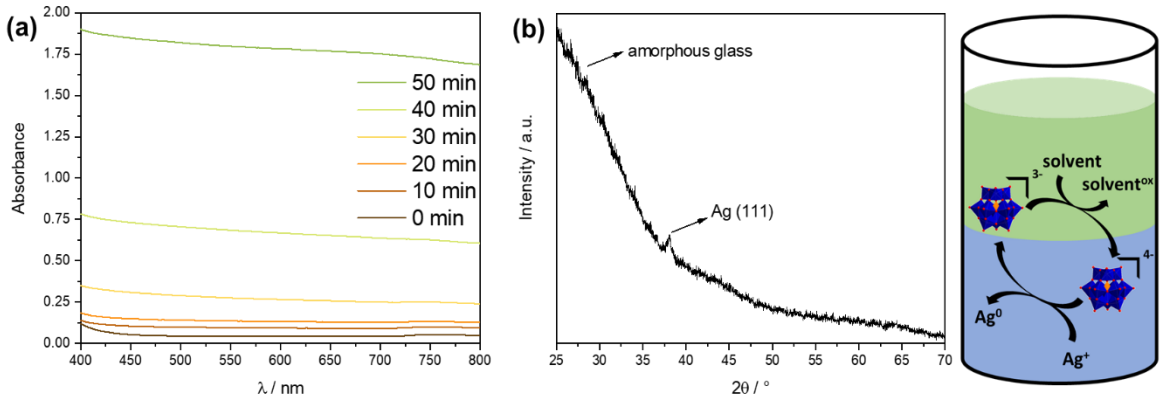

Figure 7.5. Photoreduction of Ag^+ to Ag^0 in the aqueous phase as a function of illumination time. The catalytic cycle is closed by 1-OctOH oxidation in the organic phase. (a) Increasing UV/VIS absorbance owing to absorbing and scattering of Ag particles and (b) depicts a XRPD spectrum of the dried product.

As proposed by Troupis *et al.* the recovery of Ag^0 is semi-quantitatively monitored by UV-VIS spectrometry.[43] The reduction of Ag^+ leads to elemental silver which forms particles in the aqueous phase. The formation of Ag particles was observed visually, see Fig. S5 (ESI). It is worth to note that without UV illumination no formation of Ag particles was detected by the naked eye. We observe an increase of the absorbance in UV/VIS spectrometry with time, see Fig. 7.5a. This can be attributed to absorption (silver color, Fig. S5 (ESI)) and scattering. Within 50 minutes the absorbance is increased from approximately 0 to 1.7 due to the formation of Ag particles. On the contrary, in absence of HPW no evolution of the absorption spectra was obtained within 50 minutes reaction time, see Fig. S6 (ESI). Ag is here synthesized as super-micrometer particles which sediment within several tens of minutes, see discussion in section S4, Figs. S7-S8 (ESI). Moreover, a sample of the dried product was measured by X-ray powder diffraction (XRPD), see Fig. 7.5b. XRPD shows a characteristic peak at $2\Theta = 38$ °, which can be assigned to the (111) reflection of solid Ag.[65] The intensity increase at small 2Θ angles arises from the amorphous glass of the sample container (0.5 mm capillary). As a summary, Ag can be recovered from aqueous Ag^+ solution by oxidizing 1-OctOH (org. phase). According to literature, this procedure can be transferred to various metals, as the recovery of Pd,[66] Cu[67] and other metals[65] using $PW_{12}O_{40}^{4-}$ is known since pioneering works of Papaconstantinou and colleagues.

7.4.5 Reduction in the aqueous phase: UV-light controlled complexometry

Metal-organic complexes cover a broad field of research, as they are interesting in terms of synthesis,[68] complexometric titrations,[69] applications,[70] *etc*. As an example, we investigate the *in-situ* complexation of one of the most prominent metal-organic complexes, *i.e.* ferroin ($[Fe^{II}((1,10)\text{-phenanthroline})_3]^{2+}$, also known as $[Fe^{II}(phen)_3]^{2+}$).[71] Interestingly, $[Fe^{II}(phen)_3]^{2+}$

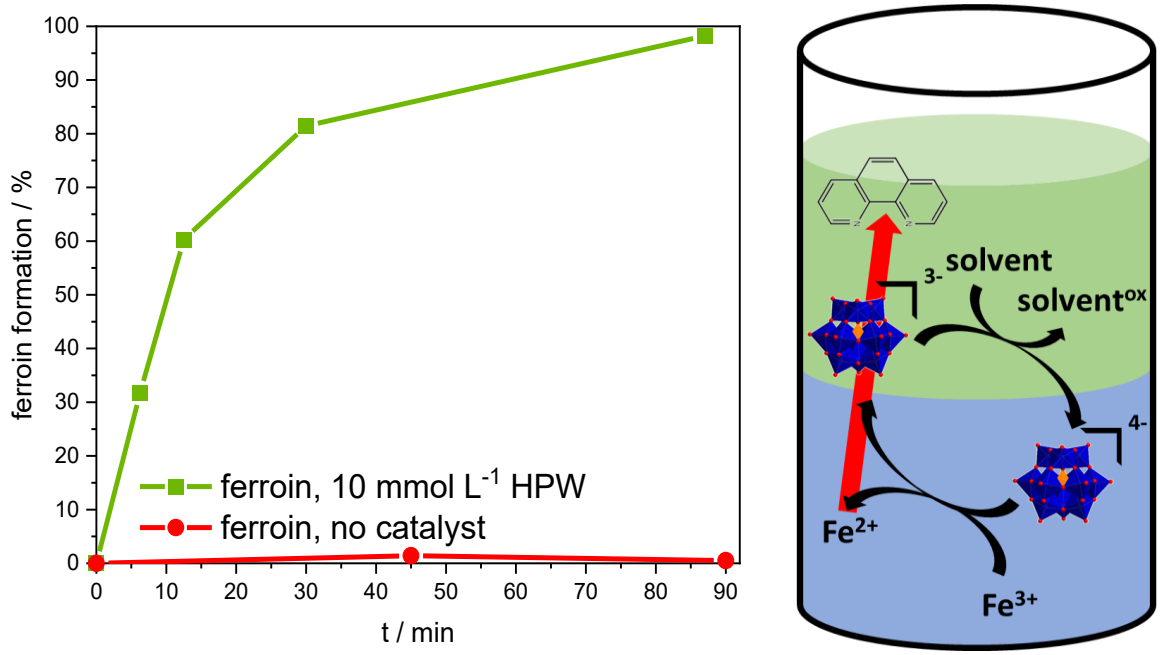

Figure 7.6. Synthesis of ferroin in the organic phase by *in-situ* photoreduction of Fe^{3+} to Fe^{2+} in the aqueous phase as a function of illumination time. The catalytic cycle is closed by 1-OctOH oxidation in the organic phase.

exhibits a characteristic red color, whereas the oxidized $[Fe^{III}(phen)_3]^{3+}$ appears deeply blue.[72] Here, we investigate the reaction of 0.5 mmol kg^{-1} (1,10)-phenanthroline in the organic phase (1-OctOH) and 2 mmol L^{-1} $Fe^{III}Cl_3$ in the aqueous phase. (1,10)-phenanthroline derivatives are known to be highly hydrophobic.[73] HPW (10 mmol L^{-1}) is used as catalyst. Before the reaction starts, Fe^{3+} and (1,10)-phenanthroline are well separated. Figure 7.6 shows the formation of the red $[Fe^{II}(phen)_3]^{2+}$ in the organic phase, *cf.* Fig. S9 (ESI), whereas no red color was observed if the sample was not illuminated. The reaction equation of the formation of Fe^{2+} is given below:

Ox.:	(C_8H_{17})-OH → (C_7H_{15})-CHO + $2e^-$ + $2H^+$
Red.:	$2Fe^{3+}$ + $2e^-$ → $2Fe^{2+}$
Redox:	2 Fe^{3+}+ (C_8H_{17})-OH → 2 Fe^{2+} + (C_7H_{15})-CHO + $2H^+$

Here, we observe 98 % $[Fe^{II}(phen)_3]^{2+}$ formation within 88 minutes. In absence of HPW only 1 % $[Fe^{II}(phen)_3]^{2+}$ and no $[Fe^{III}(phen)_3]^{3+}$ are formed. $PW_{12}O_{40}^{3-}$ oxidizes the solvent 1-OctOH, controlled by UV-illumination (λ = 365 nm). The reduced POM, $PW_{12}O_{40}^{4-}$, then migrates to the aqueous phase and performs the reduction of Fe^{3+} to Fe^{2+}. Consecutively, Fe^{2+} is extracted to the organic phase and the complex formation of $[Fe^{II}(phen)_3]^{2+}$ occurs, *cf.* sketch in Fig. 7.6 (red arrow). In conclusion, the Fe^{2+} formation and subsequent complexation with (1,10)-phenanthroline can be controlled by UV-light. Therefore, this system can serve as a "photochemical micropipette" operated by a controlled flux of photons. Such a general concept could be applied to diverse metal-organic compounds, as *e.g.* the *in-situ* reduction of Cr^{6+} to Cr^{3+} by HPW is already reported.[74]

7.4.6 Combined oxidation-reduction reactions

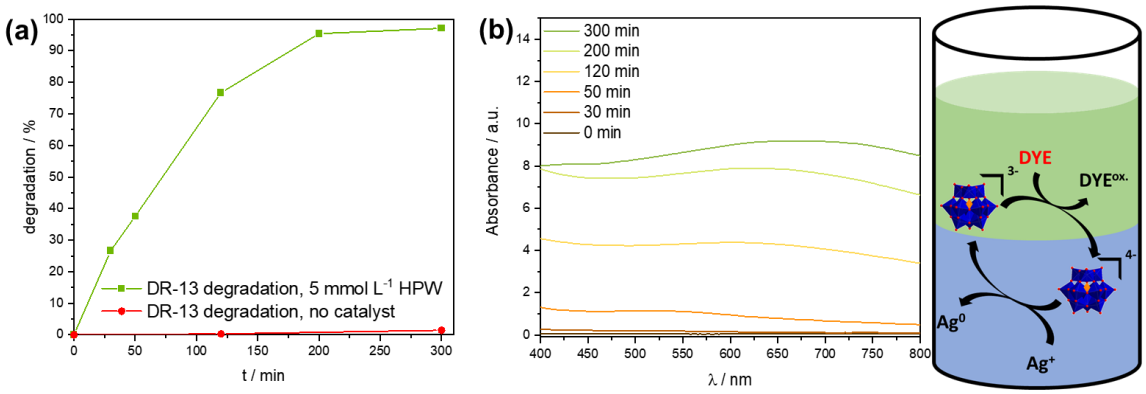

Figure 7.7. Simultaneous (a) photodegradation of 1 mmol kg^{-1} DR-13 in the organic phase (2-Me-2-HexOH) and (b) silver recovery in the aqueous phase.

As a last step, we perform two reactions of industrial relevance simultaneously: degradation of the organic dye DR-13 (in the organic phase) and recovery of silver (in the aqueous phase) using only one catalyst: HPW. We used the initial concentrations $c_{org.\ phase}$(DR-13) = 1 mmol kg^{-1} and $c_{aq.\ phase}(AgNO_3)$ = 25 mmol L^{-1}. HPW (5 mmol L^{-1}) was used as catalyst. The sample was illuminated with UV-light (λ = 365 nm). Figure 7.7 shows (a) the degradation of DR-13 and (b) the recovery of Ag, see Fig. S10 (ESI). The reaction equation is presented below:

Ox.:	"Dye → Dye^{ox} (diff. products) + $2H^+$ + $2e^-$"
Red.:	$2Ag^+ + 2e^- \rightarrow 2Ag^0$
Redox:	Dye + $2Ag^+ \rightarrow 2Ag^0$ + Dye^{ox} + $2H^+$

The degradation of DR-13 is shown in Fig. 7.7a. A degradation of 96 % is observed after 300 minutes reaction time. Note that in absence of HPW only 2 % DR-13 can be degraded within the same time. Meanwhile, Ag is recovered, as monitored by a strong increase in the UV/VIS absorbance (absorbance increases from 0 to 8, recalculated by dilution factors, see section S7.6 (ESI)) within 300 minutes, see Fig. 7.7b. In conclusion, our biphasic one-catalyst system enables to perform two "useful" oxidation- and reduction-reactions simultaneously. We assume that this general {2-phases 2-reactions 1-catalyst} concept can be applied to diverse types of coupled reactions.

7.4.7 Applicability, economy and sustainability of {2-phases 2-reactions 1-catalyst}

After showing the generality of the {2-phases 2-reactions 1-catalyst} concept, its applicability, economy and sustainability are discussed.

The concept presented here can be applied to different biphasic systems with other catalysts than POMs. The main criterion is the use of two immiscible phases, while the hydrophobicity/hydrophilicity of the two phases must be chosen to have a good separation factor of the oxidized and reduced form of a photoredox catalyst and of the reaction products. While in this paper, the basic concept is presented, the next obvious step is to find couples of valuable reactions with industrial relevance.

In an industrial context with growing environmental constraints, we can foresee advantages of the {2-phases 2-reactions 1-catalyst} concept compared to single performed reactions: *(i) Self-regeneration of the catalyst.* The performance of two single reactions requires the regeneration of the catalyst or production of the active catalyst species. In the case of two single reactions, the two active catalyst species need to be regenerated by using sacrificial reducing and oxidizing agents, *e.g.* iso-propanol and dissolved O_2, respectively. In the case of the {2-phases 2-reactions 1-catalyst} concept, we make the (molecular) economy of these two sacrificial compounds. *(ii) Economy of one reactor.* The {2-phases 2-reactions 1-catalyst} concept makes the economy of one reactor as it combines two single reactions in one reactor. Therefore, associated to the economy of one reactor, the energy (*e.g.* irradiation or heating) and maintenance costs can be strongly diminished.

Nevertheless, we can also anticipate limitations of the {2-phases 2-reactions 1-catalyst} concept: *(i) Complexity of the system.* The application of the concept requires the search for a set of 2 immiscible solvents, suitable to perform 2 industrially relevant reactions separately with 1 catalyst whose oxidized and reduced form have an opposite separation factor between the two solvents. This implies either development effort or predictability of the system. We can suggest the following strategy to overcome this limitation. The first step for a successful development is the choice of a catalyst that enables the performance of two useful reactions. The second step is to use theoretical prediction tools, such as COSMO-RS,[75,76] to investigate a large set of solvents for the prediction of separation factors of oxidized and reduced catalyst forms between two immiscible solvents. *(ii) Separation and purification of products.* Once a certain yield is reached, products need to be separated/purified from the reaction media (both phases). In addition, the products formed during the two reactions should not diffuse from one phase into the other. The overall target is to implement our concept in a continuous process in order to take full advantage of the {2-phases 2-reactions 1-catalyst} approach.

7.5 Conclusion

We show here, how HPW can be simultaneously used as a (photo-)catalyst for oxidation and reduction in a liquid-liquid biphasic system that separates oxidizing and reducing conditions in each

of the phases. As two reactions are performed in two phases with one catalyst, this methodology is called the {2-phases 2-reactions 1-catalyst} concept.

We found here that the commercially available α-Keggin POM $H_3PW_{12}O_{40}$ mainly distributes in organic alcohol phases (1-HexOH, 1-OctOH, 2-Me-2-HexOH) in a water:alcohol biphasic system. $H_4SiW_{12}O_{40}$, on the contrary, was shown to distribute mostly in the aqueous phase. We used these opposite distributions to separate $PW_{12}O_{40}^{3-}$ (organic phase) and photoreduced $PW_{12}O_{40}^{4-}$ (aqueous phase) which has the same distribution towards water as $SiW_{12}O_{40}^{4-}$. Owing to the oxidative and reductive properties of $PW_{12}O_{40}^{3-}$ and $PW_{12}O_{40}^{4-}$ respectively, we could therefore separate an oxidizing environment ($PW_{12}O_{40}^{3-}$, organic phase) and a reducing environment ($PW_{12}O_{40}^{4-}$, aqueous phase) in a biphasic system.

We investigated this coupled redox system as a biphasic reaction medium to perform several reactions, *e.g.* organic oxidative syntheses, oxidative dye degradation in the organic phase, metal recovery or iron reduction (for metal-organic *in-situ* complexation) in the aqueous phase. Finally, we combined two reactions, *i.e.* the oxidative degradation of an organic dye in the organic phase and the recovery of elemental silver from aqueous Ag^+ solution. For all reactions, no blue color (attributed to the one-electron reduced species) was observed in the aqueous phase during the reaction. Therefore, $PW_{12}O_{40}^{4-}$ does not accumulate in the aqueous phase suggesting that it is re-oxidized rapidly as soon as it crosses the alcohol:water interface.

A controlled reaction in one particular phase of a multiphasic system is usually difficult to perform in a laboratory. For example, Pd-doped carbon nano-tubes or Janus particles were used to stabilize biphasic emulsions by Resasco and colleagues. Reactions can be catalyzed in the organic or the aqueous phase depending on the way how the catalyst is prepared.[77–79] Furthermore, the use of POMs as catalysts in biphasic media is only rarely investigated so far,[80] except for photocatalytic active POM-surfactants[81] and Pickering-emulsion stabilizing POM particles.[82,83] Nevertheless, in these systems only one reaction (either oxidation or reduction) is performed and/or the preparation of the catalyst requires multi-step synthesis, *i.e.* synthesis of nano-particles or covalently bound POM-surfactants.

In summary, the biphasic model system designed here *(i)* offers a very simple way to separate reduction and oxidation reactions, *(ii)* requires only one catalyst and one reactor to perform two redox reactions and *(iii)* does not demand a complicated preparation of the catalyst compared to previously reported multiphasic reaction systems.[77–79,81–83] Consequently, the {2-phases 2-reactions 1-catalyst} concept is a sustainable and economical methodology for performing coupled reactions.

As a perspective, we suggest the {2-phases 2-reactions 1-catalyst} concept can be extended to diverse catalytic processes. The key for using this concept efficiently, lies in the rational choice of

the solvents, which need to *(i)* be immiscible with each other and *(ii)* separate two active forms of a catalyst, *i.e.* the oxidized and reduced forms of the catalyst distribute oppositely in each phase. Accordingly, differently charged, active species of powerful catalysts such as Ru-based metal-organic catalysts,[84] organic redoxcatalysts[85] or boron-based photocatalysts[86] could be applied in the {2-phases 2-reactions 1-catalyst} concept.

7.6 Bibliography

[1] J. J. Borrás-Almenar, E. Coronado, A. Müller, M. Pope, *Polyoxometalate Molecular Science*, Springer, Netherlands, Dondrecht, **2003**.

[2] M. T. Pope, A. Müller, *Angew. Chem. - Int. Ed.* **1991**, *30*, 34–48.

[3] H. Stephan, M. Kubeil, F. Emmerling, C. E. Müller, *Eur. J. Inorg. Chem.* **2013**, *2013*, 1585–1594.

[4] M. Aureliano, G. Fraqueza, C. A. Ohlin, *Dalt. Trans.* **2013**, *42*, 11770-11777.

[5] A. Bijelic, A. Rompel, *Coord. Chem. Rev.* **2015**, *299*, 22–38.

[6] J. T. Rhule, C. L. Hill, D. A. Judd, R. F. Schinazi, *Chem. Rev.* **1998**, *98*, 327–357.

[7] G. Izzet, F. Volatron, A. Proust, *Chem. Rec.* **2017**, *17*, 250–266.

[8] H. N. Miras, J. Yan, D.-L. Long, L. Cronin, *Chem. Soc. Rev.* **2012**, *41*, 7403-7430.

[9] Y.-F. Song, R. Tsunashima, *Chem. Soc. Rev.* **2012**, *41*, 7384–7402.

[10] M. Misono, Catalysis of Heteropoly Compounds (Polyoxometalates), *Stud. Surf. Sci. Catal.* **2013**, *176*, 97-155.

[11] C. L. Hill, *Comprehensive Coordination Chemistry II:From Biology to Nanotechnology*, Elsevier, Oxford, **2004**.

[12] L. Marzo, S. K. Pagire, O. Reiser, B. König, *Angew. Chem. - Int. Ed.* **2018**, *57*, 10034–10072.

[13] C. Streb, *Dalt. Trans.* **2012**, *41*, 1651–1659.

[14] S. Roy, D. C. Crans, T. N. Parac-Vogt, *Front. Chem.* **2019**, *7*, 1–2.

[15] E. Papaconstantinou, *Chem. Soc. Rev.* **1989**, *18*, 1–31.

[16] K. Suzuki, N. Mizuno, K. Yamaguchi, *ACS Catal.* **2018**, *8*, 10809–10825.

[17] C. Streb, K. Kastner, J. Tucher, *Phys. Sci. Rev.* **2019**, *4*, 1–10.

[18] E. Papaconstantinou, A. Hiskia, in *Polyoxometalate Mol. Sci.*, Springer, Nederlands, Dondrecht, **2003**, 381–416.

[19] B. Naskar, O. Diat, V. Nardello-Rataj, P. Bauduin, *J. Phys. Chem. C* **2015**, *119*, 20985–20992.

[20] M. Hohenschutz, I. Grillo, C. D. Dewhurst, P. Schmid, L. Girard, A. Jonchère, O. Diat, P. Bauduin, *J. Colloid Interface Sci.* **2021**, *603*, 141–147.

[21] T. Buchecker, X. LeGoff, B. Naskar, A. Pfitzner, O. Diat, P. Bauduin, *Chem. - A Eur. J.* **2017**, *23*, 8434–8442.

[22] T. Buchecker, P. Schmid, I. Grillo, S. Prévost, M. Drechsler, O. Diat, A. Pfitzner, P. Bauduin, *J. Am. Chem. Soc.* **2019**, *141*, 6890–6899.

[23] Y. Wu, R. Shi, Y. Wu, J. M. Holcroft, Z. Liu, M. Frasconi, M. R. Wasielewski, H. Li, J. F. Stoddart, *J. Am. Chem. Soc.* **2015**, *137*, 4111–4118.

[24] C. Falaise, M. A. Moussawi, S. Floquet, P. A. Abramov, M. N. Sokolov, M. Haouas, E. Cadot, *J. Am. Chem. Soc.* **2018**, *140*, 11198–11201.

[25] S. Yao, C. Falaise, A. A. Ivanov, N. Leclerc, M. Hohenschutz, M. Haouas, D. Landy, M. A. Shestopalov, P. Bauduin, E. Cadot, *Inorg. Chem. Front.* **2021**, *8*, 12–25.

[26] S. Yao, C. Falaise, S. Khilfi, N. Leclerc, M. Haouas, D. Landy, E. Cadot, *Inorg. Chem.* **2021**, *60*, 7433–7441.

[27] T. Buchecker, P. Schmid, S. Renaudineau, O. Diat, A. Proust, A. Pfitzner, P. Bauduin, *Chem. Commun.* **2018**, *54*, 1833–1836.

[28] M. Hohenschutz, I. Grillo, O. Diat, P. Bauduin, *Angew. Chem. - Int. Ed.* **2020**, *59*, 8084–8088.

[29] B. Qi, S. An, J. Luo, T. Liu, Y.-F. Song, *Chem. - A Eur. J.* **2020**, *26*, 16802–16810.

[30] K. I. Assaf, M. S. Ural, F. Pan, T. Georgiev, S. Simova, K. Rissanen, D. Gabel, W. M. Nau, *Angew. Chem. - Int. Ed.* **2015**, *54*, 6852–6856.

[31] W. Kunz, P. Lo Nostro, B. W. Ninham, *Curr. Opin. Colloid Interface Sci.* **2004**, *9*, 1–18.

[32] A. T. Merhi, A. Jonchère, L. Girard, O. Diat, M. Nuez, C. Viñas, P. Bauduin, *Chem. - A Eur. J.* **2020**, *26*, 13935–13947.

[33] K. I. Assaf, B. Begaj, A. Frank, M. Nilam, A. S. Mougharbel, U. Kortz, J. Nekvinda, B. Grüner, D. Gabel, W. M. Nau, *J. Org. Chem.* **2019**, *84*, 11790–11798.

[34] K. I. Assaf, O. Suckova, N. Al Danaf, V. Von Glasenapp, D. Gabel, W. M. Nau, *Org. Lett.* **2016**, *18*, 932–935.

[35] M. Tarres, E. Canetta, E. Paul, J. Forbes, K. Azzouni, C. Vinas, F. Teixidor, A. J. Harwood, *Sci. Rep.* **2015**, *5*, 1–8.

[36] K. I. Assaf, W. M. Nau, *Angew. Chem. - Int. Ed.* **2018**, *57*, 13968–13981.

[37] P. Schmid, T. Buchecker, A. Khoshsima, D. Touraud, O. Diat, W. Kunz, A. Pfitzner, P. Bauduin, *J. Colloid Interface Sci.* **2021**, *587*, 347–357.

[38] A. Chaumont, G. Wipff, *Phys. Chem. Chem. Phys.* **2008**, *10*, 6940–6953.

[39] M. K. Bera, B. Qiao, S. Seifert, B. P. Burton-Pye, M. Olvera De La Cruz, M. R. Antonio, *J. Phys. Chem. C* **2016**, *120*, 1317–1327.

[40] M. R. Antonio, M. K. Bera, *Eur. J. Inorg. Chem.* **2019**, *2019*, 367–373.

[41] A. Malinenko, A. Jonchère, L. Girard, S. Parrès-Maynadié, O. Diat, P. Bauduin, *Langmuir* **2018**, *34*, 2026–2038.

[42] R. Winkler, T. Buchecker, F. Hastreiter, D. Touraud, W. Kunz, *Phys. Chem. Chem. Phys.* **2017**,

19, 25463–25470.

[43] A. Troupis, A. Hiskia, E. Papaconstantinou, *Appl. Catal. B Environ.* **2003**, *42*, 305–315.

[44] D. Stoe & Cie GmbH, Darmstadt, **2014**.

[45] K. Kinoshita, H. Ishiskawa, K. Shinoda, *Bull. Chem. Soc. Jpn.* **1958**, *31*, 1081–1082.

[46] M. L. Dekker, M. Clausse, H. L. Rosano, A. Zradba, *Microemulsion Systems, Surfactant Science Ser.*, New York, **1987**.

[47] R. Stephenson, J. Stuart, M. Tabak, *J. Chem. Eng. Data* **1984**, *29*, 287–290.

[48] N. I. Gumerova, A. Rompel, *Chem. Soc. Rev.* **2020**, *49*, 7568–7601.

[49] S. Yao, C. Falaise, N. Leclerc, C. Roch-Marchal, M. Haouas, E. Cadot, *Inorg. Chem.* **2022**, *61*, 4193-4203.

[50] S. S. Wang, G. Y. Yang, *Chem. Rev.* **2015**, *115*, 4893–4962.

[51] R. I. Maksimovskaya, G. M. Maksimov, *Coord. Chem. Rev.* **2019**, *385*, 81–99.

[52] M. Kozik, C. F. Hammer, L. C. W. Baker, *J. Am. Chem. Soc.* **1986**, *108*, 7627–7630.

[53] G. G. Briggs, *J. Aggricultural Food Chem.* **1981**, *29*, 1050–1059.

[54] D. Forschungsgemeinschaft, H. Greim, *The MAK-Collection for Occupational Health and Safety*, Wiley-VCH Verlag GmbH& Co. KGaA, Weinheim, **2012**.

[55] S. Krickl, T. Buchecker, A. U. Meyer, I. Grillo, D. Touraud, P. Bauduin, B. König, A. Pfitzner, W. Kunz, *Phys. Chem. Chem. Phys.* **2017**, *19*, 23773–23780.

[56] B. Lellis, C. Z. Fávaro-Polonio, J. A. Pamphile, J. C. Polonio, *Biotechnol. Res. Innov.* **2019**, *3*, 175–290.

[57] F. M. Drumond Chequer, T. M. Lizier, R. De Felício, M. V. Boldrin Zanoni, H. M. Debonsi, P. N. Lopes, D. Palma de Oliveira, *Toxicol. Vitr.* **2015**, *29*, 1906–1915.

[58] N. F. Desai, C. H. Giles, *J. Soc. Dye. Colour.* **1949**, *65*, 639–649.

[59] I. Arslan-Alaton, *Dye. Pigment.* **2004**, *60*, 167–176.

[60] A. Troupis, E. Gkika, A. Hiskia, E. Papaconstantinou, *J. Adv. Oxid. Tech.* **2007**, *10*, 79–84.

[61] I. Arslan-Alaton, S. Dogruel, *Water Sci. Technol.* **2001**, *49*, 171–176.

[62] W. Wang, S. Yang, *J. Water Resour. Prot.* **2010**, *2*, 979–983.

[63] Y. Wang, K. Lu, C. Feng, *J. Rare Earths* **2011**, *29*, 866–871.

[64] P. Lei, C. Chen, J. Yang, W. Ma, J. Zhao, L. Zang, *Environ. Sci. Technol.* **2005**, *39*, 8466–8474.

[65] A. Troupis, E. Gkika, A. Hiskia, E. Papaconstantinou, *Comptes Rendus Chim.* **2006**, *9*, 851–857.

[66] A. Troupis, A. Hiskia, E. Papaconstantinou, *Appl. Catal. B Environ.* **2004**, *52*, 41–48.

[67] A. Troupis, A. Hiskia, E. Papaconstantinou, *Environ. Sci. Technol.* **2002**, *36*, 5355–5362.

[68] S. M. Wilkinson, T. M. Sheedy, E. J. New, *J. Chem. Educ.* **2016**, *93*, 351–354.

[69] J. Kozak, A. Townshend, *Titrimetry Overview*, Elsevier Inc., **2018**.

[70] A. M. Abu-Dief, I. M. A. Mohamed, *Beni-Suef Univ. J. Basic Appl. Sci.* **2015**, *4*, 119–133.

[71] R. K. Adhikamsetty, N. R. Gollapalli, S. B. Jonnalagadda, *Int. J. Chem. Kinet.* **2008**, *40*, 515–523.

[72] A. F. Hollemann, E. Wiberg, N. Wiberg, *Lehrbuch Der Anorganischen Chemie*, Walter De Gruyter, Berlin, **2007**.

[73] C. Al Hageh, M. Al Assaad, Z. El Masri, N. Samaan, M. El-Sibai, C. Khalil, R. S. Khnayzer, *Dalt. Trans.* **2018**, *47*, 4959–4967.

[74] E. Gkika, A. Troupis, A. Hiskia, E. Papaconstantinou, *Appl. Catal. B Environ.* **2006**, *62*, 28–34.

[75] A. Klamt, G. Schüürmann, *J. Chem. Soc. Perkin Trans. 2* **1993**, 799–805.

[76] A. Klamt, *J. Phys. Chem.* **1995**, *99*, 2224–2235.

[77] S. Crossley, J. Faria, M. Shen, D. E. Resasco, *Science* **2010**, *327*, 68–72.

[78] D. E. Resasco, *Chinese J. Catal.* **2014**, *35*, 798–806.

[79] J. Faria, M. P. Ruiz, D. E. Resasco, *Adv. Synth. Catal.* **2010**, *352*, 2359–2364.

[80] H. Su, C. Yang, *Chinese J. Catal.* **2014**, *35*, 1224–1234.

[81] X. Bai, X. Huang, L. Wen, N. Song, J. Zhang, Y. Zhang, Y. Zhao, *Chem. Commun.* **2019**, *55*, 3598–3601.

[82] L. Leclercq, A. Mouret, A. Proust, V. Schmitt, P. Bauduin, J. M. Aubry, V. Nardello-Rataj, *Chem. - A Eur. J.* **2012**, *18*, 14352–14358.

[83] D. Dedovets, Q. Li, L. Leclercq, V. Nardello-Rataj, J. Leng, S. Zhao, M. Pera-Titus, *Angew. Chem. - Int. Ed.* **2021**, *61(4)*, e202107537.

[84] S. Angerani, N. Winssinger, *Chem. - A Eur. J.* **2019**, *25*, 6661–6672.

[85] N. A. Romero, D. A. Nicewicz, *Chem. Rev.* **2016**, *116*, 10075–10166.

[86] I. Guerrero, Z. Kelemen, C. Vinas, I. Romero, F. Teixidor, *Chem. - A Eur. J.* **2020**, *26*, 5027–5036.

8 Conclusion and Outlook

8.1 Discussion

The first goal of this thesis was to ***extend the spectrum of solutes interacting with POMs, driven by the (super-)chaotropic effect***. Indeed, the hydrophobicity of solutes/organic matter was continuously increased throughout this work, ranging from water-soluble polymeric surfactants ***(chapter 2)*** over partially water-miscible propylene glycol oligomers ***(chapters 3-5)*** and short-chain alcohols ***(chapter 6)*** to water-immiscible long-chain alcohols ***(chapter 7)***.

The results of ***chapter 2 "Polymeric surfactant P84/polyoxometalate α-$PW_{12}O_{40}^{3-}$ – A model system to investigate the interplay between chaotropic and hydrophobic effects"*** suggested that the chaotropic effect may act as a competitor to the hydrophobic effect, as proposed by Nau *et al.*[1] Based on the chaotropic effect, and reinforced by the hydrophobic effect, the nanometric α-Keggin $PW_{12}O_{40}^{3-}$ bound strongly to propylene oxide moieties in the model triblock polymer P84 unimer (P84 provides ABA architecture with A: polyethylene oxide and B: polypropylene oxide) at room temperature. The preferential binding of $PW_{12}O_{40}^{3-}$ to the propylene oxide chain was explained by the higher hydrophobic character of propylene oxide, compared to ethylene oxide. By increasing temperature, P84 underwent a transition from unimers to spherical micelles. This micellization process is driven by dehydration of surfactant moieties which form the micellar core, here polypropylene oxide, known as the hydrophobic effect.[2] After this temperature-induced self-assembly of P84, $PW_{12}O_{40}^{3-}$ was displaced from the propylene oxide moiety to the polyethylene oxide chains, representing the micellar corona. Nevertheless, $PW_{12}O_{40}^{3-}$ also penetrated the polypropylene oxide micellar core partially. Therefore, both effects – the chaotropic effect and the hydrophobic effect and their competition – could be explained and discussed by considering the free energy of hydration of solutes in water. In summary, the key results of this chapter were: *(i)* the improved predictability of assembly phenomena related to dehydration processes, *(ii)* the experimental proof of the orthogonality of chaotropic and hydrophobic effect and *(iii)* the relation of the competition "chaotropic effect *vs.* hydrophobic effect" to the extended law of matching water affinities, proposed by Leontidis *et al.*[3] It is worth mentioning that a detailed study on the question *"How to distinguish between the chaotropic and the hydrophobic effect?"* is currently performed in the group of Dr. Bauduin.

The studies presented in ***chapter 3 "Self-assembly of a short amphiphile in water controlled by superchaotropic polyoxometalates: $H_4SiW_{12}O_{40}$ vs. $H_3PW_{12}O_{40}$"*** showed the strong association of $H_4SiW_{12}O_{40}$ and $H_3PW_{12}O_{40}$ with a short amphiphilic molecule, namely dipropylene glycol *n*-propylether (C_3P_2). Therefore, C_3P_2 was one of the shortest molecules, showing strong interaction

with superchaotropic anions, so far. Before this thesis, especially longer chained polymers and surfactants have been investigated. Even though both POMs, $H_4SiW_{12}O_{40}$ and $H_3PW_{12}O_{40}$, showed a strong association with C_3P_2, their different charge density led to completely different POM-C_3P_2 arrangements. In case of $SiW_{12}O_{40}^{4-}$, stoichiometric complexes of $[SiW_{12}O_{40}^{4-}][C_3P_2]_{1-2}$ were present at millimolar $SiW_{12}O_{40}^{4-}$ concentrations and 570 mmol kg^{-1} C_3P_2. For $PW_{12}O_{40}^{3-}$, mesoscopic aggregates were formed with the general sum formula $[PW_{12}O_{40}^{3-}]_m[C_3P_2]_n$ ($m \approx 4$ and $n \approx 30$ for 50 mmol kg^{-1} $H_3PW_{12}O_{40}$ and 570 mmol kg^{-1} C_3P_2). This tremendous discrepancy between $H_4SiW_{12}O_{40}$ and $H_3PW_{12}O_{40}$ was explained by the general tendency of $H_3PW_{12}O_{40}$ to self-assemble even in pure water due to weak electrostatic repulsions and strong short-range attractions between single $PW_{12}O_{40}^{3-}$ clusters, compared to $H_4SiW_{12}O_{40}$.[4,5] Indeed, the formation of colloidal aggregates, $[PW_{12}O_{40}^{3-}]_m[C_3P_2]_n$, and their coalescence, produced a CP decrease of C_3P_2 at high HPW concentrations, although a strong CP increase (highly salting-in) was usually observed for the addition of superchaotropic ions.[6]

The second goal in this thesis was to ***explain and discuss unconventional ion effects related to superchaotropic POMs and the potential role of the chaotropic effect in life evolution.***

In ***chapter 4 "Counterion effect on α-Keggin polyoxometalates in water: the peculiar role of H^+ on their salting-in effect and co-assembly with organics"***, the system $H_3PW_{12}O_{40}$-C_3P_2 was further investigated. Indeed, the formation/size of $[PW_{12}O_{40}^{3-}]_m[C_3P_2]_n$ strongly depended on the choice of the counterion of $PW_{12}O_{40}^{3-}$. Only in combination with protons, the ability of $PW_{12}O_{40}^{3-}$ to self-assemble with C_3P_2 was strongly pronounced. This was explained by the "bridging" effect of H^+ (in the form of hydrated protons, *i.e.* H_3O^+ and $H_5O_2^+$), that "glued" monomeric $PW_{12}O_{40}^{3-}$ molecules, as proposed previously.[4,5] This peculiarity of $H_3PW_{12}O_{40}$ in the presence of C_3P_2 (and also C_8E_4 or PNiPAM) could be overcome by titrating the self-assembly promoting protons. For such titrations common inorganic bases, such as NaOH (or LiOH and KOH), were used, leading to the counterion exchange of phosphotungstate, *e.g.* $H_3PW_{12}O_{40} \rightarrow Na_3PW_{12}O_{40}$. Consequently, $[PW_{12}O_{40}^{3-}]_m[C_3P_2]_n$ aggregates are disrupted and the CP increases. The same phenomenon occurred for the titration with organic amine bases. Interestingly, a similar CP increase was also observed for the titration with strongly salting-out anions, such as SO_4^{2-} or PO_4^{3-}. These latter ion species usually lead to a drastic CP decrease due to their high kosmotropic character. Here, SO_4^{2-} and PO_4^{3-} led to a strong CP increase, as they consumed self-assembly promoting protons via an acid-base reaction according to $SO_4^{2-} + H^+ \rightarrow HSO_4^-$ and $PO_4^{3-} + H^+ \rightarrow HPO_4^{2-}$, respectively. This showed the usually neglected duality of salting-out anions: their kosmotropic and their typically overlooked basic character.

The results in ***chapter 5 "The potential role of chaotropic polyoxometalates in the origin of life"*** proposed that polyoxometalates and the (super-)chaotropic effect may have played a role in the emergence of life. As an experimental model system, again $[PW_{12}O_{40}^{3-}]_m[C_3P_2]_n$ aggregates were

chosen. Upon photoreduction of $PW_{12}O_{40}^{3-} \rightarrow PW_{12}O_{40}^{4-}$, the $[POM]_m[C_3P_2]_n$ aggregates disassembled due to increased Coulomb repulsions between POM clusters. After reoxidizing $PW_{12}O_{40}^{4-} \rightarrow PW_{12}O_{40}^{3-}$ with environmental oxygen, the mesoscopic $[PW_{12}O_{40}^{3-}]_m[C_3P_2]_n$ assembled again. This disassembly-assembly process was synchronized with the day/night cycle, *i.e.* disassembly during the day (sunlight illumination) and assembly during the night (exposure to oxygen). Such an adaptability to environmental conditions was explained as a characteristic property of emerging life.[7] During the evolution of life, the local enrichment of concentrations, such as the C_3P_2 concentration in $[PW_{12}O_{40}^{3-}]_m[C_3P_2]_n$ aggregates, was a key for the performance of chemical reactions. Furthermore, $[PW_{12}O_{40}^{3-}]_m[C_3P_2]_n$ display enclosed aggregates, while such a compartmentalization is unambiguously linked to the emergence of living systems (coacervates, cells, cell organelles, *etc.*). The availability of phosphate[8] and tungstate[9] in the prebiotic ocean suggests that superchaotropic POMs may have formed. Driven by the chaotropic effect, similar stimuli-responsive self-assembled systems may have formed, which could have strongly promoted the emergence of life. As a conclusion, the (super-)chaotropic effect was here proposed as (an additional) driving force for the origin of life.

As a last goal ***the application of low charge density POMs for selective solubilization and organic synthesis*** was formulated.

Chapter 6 "A paradox: Hydrophilic molecular metal-oxides are selective solubilizers for moderately hydrophobic compounds". Diverse superchaotropic α-Keggin polyoxometalates were shown to act as solubilizers for moderately hydrophobic molecules, such as short-chain alcohols. Next to the remarkable solubilization effectivity of $H_3PW_{12}O_{40}$ and $H_4SiW_{12}O_{40}$, especially $Na_3PW_{12}O_{40}$ was found comparably efficient as the model surfactant sodium dodecyl sulfate (and much more efficient as the hydrotrope sodium xylene sulfonate (SXS)) in solubilizing short-chain aliphatic alcohols and. For example, millimolar concentrations of $Na_3PW_{12}O_{40}$ allowed us to reach full miscibility of water and 2-butanol. For π-electron containing molecules, *e.g.* benzyl alcohol, $Na_3PW_{12}O_{40}$ was an even more efficient solubilizer than sodium dodecyl sulfate due to the combination of the superchaotropic effect and strong POM-π attractions. These specific POM-π attractions resulted in the selective binding of $Na_3PW_{12}O_{40}$ to benzyl alcohol in competitive media of benzyl alcohol/1-butanol. This selectivity was used to perform selective solubilization of aromatic alcohols in water, which appeared as a unique property of NaPW by comparing it to the surprisingly non-selective SXS.

In ***chapter 7 "{2-phases 2-reactions 1-catalyst} concept for the sustainable performance of coupled reactions"*** a liquid-liquid biphasic system (alcohol:water) was designed to perform coupled redox reactions with only one catalyst. Due to its hydrophobic character, $PW_{12}O_{40}^{3-}$ distributed in the organic alcohol phase (1-octanol, 1-hexanol or 2-methyl-2-hexanol). After photoreduction of

$PW_{12}O_{40}^{3-} \rightarrow PW_{12}O_{40}^{4-}$, the hydrophilicity of the POM increased and subsequently $PW_{12}O_{40}^{4-}$ migrated to the water phase. $PW_{12}O_{40}^{3-}$ is known as a strong oxidizing agent, whereas $PW_{12}O_{40}^{4-}$ is a reducing agent. As a consequence, the designed reactor separated oxidizing ($PW_{12}O_{40}^{3-}$, alcohol phase) and reducing ($PW_{12}O_{40}^{4-}$, aqueous phase) conditions. This allowed us to perform oxidations and reductions simultaneously in separated phases, while only one catalyst (commercially available $H_3PW_{12}O_{40}$) was required. Several example reactions were performed within this {2-phases 2-reactions 1-catalyst} concept: oxidation of aromatic alcohols, oxidative degradation of azo-dyes, reductive recovery of metals from metal-ions solutions and *in-situ* complexation of organo-metallic complexes. As a master example, the azo-dye Disperse Red-13 was oxidatively degraded (in the organic phase), next to the simultaneous recovery of silver from Ag^+-solution (aqueous phase). This concept was proposed to be extendable to diverse biphasic systems, which allow the separation of two reactive species of a catalyst, *e.g.* depending on the redox state or protonation. Here, only one reactor and one catalyst were required to perform coupled reactions, while the reaction medium was composed of two green immiscible solvents (alcohol and water). The catalyst, which was consumed by one reaction, was recycled by performing a second reaction in another phase. As a conclusion, the {2-phases 2-reactions 1-catalyst} concept represented a sustainable and green methodology to perform catalytic reactions.

In this thesis, the superchaotropic effect of (photo-catalytically active) polyoxometalates was shown to have implications on diverse systems, leading to promising results on *(i)* the predictability of assembly motives, *(ii)* the self-assembly of POMs in the presence of organic co-solvents, *(iii)* the explanation of unconventional ion effects related to superchaotropic POMs, *(iv)* the potential role of superchaotropic POMs and the chaotropic effect in the evolution of life, *(v)* superchaotropic POMs as selective solubilizers and *(vi)* the design of sustainable, green reaction media. Nevertheless, investigations on the superchaotropicity of POMs can be extended to different subjects.

As proposed in ***chapter 5***, superchaotropic POMs may have played a key role in the evolution of life. To gain deeper knowledge on the role of the chaotropic effect in emerging life, a future focus should be put on the investigation of chaotropic POMs in interaction with building blocks of life, such as nucleobases, peptides, nucleosides, nucleotides, deoxyribonucleic acid (DNA), *etc*. In such studies, especial attention should be paid on the effect of the counterion of the POM and the competition of the chaotropic effect with the hydrophobic effect, based on findings in this thesis ***(chapter 2-5)***.

Here, POMs were presented as a novel class of selective solubilizers for moderately hydrophobic molecules ***(chapter 6)***. A decisive short-coming of POMs as solubilizers is their potential toxicity (heavy metal compounds). Therefore, a future key task to tackle in this context, and in general, is

the targeted search for environmentally friendly "green nano-ions". Moreover, first tests showed that self-assembled systems composed of POMs and an organic solute, *e.g.* $PW_{12}O_{40}^{3-}$-C_3P_2, provide an even higher solubilization efficiency/effectivity compared to POMs or C_3P_2 alone, *i.e.* a synergistic phenomenon related to facilitated hydrotropy occurs. As a consequence, strongly hydrophobic compounds, such as the hydrophobic azo-dye Disperse Red-13 can be solubilized in water by penetrating into $PW_{12}O_{40}^{3-}$-C_3P_2 aggregates. These investigations should be deepened in order to establish superchaotropic POMs as a novel class of functional solubilizers for a broad spectrum of highly hydrophobic molecules. Moreover, the selective interaction of superchaotropic POMs with aromatic molecules should be used to perform targeted (photo-)reactions with POMs as catalysts.

The {2-phases 2-reactions 1-catalyst} concept ***(chapter 7)*** is based on the opposite distribution of two active forms of a catalyst in a liquid-liquid biphasic system. This approach should be further exploited by applying it to more complex systems. Especially, as POMs were recently shown to enable the reduction of CO_2 in aqueous solution and the oxidative formation of H_2 from alcoholic solution,[10,11] the {2-phases 2-reactions 1-catalyst} concept could be used to "produce the fuel H_2 (in the organic phase) from the degradation of noxious CO_2 (in the aqueous phase)". Solving such tasks is indeed a key challenge in the 2020s.

8.2 Bibliography

[1] K. I. Assaf, W. M. Nau, *Angew. Chem. - Int. Ed.* **2018**, *57*, 13968–13981.

[2] D. Evans, H. Wennerström, *The Colloidal Domain*, Wiley, New York, **1999**.

[3] E. Leontidis, M. Christoforou, C. Georgiou, T. Delclos, *Curr. Opin. Colloid Interface Sci.* **2014**, *19*, 2–8.

[4] M. K. Bera, B. Qiao, S. Seifert, B. P. Burton-Pye, M. Olvera De La Cruz, M. R. Antonio, *J. Phys. Chem. C* **2016**, *120*, 1317–1327.

[5] A. Chaumont, G. Wipff, *Phys. Chem. Chem. Phys.* **2008**, *10*, 6940–6953.

[6] T. Buchecker, P. Schmid, S. Renaudineau, O. Diat, A. Proust, A. Pfitzner, P. Bauduin, *Chem. Commun.* **2018**, *54*, 1833–1836.

[7] Editorial, *Nat. Nanotechnol.* **2016**, *11*, 909.

[8] N. J. Planavsky, O. J. Rouxel, A. Bekker, S. V Lalonde, K. O. Konhauser, C. T. Reinhard, T. W. Lyons, *Nature* **2010**, *467*, 1088–1090.

[9] A. Sigel, H. Sigel, R. Sigel, *Metallomics and the Cell (Metal Ions in Life Sciences Book 12)*, Springer, Dondrecht, **2013**.

[10] S. Das, T. Balaraju, S. Barman, S. S. Sreejith, R. Pochamoni, S. Roy, *Front. Chem.* **2018**, *6*, 1–11.

[11] F. Sheng, Q. Yang, D. Cui, C. Liu, Y. Sun, X. Wang, W. Su, *Energy fuels* **2020**, *34*, 10282–10289.

9 List of scientific contributions

List of Publications

Published:

[1] T. Buchecker, **P. Schmid**, S. Renaudineau, A. Proust, O. Diat, A. Pfitzner and P. Bauduin: Polyoxometalates in the Hofmeister series. *Chem. Commun.* **2018**, *54*, 1833-1836.

[2] T. Buchecker, **P. Schmid**, I. Grillo, S. Prévost, M. Drechsler, O. Diat, A. Pfitzner and P. Bauduin: Self-Assembly of Short Chain Poly-*N*-isopropylacrylamid Induced by Superchaotropic Keggin Polyoxometalates: From Globules to Sheets. *J. Am. Chem. Soc.* **2019**, *141*, *17*, 6890-6899.

[3] **P. Schmid**, T. Buchecker, A. Khoshsima, D. Touraud, O. Diat, W. Kunz, A. Pfitzner and P. Bauduin: Self-assembly of a short amphiphile in water controlled by superchaotropic polyoxometalates: $H_4SiW_{12}O_{40}$ vs. $H_3PW_{12}O_{40}$. *J. Colloid Interface Sci.* **2021**, *587*, 347-357.

[4] C. Falaise, S. Khlifi, P. Bauduin, **P. Schmid**, W. Shepard, A.A. Ivanov, M.N. Sokolov, M.A. Shestopalov, P.A. Abramov, S. Cordier, J. Marrot, M. Haouas, E. Cadot: "Host in host" supramolecular core-shell type systems based on a giant ring-shaped polyoxometalate. *Angew. Chem. - Int. Ed.* **2021**, *60*, *25*, 14146-14153, *Angew. Chem.* **2021**, *133*, *25*, 14265-14272.

[5] M. Hohenschutz, I. Grillo, C. Dewhurst, **P. Schmid**, L. Girard, A. Jonchère, O. Diat, P. Bauduin: Superchaotropic nano-ions as foam stabilizers. *J. Colloid Interface Sci.* **2021**, 603, 141-147.

[6] **P. Schmid**, X. Graß, P. Bahadur, I. Grillo, O. Diat, A. Pfitzner, P. Bauduin: Polymeric Surfactant P84/Polyoxometalate α-$PW_{12}O_{40}^{3-}$ - A Model System to Investigate the Interplay between Chaotropic and Hydrophobic Effects. *Colloids Interfaces* **2022**, 6(1), 16.

[7] **P. Schmid**, G. Jost, X. Graß, D. Touraud, O. Diat, A. Pfitzner, P. Bauduin: {2-phases 2-reactions 1-catalyst} concept for the sustainable performance of coupled reactions. *Green Chem.* **2022**, 24, 2516-2526.

[8] **P. Schmid**, M. Hohenschutz, X. Graß, M. Witzmann, D. Touraud, O. Diat, A. Pfitzner, P. Bauduin: Counterion effect on α-Keggin polyoxometalates in water: the peculiar role of H^+ on their salting-in effect and co-assembly with organics. *J. Mol. Liq.* **2022**, *359*, 119214.

In preparation:

[9] C. Falaise, S. Khlifi, P. Bauduin, **P. Schmid**, W. Shepard, J. Marrot, M. Haouas, D. Landy, C. Mellot-Draznieaks, E. Cadot: Disrupting Self-Assembly Process of Non-Ionic Surfactant by Super-Chaotropic Wheel-Shaped Giant Polyoxometalate. *Angew. Chem. - Int. Ed.*

[10] **P. Schmid**, D. Touraud, M. Hohenschutz, O. Diat, A. Pfitzner, P. Bauduin: The potential role of chaotropic polyoxometalates in the origin of life. *Nat. Chem.*

[11] **P. Schmid**, X. Graß, D. Touraud, A. Pfitzner, P. Bauduin: A paradox: Hydrophilic molecular metal-oxides are selective solubilizers for moderately hydrophobic compounds. *Chem. Commun.*

List of oral presentations

P. Schmid, O. Diat, A. Pfitzner, P. Bauduin: {2-phases 2-reactions 1-catalyst} concept for the sustainable performance of coupled reactions, **2022**, International Symposium on Green Chemistry, La Rochelle (France).

P. Schmid, O. Diat, A. Pfitzner, P. Bauduin: Superchaotropic Polyoxometalates – From Fundamental Investigations Towards Potential Applications, **2022**, during a research stay, Institut de Chimie Séparative de Marcoule (France).

P. Schmid: diverse topics, **regularly**, Co-worker seminar in the laboratory of ions at active interfaces (L2IA), Institut de Chimie Séparative de Marcoule (France).

P. Schmid: diverse topics, **regularly**, Co-worker seminar at the Institute of Inorganic Chemistry, University of Regensburg (Germany).

10 Declaration of Authorship

(1) Ich erkläre hiermit an Eides statt, dass ich die vorliegende Arbeit ohne unzulässige Hilfe Dritter und ohne Benutzung anderer als der angegebenen Hilfsmittel angefertigt habe; die aus anderen Quellen direkt oder indirekt übernommenen Daten und Konzepte sind unter Angabe des Literaturzitats gekennzeichnet.

(2) Bei der Auswahl und Auswertung haben mir die zu Beginn des jeweiligen Kapitels aufgeführten Personen in der jeweils beschriebenen Weise unentgeltlich geholfen.

(3) Weitere Personen waren an der inhaltlich-materiellen Herstellung der vorliegenden Arbeit nicht beteiligt. Insbesondere habe ich hierfür nicht die entgeltliche Hilfe eines Promotionsberaters oder anderer Personen in Anspruch genommen. Niemand hat von mir weder unmittelbar noch mittelbar geldwerte Leistungen für Arbeiten erhalten, die im Zusammenhang mit dem Inhalt der vorgelegten Dissertation stehen.

(4) Die Arbeit wurde bisher weder im In- noch im Ausland in gleicher oder ähnlicher Form einer anderen Prüfungsbehörde vorgelegt.

Regensburg, August 03, 2022 _____

Philipp Schmid